Functional supramolecular materials : fundamentals, copolymers and applications

Functional supramolecular materials

Fundamentals, copolymers and applications

PROEFSCHRIFT

ter verkrijging van de graad van doctor aan de
Technische Universiteit Eindhoven, op gezag van de
rector magnificus prof.dr.ir. F.P.T. Baaijens,
voor een commissie aangewezen door het College voor Promoties, in het
openbaar te verdedigen
op donderdag 7 maart 2019 om 16:00 uur

door

Beatrice Adelizzi

geboren te Monza, Italië

Dit proefschrift is goedgekeurd door de promotoren en de samenstelling van de promotiecommissie is als volgt:

voorzitter:	prof. dr. A. P. H. J. Schenning
1e promotor:	prof. dr. E. W. Meijer
copromotor:	dr. ir. A. R. A. Palmans
leden:	prof. dr. J. Lacour (Université de Genève)
	prof. dr R. J. M. Nolte (Radboud Universiteit)
	prof. dr. R. P. Sijbesma
adviseurs:	dr. S. C. J. Meskers
	prof. dr. A. Abbotto (Università degli studi di Milano Bicocca)

Het onderzoek of ontwerp dat in dit proefschrift wordt beschreven is uitgevoerd in overeenstemming met de TU/e Gedragscode Wetenschapsbeoefening.

A mia Nonna,
Alla sua forza e alla sua gentilezza

"All sort of things can happen
when you are open to new ideas
and playing around with things"

Stefanie Kwolek
Polymer chemist, inventor of Kevlar®

A catalogue record is available from the Eindhoven University of Technology Library
ISBN: 978-90-386-4712-8

Cover design: Beatrice Adelizzi

Printed by: Gildeprint, Enschede (the Netherlands)

This project has been financially supported by the European Union Horizon 2020 and innovation program (Marie-Sklodowska-Curie grant agreement No. 642083) and from the Ministry of Education, Culture and Science of The Netherlands (Gravity program 024.001.035)

Table of Contents

1.

The future of supramolecular copolymers unveiled by reflecting on covalent copolymerization

The results of this work are summarized in the perspective:

B. Adelizzi, N. J. Van Zee, L. N. J. de Windt, A. R. A. Palmans, E. W. Meijer
Submitted

Abstract: Supramolecular copolymers are an emerging class of materials and in the last year their potential has been demonstrated on a broad scale, from biomaterials to electronics. Implementing non-covalent polymers with multiple components can bring together useful features such as reversibility and new functionalities. However, mastering and tuning the microstructure of these systems is still an open challenge. In this introductory chapter, we aim to trace the general principles of supramolecular chain copolymerization by analyzing them through the lens of the well-established field of covalent copolymerization. Our goal is to delineate guidelines that classify and analyze supramolecular copolymers in order to create a fruitful platform to design and investigate new multicomponent systems.

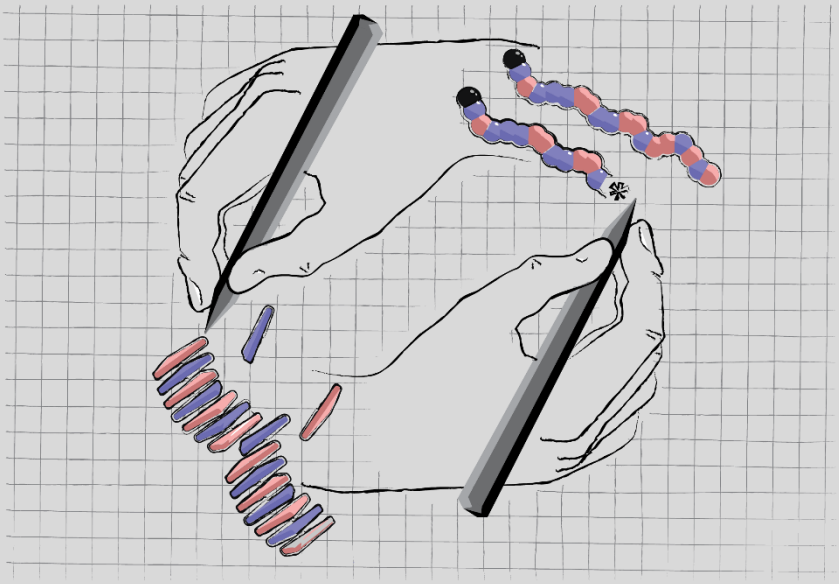

1.1 Introduction

While one-dimensional supramolecular polymers have long been employed by Nature as a powerful structural motif, scientists have only recently begun to exploit their dynamicity, directionality, and functionality. This confluence of properties makes them promising for applications in pharmaceuticals, nanoelectronics and catalysis, but many fundamental principles that dictate the structure of supramolecular polymers remain unresolved. In 2009, we proposed to draw inspiration for future research directions by carefully considering the maturation of its older sister, covalent polymerization.[1] Following Carothers's classic classification of covalent polymers, supramolecular polymers have been categorized based on the process through which each aggregate is formed. As a result, connections between the two fields became strikingly clear. Isodesmic polymerization can be considered a non-covalent analogue of step growth polymerization, characterized by high polydispersity and a degree of polymerization that depends on the association constant of the supramolecular units. Ring-opening supramolecular polymerization is similar to ring opening polymerization and depends on the equilibrium between linear and cyclic aggregates. Finally, cooperative supramolecular polymerization can be correlated to chain growth polymerization. These connections helped to highlight the distinctions between covalent and supramolecular polymerization processes, rendering underlying research needs into tangible goals.

In this context, one of the directions that we identified was the fascinating challenge to make well-defined supramolecular copolymers. At that time, in stark contrast to the multitude of methods available to tailor covalent copolymers, there were few synthetic strategies to control the microstructure of supramolecular copolymers. The origin of this challenge is the inherent lability of non-covalent bonds, which are typically less kinetically and thermodynamically stable than covalent bonds. However, in the past 10 years, considerable inroads have been made to reconcile the dynamicity of supramolecular polymers with the demand for microstructural control. Many studies and comprehensive reviews[2-6] have since been published focusing on nucleation-elongation processes, kinetic control, competition, pathway complexity, and supramolecular monomer design.

In this introductory chapter, we reflect on this progress through the lens of covalent copolymerization to illuminate challenges and opportunities for the future. Considering the ubiquity of well-defined covalent copolymers, we sustain that controlling the structure of one-dimensional supramolecular copolymers is paramount to realize next-generation functional materials. The objective of this introductory chapter is to generate insight into urgent research directions by creating a strong link between covalent and non-covalent copolymerization worlds. Although the first supramolecular copolymers, as the one reported by Lehn and coworkers,[7] are based on isodesmic mechanism and non-covalent interactions among complementary units, in this chapter we mainly focus on cooperative copolymerization. As a point of reference, we chose to

structure this work based on the organization employed in the chain copolymerization chapter of Odian's classic textbook *Principles of Polymerization*.[8] We particularly focus on the synthesis of the copolymers and of the state-of the art of the structures today achievable, discussing on the parallel roles of developing theoretical models and characterization techniques fundamental for the development of the field.

1.2 Supramolecular chain growth copolymerization

1.2.1 Covalent and non-covalent copolymerization. Similarities and differences

We named supramolecular chain growth copolymerization (or cooperative supramolecular copolymerization) as the direct analogue of covalent chain growth copolymerization since the two classes share several similitudes. At first, the growth mechanism requires a certain activation to obtain a cooperative fast growth of the polymer. For covalent polymers, the presence of an initiator allows the activation of the monomers, followed by the growth of the polymer (Figure 1a).[9] Similarly, cooperative supramolecular polymers require the unfavorable formation of nuclei (formed by small aggregates) to allow the growth of the polymers (Figure 1b).[1]

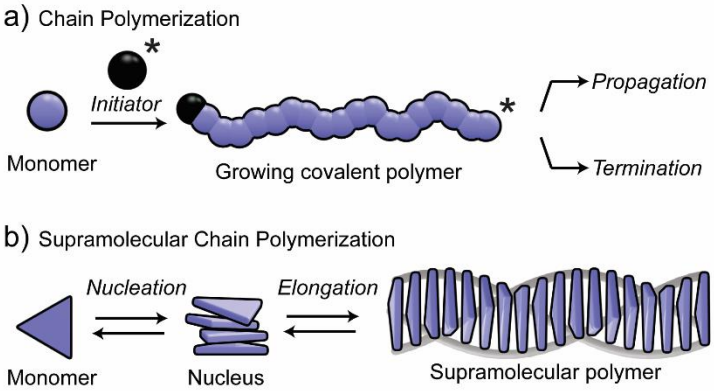

Figure 1: Growth mechanism for chain polymerization. (a) For covalent polymer, the polymerization is activated by an initiator, then active chain ends attack sequentially monomer after monomer creating a progressively longer polymer chain (propagation). The polymerization is interrupted (termination) when the active chain ends is deactivated. (b) Supramolecular polymers which are formed by a cooperative mechanism present a process comparable to the chain growth. The supramolecular polymerization is activated by the formation of a nucleus which then sequentially incorporates a growing number of monomers. The formation of the nucleus (nucleation) is thermodynamically unfavorable, whereas the propagation of the supramolecular polymer (elongation) is thermodynamically favorable. This leads to the formation of few nuclei which evolve cooperatively into long supramolecular polymers

The polymerization process is in both the cases sensitive to the presence of impurities,[10,11] co-solvents,[12-14] differences in the reaction time and temperature. All these factors strongly affect the chain length of the polymers and sometimes also of the copolymer's microstructure.[15,16] Nevertheless, once the polymer is formed, macroscopic changes such as viscosity,[16-18] or optical properties[18-21] occur and the aggregated states present new, interesting functionalities absent in the related monomers.

Moreover, several synthetic strategies used to control structure in both covalent and supramolecular chemistries share mechanistic similarities. However, before describing those, the distinction in the kinetics of polymerization has to be cited. Covalent chain polymerization occurs upon a fast initiation step and a slow polymerization. Instead, classic cooperative supramolecular polymerization has as rate determining step the formation of nuclei, while the growth of the polymer occurs faster. Despite this difference, the two classes share the possibility of using chain transfer agents and chain stoppers to provide control over the average length of the polymers.[22-24] In addition, the recent introduction of supramolecular living polymerization[25] by activation of dormant supramolecular monomers with some molecular[26-28] or aggregated[29-31] initiators unlocked the possibility of achieving self-assembled polymers with controlled length similarly to living chain copolymerization.

However, the nature of the bonds that hold supramolecular and covalent polymers together are sharply distinct. In contrast to the thermodynamic stability of covalent copolymers, supramolecular copolymers are dynamic and reversible because they are held together by relatively weak non-covalent interactions (*e.g.*, hydrogen bonding, π-π stacking, and van der Waal's forces). The monomers' sequence of a supramolecular copolymer is thus fluxional, as monomers can exchange their relative positions within a given polymer chain or integrate into other chains. Consequently, supramolecular polymers don't terminate in the way that covalent polymers do. These properties impart unique adaptability and modularity to the resulting materials, but they render the analysis of their structure a great challenge. Another striking difference is that supramolecular polymerizations often show pathway complexity.[32] Small differences to the conditions of aggregation (*e.g.*, variation in temperature or solvent) can cause a given set of monomers to form different self-assembled structures.[33-35] Covalent polymerizations are also sensitive to changes in reaction conditions, giving rise to fluctuations in, for example, polydispersity, tacticity, and monomer sequence. These changes, however, are permanently encoded into the final covalent polymers. In the case of pathway complexity of supramolecular polymers, the concentration of each type of aggregate is not constant and dynamically responds to changes in reaction conditions. The ability to tune aggregate structure at will highlights the extreme sensitivity and potential utility of these structures.[36]

1.2.2. The non-innocent effect of solvents in supramolecular polymerization

Before proceeding, it is important to consider solvent in defining copolymer compositions. In the case of covalent copolymerization, the choice of solvent can be an important tool for tuning relative polymerization rates, which ultimately determines the microstructure of a copolymer. The interaction between the solvent and the propagating polymer species is frequently supramolecular in nature. For example, solvent polarity dictates the strength of ion pairing in the anionic copolymerization of vinyl monomers, which consequently modulates the reactivity of the propagating carbanion chain-end toward different monomers depending on their respective structures.[9] The resulting polymers are then typically represented in terms of their polymerized monomer units. When dispersed in a solvent, the solvent interacts with the polymer to some degree depending on the temperature and the reactivities of the polymer and the solvent. However, these associated solvent molecules are generally not included in the polymer's chemical structure because they are not covalently bonded to the polymer.

This distinction does not exist in the case of supramolecular copolymerization because solvent molecules interact with the resulting supramolecular copolymer via the same kind of non-covalent forces that hold the monomers of the aggregate together. For this reason, a supramolecular "homopolymerization" of a single monomer may not be a homopolymerization at all—solvent molecules could serve an essential role in supporting the fiber's supramolecular structure, and thus such a naming convention is potentially misleading because it deemphasizes the importance of solvent molecules as structural units. It is nevertheless difficult to unambiguously assign the role of solvent in most supramolecular systems, and so we acknowledge the necessity of simplifying supramolecular polymer structures by describing them primarily in terms of their principle monomer component(s).

Solvent effects have been reviewed elsewhere,[37,38] but here we would like to highlight recent efforts to exploit the action of solvents as a means to control supramolecular structure. The most common manifestation of this approach is to add a "good" solvent (*i.e.*, a solvent that competitively associates with the supramolecular units) to denature supramolecular fibers, thereby controlling their average size. Aida and co-workers[39] recently expanded this principle by balancing denaturation with the self-association of the denaturant to realize bisignated supramolecular polymerization as a function of temperature. Others have shown that the helicity of one-dimensional fibers—usually evaluated using circular dichroism spectroscopy—can be controlled through tuning the interplay of structure and reactivity between both the supramolecular polymer and the solvent. Our group and others[40,41] have shown that the shape of the solvent can directly influence the helicity of supramolecular fibers, suggesting that molecular packing of solvent into the fiber's corona gives rise to perturbations to the inner core of the fiber.

Water must also be acknowledged for its importance as a structural element in supramolecular polymers in bulk and in solution. In the bulk, Qi, Schalley, and co-workers[42] demonstrated that water acts as an essential structural component that unlocks impressive adhesive properties to supramolecular polymers formed with crown ether-functionalized benzene tricarboxamides. In aqueous media, Han, Stupp and co-workers[43] establish a striking resemblance between the interaction of water and synthetic peptide nanofibers with the interaction between water and natural supramolecular materials such as proteins. Water in the interior of such fibers exhibit rapid diffusion, while water at the surface of the fiber is essentially immobilized, suggesting that these water molecules form hydrogen bonds with the fiber and serve an integral role in supporting the fiber's structure. In organic solvents as well, several reports[44–50] point to the fundamental relationship between supramolecular structure and the presence of water—even trace amounts in highly apolar solvents. Our group[49] recently reported that the monomeric nature of water in alkanes gives rise to a potent thermodynamic driving force for it to bind to co-dissolved supramolecular polymers and effect profound changes to their structures. We believe that this growing body of research expresses both the complexity and import of solvent molecules as not merely spectators but as active participants in one-dimensional supramolecular polymerization.

1.2.3. Type of copolymers

Covalent copolymers are commonly categorized by their structure, which can be block, blocky, periodic, random, or alternating (Figure 2). In addition, graft copolymers are branched polymers where the backbone is constituted by one type of monomer whereas the side-chains exclusively comprise the second type of monomers.

Random copolymers do not present a defined organization in the monomer distribution within the polymer chains. Alternating copolymers, identified as **poly(A-*alt*-B)**, contain two monomers in a regular alternate distribution $(\mathbf{AB})_n$, whereas in periodic copolymers the two monomers are arranged in a periodic fashion. Block and blocky copolymers contain both long sequences of each monomers in the copolymer chain. Block copolymers, **poly(A-*b*-B)**, are linear polymers with long sequences of each monomers species $(\mathbf{A}_m\mathbf{B}_n)_p$, while blocky copolymers show shorter sequences of each monomer.

In supramolecular copolymerization, the formation of linear structures has been prevalent, although some recent, outstanding works on nanocrystals are currently initiating the grafting field.[51,52] Our focus is here centered on 1D copolymers (Figure 2c), from the synthesis to the study of their composition and microstructure. Our ultimate aim is to create the basis for drawing a direct relation between the molecular structure of the monomers and the resulting copolymer microstructure.

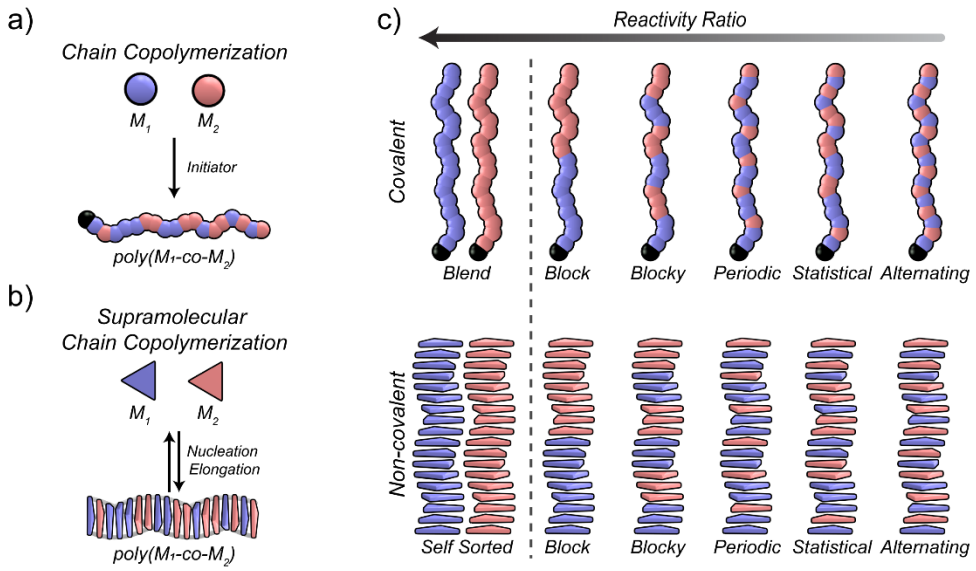

Figure 2: Analogies between covalent and supramolecular chain copolymerization. General copolymerization mechanism for (a) covalent polymers and (b) supramolecular polymers. (c) List of possible copolymer microstructures for both covalent and supramolecular (non-covalent) copolymers. Polymers ordered from high reactivity ration (with no inter-reactivity: blend for covalent and self-sorted for supramolecular polymers) to low reactivity ration, (with high inter-reactivity: alternating copolymers).

1.3 Supramolecular copolymer composition

As in covalent copolymerization, theoretical models are essential for understanding the composition of supramolecular copolymers. Theory is especially valuable here because the inherent dynamicity of supramolecular copolymers makes it difficult to experimentally determine the microstructure. For supramolecular copolymers which are obtained under thermodynamic equilibrium, the model developed by ten Eikelder and Markvoort,[53] aids the composition analysis by treating supramolecular copolymerizations as a set of reversible reactions between monomers and polymers. Similar to the terminal model of chain copolymerization, the equilibrium constant of a reaction is assumed to depend only on the identity of the last-enchained monomer; an added assumption is that monomers can only add to the end of a growing chain. For example, the assembly of **A** and **B** to form supramolecular copolymer **P** can thus be described by four reactions (Figure 3a) that provide the basis for deriving expressions for the concentration and composition of the copolymers.

The concentration of copolymers is expressed in terms of the concentration of polymerized monomer units ($[\boldsymbol{M}]_{pol}$), which in turn can be expressed in terms of the total concentration of monomer ($[\boldsymbol{M}]_{tot}$) and the concentration of free monomer ($[\boldsymbol{M}]_{free}$, Figure 3b, top). A similar equation can be derived for the fraction of polymerized

monomers ϕ_{pol} (Figure 3b, bottom). To determine the concentration of free monomer as well as the concentration and composition of the copolymers, the elaborated forms of these mass balance equations are solved numerically with the input consisting of the known $[\boldsymbol{M}]_{tot}$ and the experimentally determined equilibrium constants $K_{\mathbf{A}\text{-}\mathbf{A}}$, $K_{\mathbf{A}\text{-}\mathbf{B}}$, $K_{\mathbf{B}\text{-}\mathbf{A}}$, and $K_{\mathbf{B}\text{-}\mathbf{B}}$ (Figure 3a).

From this model and subsequent simulation, we can extract thermodynamic parameters that help us to understand the supramolecular microstructure. As in covalent copolymerization, reactivity ratios are a useful tool for comparing microstructures when the monomers are less, equally, or more reactive in copolymerization compared to homopolymerization. Here, the reactivity ratio R is defined as the ratio of Gibbs free energy change of the homo-aggregation ($\Delta G_{\mathbf{A}\text{–}\mathbf{A}}$ + $\Delta G_{\mathbf{B}\text{–}\mathbf{B}}$) to the Gibbs free energy change of the hetero-aggregation ($\Delta G_{\mathbf{A}\text{–}\mathbf{B}}$ + $\Delta G_{\mathbf{B}\text{–}\mathbf{A}}$, Figure 3c). For values of R greater than unity, monomers preferentially interact with their own type of monomer, while for values of R smaller than unity, the monomers tend to co-assemble.

This behavior is reflected in the shape of the copolymerization curve obtained for each class of R. As an example, we simulated the results for the temperature-induced supramolecular copolymerization of **A** and **B**. We arbitrarily set the thermodynamic parameters such that the elongation temperatures for **poly(A)** and **poly(B)** sit at 70 and 60 °C, respectively. We then varied the value of R by keeping the values of $\Delta G_{\mathbf{A}\text{–}\mathbf{A}}$ and $\Delta G_{\mathbf{B}\text{–}\mathbf{B}}$ constant and modifying the values of $\Delta G_{\mathbf{A}\text{–}\mathbf{B}}$ and $\Delta G_{\mathbf{B}\text{–}\mathbf{A}}$. In this way, we modulate the tendency of the monomers to interact with each other while holding their tendency to homopolymerize constant. The resulting copolymerization curves (from black to light gray), as well as the fraction of polymerized **A** and **B** (red and blue, respectively), are presented in Figure 3d. As R approaches infinity, two elongation temperatures are clearly evident, consistent with self-sorted homopolymerization of **A** and **B**. As the value of R is reduced, only one elongation temperature is evident, suggesting some degree of copolymerization. This elongation temperature shifts toward higher temperatures as the value of R is decreased—that is, the copolymer forms at higher temperature as hetero-aggregation becomes more favorable. The incorporation of **A** and **B** in **poly(A-*co*-B)** depends on R as well. A coinciding incorporation of the two monomers is visible for alternating systems (R <1) whereas increasing the value of R results in a greater disparity between the two curves.

A useful extrapolation is the calculation of the fraction of polymerized **A** as a function of temperature (Figures 3e, 3f). For R > 1, at high temperatures, the copolymers are rich in monomers of type **A**. As temperature decreases, monomers of type **B** enter into the copolymers, and the composition of the copolymers approaches the composition of the mixture of monomers. For R < 1, where alternating structures can be formed, at high temperatures monomers **B** are already incorporated into the copolymers and the copolymers' composition already resembles the composition of the mixture. Thus, as the value of R decreases, monomers enter into the copolymers more by interacting with the other type of monomer and less by interacting with their own type of monomers.

An important issue to keep in mind, as with all models, is that care must be taken to evaluate the validity of the assumptions for the system at hand. This model strictly considers the interactions between two monomers—complications due to solvent interactions or pathway complexity are excluded. In cases where such factors strongly influence self-assembly, one can either modify the model to account for new interactions or use the base model without fitting to generate qualitative comparisons.

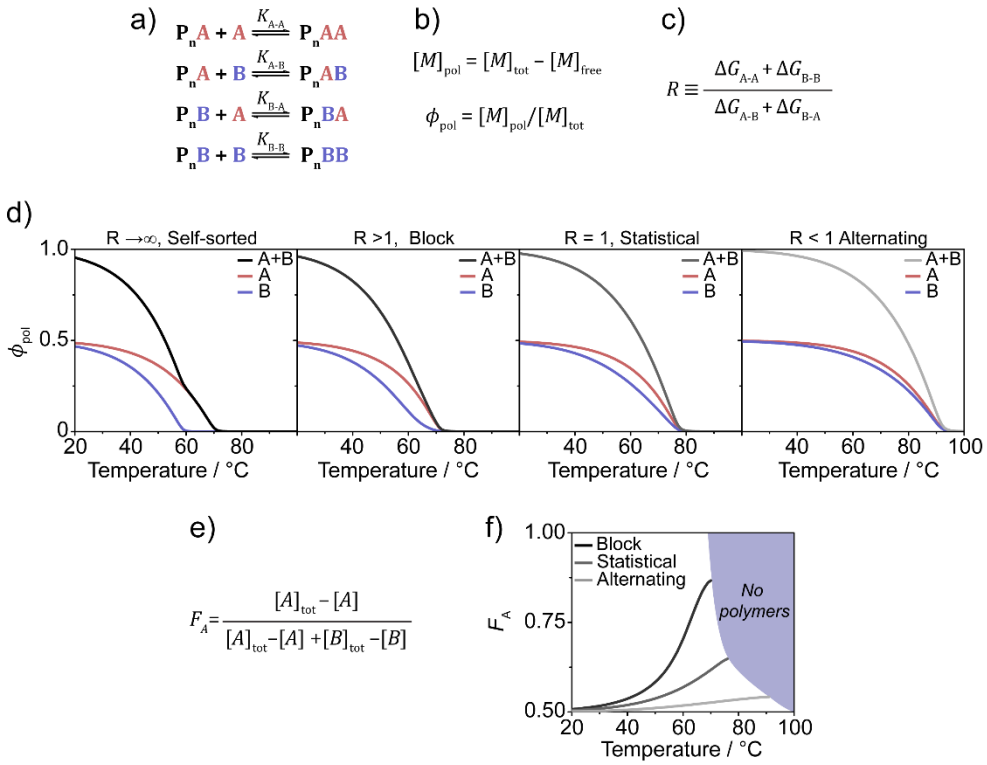

Figure 3. (a) Terminal model of the supramolecular copolymerization between two types of monomers. The model assumes that the equilibrium constant (K) is dependent on the types of the terminal monomer unit (P_nA or P_nB) and the polymerizing monomer (A or B). (b) The mass balance defines the concentration of polymerized monomer $[M]_{pol}$ as the difference between the total concentration of monomer $[M]_{tot}$ and the free monomer $[M]_{free}$ and the fraction of polymerized monomer units as ϕ_{pol}. (c) The composition and microstructure of the copolymer is dominated by the value R which is defined as the ratio of the sum of changes in Gibbs free energy of interactions between the same types of monomer ($\Delta G_{A-A} + \Delta G_{B-B}$) to the sum of changes in Gibbs free energy of interactions between different types of monomer ($\Delta G_{A-B} + \Delta G_{B-A}$). (d) The resulting copolymerization curves as a function of R are reported. From left to the right, descending order from R approaching infinite values for self-sorted systems (black curve) to R smaller than 1 (light gray curve). The incorporation of the single monomers into the copolymer is also reported (red lines for A and blue lines for B). (e) Equation defining the fraction of monomers A in the copolymer and (f) related graph display how of F_A varies as a function of temperature and R.

1.4 Microstructures observed in supramolecular copolymers

1.4.1 Sequence length distribution

The copolymerization equations for covalent copolymers define macroscopically the composition of copolymers, namely, the overall composition of a copolymer obtained from a specific co-monomer feed. However, two further details concerning the copolymer at a molecular level can be unraveled. First, the exact arrangement of the two monomers along the polymer chain, which eventually determines the copolymer microstructure, and the difference in composition from one copolymer chain to another.

The difference in composition from one copolymer chain to another represents a crucial point in covalent polymer chemistry since it has been demonstrated that small fluctuations in the monomer sequence (naturally present in the covalent copolymer chains) can strongly influence the properties of the material.[54] This uncontrolled variation motivated the field to achieve sequence controlled polymers and eliminate the chain-to-chain variation.[55] Interestingly, this issue partly loses its importance in supramolecular copolymers. The dynamicity of these systems and the constant exchange of the monomers along the polymer chain, and especially among different chains, tents to homogenize the composition for all the copolymer chains in the system.[56]

However, the determination of the monomer arrangement along the polymer chain is today a key challenge in supramolecular copolymers as it has been in covalent polymer chemistry. In this case, the monomers' exchange and the intrinsic dynamicity complicate the characterization of the microstructure. Nowadays in supramolecular chemistry examples of alternating, periodic and block copolymers have been described and can be taken as guidelines to reconsider some seminal works (where the microstructure determination was not possible) and rationalize the molecular designs of supramolecular co-monomers.

1.4.2. Alternating copolymers

Alternating supramolecular copolymers were probably the first category of supramolecular copolymers reported in literature. In 1990 Jean Marie Lehn and coworkers presented seminal works on 1D $(AB)_n$ structures based on multiple hydrogen-bonded complementary units.[57,7] Few years later other examples of complementary units[58-60] and organometallic supramolecular systems[61] were proposed by several groups. Still today, the general strategy applied to form alternated microstructures consists of using monomers with a high tendency to co-interact. Together with complementary units, the other common strategy is the exploitation of donor-acceptor monomers which copolymerize via charge transfer interactions.[62-64]

Most recently, Besenius and coworkers demonstrated the formation of alternating supramolecular copolymers in aqueous solutions,[65,23] (Figure 4a) and by sequential growth from Au-surface.[66,67] Monomers based on benzene triamides bearing positively, **1**, and negatively, **2**, charged β-sheet encoded oligopeptides form alternating copolymers **poly(1-*alt*-2)** via electrostatic interactions. Another example on peptide assembly has been reported by Giuseppone's group.[68] Copolymerization in water between bisurea domains functionalized with bioactive peptide or fluorescent cyanine dyes resulted in fibers with an alternated fashion as sustained by fluorescence experiments.[68]

Alternatively, Araki and coworkers in 2003 reported the formation in bulk of alternating supramolecular copolymers between cyclohexane triamides (CHTA) functionalized with linear (l-CTHA) and branched (b-CHTA) side chains.[69] The bulky side chains of b-CHTA do not allow the formation of stable hydrogen bonding with analogous monomers preventing homopolymerization. However, b-CHTA can intercalate into the hydrogen bonding network of l-CHTA in an alternate fashion as detected by IR spectroscopy.

Another interesting example is reported by Chen *et al.* in which the formation of an alternating supramolecular copolymer is described with an $[(A)_6B]$ structure via hierarchical organization (Figure 4b).[70] The origin of the alternating position of the monomers in the copolymer chain is because six monomers, **3**, form a planar hexagonal structure held by complementary hydrogen bonds. The so-formed hexagonal supramolecular monomer $\mathbf{3_6}$ bears 6 Zn-porphyrins which are then coordinated by the multivalent monomer, **4**, resulting in the alternated supramolecular copolymer **poly[$(3)_6$-*alt*-4]**.

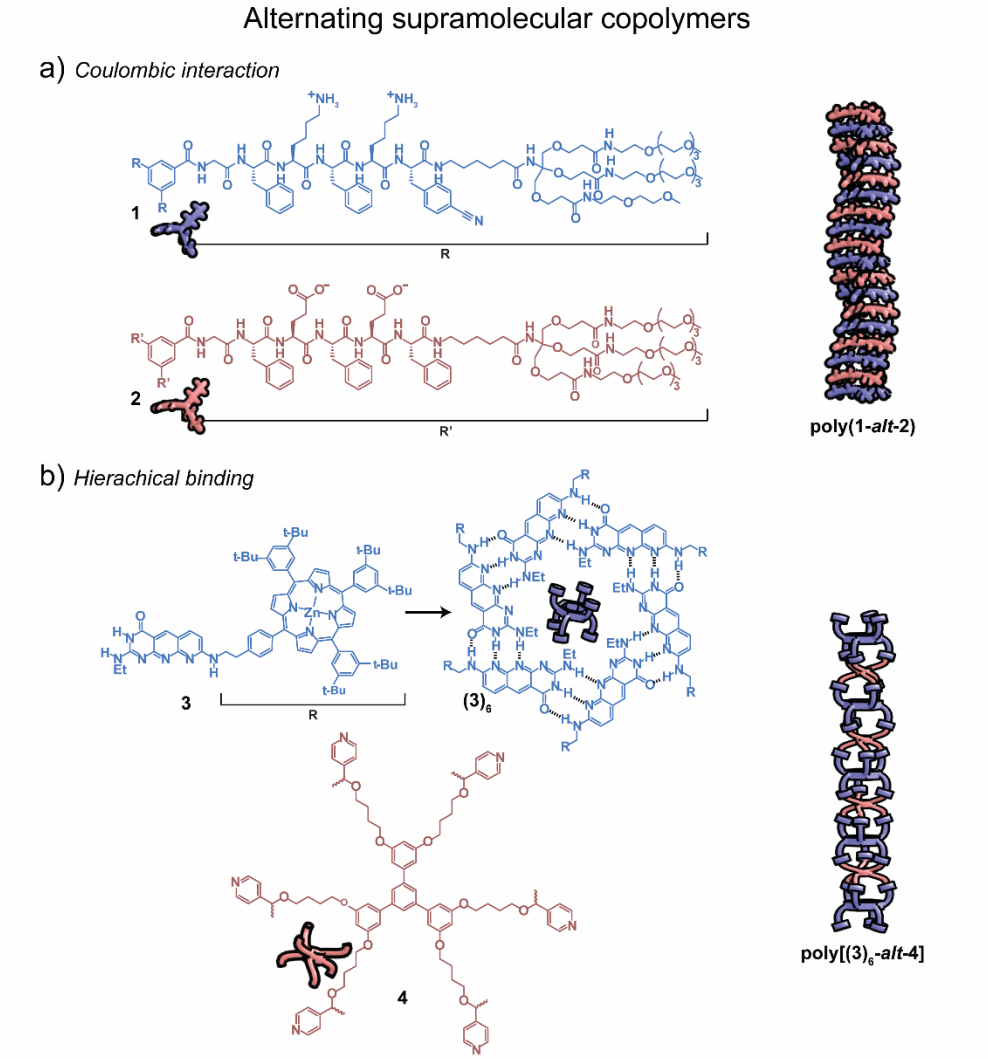

Figure 4. Examples of alternating supramolecular copolymers achieved with different strategies. The alternate microstructure is obtained via (a) Coulombic interaction, (b) with complementary hierarchical interactions.

1.4.3. Periodic copolymers

Few examples of periodic supramolecular copolymers have been reported in the last 10 years. Würthner's group described in 2009 the formation of $[(A)_2B]$ structured copolymers via unconventional interactions between complementary monomers: a perylene bisimide (**6**) and an azobenzene-functionalized melamine (**5**).[71] They reported that **5** and **6** do not form long organized structures in methylcyclohexane (MCH) in a 1:1 ratio as expected by ditopic 3-folded hydrogen bonding complementary units. Contrarily, the polymerization with a 2:1 ratio (in favor of **5**) unexpectedly formed organized copolymers **poly[(5)$_2$-*per*-6]** characterized by *J*-type aggregates (Figure 5a). Würthner and coworkers stressed the importance of the assembly procedure to get organized structures, which required an equilibration time of 15 h at 20 °C. Atomic force microscopy (AFM) imaging showed the presence of tightly coiled helical polymers with defined pitch (6 nm) and length (100-200 nm).

More recently, the same group reported how a similar distorted perylene bisimides, bearing the imides protected with water-soluble chains (**8**) can copolymerize in a (A_mB_2) fashion with a planar analogue (**7**).[72] The homopolymerization of **7** in water followed an isodesmic path forming stiff short nanorods via π-π interaction. The distorted **8** formed dimers which then created less-defined nanoworms via hydrophobic interactions. The kinetically controlled copolymer was obtained by injecting water in a molecularly dissolved tetrahydrofuran (THF) solution of **8** and **7** in a 1:2 ratio, followed by the evaporation of THF under ambient conditions. By combined optical, NMR and transmission electron microscopy (TEM) techniques they unraveled the supramolecular structure as **poly[(7)$_4$-*per*-(8)$_2$]** in which **8** was dimerized and intercalated into the polymer of **7** (Figure 5b). Interestingly, **poly[(7)$_4$-*per*-(8)$_2$]** showed long and thin flexible fibers which significantly deviated from the original morphology of the two homopolymers. The flexibility of the dimers of **8** combined with the rigidity of the block formed by **7** cooperated to form long and well-defined 1D copolymers, similarly to covalent elastomers where soft and hard block alternate to give new functionality.[73]

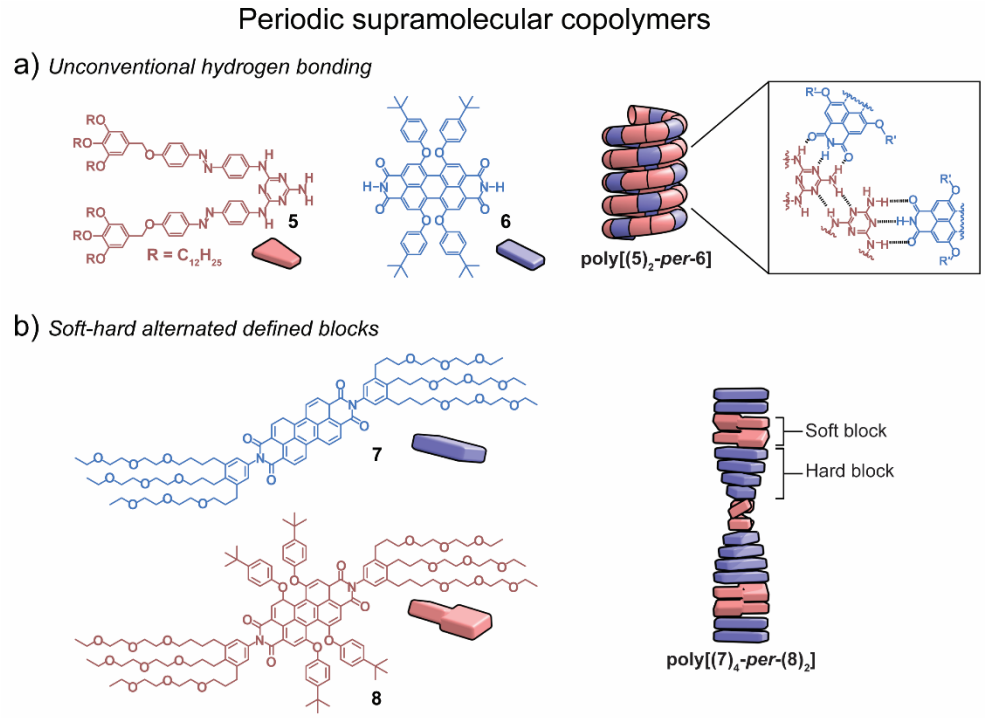

Figure 5. Examples of periodic supramolecular copolymers achieved with different strategies. (a) Stable helical copolymers with $[(A)_2B]$ pattern were obtain by unconventional hydrogen bonding interaction between complementary units of malemine-funcitonalized azobenzene (**5**) and perylene bisimide (**6**) resulting in **poly[(5)$_2$-*per*-6]**. (b) Planar (**7**) and twisted (**8**) perylene bisimide have found to copolymerize via kinetic control with $[(A)_m(B)_2]$ sequence. Stable long copolymers were obtained for 2:1 ratio giving **poly[(7)$_4$-*per*-(8)]**.

1.4.4. Block copolymers

The field of supramolecular block copolymers has attracted much interest in multicomponent supramolecular copolymerization. The formation of defined block structures can potentially offer a great platform for new functionalities and a direct use in optoelectronics. However the non-covalent nature of the bonds, the intrinsic reversibility of the polymerization and the rapid exchange of monomers among different polymer chains represent great challenges. Seminal works in the field leaded by Winnik, Manners and Aida overcame the issue of random mixing using kinetic control in the form of sequential addition of the monomers.

In 2007, Winnik, Manners and coworkers published the first block co-micelles with **A-B-A** structures made of polyferrocenyldimethylsilane (PFS) block copolymers as monomeric units.[74] Via a kinetic process named living crystallization (closely related to the living polymerization previously mentioned) they were able to create short homo-micelles. These were found to show uniform growth upon the addition of further monomers, and maintained a narrow length distribution. Upon addition of a different

dissolved polymer, they achieved the formation of triblock copolymers with controlled length. This strategy exploited the low dynamicity of the homo-aggregates and the sequential seeding of the second monomer.

The living nature of these supramolecular micelles allows the formation of a great variety of supramolecular block copolymers. The extensive work on PFS block copolymers included the formation of regular crossed co-micelles,[75] di- and tri- block comicelles,[76] fluorescent multi-block micelles[77,78] and co-micelles between linear and brush units.[79] In the last years, photocleavable units were introduced to add responsiveness to the system,[80] and different multidimensional micelles were synthesized.[51,52,81] Lately, the universality of this approach has been further proven by the possibility of using different conjugated, crystallizable units. A–B–A co-micelles were reported by Choi's group with photoswitchable poly(*p*-phenylvinylene)[82] and by Friend, Whittell and Manners's groups with poly(di-*n*-hexylfluorene).[83] The latter, based on electronpoor (**9**) and electronrich (**10**) poly(di-*n*-hexylfluorene) block copolymers **poly(10-*b*-9-*b*-10)**, displayed long range exciton transport (Figure 6a).

Recently, joint efforts of the groups of Pavan, Takeuchi and Sugiyasu led to the application of the seeded-growth copolymerization strategy on small molecules achieving dynamic supramolecular block copolymers.[84] Their work showed that zinc based porphyrins (**11**) can copolymerize with copper based analogues (**12**) under kinetic control using a living seeded-growth strategy by a solvent mixing protocol. The obtained supramolecular A–B–A block copolymers **poly(12-*b*-11-*b*-12)** displayed controlled length and narrow polydispersity (Figure 6b). Remarkably, the block copolymer imparted additional stability to the **poly(11)** mid-block, which resulted stabilized against the presence of denaturant agents.

Another remarkable example was presented by Aida's group, who described the only supramolecular diblock copolymer so far reported.[85] Similarly to the examples described above, the block copolymerization of hexabenzocoronenes-based monomers was achieved by sequential steps (Figure 6c). The hexabenzocoronenes terminated with bipyridine units (**13**) homopolymerized in MeOH, giving **poly(13)** which created bundles. Consecutive metalation of the dangling bipyridine units with copper resulted in the creation of dispersed charged assemblies **poly(13*)**. These latter were then dispersed in acetone and fragmented to create seeds for the growth of the electronpoor analogue (**14**). The mixture of seeds of **poly(13*)** and **14** were assembled by cooling from 50 °C to 25 °C, giving mainly A–B and few A–B–A copolymers, **poly(13*-*b*-14)** and **poly(14-*b*-13*-*b*-14)**, respectively. As results, similarly to covalent block copolymers, the majority of the supramolecular block copolymers is achieved via a kinetic approach with highly stable (with slow-exchange rate) supramolecular polymers which can be fed with different monomers forming block structures.

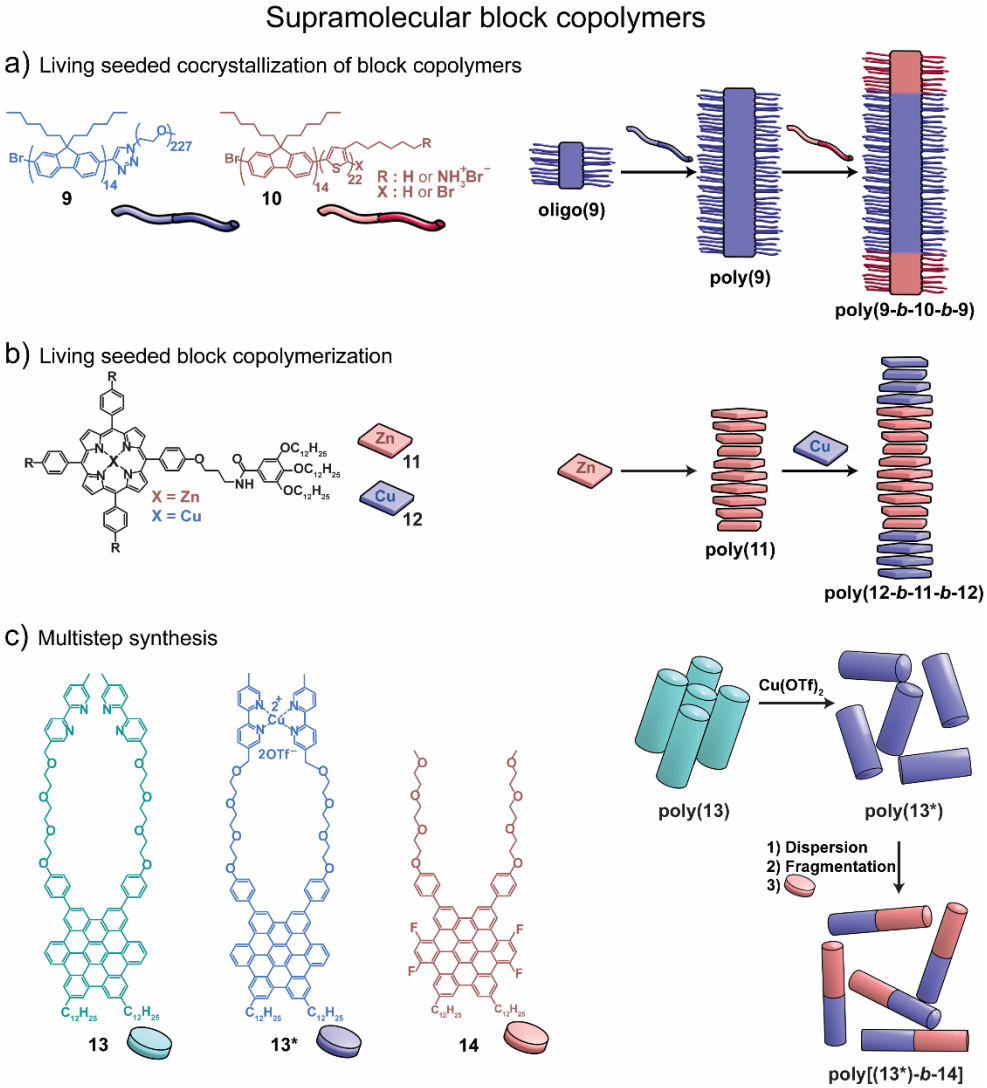

Figure 6. Examples of block and multiblock supramolecular copolymers achieved with different strategies. A–B–A block copolymers can be obtained under kinetic control via supramolecular living (a) cocrystallization or (b) copolymerization. Living homopolymers as **poly(9)** or **poly(11)** are fed with analogous monomers achieving **poly(10-*b*-9-*b*-10)** and **poly(12-*b*-11-*b*-12)** with controllable length. (c) A–B and A–B–A block copolymers are obtained by multistep non-covalent synthesis using electronrich (**13**) and electronpoor (**14**) hexabenzocoronene-based monomers (c). Bundled homopolymers **poly(13)** are formed in methanol upon equilibration. Addition of copper salt allow the complexation between Cu^{2+} and the peripheral biprydirines group of **13** causing the de-agglomeration of the single homopolymers into **poly(13*)**, now positively charged. The copolymerization occurs in acetone via the growth of **14** blocks on the dispersed seeds of **poly(13*)** giving mainly **poly(14-*b*-13)**.

1.4.5. Random and unresolved structures

Unlike the examples above described, which represent outstanding exceptions, the majority of the work on supramolecular copolymers so far reported has not resulted in the detailed elucidation of the obtained microstructures. In fact, already at the origin of supramolecular polymer field, mixing experiments were performed by taking direct inspiration from the work on covalent analogues developed by Green *et al*.[86-88] Mixing experiments performed on chiral, enantiomerically related monomers (majority rules experiment),[89–93] mixtures of achiral monomers and optically pure, chiral monomers (sergeants and soldiers experiment)[91,94–104] or even mixing enantiomers in different ratios in the presence of an achiral counterpart (diluted majority rules experiment)[105–107] are, in fact, examples of supramolecular copolymerizations. Typically, these monomers comprise identical cores and only differ in the nature of their side chains. Their copolymerization is typically assumed to be random.

These mixtures have been predominantly characterized using spectroscopic measurements such as fluorescence, UV-Vis spectroscopy and especially circular dichroism (CD). Apart from some notable exceptions,[108] very few studies have corroborated the spectroscopy results with other types of characterization techniques. The non-proportional increase of the chiroptical activity (quantified by CD spectroscopy) as a function of the enantiomeric excess (*e.e.*) or percentage of chiral sergeant in these systems—referred to as amplification of chirality—typically arises from helical superstructures in which one helical sense is more preferred than the other. Because of the identical spectroscopic features of the monomers once copolymerized, the investigation of the copolymer's microstructure is often not performed and assumed random.

Interestingly, several supramolecular copolymer systems revealed linear responses when optical activity was measured as a function of the enantiomeric excess (*e.e.*) or percentage of chiral sergeant added. This lack of amplification of chirality is indicative of self-sorting, and points to the helical supramolecular homopolymers co-existing rather than mixing into copolymers. Detailed investigations by the groups of Würthner, Sanchez and our group indicated that these systems were often kinetically trapped and either heat[109–111] or the addition of a co-solvent[112] was required to attain sufficient mobility and monomer exchange for copolymerization. Over time, some copolymers slowly segregated back into more blocky structures, as evidence by a reduction in the degree of chiral amplification.[10] In some cases, however, the steric bulk of the stereocenter in the side chains was too demanding, precluding mixing of the two monomers in one copolymer, and resulting in the formation of homopolymers only. This behavior has been observed, for example, in BTA monomers with bulky siloxane-based side chains and porphyrin-based monomers (**15** and **16**) (Figure 7a).[105,114] In a way, such systems resemble conglomerate behavior in crystallizations.

More recently, unresolved structures were also reported for monomers that have different supramolecular units,[99] or have different cores.[93,113,115] For example, the copolymerization of a chiral benzene tricarboxamide with an achiral benzene trisurea

showed the formation of kinetically trapped copolymers which spontaneously evolve into self-sorted homopolymers after 1 h.[99] In contrast, the copolymerization of N-centered and CO-centered BTAs resulted, most likely, in an alternating copolymer based on their donor-acceptor structure and chiral amplification studies.[93] Finally, mixtures of copolymers of oligo(*p*-phenylvinylene) with different sizes and opposite chirality (ROPV3 and SOPV4) showed the formation of homopolymers with either preferred *P*-helicity (for ROPV3) or *M*-helicity (for SOPV4) at room temperature. Heating followed by slow cooling induced the formation of copolymers with the helical sense bias depending on the composition of the mixture.[115]

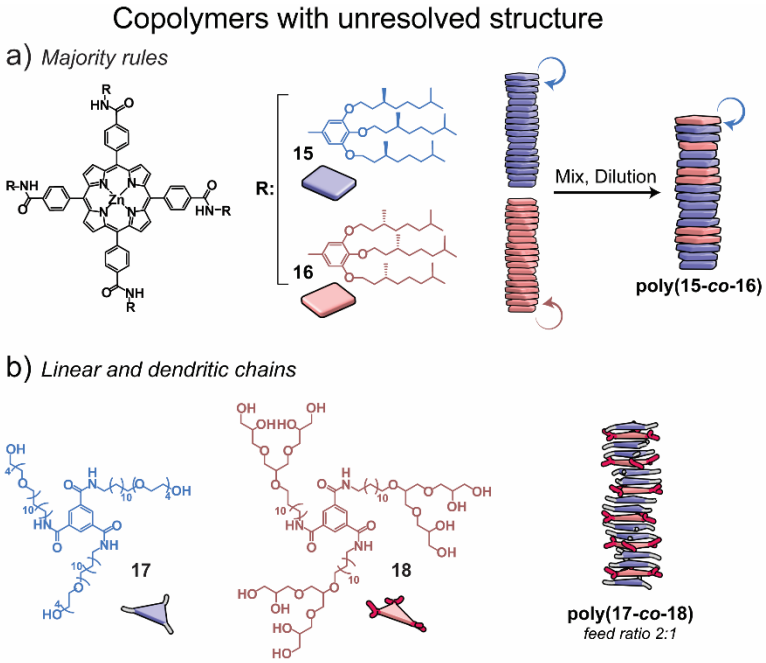

Figure 7. Example of supramolecular copolymers with unresolved structures. (a) Majority rules upon dilution based on *S* and *R* (**15** and **16**) zinc porphyrins. (b) Copolymerization of linear (**17**) and dendronized (**18**) water-soluble BTA.

Supramolecular copolymers in water, however, present other challenges. Water induces hydrophobic interactions, which in many supramolecular (co)polymerizations are the dominant driving force for aggregation.[116,117] Recent work from our group showed that dendronized pegylated BTA (**18**), that does not form supramolecular homopolymers, forms stable aggregates **poly(17-*co*-18)** when mixed with linear pegylated (**17**), (Figure 7b).[118] Experimental studies (UV-Vis, hydrogen-deuterium exchange, cryoTEM) on the copolymer (feed ratio 2:1) revealed a higher degree of order, slower dynamics and higher stability compared to **poly(17)** homopolymer. Although a complete elucidation of the copolymer structure at a molecular level remained impossible, molecular dynamic simulations indicated that a periodic 2:1

copolymer composition allowed an optimal compromise between steric hindrance of the dendronized side chains and the formation of a structure stabilized by intermolecular hydrogen bonds. This behavior can be considered the supramolecular equivalent of covalent styrene-maleic anhydride copolymers.

In addition, another elegant system based on bipyridine-derived BTAs has been described by Brunsveld and coworkers.[119,120] Multicomponent mixtures were created comprising monomers with charged groups, fluorescent dyes and biotine residues in water, using the auto-fluorescence of the bipyridine-based core as a read-out, even in cells. However, detailed information on the sequence and actual incorporation of the different monomers remained very challenging to obtain.

The examples described above highlight the need for a broad spectrum of adequate characterization techniques in combination with mathematical models to permit a complete elucidation of the formed supramolecular copolymers.

1.5 Characterization challenges

The growing interest in developing non-covalent copolymers requires the parallel progress and standardization in characterization techniques. The analysis reported above suggests that such uniformity remains elusive. Other established fields, such as covalent copolymers, teach us that having a systematic, universally applied characterization routine is crucial to achieve concrete progresses. However, the high dynamicity of supramolecular polymers, and the non-covalent nature of the bonds between monomers makes the characterization of the microstructure and the sequence analysis extremely challenging. Nevertheless, nowadays a clear trend on the characterization routine of the supramolecular homopolymers can be identified. This combines spectroscopy measurements (especially useful for variable temperature or variable solvent measurements), microscopy (the most used are AFM, TEM or cryoTEM, super resolution microcopy), light scattering techniques, molecular dynamics simulations, complemented with the application of mass balance models.

The outstanding work on supramolecular copolymers in which a detailed structure analysis is reported,[85,53,121] adapts and combines these techniques to resolve the supramolecular copolymer microstructure. Spectroscopy measurements (UV, CD, fluorescence, etc.) are powerful tools to unravel both copolymerization mechanism[53] and composition[122] of the system by quantifying the changes in the spectroscopic features. Thereafter, spectroscopic results can be used in combination with theoretical modeling to predict the microstructure and the relative stability of the copolymer with respect to the homopolymers.[53,122] The microstructure analysis obtained theoretically can then be confirmed by judicious use of microscopy techniques. If applicable TEM has been proved to be excellent technique to unravel the structure.[85] Otherwise, recent development on super resolution techniques demonstrated to be helpful in unravelling the polymer growth[123], its dynamics[124,56] and copolymers' structure.[125-127]

What emerges from these seminal works is the lack of a leading technique to determine unambiguously the copolymer's structure and a need of bridging this gap with a combination of multiple techniques. This differs from covalent copolymers, where ^{1}H and ^{13}C NMR have proved to be the primary tools for the determination of the secondary structure of covalent polymers. We believe that further studies for developing techniques which allow similar analysis for supramolecular analogues are needed and will permit a most efficient growth of the field. Microscopy and modeling so far resulted to be promising strategies. More progress in these directions could lead towards the possibility of analyzing in detail the block length of supramolecular copolymers.

1.6 Application and future perspectives

The introduction and the development of covalent copolymers (from block to alternating copolymers) resulted to be invaluable in time. The realization of copolymers made with different monomers gave great technological advancements and opportunity to get properties completely not achievable just by homopolymers or blending.

Evaluating supramolecular copolymers by this model, we can just guess the great advancements we could achieve by mastering these dynamic multicomponent structures. The potential applications for these systems are exceptionally broad. Mastering the microstructure of supramolecular copolymers permits to achieve control in systems where complexity is required. Looking at bio-applications, the prospect of including multiple units (*i.e.*, sensors, bio-active molecules, recognition units) in non-covalent systems in a defined order can be a breakthrough to achieve complex bio-responses which intrinsically requires a cooperative action of multiple units.[128,129,119] This may enable for example adaptive multivalency. The same cooperative effect can be exploited in organic electronics where tuning the arrangements of dynamic copolymers can modify the optoelectronic properties of the systems thereby high performing photoelectronic switches, sensors or chiral devices could be achieved.[130-132]

The analysis of research reported here is meant to be a first step toward a joint effort to advance in this new and fascinating field. Despite the great progresses achieved in the last years, much more have to be expected. A key point which would bring the field notably ahead is a deeper comprehensive understanding of the relation between molecular design and copolymer microstructure. It would give the opportunity to set *a priori* the multiple functionalities in the right place and achieve nano-controlled architectures. Strictly related to this argument, another goal is getting closer to having a molecular view of the supramolecular copolymers. We believe that, in order to soar, the supramolecular copolymer field needs a growth all-round, from strategic molecular design, to the exploitation of theoretical models through the development of powerful characterization techniques. This, achievable by collaborative works and a more

standardize analysis routine, can lead supramolecular copolymers to be competitive in the high-tech market.

1.7 Aim and outline of the thesis

From the analysis above, the great potential yet also the large complexity of supramolecular (co)polymers emerges. The progress achieved in the fundamental understanding of supramolecular polymerization aided to push the field towards a real exploitation of these systems into applications. However, combining both structural control and functionality in supramolecular polymers is still an open challenge. Highly controllable supramolecular polymerizations are achieved with monomers which lack functionality, while functional monomers often present a complex assembly behavior which renders their control less straightforward.

The research presented here aims to explore functional supramolecular polymer and copolymers and to exploit them in opto-electronic applications. In a stepwise growth in complexity, the thesis begins with fundamental studies on controlling the polymerization and concludes with the development of multicomponent supramolecular systems and their use in solar cells.

For this purpose, **Chapter 2** reports on the design and the study of a family of C_3 symmetric supramolecular monomers which possess as core a classic functional unit used in organic electronics: triarylamine. Variable temperature spectroscopic measurements displayed a comparable behavior for triphenylamine and tripyridylamine systems revealing the complexity of the homopolymerization. The systems exhibit exceptional properties in their assembling such as their ability of sharply inverting the helicity of the supramolecular polymers formed in a range of few degree Celsius. Through a combination of DFT calculation and spectroscopy analysis, we revealed the fundamental role that water molecules (co-dissolved in alkane solvents) play.

In parallel to the fundamental study, the use of these functional supramolecular polymers in optoelectronic devices has been investigated. In **Chapter 3**, in a collaborative effort with Ron Naaman and coworkers, at the Weizmann Institute of Science (IL), we studied the positive effect of functionalizing water-splitting dye sensitized photoelectrochemical cells (DS-PECs) with chiral supramolecular polymers. The deposition of chiral supramolecular polymers on the anode (TiO_2 based) of the water-splitting cell enhances the performance due to a physical effect called chiral induced spin selectivity (CISS effect). In detail, the chiral supramolecular polymers used as sensitizers cause not only an increase of the device's current but, more interestingly, the depletion of the water peroxide formed as byproduct of the reaction.

Subsequently, **Chapter 4** aims to improve the chiral-functionalized water-splitting devices combing the results earlier described with a more classical design of DS-PECs. The chapter is focused on confirming the reproducibility of the effect and improving

efficiency and stability of the cells. A standardize protocol for the fabrication of porous TiO_2 anodes has been introduced together with an optimized procedure for the deposition of supramolecular polymers. Consecutively, the issue of stability overtime was addressed including supramolecular anchors as linkers between the inorganic surface and the chiral polymers. The effect of the addition of the anchoring layer, studied via multiple techniques, evidenced the enhancement of chiral order in the supramolecular layer. Device testing proved an increase of the stability of few minutes. Finally, the possibility of creating chiral supramolecular polymers able to act as photosensitizer for visible light was investigated. Classic triphenylamine based D-π-A dyes were modified to assemble into chiral supramolecular polymers. Supramolecular characterization and initial testing displayed promising results as increase in device current, this time possible under a source of visible light.

In **Chapter 5,** we return to fundamental research investigating multicomponent supramolecular systems in solution. In particular, a detailed study of the copolymerization between triphenylamine- and tripyridylamine-based monomers is investigated. The study focuses on unveiling the composition and microstructure of the copolymers through a combination of spectroscopic techniques, mathematical modelling and super resolution microscopy. The formation of supramolecular block copolymers and their thermodynamic stability overtime has been demonstrated giving a fundamental background for further copolymer characterization.

Finally, **Chapter 6** aims to develop and study supramolecular copolymers with new emerging functionalities. In collaboration with Shigehiro Yamaguchi's group, Nagoya University (JP), we aimed to study possible boron-nitrogen supramolecular copolymers. Triarylborane-based supramolecular monomers and triphenylamine analogues were designed and studied individually and mixed. Spectroscopic techniques confirmed the formation of boron-based supramolecular polymers and their suitability to interact with triphenylamine-based analogues. Mixing experiment between boron and nitrogen monomers originated new emerging fluorescence properties in the polymerized state.

1.8 References

[1] De Greef, T. F. A.; Smulders, M. M. J.; Wolffs, M.; Schenning, A. P. H. J.; Sijbesma, R. P.; Meijer, E. W. *Chem. Rev.* **2009**, 109 (11), 5687–5754.

[2] Liu, M.; Zhang, L.; Wang, T.; Yashima, E.; Maeda, K.; Iida, H.; Furusho, Y.; Nagai, K. *Chem. Rev.* **2015**, 115 (15), 6102–6211.

[3] Yashima, E.; Ousaka, N.; Taura, D.; Shimomura, K.; Ikai, T.; Maeda, K. *Chem. Rev.* **2016**, 116 (22), 13752–13990.

[4] Das, A.; Ghosh, S. *Chem. Commun.* **2016**, 52 (42), 6860–6872.

[5] Yang, S. K.; Zimmerman, S. C. *Isr. J. Chem.* **2013**, 53 (8), 511–520.

[6] van der Zwaag, D.; de Greef, T. F. A.; Meijer, E. W. *Angew. Chem. Int. Ed.* 2015, 54 (29), 8334–8336.

[7] Lehn, J. M. *Angew. Chem. Int. Ed.* **1990**, 29 (11), 1304–1319.

[8] Odian, G. G. Principle of Polymerization, Third Edit.; *Wiley, Ed.*; **1991**.

[9] Odian, G. Principles of Polymerization; *Wiley, Ed.* **2004**.

[10] Szwarc, M. *J. Phys. Chem.* **1958**, 62 (5), 568–569.

[11] Hirschberg, J. H. K. K.; Beijer, F. H.; Van Aert, H. A.; Magusin, P. C. M. M.; Sijbesma, R. P.; Meijer, E. W. *Macromolecules* **1999**, 32 (8), 2696–2705.

[12] Xu, Q.; Han, B.; Yan, H. Polymer **2001**, 42 (4), 1369–1373.

[13] Korevaar, P. A.; Schaefer, C.; de Greef, T. F. A.; Meijer, E. W. *J. Am. Chem. Soc.* **2012**, 134 (32), 13482–13491.

[14] Weng, W.; Li, Z.; Jamieson, A. M.; Rowan, S. J. *Macromolecules* **2009**, 42 (1), 236–246.

[15] Greenley, R. Z. *The Wiley Database of Polymer Properties*. **2003**.

[16] Flory, P. J. Principle of polymer chemistry; *Cornell University press*, **1953.**

[17] Burnworth, M.; Tang, L.; Kumpfer, J. R.; Duncan, A. J.; Beyer, F. L.; Fiore, G. L.; Rowan, S. J.; Weder, C. Nature **2011**, 472, 334.

[18] Mark, J.; Ngai, K.; Graessley, W.; Mandelkern, L.; Samulski, E.; Koenig, J.; Wignall, G. Physical Properties of Polymers, 3rd ed.; *Cambridge University Press*, **2004**.

[19] Verbiest, T.; Elshocht, S. Van; Kauranen, M.; Hellemans, L.; Snauwaert, J.; Nuckolls, C.; Katz, T. J.; Persoons, A. *Science* **1998**, 282 (5390), 913-915.

[20] Jelley, E. E. *Nature* **1936**, 138, 1009.

[21] Eisfeld, A.; Briggs, J. *Chem. Phys.,* 2006, 324, 2-3, 376-384

[22] Lortie, F.; Boileau, S.; Bouteiller, L.; Chassenieux, C.; Lauprêtre, F. *Macromolecules* **2005**, 38 (12), 5283–5287.

[23] Ahlers, P.; Fischer, K.; Spitzer, D.; Besenius, P. *Macromolecules* **2017**, 50 (19), 7712–7720.

[24] Smulders, M. M. J.; Nieuwenhuizen, M. M. L.; Grossman, M.; Filot, I. A. W.; Lee, C. C.; De Greef, T. F. A.; Schenning, A. P. H. J.; Palmans, A. R. A.; Meijer, E. W. *Macromolecules* **2011**, 44 (16), 6581–6587.

[25] Würthner, F. *Nat. Chem.* 2014, 6 (3), 171–173.

[26] Kang, J.; Miyajima, D.; Mori, T.; Inoue, Y.; Itoh, Y.; Aida, T. *Science* **2015**, 347 (6222), 646–651.

[27] Ogi, S.; Stepanenko, V.; Thein, J.; Würthner, F. *J. Am. Chem. Soc.* **2016**, 138 (2), 670–678.

[28] Ogi, S.; Stepanenko, V.; Sugiyasu, K.; Takeuchi, M.; Würthner, F. *J. Am. Chem. Soc.* **2015**, 137 (9), 3300–3307.

[29] Ogi, S.; Sugiyasu, K.; Manna, S.; Samitsu, S.; Takeuchi, M. *Nat. Chem.* **2014**, 6 (3), 188–195.

[30] Endo, M.; Fukui, T.; Jung, S. H.; Yagai, S.; Takeuchi, M.; Sugiyasu, K. *J. Am. Chem. Soc.* **2016**, 138 (43).

[31] Aliprandi, A.; Mauro, M.; De Cola, L. *Nat. Chem.* **2016**, 8 (1), 10–15.

[32] Korevaar, P. A.; George, S. J.; Markvoort, A. J.; Smulders, M. M. J.; Hilbers, P. A. J.; Schenning, A. P. H. J.; De Greef, T. F. A.; Meijer, E. W. *Nature* **2012**, 481 (7382), 492–496.

[33] Korevaar, P. A.; de Greef, T. F. A.; Meijer, E. W. *Chem. Mater.* **2014**, 26 (1), 576–586.

[34] van der Zwaag, D.; Pieters, P. A.; Korevaar, P. A.; Markvoort, A. J.; Spiering, A. J. H.; de Greef, T. F. A.; Meijer, E. W. *J. Am. Chem. Soc.* **2015**, 137 (39), 12677–12688.

[35] Valera, J. S.; Gómez, R.; Sánchez, L. *Small* **2018**, 14 (3), 1–9.

[36] Ogi, S.; Fukui, T.; Jue, M. L.; Takeuchi, M.; Sugiyasu, K. *Angew. Chemie Int. Ed.* **2014**, 53 (52), 14363–14367.

[37] Liu, M.; Zhang, L.; Wang, T. *Chem. Rev.* **2015**, 115 (15), 7304–7397.

[38] Biedermann, F.; Schneider, H. J. *Chem. Rev.* **2016**, 116 (9), 5216–5300.

[39] Venkata Rao, K.; Miyajima, D.; Nihonyanagi, A.; Aida, T. *Nat. Chem.* **2017**, 9 (November), 1133–1139.

[40] Kulkarni, C.; Korevaar, P. A.; Bejagam, K. K.; Palmans, A. R. A.; Meijer, E. W.; George, S. J. *J. Am. Chem. Soc.* **2017**, 139 (39), 13867–13875.

[41] Cantekin, S.; Nakano, Y.; Everts, J. C.; van der Schoot, P.; Meijer, E. W.; Palmans, A. R. A. *Chem. Commun.* **2012**, 48 (32), 3803.

[42] Dong, S.; Leng, J.; Feng, Y.; Liu, M.; Stackhouse, C. J.; Schönhals, A.; Chiappisi, L.; Gao, L.; Chen, W.; Shang, J.; Jin, L.; Qi, Z.; Schalley, C. A. *Sci. Adv.* **2017**, 3 (11), 1–9.

[43] Ortony, J. H.; Qiao, B.; Newcomb, C. J.; Keller, T. J.; Palmer, L. C.; Deiss-Yehiely, E.; Olvera De La Cruz, M.; Han, S.; Stupp, S. I. *J. Am. Chem. Soc.* **2017**, 139 (26), 8915–8921.

[44] Johnson, R. S.; Yamazaki, T.; Kovalenko, A.; Fenniri, H. *J. Am. Chem. Soc.* **2007**, 129 (17), 5735–5743.

[45] Gillissen, M. A. J.; Koenigs, M. M. E.; Spiering, J. J. H.; Vekemans, J. A. J. M.; Palmans, A. R. A.; Voets, I. K.; Meijer, E. W. J. *Am. Chem. Soc.* **2014**, 136 (1), 336–343.

[46] Liu, C.; Jin, Q.; Lv, K.; Zhang, L.; Liu, M. *Chem. Commun.* **2014**, 50 (28), 3702–3705.

[47] Liu, Y.; Jia, Y.; Zhu, E.; Liu, L.; Qiao, Y.; Che, G.; Yin, B. *New J. Chem.* **2017**, 41 (19), 11060–11068.

[48] Yu, X.; Xie, D.; Lan, H.; Li, Y.; Zhen, X.; Ren, J.; Yi, T. J. *Mater. Chem. C* **2017**, 5 (24), 5910–5916.

[49] Zee, N. J. Van; Adelizzi, B.; Mabesoone, M. F. J.; Meng, X.; Aloi, A.; Zha, H.; Lutz, M.; Filot, I. A. W.; Palmans, A. R. A.; Meijer, E. W. *Nature* **2018**, 558 (7708), 100–103.

[50] Xing, P.; Li, Y.; Wang, Y.; Li, P. Z.; Chen, H.; Phua, S. Z. F.; Zhao, Y. *Angew. Chemie Int. Ed.* **2018**, 57 (26), 7774–7779.

[51] Li, X.; Gao, Y.; Boott, C. E.; Winnik, M. A.; Manners, I. *Nat. Commun.* **2015**, 6, 1–8.
[52] Li, X.; Gao, Y.; Boott, C. E.; Hayward, D. W.; Harniman, R.; Whittell, G. R.; Richardson, R. M.; Winnik, M. A.; Manners, I. *J. Am. Chem. Soc.* **2016**, 138 (12), 4087–4095.
[53] Adelizzi, B.; Aloi, A.; Markvoort, A. J.; Ten Eikelder, H. M. M.; Voets, I. K.; Palmans, A. R. A.; Meijer, E. W. *J. Am. Chem. Soc.* **2018**, 140 (23), 7168–7175.
[54] Ouchi, M.; Nakano, M.; Nakanishi, T.; Sawamoto, M. *Angew. Chemie Int. Ed.* **2016**, 55 (47), 14584–14589.
[55] Lutz, J.-F.; Ouchi, M.; Liu, D. R.; Sawamoto, M. *Science* **2013**, 341 (6146), 1238149–1238149.
[56] Albertazzi, L.; Hofstad, R. W. Van Der; Meijer, E. W. *Science* **2014**, 491 (6183), 10–15.
[57] Fouquey, C.; Lehn, J. -M; Levelut, A. -M. *Adv. Mater.* **1990**, 2 (5), 254–257.
[58] Sivakova, S.; Rowan, S. *J. Chem. Soc. Rev.* **2005**, 34 (1), 9–21.
[59] Sijbesma, R. P.; Beijer, F. H.; Brunsveld, L.; Folmer, B. J. B.; Hirschberg, J. H. K. K.; Lange, R. F. M.; Lowe, J. K. L.; Meijer, E. W. *Science.* **1997**, 278 (5343), 1601–1604.
[60] Blight, B. A.; Camara-Campos, A.; Djurdjevic, S.; Kaller, M.; Leigh, D. A.; McMillan, F. M.; McNab, H.; Slawin, A. M. Z. *J. Am. Chem. Soc.* **2009**, 131 (39), 14116–14122.
[61] Gohy, J.-F. *Coord. Chem. Rev.* **2009**, 253 (17), 2214–2225.
[62] Das, A.; Ghosh, S. *Angew. Chemie - Int. Ed.* **2014**, 53 (8), 2038–2054.
[63] Jalani, K.; Kumar, M.; George, S. J. *Chem. Commun.* **2013**, 49 (45), 5174–5176.
[64] Rizkov, D.; Gun, J.; Lev, O.; Sicsic, R.; Melman, A. *Langmuir* **2005**, 21 (26), 12130–12138.
[65] Frisch, H.; Unsleber, J. P.; Lüdeker, D.; Peterlechner, M.; Brunklaus, G.; Waller, M.; Besenius, P. *Angew. Chemie Int. Ed.* **2013**, 52 (38), 10097–10101.
[66] Frisch, H.; Fritz, E. C.; Stricker, F.; Schmüser, L.; Spitzer, D.; Weidner, T.; Ravoo, B. J.; Besenius, P. *Angew. Chemie - Int. Ed.* **2016**, 55 (25), 7242–7246.
[67] Engel, S.; Spitzer, D.; Rodrigues, L. L.; Fritz, E. C.; Straßburger, D.; Schönhoff, M.; Ravoo, B. J.; Besenius, P. *Faraday Discuss.* **2017**, 204, 53–67.
[68] Xiang, Y.; Moulin, E.; Buhler, E.; Maaloum, M.; Fuks, G.; Giuseppone, N. *Langmuir* **2015**, 31 (28), 7738–7748.
[69] Takasawa, R.; Murota, K.; Yoshikawa, I.; Araki, K. *Macromol. Rapid Commun.* **2003**, 24 (4), 335–339.
[70] Chen, S. G.; Yu, Y.; Zhao, X.; Ma, Y.; Jiang, X. K.; Li, Z. T. *J. Am. Chem. Soc.* **2011**, 133 (29), 11124–11127.
[71] Yagai, S.; Hamamura, S.; Wang, H.; Stepanenko, V.; Seki, T.; Unoike, K.; Kikkawa, Y.; Karatsu, T.; Kitamura, A.; Würthner, F. *Org. Biomol. Chem.* **2009**, 7 (19), 3926–3929.
[72] Görl, D.; Zhang, X.; Stepanenko, V.; Würthner, F. *Nat. Commun.* **2015**, 6, 7009.
[73] Hepburn, C. Polyurethane Elastomers; *Springer* **1992**.
[74] Wang, X.; Guerin, G.; Wang, H.; Wang, Y.; Manners, I.; Winnik, M. a. *Science* **2007**, 317 (5838), 644–647.
[75] Qiu, H.; Russo, G.; Rupar, P. A.; Chabanne, L.; Winnik, M. A.; Manners, I. *Angew. Chem. Int. Ed.* **2012**, 51 (47), 11882–11885.
[76] Rupar, P. A.; Chabanne, L.; Winnik, M. A.; Manners, I. *Science* **2012**, 337 (6094), 559–562.
[77] Hudson, Z. M.; Lunn, D. J.; Winnik, M. A.; Manners, I. *Nat. Commun.* **2014**, 5, 1–8.
[78] Xu, J.; Zhou, H.; Yu, Q.; Manners, I.; Winnik, M. A. *J. Am. Chem. Soc.* **2018**, 140 (7), 2619–2628.
[79] Finnegan, J. R.; Lunn, D. J.; Gould, O. E. C.; Hudson, Z. M.; Whittell, G. R.; Winnik, M. A.; Manners, I. *J. Am. Chem. Soc.* **2014**, 136 (39), 13835–13844.
[80] Gao, Y.; Qiu, H.; Zhou, H.; Li, X.; Harniman, R.; Winnik, M. A.; Manners, I. *J. Am. Chem. Soc.* **2015**, 137 (6), 2203–2206.
[81] Hudson, Z. M.; Boott, C. E.; Robinson, M. E.; Rupar, P. A.; Winnik, M. A.; Manners, I. *Nat. Chem.* **2014**, 6 (10), 893–898.
[82] Shin, S.; Menk, F.; Kim, Y.; Lim, J.; Char, K.; Zentel, R.; Choi, T. L. *J. Am. Chem. Soc.* **2018**, 140 (19), 6088–6094.
[83] Jin, X.; Price, M. B.; Finnegan, J. R.; Boott, C. E.; Richter, J. M.; Rao, A.; Menke, S. M.; Friend, R. H.; Whittell, G. R.; Manners, I. *Science* **2018**, 360 (6391), 897–900.
[84] Sugiyasu, K.; Jung, S. H.; Bochicchio, D.; Pavan, G. M.; Takeuchi, M.; Sugiyasu, K. *J. Am. Chem. Soc.* **2018**, 140 (33), 10570–10577.
[85] Zhang, W.; Jin, W.; Fukushima, T.; Saeki, A.; Seki, S.; Aida, T. *Science* **2011**, 334 (6054), 340–343.
[86] Green, M. M.; Khatri, C. A.; Reidy, M. P.; Levon, K. *Macromolecules* **1993**, 26 (17), 4723–4725.
[87] Green, M. M.; Andreola, C.; Muñoz, B.; Reidy, M. P.; Zero, K. *J. Am. Chem. Soc.* **1988**, 110 (12), 4063–4065.
[88] Green, M. M.; Peterson, N. C.; Sato, T.; Teramoto, A.; Cook, R.; Lifson, S. *Science* **1995**, 268 (5219), 1860–1866.
[89] Van Gestel, J.; Palmans, A. R. A.; Titulaer, B.; Vekemans, J. A. J. M.; Meijer, E. W. *J. Am. Chem. Soc.* **2005**, 127 (15), 5490–5494.
[90] Jin, W.; Fukushima, T.; Niki, M.; Kosaka, A.; Ishii, N.; Aida, T. *Proc. Natl. Acad. Sci.* **2005**, 102 (31), 10801–10806.
[91] Langeveld-Voss, B. M. W.; Waterval, R. J. M.; Janssen, R. A. J.; Meijer, E. W. *Macromolecules* **1999**, 32 (1), 227–230.
[92] Isare, B.; Linares, M.; Zargarian, L.; Fermandjian, S.; Miura, M.; Motohashi, S.; Vanthuyne, N.; Lazzaroni, R.; Bouteiller, L. *Chem. Eur. J.* **2010**, 16 (1), 173–177.
[93] Stals, P. J. M.; Everts, J. C.; de Bruijn, R.; Filot, I. A. W.; Smulders, M. M. J.; Martín-Rapún, R.; Pidko, E. A.; de Greef, T. F. A.; Palmans, A. R. A.; Meijer, E. W. *Chem. Eur. J.* **2010**, 16 (3), 810–821.
[94] Palmans, A. R. A.; Vekemans, J. a. J. M.; Havinga, E. E.; Meijer, E. W. *Angew. Chemie Int. Ed.* **1997**, 36 (23), 2648–2651.
[95] Kulkarni, C.; Munirathinam, R.; George, S. J. *Chem. Eur. J.* **2013**, 19 (34), 11270–11278.
[96] Wang, F.; Gillissen, M. A. J.; Stals, P. J. M.; Palmans, A. R. A.; Meijer, E. W. *Chem. Eur. J.* **2012**, 18 (37), 11761–11770.
[97] Kim, T.; Mori, T.; Aida, T.; Miyajima, D. *Chem. Sci.* **2016**, 7 (11), 6689–6694.
[98] Smulders, M. M. J.; Schenning, A. P. H. J.; Meijer, E. W. *J. Am. Chem. Soc.* **2008**, 130 (2), 606–611.
[99] van Gorp, J. J.; Vekemans, J. A. J. M.; Meijer, E. W. *J. Am. Chem. Soc.* **2002**, 124 (49), 14759–14769.
[100] Lohr, A.; Würthner, F. *Chem. Commun.* **2008**, 19, 2227.
[101] Ajayaghosh, A.; Varghese, R.; George, S. J.; Vijayakumar, C. *Angew. Chemie Int. Ed.* **2006**, 45 (7), 1141–1144.

[102] Brunsveld, L.; Vekemans, J. a J. M.; Hirschberg, J. H. K. K.; Sijbesma, R. P.; Meijer, E. W. *Proc. Natl. Acad. Sci.* **2002**, 99 (8), 4977–4982.
[103] Kaiser, T. E.; Stepanenko, V.; Würthner, F. *J. Am. Chem. Soc.* **2009**, 131 (19), 6719–6732.
[104] Anderson, T. W.; Sanders, J. K. M.; Pantoş, G. D. *Org. Biomol. Chem.* **2010**, 8 (19), 4274.
[105] Helmich, F.; Smulders, M. M. J.; Lee, C. C.; Schenning, A. P. H. J.; Meijer, E. W. *J. Am. Chem. Soc.* **2011**, 133 (31), 12238–12246.
[106] Smulders, M. M. J.; Stals, P. J. M.; Mes, T.; Paffen, T. F. E.; Schenning, A. P. H. J.; Palmans, A. R. A.; Meijer, E. W. *J. Am. Chem. Soc.* **2010**, 132 (2), 620–626.
[107] Wilson, A. J.; van Gestel, J.; Sijbesma, R. P.; Meijer, E. W. *Chem. Commun.* **2006**, No. 42, 4404.
[108] Roche, C.; Sun, H.-J.; Prendergast, M. E.; Leowanawat, P.; Partridge, B. E.; Heiney, P. A.; Araoka, F.; Graf, R.; Spiess, H. W.; Zeng, X.; Ungar, G.; Percec, V. *J. Am. Chem. Soc.* **2014**, 136 (19), 7169–7185.
[109] Wolffs, M.; Van Velthoven, J. L. J.; Lou, X.; Bovee, R. A. A.; Pouderoijen, M.; Van Dongen, J. L. J.; Schenning, A. P. H. J.; Meijer, E. W. *Chem. Eur. J.* **2012**, 18 (47), 15057–15064.
[110] Korevaar, P. A.; Grenier, C.; Markvoort, A. J.; Schenning, A. P. H. J.; de Greef, T. F. A.; Meijer, E. W. *Proc. Natl. Acad. Sci.* **2013**, 110 (43), 17205–17210.
[111] Lohr, A.; Würthner, F. *Chem. Commun.* **2008**, No. 19, 2227.
[112] Buendía, J.; García, F.; Yélamos, B.; Sánchez, L. *Chem. Commun.* **2016**, 52 (57), 8830–8833.
[113] van Gorp, J. J.; Vekemans, J. A. J. M.; Meijer, E. W. *J. Am. Chem. Soc.* **2002**, 124 (49), 14759–14769.
[114] García-Iglesias, M.; de Waal, B. F. M.; de Feijter, I.; Palmans, A. R. A.; Meijer, E. W. *Chem. Eur. J.* **2015**, 21 (1), 377–385.
[115] Korevaar, P. A.; Grenier, C.; Meijer, E. W. *J. Polym. Sci. Part A Polym. Chem.* **2015**, 53 (2), 385–391.
[116] Baker, M. B.; Albertazzi, L.; Voets, I. K.; Leenders, C. M. A.; Palmans, A. R. A.; Pavan, G. M.; Meijer, E. W. *Nat. Commun.* **2015**, 6, 6234.
[117] Garzoni, M.; Baker, M. B.; Leenders, C. M. A.; Voets, I. K.; Albertazzi, L.; Palmans, A. R. A.; Meijer, E. W.; Pavan, G. M. *J. Am. Chem. Soc.* **2016**, 138 (42), 13985–13995.
[118] Thota, B. N. S.; Lou, X.; Bochicchio, D.; Paffen, T. F. E.; Lafleur, R. P. M.; van Dongen, J. L. J.; Ehrmann, S.; Haag, R.; Pavan, G. M.; Palmans, A. R. A.; Meijer, E. W. *Angew. Chemie Int. Ed.* **2018**, 57 (23), 6843–6847.
[119] Petkau-Milroy, K.; Sonntag, M. H.; Van Onzen, A. H. A. M.; Brunsveld, L. *J. Am. Chem. Soc.* **2012**, 134 (19), 8086–8089.
[120] Müller, M. K.; Brunsveld, L. *Angew. Chemie Int. Ed.* **2009**, 48 (16), 2921–2924.
[121] Görl, D.; Zhang, X.; Stepanenko, V.; Würthner, F. *Nat. Commun.* **2015**, 6, 1–8.
[122] Das, A.; Vantomme, G.; Markvoort, A. J.; ten Eikelder, H. M. M.; Garcia-Iglesias, M.; Palmans, A. R. A.; Meijer, E. W. *J. Am. Chem. Soc.* **2017**, 139 (20), 7036–7044.
[123] Boott, C. E.; Leitao, E. M.; Hayward, D. W.; Laine, R. F.; Mahou, P.; Guerin, G.; Winnik, M. A.; Richardson, R. M.; Kaminski, C. F.; Whittell, G. R.; Manners, I. *ACS Nano* **2018**, 12 (9), 8920–8933.
[124] Baker, M. B.; Gosens, R. P. J.; Albertazzi, L.; Matsumoto, N. M.; Palmans, A. R. A.; Meijer, E. W. *ChemBioChem* **2016**, 17 (3), 207–213.
[125] Bakker, M. H.; Lee, C. C.; Meijer, E. W.; Dankers, P. Y. W.; Albertazzi, L. *ACS Nano* **2016**, 10 (2), 1845–1852.
[126] Adelizzi, B.; Aloi, A.; Van Zee, N. J.; Palmans, A. R. A.; Meijer, E. W.; Voets, I. K. *ACS Nano* **2018**, 12 (5), 4431–4439.
[127] Boott, C. E.; Laine, R. F.; Mahou, P.; Finnegan, J. R.; Leitao, E. M.; Webb, S. E. D.; Kaminski, C. F.; Manners, I. *Chem. Eur. J.* **2015**, 21 (51), 18539–18542.
[128] Hendrikse, S. I. S.; Wijnands, S. P. W.; Lafleur, R. P. M.; Pouderoijen, M. J.; Janssen, H. M.; Dankers, P. Y. W.; Meijer, E. W. *Chem. Commun.* **2017**, 53 (14), 2279–2282.
[129] Wijnands, S. P. W.; Engelen, W.; Lafleur, R. P. M.; Meijer, E. W.; Merkx, M. *Nat. Commun.* **2018**, 9 (1).
[130] Ellis, T. K.; Galerne, M.; Armao IV, J. J.; Osypenko, A.; Martel, D.; Maaloum, M.; Fuks, G.; Moulin, E.; Gavat, O.; Giuseppone, N. *Angew. Chemie Int. Ed.* **2018**, 0 (ja).
[131] Adhikari, B.; Suzuki, T.; Xu, L.; Yamauchi, M.; Karatsu, T.; Yagai, *S. Polym.* **2017**, 128, 356–362.
[132] Hafner, R. J.; Tian, L.; Brauer, J. C.; Schmaltz, T.; Sienkiewicz, A.; Balog, S.; Flauraud, V.; Brugger, J.; Frauenrath, H. *ACS Nano* **2018**, 12 (9), 9116–9125.

2.

Study of triarylamine-based supramolecular homopolymers

The results of this work are summarized in:

B. Adelizzi, I. A. W. Filot, A. R. A. Palmans, E. W. Meijer
Chem. Eur. J., **2017**, 23 (25), 6103-6110

N. J. Van Zee, B. Adelizzi, M. F. J. Mabesoone, X. Meng, A. Aloi, R. H. Zha, M. Lutz, I. A. W. Filot, A. R. A. Palmans, E. W. Meijer
Nature, **2018**, 558, 100-103

Abstract: Two families of C_3-symmetrical triarylamine-triamides comprising a triphenylamine or a tri(pyrid-2-yl)amine core are presented. Both families assemble in apolar solvents via cooperative hydrogen-bonding interactions into helical supramolecular polymers as evidenced by spectroscopic measurements, and corroborated by DFT calculations. The introduction of stereocenters in the side chains biases the helical sense of the supramolecular polymers formed. Compared to other C_3-symmetrical compounds, a much richer assembly landscape is observed. Temperature-dependent spectroscopy measurements highlight the presence of two assembled states of opposite handedness. One state is formed at high temperature from a molecularly dissolved solution via a nucleation-elongation mechanism. The second state is formed below room temperature through a sharp transition from the first assembled state. DFT calculations indicate that the change in helicity can be attributed to two different conformations in the assembled state. In addition to this, we observe that co-dissolved water in alkanes plays a fundamental role in the transition between the two assembled states. In fact, we find that other supramolecular polymers that possess conformational flexibility also show a high sensitivity to the amount of co-dissolved water.

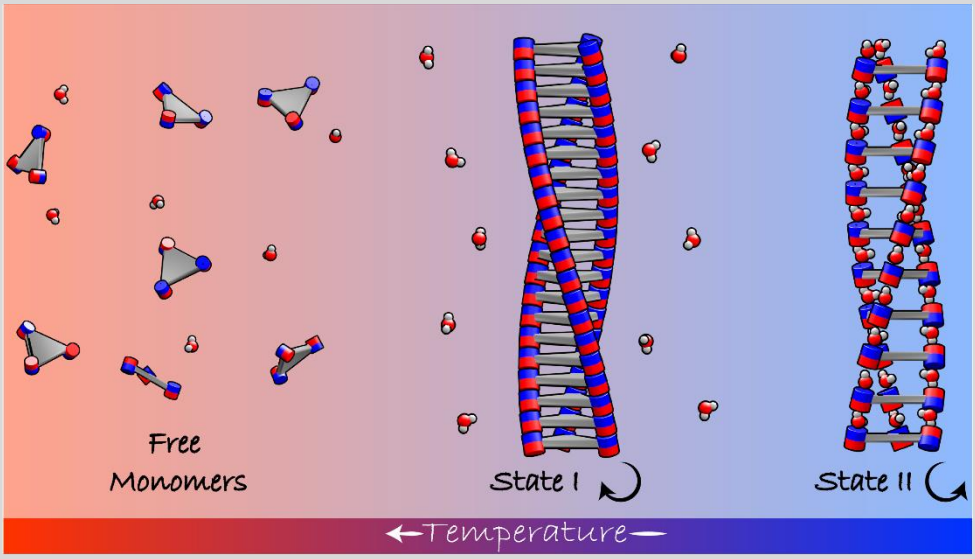

2.1 Introduction

The continuous growth of high-tech products relying on organic semiconductors demonstrates the notable technological maturity and competitiveness of these materials compared to their inorganic analogues. The relatively cheap fabrication, easy processing, and intrinsic flexibility are the leading qualities of organic electronics. However, although great progress has been achieved in this regard, the improvement of their conductive properties is still an open challenge. It has been demonstrated that exerting full control during the formation of the desired nanostructures minimizes defects and localized electronic states and enhances the performance of the material.[1,2] A smart strategy to achieve control over the molecular organization is to include a supramolecular approach in the preparation of functional materials.[3,9] For example, Giuseppone and co-workers studied in detail the self-assembly of N-centered triphenylamine-triamide in apolar solvents and the photo-induced supramolecular polymerization upon oxidation of triphenylamine into triphenylammonium in the presence of chloroform.[10,11] The improved conductive properties, in combination with easy processability, highlight that self-assembly is an attractive strategy to achieve well-performing supramolecular electronics.[12,13] In addition, Seu and Kim have demonstrated that opposite helical senses in photo-oxidized triphenylamine stacks can be induced by applying circularly polarized light of opposite handedness, opening a new route towards the formation of supramolecular chiral conductors.[14]

However, programming supramolecular interactions into the monomers' structure is not trivial. Often supramolecular interactions do not result in the formation of one single aggregate state. This effect, commonly called pathway complexity, has recently been reported for several systems and highlights the fundamental importance of controlling complex self-assembly processes.[15-18] Conversely, the ability to access different assembled states and the quantification of the energetic barriers of a complex supramolecular landscape creates opportunities to realize living supramolecular polymerizations.[19-22] Understanding and mastering the complexity of these systems, as initially envisioned by Mukhopadhyay and Ajayaghosh,[28] can be a powerful tool to design functional materials and can represent a step forward to high-performance soft electronics.

In this chapter, we present a study on the control and pathway selection on the supramolecular homopolymerization of two triarylamine families and report the importance of conformational flexibility. The triarylamines-based monomers are selected because of their importance in organic electronics and their versatile properties.[29-40] In addition, the intrinsic flexibility of the core gives interesting new properties to these assembling system. Here, we show how a small energetic gap in the molecular conformation can play an essential role in the resulting supramolecularly polymerized state, leading to a fast inversion of helical bias as a function of the temperature. After a fundamental study on the polymerization, we also report how the

presence of multiple assembled state is governed by co-dissolved water in alkane solvents.

The two selected cores, *i.e.* classic triphenylamine and tri(pyrid-2-yl)amine, possess the same geometry but differ in electronic properties and intermolecular interactions. The monomer structures are designed with a standard C_3 symmetry, similar to the 1,3,5-benzenetricarboxamide (BTAs),[41-43] with an aromatic core, C=O centered amides as three-folded H-bonding unit and alkyl solubilizing chains (Scheme 1). The conjugation between the central donating nitrogen and the amide moieties is enhanced in the triphenylamine whereas the electron-poor pyridyl group partially reduces the conjugation. Unlike the triphenylamine core, the assembly properties of tri(pyrid-2-yl)amine are unexplored. The high flexibility of the molecule is known and exploited in various metal complexes and chiral molecular organic nanotubes (MONTs)[44-46] making it interesting to explore its application in supramolecular chemistry.

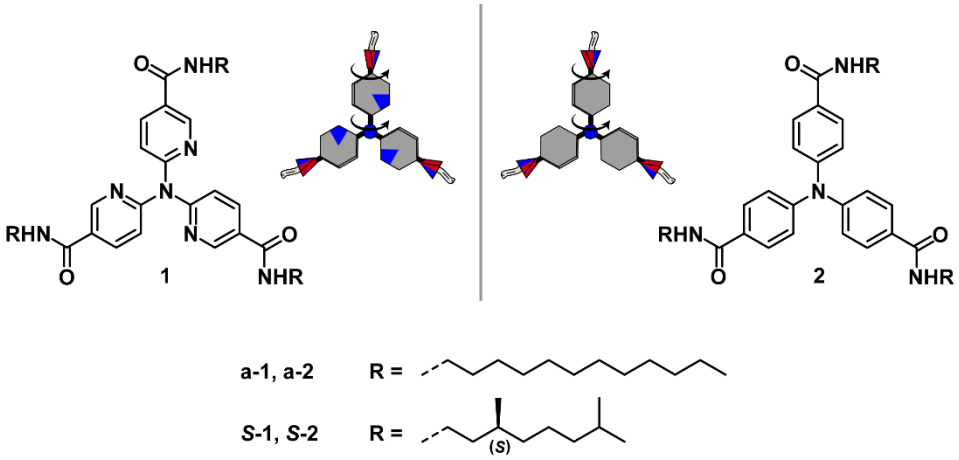

Scheme 1. Chemical structures of tri-5-carboxamides tri(pyrid-2-yl)amine (with achiral *n*-dodecyl chain, **a-1,** and with (*S*)-dimethyloctyl chain, ***S*-1**) and tri-p-carboxamides triphenylamine (with achiral *n*-dodecyl chain, **a-2,** and with (*S*)-dimethyloctyl chain, ***S*-2**).

2.2 Results and discussion

2.2.1 Synthesis

The synthetic approach to access trialkyl-substituted carbonyl-centered tripyridylamine-triamides (TPyAs, **1**) and triphenylamine-triamides (TPAs, **2**) is depicted in Scheme 2. The carboxylic acid precursors were synthesized using procedures described in literature.[47,45] The amide coupling was performed with both achiral *n*-dodecylamine (**a-1** and **a-2**) and chiral (*S*)-3,7-dimethyloctylamine (***S*-1** and **S-2**).

The triphenylamines **a-2** and ***S*-2** were obtained via first converting the tricarboxylic triacid into the triacid trichloride using oxalyl chloride, followed by coupling to the

desired amines (*n*-dodecylamine and (*S*)-3,7-dimethyloctylamine).[48] For **a-1** and ***S*-1**, in contrast, the acyl chloride intermediate was unstable and therefore the amide coupling was achieved through activation of the triacid via 1,1'-Carbonyldiimidazole (CDI) coupling.[45] After purification by column chromatography and recrystallization, **1** and **2** were obtained in high purity as verified by ^{1}H and ^{13}C NMR spectroscopy and mass spectroscopy (MALDI-TOF-MS). Bulk analysis with differential scanning calorimetry (DSC) and temperature-dependent infrared (TD-IR) spectroscopy completed the molecular characterization.

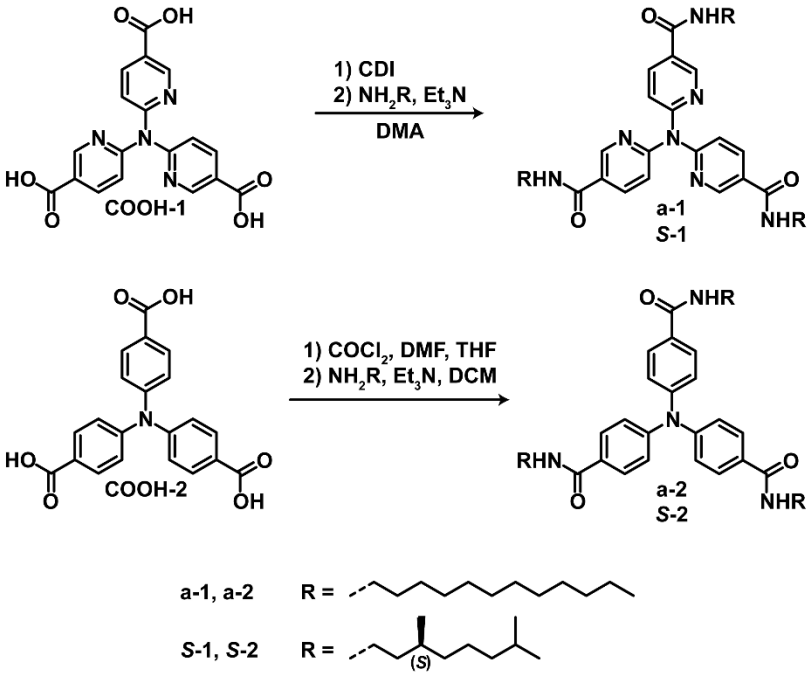

Scheme 2. Amide coupling of **1** and **2** with achiral *n*-dodecyl (**a-1** and **a-2**) and chiral (*S*)-3,7-dimethyloctyl chains (***S*-1** and ***S*-2**).

2.2.2. Assembly in methylcyclohexane

Supramolecular polymerization processes are often studied via optical spectroscopy. Variations in the molecular environment, such as a assembling process, perturbs the electronic transitions of the monomers and can be detected by UV-Vis spectroscopy in solution. The study of both triamides is performed using temperature-dependent spectroscopic measurements in methylcyclohexane (MCH) and chloroform ($CHCl_3$). In $CHCl_3$, all triarylamines are molecularly dissolved, whereas non-polar solvents, such as MCH, promote self-assembly at room temperature via directional H-bonding. This is evidenced by changes in the optical properties upon cooling as a result of supramolecular polymerization in MCH; effect not present in $CHCl_3$ at these concentrations.[64]

The absorption and emission spectra of ***S*-2** and ***S*-1** in MCH (c = 50 μM) were measured in a temperature range between 100 °C and 25 °C (Figure 1). Upon cooling UV-vis spectra show a blue-shift of the main absorption band and the rise of a blue-shifted shoulder (Figure 1a, 1c). The emission spectra of both the molecules at 25 °C display red-shifted emission compared to the ones at 100 °C or 90 °C (Figure 1b, 1d). These variations can be attributed to an aggregation process that affects the energy levels of the entire molecule. However, it is arduous to understand the aggregation processes involved based only on absorption and emission spectra. Often, supramolecular polymerization mechanisms can be unraveled by following the intensities of the absorption and emission maxima upon cooling, but ***S*-1** and ***S*-2** exhibit non-standard trend upon cooling which further complicates the analysis (Figure 1 insets).

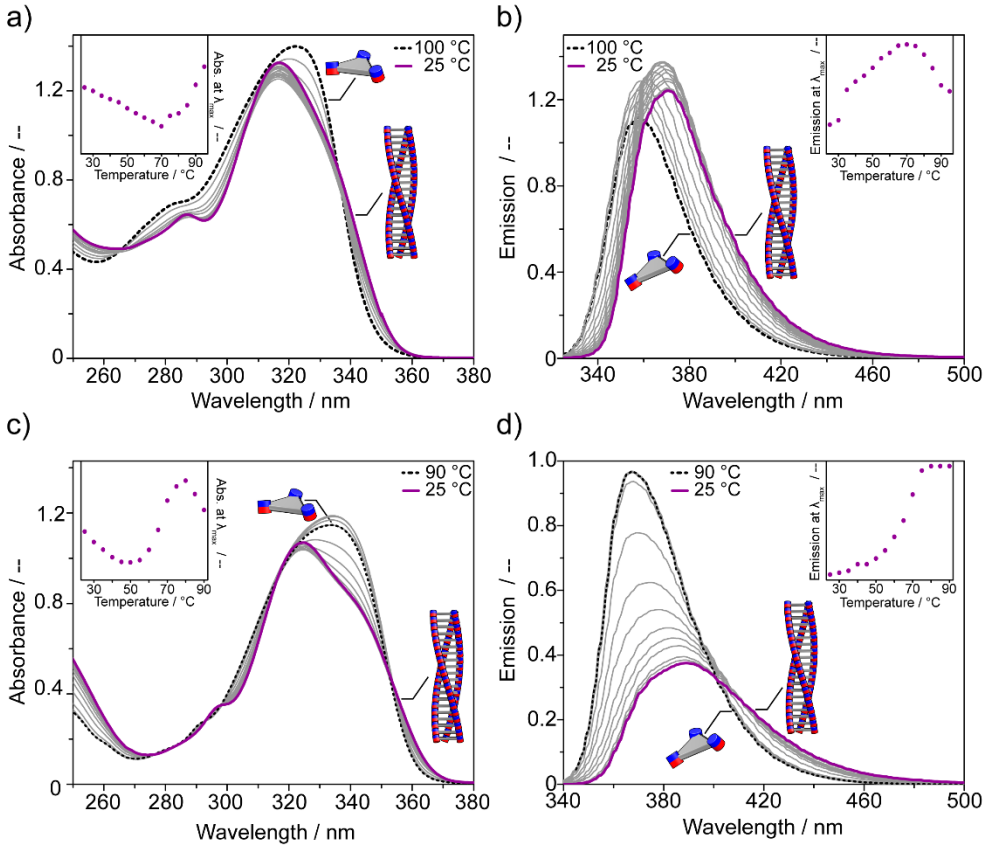

Figure 1. Absorbance and emission spectra for (a, b) ***S*-1** and (c, d) ***S*-2** and related cooling curves followed at absorption and emission maxima (insets). Spectra recorded in MCH (c = 50 μM, cooling rate = 60 °C h^{-1}). Spectra of molecularly dissolved solution at 100 °C or 90 °C (black dotted line) and at the assembled state at 25 °C (purple line), grey steps recorded every 5 °C.

With the aim of better understanding the processes, we acquired circular dichroism (CD) spectra over a broad temperature range (Figure 2). Owing to the chirality of the monomers that impose a preferred helicity to the supramolecular aggregate, CD allows the investigation of the supramolecular polymerization of these macromolecular helical assemblies. Both systems display no CD effect at high temperature while, upon cooling and assembly, a strong positive Cotton effect is recorded in the triarylamine absorption bands around λ = 347 nm for ***S*-2** and λ = 331 nm for **S-1**. The positive Cotton effect recorded upon aggregation for both samples indicates that the chirality of the chains dominates the sign and shape of the CD regardless of the structure of the central core. This finding, in combination with a blue shifted UV, suggests that the main driving force of the polymerization is the H-bonding interaction. In order to probe the evolution in detail, the CD in the maximum Cotton effect was monitored as a function of temperature. The experimental melting curves were recorded starting at high temperature in a molecularly dissolved solution and cooled down at 60 °C h^{-1}.

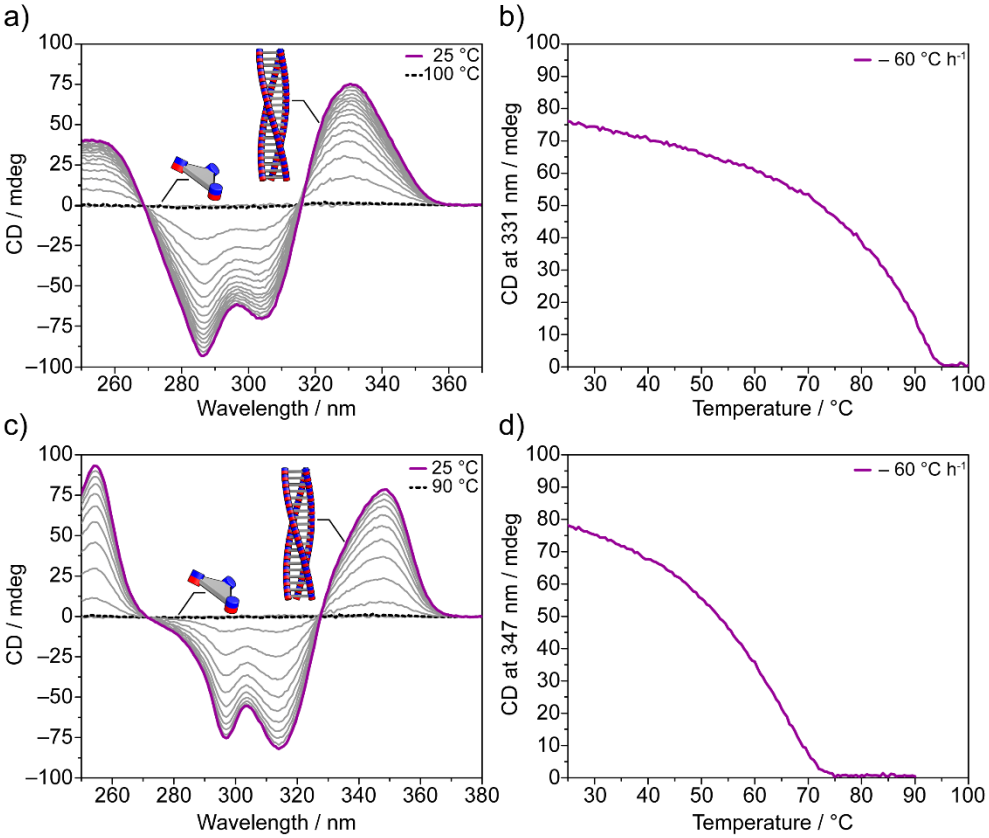

Figure 2. CD spectra of (a) ***S*-1** and (c) ***S*-2** as a function of temperature. Spectra acquired from the molecularly dissolved state (black dotted lines) every 5 °C (grey lines) till 25 °C (purple lines). CD cooling curves recorded at the respective CD maxima for (b) ***S*-1** (λ = 331 nm) and (d) for ***S*-2** (λ = 347 nm). Measurements in MCH, *c* = 50 μM, cooling rate 60 °C h^{-1}.

The melting curves recorded show two regimes, an initial phase at high temperature where no long aggregates are formed, characterized by no CD effect, followed by a rapid transition to positive CD values that occurs at 75.2 °C for ***S*-2** and 95.0 °C for ***S*-1**. The transition temperature, commonly called elongation temperature T_e, reveals that ***S*-1** shows the formation of supramolecular polymers, **poly(*S*-1)**, very close to the boiling point of the solvent ($c_{S\text{-}1}$ = 50 µM) while ***S*-2** polymerizes into **poly(*S*-2)** at a temperature 20 °C lower than ***S*-1**. The melting curves were also recorded at different concentrations and a shift of the T_e to lower temperatures was observed upon decreasing the concentration (Figure 3a, 3b). The recorded cooling curves indicate that both ***S*-1** and ***S*-2** exhibit a strongly cooperative supramolecular polymerization in alkane solvents. The van 't Hoff plot for ***S*-2** and ***S*-1** (Figure 3c, 3d) showed a larger thermodynamic gain upon aggregation of ***S*-1** to **poly(*S*-1)** than ***S*-2** to **poly(*S*-2)**, which is in agreement with the higher T_e observed at c = 50 µM.

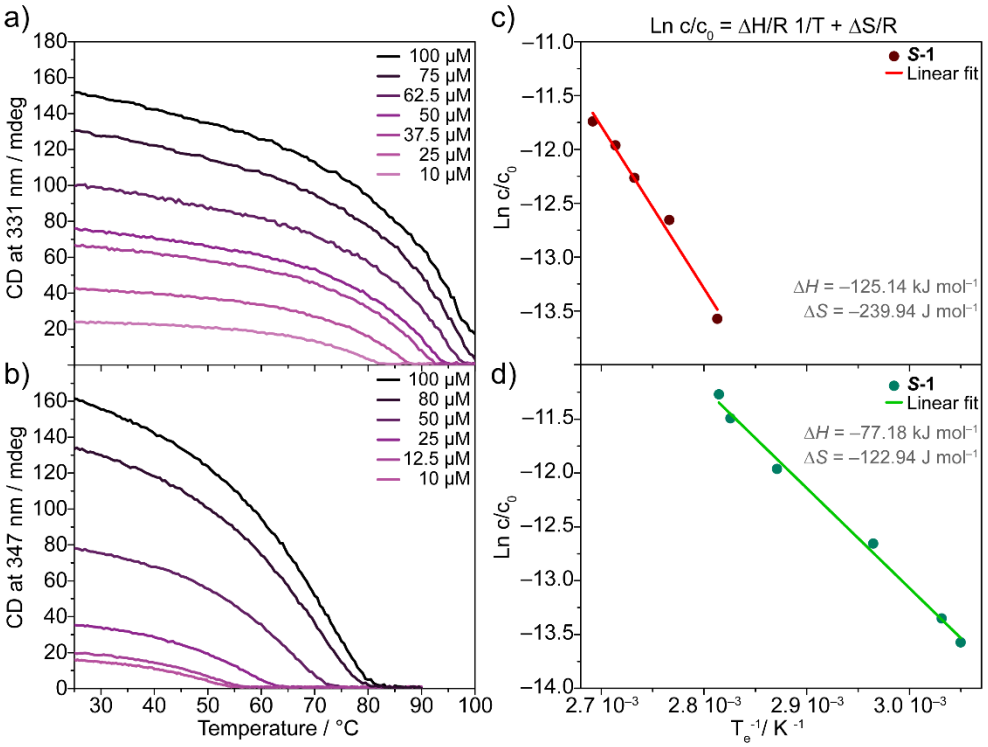

Figure 3. CD cooling curves recorded at different concentration followed at (a) λ = 331 nm for ***S*-1** at (b) λ = 347 nm for ***S*-2**; related van't Hoff plots for (c) ***S*-1** and (d) ***S*-2**. Measurements in MCH, cooling rate of 60 °C h^{-1}.

In addition, we fitted the melting curves to the nucleation–elongation model developed by Ten Eikelder and Markvoort[49] to calculate the released enthalpy upon elongation. Interestingly, we observe that for both the triarylamines the model does not fit properly showing a significant deviation in the multicurve fit[64] (data not shown). The deviation from a classic cooperative model is coherent with the trends recorded in the temperature-dependent UV-Vis and fluorescence measurements and clearly indicates that a second process competes with the nucleation–elongation mechanism at lower temperatures.

2.2.3. Assembly behavior below room temperature

We further investigated the self-assembly behavior in MCH solution by reducing the temperature to -10 °C. UV-Vis and emission spectra at -10 °C are then compared with the data recorded in the first assembled state at 50 °C and in the monomerically dissolved state (100 °C for ***S*-1** and 90 °C for ***S*-2**) (Figure 4). The comparison shows resembling spectra at -10 °C and at 50 °C for **poly(*S*-1)** and only a net decrease in intensity is recorded (Figure 4a, 4b). In contrast, UV-Vis spectrum of **poly(*S*-2)** at -10 °C shows an evident increment of the red-shifted shoulder at 350 nm while the main peak and the blue-shifted shoulder decrease (Figure 4c). Similarly, the fluorescence displays a 20 nm red-shift of the aggregate peak while the monomer fluorescence almost completely vanishes (Figure 4d).

We repeated the analysis by measuring the evolution of the CD as a function of temperature. The CD effect was probed at λ = 331 nm for **S-1** and λ = 347 nm for ***S*-2**, the data were recorded starting at high temperature in a molecularly dissolved solution and cooling the solution at 60 °C h^{-1}. After equilibrating the system at -10 °C, the following heating ramp was performed (rate: 60 °C h^{-1}) (Figure 5). The CD cooling-heating curve of **poly(*S*-1)** displayed a small decrease of the CD intensity below room temperature combined with a small red-shift in the CD spectrum (Figures 5a, 5c). The following heating run exhibits a large hysteresis that disappears just above 77 °C, displaying the reversibility of the system.

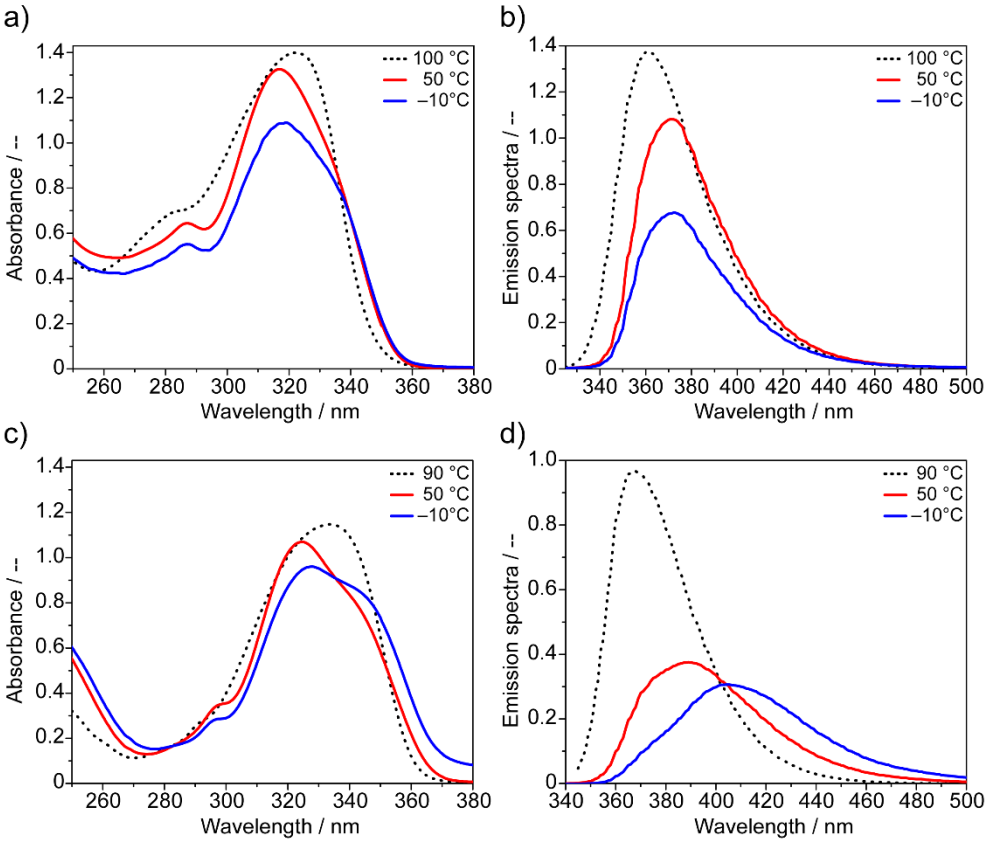

Figure 4. UV-vis and emission spectra of (a, b) ***S*-1** and (c, d) ***S*-2** in MCH (c = 50 µM) at the three states observed, monomerically dissolved (dotted black lines, T = 100 °C for ***S*-1** and 90 °C for ***S*-2**), **state I** (red lines, T = 50 °C) and **state II** (blue lines, T = -10 °C).

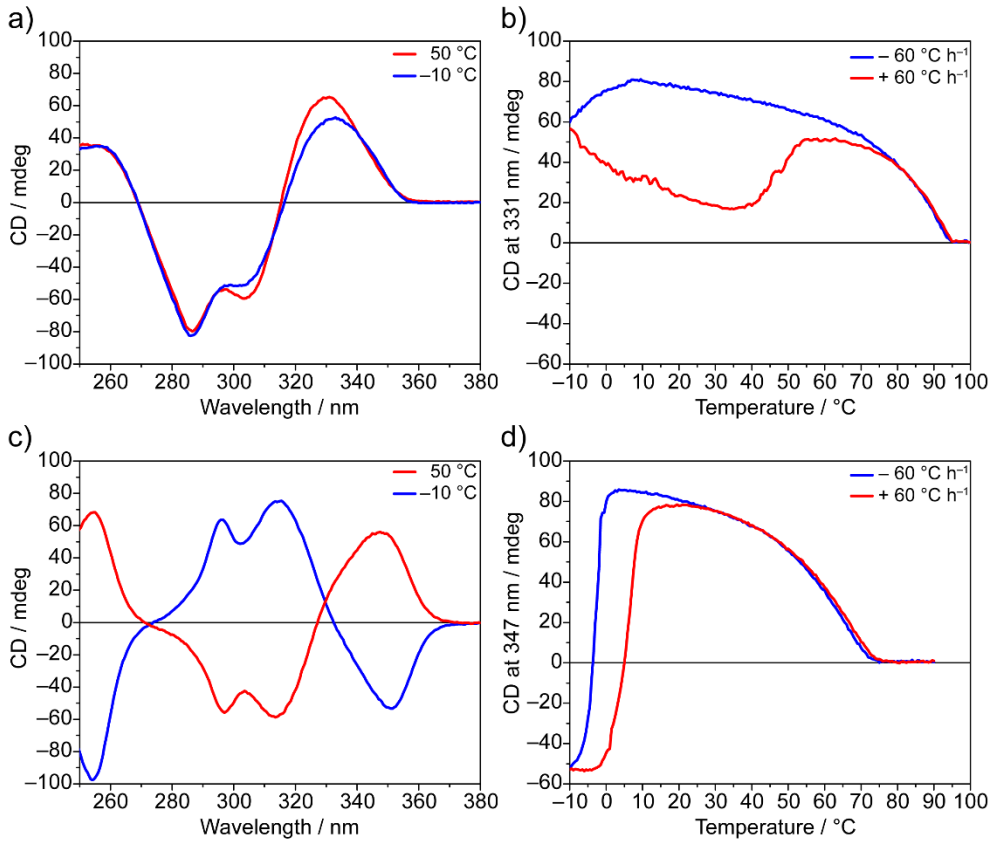

Figure 5. CD spectra of (a) **poly(*S*-1)** and (c) **poly(*S*-2)** in MCH (c = 50 µM). CD spectra recorded at 50 °C (red lines) and at -10 °C (blue lines). Melting curves of (b) **poly(*S*-1)** and (d) **poly(*S*-2)** at a cooling-heating rate of ±60 °C h^{-1}, cooling curve (blue lines) and heating curve (red lines).

Interestingly, the effect observed for **poly(*S*-1)** is amplified in the case of **poly(*S*-2).** The cooling curve of **poly(*S*-2)** exhibits a pronounced inversion of the Cotton effect at 0 °C leading to negative values at -10 °C. Upon heating, the curve is not superimposable with the cooling curve. The negative Cotton effect persists for 10 °C and shows a drastic inversion around 0 °C. Above 25 °C the two curves are superimposable again (Figures 5b, 5d). Fascinatingly, the shape of the CD spectra at 50 °C and -10 °C temperatures are nearly mirror images displaying a shift of a few nanometers only. The changes in the CD spectra and the other spectroscopic measurements suggest that a transition within the aggregated state occurs below room temperature. Whereas **poly(*S*-1)** displays distinct changes in all spectra, the thermal treatment on **poly(*S*-2)** promotes even an inversion of handedness. Due to the similarities between the two triarylamines, we speculated on the possibility of having an analogous behavior with **poly(*S*-1)**. Therefore, we studied the supramolecular polymerization of ***S*-1** in decalin (mixture of isomers) in order to decrease the strength of the interaction among monomers. The solubility of ***S*-1** in

decalin is better than in MCH and the thermodynamic parameters of **poly(*S*-1)** in decalin are closer to the values of **poly(*S*-2)** in MCH (From van 't Hoff analysis on ***S*-1** in decalin: ΔH = -92.38 kJ mol^{-1}, ΔS = -0.16 kJ mol^{-1}, to be compared with ***S*-2** in MCH Figure 3d). The recorded spectra and the cooling-heating curve of ***S*-1** in decalin are indeed more similar to ***S*-2** in MCH (Figure 6). The absorption peak of ***S*-1** in decalin shows a general broadening below 0 °C with an evident increment of the blue-shifted shoulder and a decrease of the main peak (Figure 6a). Similarly to what was observed in MCH, the fluorescence is half-quenched (Figure 6b). The CD melting curves at λ = 333 nm display the same handedness and cooperativity than those in MCH but, below room temperature a sharp inversion results in opposite CD values like ***S*-2** in MCH (Figures 6c, 6d).

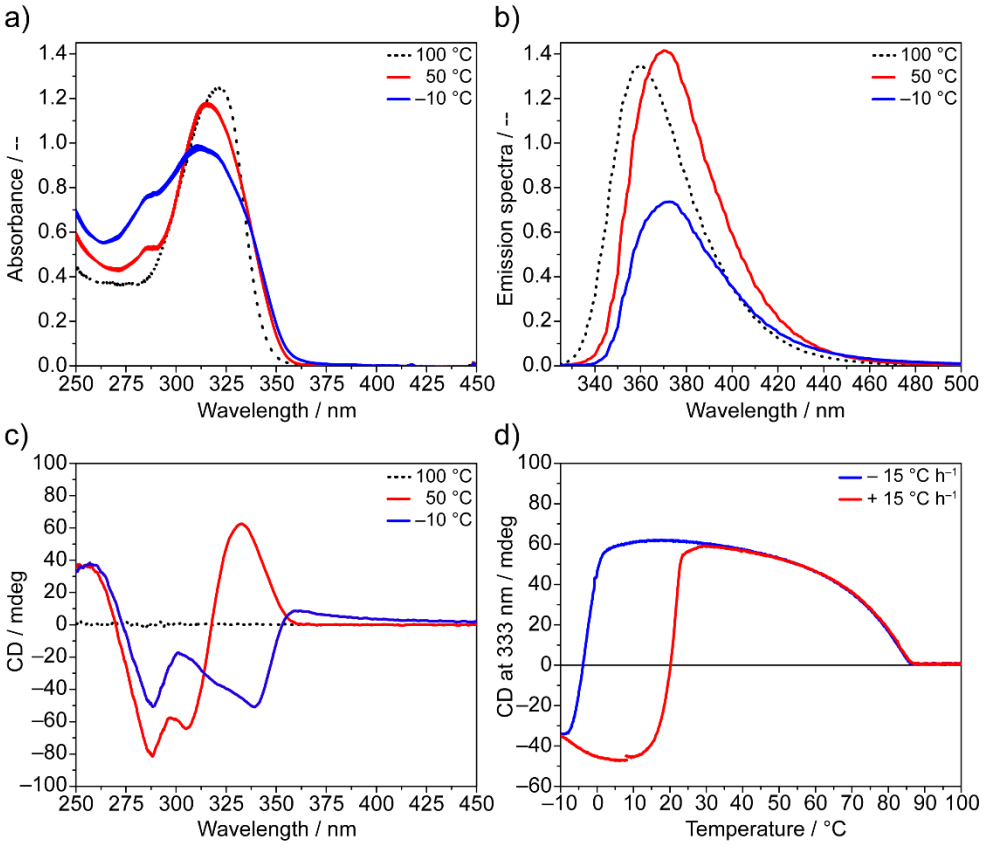

Figure 6. Recorded spectra of **poly(*S*-1)** in decalin isomers mixture (c = 50 μM), (a) UV-vis, (b) fluorescence, (c) CD spectra and (d) related cooling-heating curve followed at λ = 333 nm at a cooling-heating rate of 15 °C h^{-1}. Dotted black lines represent the CD spectrum of the monomerically dissolved solutions recorded at 100 °C. Red lines are the spectra recorded at 50 °C, blue lines are the spectra recorded at -10 °C.

The hysteresis recorded in the heating curve is around 30 °C. Nevertheless, in contrast with **poly(*S*-2)**, the CD spectra of **poly(*S*-1)** below and above room temperature are not mirror images: the inversion of the bisignated CD is only partial, the high-energy couplet displays just a small decrease while the peaks above λ = 300 nm are inverted. Moreover, the low temperature spectrum shows a small positive Cotton effect at λ = 350 nm that can probably be assigned to the presence of large aggregates that scatter the light since almost no absorption is recorded in that region. This hypothesis is supported by DLS data (Figure 7) which show much larger aggregates at –10 °C compared to 50 °C, as visible by the larger decay and higher countrates' intensity.

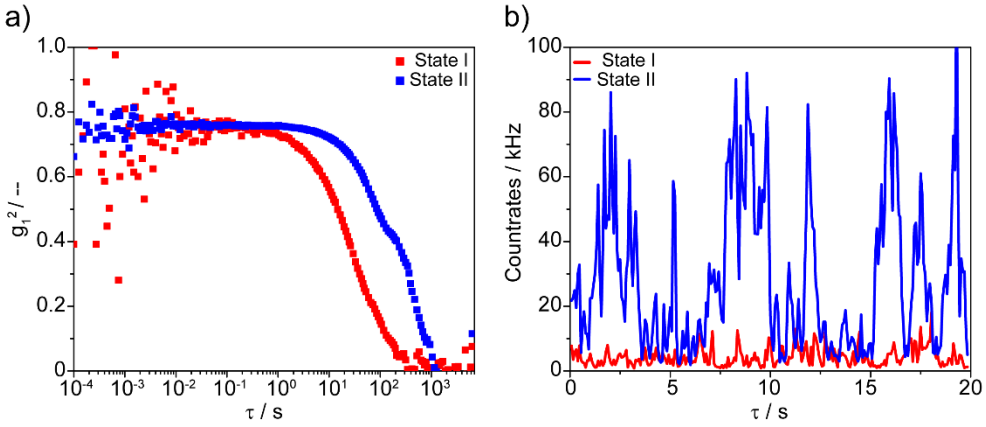

Figure 7. DLS (a) decay and (b) countrates for **poly(*S*-1)** (decalin *c* = 100 μM) recorded in **State I** (red lines, recorded at 50 °C) and **State II** (blue lines, recorded at -10 °C).

2.2.4. State analysis

The thermal analysis performed on both systems highlights a general behavior. A first assembled state (**state I**), with positive CD extrema (λ = 333 nm for **poly(*S*-1)** in decalin and λ = 347 nm for **poly(*S*-2)** in MCH) is cooperatively formed at higher temperature from the molecularly dissolved solution. A second state begins to take part in the assembly process upon gradually lowering the temperature. Below a certain threshold, it dominates leading to a second state (**state II**), which shows a negative CD extremum, indicative of an inverted handedness.

For both systems, melting curves were measured at different concentrations (range: 10 µM - 100 µM) to investigate how the inversion temperature (T_i) depends on the concentration. Whereas T_e is, as expected, highly concentration-dependent, we observed that T_i is roughly invariant with the concentration (Figure 8). This result indicates that the conversion from **state I** to **state II** is a concentration-independent process. Typically such concentration-independent processes are related to intra-helical conformational changes or a transition between two types of assembled states,[38,39,52-55] making bundling of supramolecular assemblies a less likely explanation for rationalizing the changes in the CD spectra.[56]

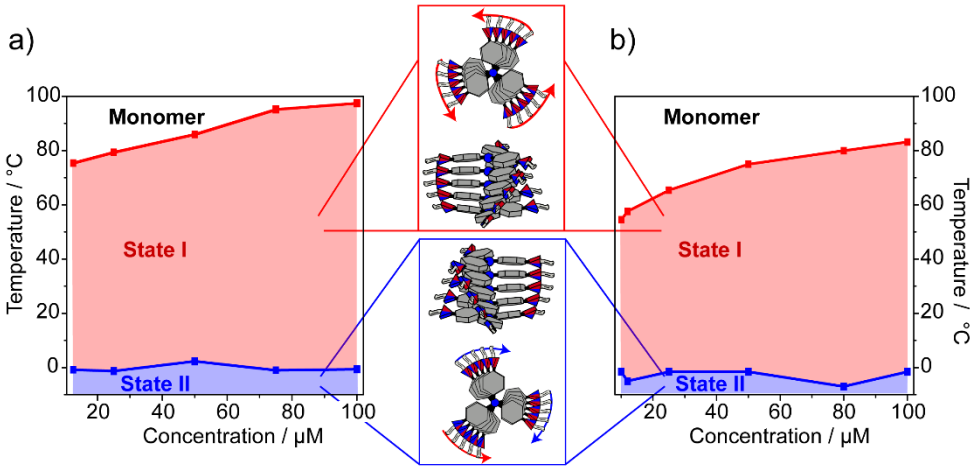

Figure 8. Diagram of states as a function of temperature and concentration. Elongation temperature (T_e, red squares) and inversion temperature (T_i, blue squares) of (a) **poly(*S*-1)** in decalin (mixture of isomers) and (b) **poly(*S*-2)** in MCH recorded at different concentrations. Depending on temperature, both systems assemble in distinctly different aggregates which show opposite handedness.

2.2.5. Computational analysis

In order to further analyze the systems, DFT calculations were performed by Ivo Filot. To reduce the computational time, calculations were performed on oligomers and infinite chains of **Me-1** and **Me-2**, in which the aliphatic chains are replaced by methyl groups (Figure 9a). Upon supramolecular aggregation, **Me-1** and **Me-2** can assemble in such a way that the H-bonding dipoles either align in a parallel or in a quasi-antiparallel fashion. The dipole moments are oriented from the carbonyl oxygen of one discotic to the amide hydrogen of a neighboring discotic. Herein, we refer to these two different conformations as 3:0 (where all three dipoles are parallel) and 2:1 (two parallel and one antiparallel), respectively.[50] The calculated structures of **poly(Me-1)** and **poly(Me-2)** for these two possible conformations are reported together with a schematic representation (Figures 9 and 10).[64]

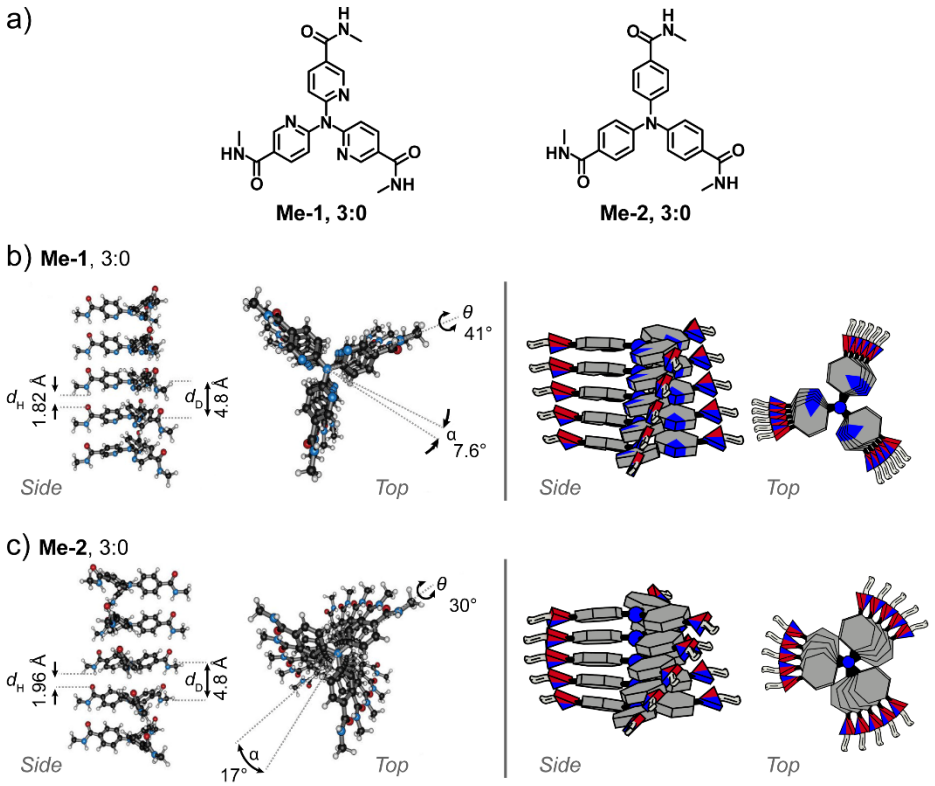

Figure 9. (a) Chemical structures of **Me-1** and **Me-2** used for the computational calculation in 3:0 state (parallel orientation of the dipoles). Three-dimensional structures of (b) **poly(Me-1)**, and (c) **poly(Me-2)** in 3:0 conformation. On the left, DFT calculated structures. The interdiscotic distance, d_D, and interdiscotic angle, α, the hydrogen bond length, d_H, and the carbonyl-aryl dihedral angle, θ, are given. On the right, a schematic representation of the structures is reported to represent the molecular organization.

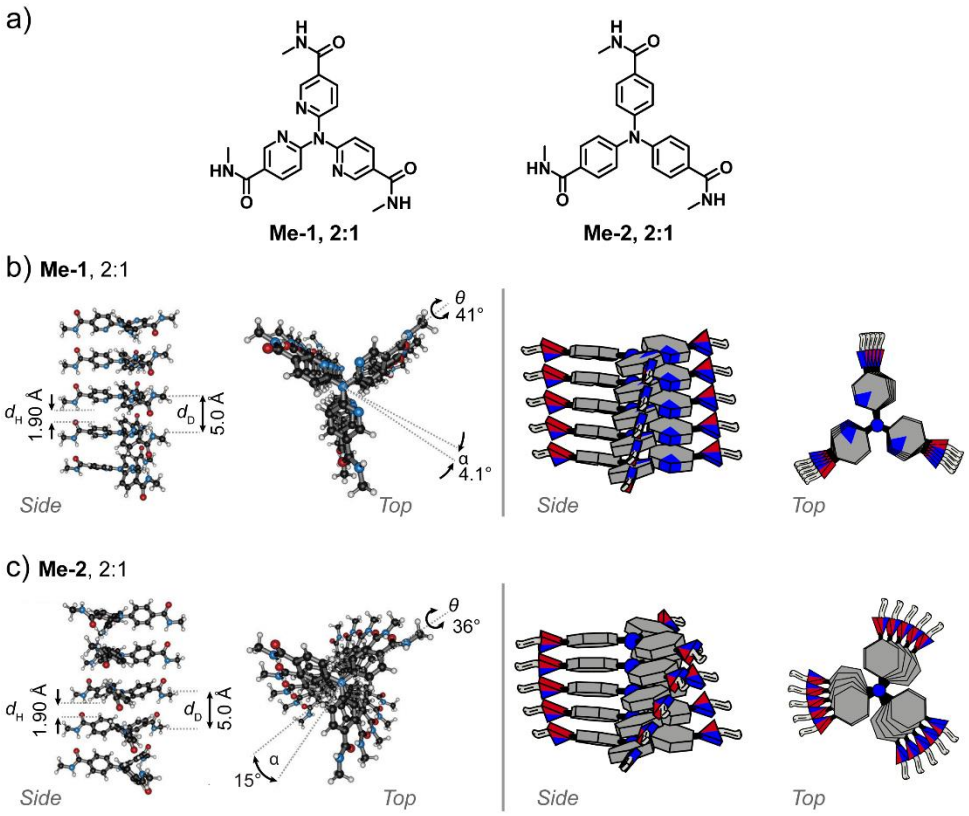

Figure 10. (a) Chemical structures of **Me-1** and **Me-2** used for the computational calculation in 2:1 state (antiparallel orientation of the dipoles). Three-dimensional structure of (b) **poly(Me-1)**, and (c) **poly(Me-2)** in 2:1 conformation. On the left, DFT calculated structures. The interdiscotic distance, d_D, and interdiscotic angle, α, the H-bond length, d_H, and the carbonyl-aryl dihedral angle, θ, are given. On the right, a schematic representation of the structures is reported to represent the molecular organization.

Interestingly, for **poly(Me-1)** the inversion of the amide between 3:0 and 2:1 occurs with a coherent torsion of the pyridine ring in order to maintain the antiparallel orientation of the pyridine dipole and amide dipole. Thus, the conformation 2:1 of **poly(Me-1)** loses the C_3 symmetry of the triarylamine core. In both the conformational states, **poly(Me-1)** shows a carbonyl dihedral angle (θ) moderately larger compared to **poly(Me-2)** and BTA.[51] The greater rotational mobility of the carbonyl group is rationalized by the deactivation of the conjugated π-system by the presence of the nitrogen in the pyridyl ring. As the pyridyl nitrogen withdraws electronic density from the π-system, less overlap between the latter and the carbonyl group results in an enhanced rotational flexibility. This greater torsion is reflected in a smaller interdiscotic angle (α) and hydrogen bond length (d_H) compared to **poly(Me-2)**.

Therefore, the carbonyl groups of **poly(Me-1)** have a higher out-of-plane rotation resulting in a more favorable conformation for hydrogen bond formation leading to a stronger interaction energy (Figures 5, 6, 11). Regardless of the number of monomers in the supramolecular chain and the conformation assumed, the binding energy is larger (*i.e.*, more stable) for **poly(Me-1)** compared to the **poly(Me-2)**, corroborating our experimental observations (Figure 11, Figure 3c, 3d). Furthermore, the binding energy analysis reveals that the supramolecular polymerization is cooperative, *i.e.*, the consecutive addition of monomers to the supramolecular aggregate results in an increasingly stronger binding energy between the monomers. For both the molecules, the antiparallel conformation (2:1) in the oligomer is more stable. The infinite chain calculation follows the same trend.

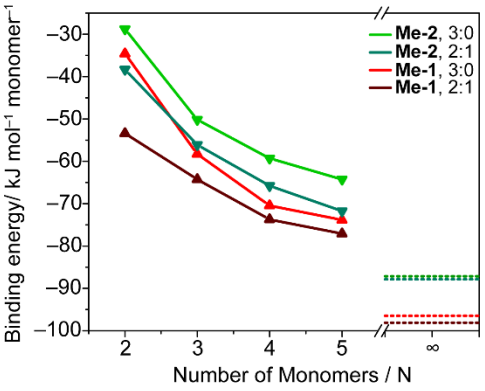

Figure 11. Average binding energy per monomer of **poly(Me-1)** for both the 3:0 and 2:1 conformations (up-facing triangles, red for 3:0 and bordeaux for 2:1) and **poly(Me-2)** (down-facing triangles, light green for 3:0 and dark green for 2:1). Energy calculated for the dimer up to and including the pentamer. The dotted lines depict the asymptotic value of the average binding energy of the periodic chains. All energies are given in kJ mol^{-1}.

2.3. The discovery of the effect played by water dispersed in oil

Coinciding with this reseach,[64] Van Zee *et al.* investigated another conformationally flexible supramolecular monomer, biphenyl tetracarboxamide, ***S*-3**.[65] ***S*-3** has been selected for its intrinsic axial flexibility[60] and its close resemblance to the model BTA.[41] Interestingly, supramolecular polymerization studies on ***S*-3** (Figure 12a) in MCH were strikingly similar to those of ***S*-1** and ***S*-2. *S*-3** displays a cooperative transition from molecular dissolved state to a first, CD positive, state named **state I**. Then, around 25 °C a sharp transition leads ***S*-3** to **state II**, which presents a shifted positive CD signal. Further cooling of the sample results in a second drastic transition to **state III**, this time with opposite helicity (Figure 12b). Similarly to **poly(*S*-1)** and **poly(*S*-2)**, the T_e (that marks the transition from ***S*-3** to **poly(*S*-3) state I**) follows normal concentration dependence for cooperative systems, while the transitions **state I-state II** and **state II–state III** are concentration independent (Figure 12c).

Detailed studies on **poly(*S*-3)** unveiled that the transitions **state I-state II** and **state II–state III** are governed by the presence of co-dissolved water in alkanes (Figures 12c, 12d). As is well known, water is only sparingly miscible in these solvents—typical alkanes contain less than 0.01 per cent water by weight at room temperature.[61] However, a commonly overlooked feature is that water is essentially monomeric in oils.[62,63] As such, water molecules in alkanes possess potential enthalpic energy in the form of unrealized hydrogen bonds. As a results, this energy is a thermodynamic driving force for water molecules to interact with co-dissolved hydrogen-bond based aggregates in oils. By using a combination of spectroscopic, calorimetric, light-scattering and theoretical techniques, Van Zee *et al.* demonstrated that this interaction can be exploited to modulate the structure of one-dimensional supramolecular polymers.[65]

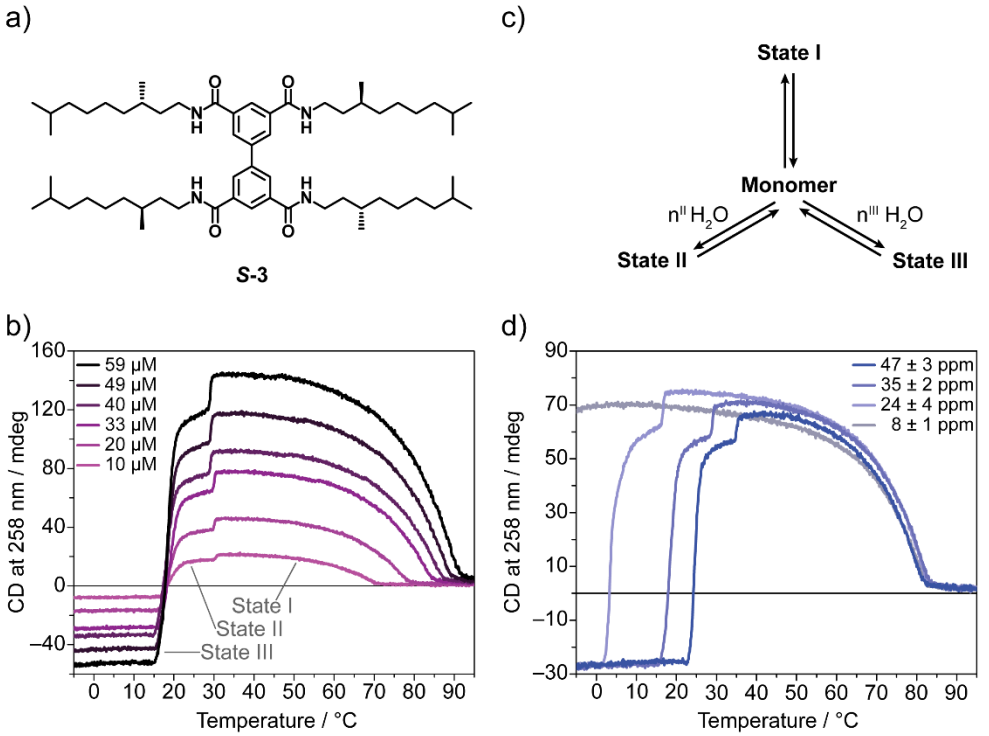

Figure 12. (a) Chemical structure of enantiopure biphenyltetracarboxamide functionalized with (*S*)-3,7-dimethyloctyl chains, ***S*-3**. (b) CD cooling curves in which the concentration of ***S*-3** was varied while the water content was held constant (c = 59 M (darkest shade), 49 µM, 40 µM, 33 µM, 20 µM and 10 µM (lightest shade); [H_2O] = 35 ± 2 p.p.m.). (c) Schematic representation of three cooperative, competitive pathways. (d) CD cooling curves in which the water content was varied while the concentration of ***S*-3** was held constant ([H_2O] = 47 ± 3 p.p.m (darkest shade), 35 ± 2 p.p.m., 24 ± 4 p.p.m., 8 ± 1 p.p.m (lightest shade); c = 30 µM). All water content measurements are reported as mean ± s.d. (n = 2).

In detail, for ***S*-3** the formation of **state I** is dominated just by the formation of hydrogen bonds among ***S*-3** molecules, while **state II** and **state III** are essentially copolymers of ***S*-3** with water molecules which intercalate in the supramolecular polymer structure. The transition temperatures where copolymerization with water occurs (**state I-state II** and **state II-state III**) are modulated by the concentration of co-dissolved water (Figures 12c, 12d).

To prove the generality of this effect, and confirm that also the transition **state I-state II** observed for ***S*-1** and ***S*-2** is dictated by the water content of the alkane solution, we performed cooling curves maintaining the molecular concentration constant (c = 50 μM) and varying the concentration of water co-dissolved in MCH. Consistent with what was reported for **poly(*S*-3)**, **poly(*S*-1)** and **poly(*S*-2)** show dependence on the water concentration in the T_i. Therefore, it is possible to drift the T_i at higher temperatures with high water content solution, or to lower temperatures with dried MCH solutions (Figure 13).

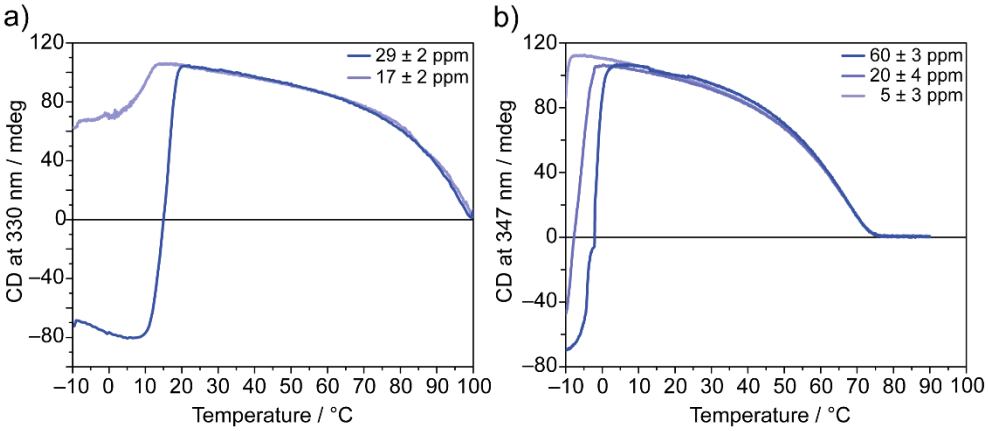

Figure 13. CD cooling curves of (a) **poly(*S*-1)** and (b) **poly(*S*-2)** in which the concentration of ***S*-1** or ***S*-2** was held constant and the concentration of water was varied. Measurements in MCH, c = 50 μM. All water content measurements are reported as mean ± s.d. (n = 2).

A common feature of ***S*-1**, ***S*-2** and ***S*-3** is their axial flexibility; we propose that this conformational freedom positively contributes to accommodate water molecules within the supramolecular polymers and allow the formation of multiple assembled states. However, the presence of monomerically dissolved water in alkanes likely influences more rigid supramolecular polymers as well. To address this, we re-examined the self-assembly of chiral benzene tricarboxamide (BTA) ***S*-4** (Figure 14a) as a function of water concentration. ***S*-4** has been the subject of many previous studies[41] and can be considered as the reference model for supramolecular polymers in MCH. Although variation of the water content does not affect the helicity of **poly(*S*-4)**, aggregates of ***S*-4** prepared in wet MCH scatter more light than fibers formed in dry MCH.[65] Measurements by atomic force microscopy (AFM) suggest an important role for water in modulating the lateral interaction between **poly(*S*-4)** fibers. Single-chain fibers are imaged via AFM when ***S*-4** is drop-cast under wet conditions (Figure 14b), whereas coils of several chains are detected in samples prepared under dry conditions (Figure 14c).

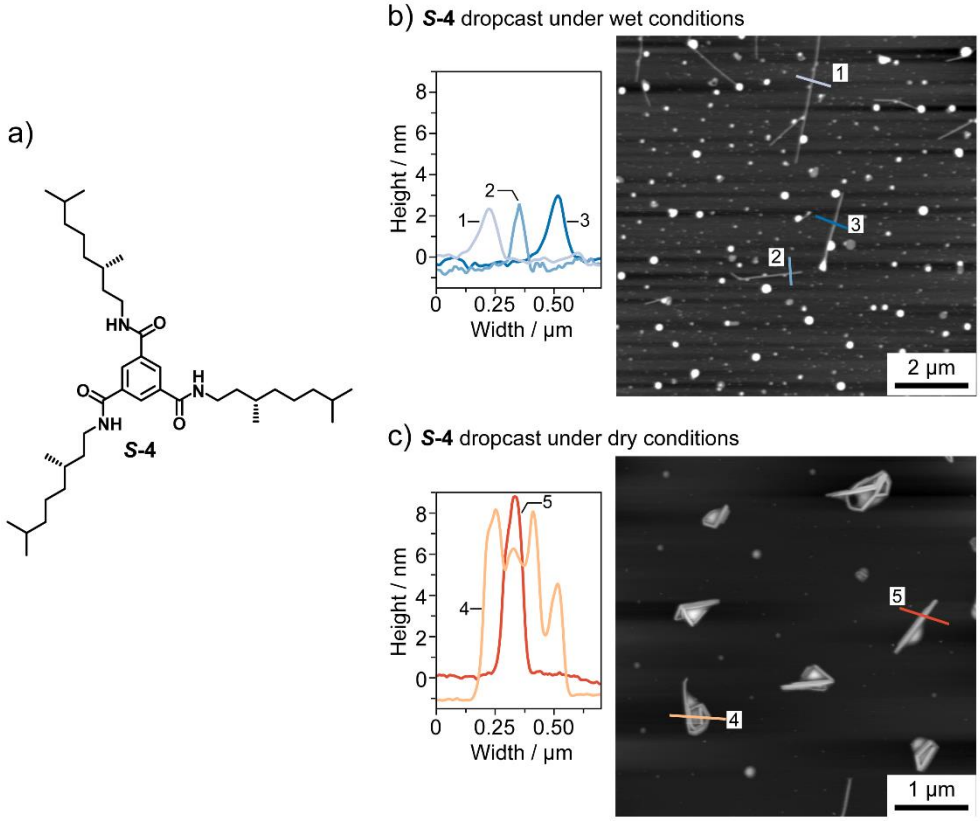

Figure 14. (a) Molecular structure of benzentricarboxamide functionalized with (*S*)-3,7-dimethyloctyl chains, ***S*-4**. AFM of **poly(*S*-4)** dropcasted under (b) wet and (c) dry conditions with relative fiber analysis. Samples prepared in MCH (c = 30 µM) and dropcasted on mica.

2.4. Conclusions

In conclusion, we showed that triarylamines bearing threefold H-bonding units supramolecularly polymerize in a strongly cooperative manner due to H-bonding interactions. In spite of the core differences, both molecules follow a general path leading to helical supramolecular polymers, at high temperature. Interestingly, the peculiar assembly of these triarylamines cannot be explained simply with the classical nucleation–elongation model due to the presence of a second process that becomes more accessible at low temperatures, and results in a second assembled state with opposite handedness.

We hypothesized that a plausible reason for the presence of two aggregate states is a change of molecular conformational coupled to a helical inversion. At high temperature, the free monomers can easily rotate around the single bonds and no conformation is defined. Consecutively, with the decrease of the temperature and the nucleation and elongation of the polymers, the molecular conformation settles to allow the formation of the H-bonding network. DFT calculations evidenced that triarylamines can form two different polymerized states which are both stable. One with high symmetry, with parallel amide dipoles, 3:0, and one with a lower level of symmetry which has one amide dipole in anti-parallel fashion, 2:1. We argued that the transition between the two assembled states is closely related to this conformation change and is reflected in the spectroscopy signature of the two molecules

This hypothesis has been further demonstrated and upgraded by the subsequent work by Van Zee *et al.* [65] We discovered that the transition between the two assembled states, which is allowed by the intrinsic conformation flexibility of the molecules, is caused by the singular effect of co-dissolved water in alkanes. The monomeric state of water in alkanes acts as driving force for itself to copolymerize with the H-bonded polymers present in solution. The incorporation of water is possible because of the rotational freedom of the supramolecular monomers which modify their conformation to accommodate the water molecules. This generates a reorganization of the supramolecular conformation causing the helical change.

Although that monomer's flexibility is fundamental to achieve a rapid handedness inversion upon copolymerization with water, we here propose that the monomeric nature of water in alkanes has a general influence on co-dissolved H-bonded supramolecular polymers. As example, we demonstrated that water affects the later forces of the model BTA system. We propose that many other unidentified structural transitions or unexpected behavior observed in H-bond-based aggregates in oils arise from this fundamental effect and we anticipate that controlling this additional interaction will bring further advances in the field.

2.5. Experimental section

2.5.1. Methods and materials

All solvents were obtained from Biosolve, Acros or Aldrich. All other chemicals were obtained from Aldrich. Dry DCM, THF, and DMF were tapped off a distillation setup which contained molsieves. $CHCl_3$ was dried over molsieves and triethylamine was stored on KOH pellets. (*S*)-(-)-Citronellol was purchased from Aldrich and converted into the corresponding (*S*)-3,7-dimethyloctan-1-amine according to a described procedure.[66] 1,1′-Carbonyldiimidazole (CDI) was vacuum-oven dried before use. ***S*-3** and ***S*-4** were synthesized by other members of the group and the synthesis reported elsewhere, ***S*-3**[65] and ***S*-4**.[41] All other chemicals were used as received. Synthesized compounds were vacuum-oven dried before use.

^1H NMR and ^{13}C NMR measurements were conducted on a Varian Mercury 200 MHz and/or a Varian Gemini 400 MHz (100 MHz for ^{13}C). Proton chemical shifts are reported in ppm downfield from tetramethylsilane (TMS). Carbon chemical shifts are reported using the resonance of $CDCl_3$ as internal standard. MALDI-TOF-MS were acquired using a PerSerptive Biosystem Voyager-DE PRO spectrometer using α-cyano-4-hydroxycinnamic acid (CHCA) and 2-[(2*E*)-3-(4-tert-butylphenyl)-2-methylprop-2-enylidene]malononitrile (DCTB) as matrices. IR spectra were recorded on a Perkin–Elmer spectrum two FTIR spectrometer. Variable temperature IR spectra were recorded on a Bruker Tensor 27 GladiATR with temperature controller. Polarization optical microscopy (POM) measurements were done using a Jenaval polarization microscope equipped with a Linkam THMS 600 heating device, with crossed polarizers. The thermal transitions were determined with DSC by using a Perkin–Elmer Pyris 1 DSC under a nitrogen atmosphere with heating and cooling rates of 10 °C min-1. Dynamic light scattering analysis was performed with ALV/CGS-2 MD-4 DLS. Three scans of 20 seconds have been recorded setting the angle at 80°. AFM was performed using an Asylum Research MFP-3D system in non-contact tapping mode. Images were processed using Gwyddion 2.49. Samples were prepared by dropcasting pre-assembled structures from diluted conditions ($c \leq 50$ μM, details in related images) onto mica.

UV/Vis and circular dichroism (CD) measurements were performed on a Jasco J-815 spectropolarimeter, for which the sensitivity, time constants and scan rates were chosen appropriately. Corresponding temperature-dependent measurements were performed with a Jasco PFD-425S/15 Peltier- type temperature controller with a temperature range of 263–393 K and adjustable temperature slope. In all experiments the linear dichroism was also measured and in all cases no linear dichroism was observed. Separate UV/Vis spectra were obtained from a Perkin–Elmer UV/Vis spectrometer Lambda 40. Fluorescence spectra were measured with Jasco FMO-427S/15 fluorimeter implemented in the CD spectrometer. For all spectroscopic measurements, cells with an optical path length of 1 cm were employed and spectroscopic grade solvents were employed. Stock solutions (1 mM) were prepared by weighing the necessary amount of compound for the given concentration and transferring it to a volumetric flask that was filled up to its meniscus. The stock solutions were heated up and sonicated till complete dissolution every time before the preparation of diluted sample solutions. All the spectroscopic measurement were performed with freshly prepared solutions (max. 1 week after the preparation of the stock solution).

CD experiments related to the water effects were performed using special precaution to control the humidity. Cuvettes equipped with a screw cap and a Teflon-lined septum were found to be best suited for these measurements. To determine the water content after analysis by CD spectroscopy, dilute samples were directly injected into the Karl Fischer titration instrument after withdrawing from the sealed cuvette by syringe. All Karl Fischer titration measurements were performed in duplicate and expressed as mean ± s.d. unless otherwise stated. At the ambient humidity in the laboratory in which this research was carried out, as-received MCH contained 20 ± 2 p.p.m. H_2O (mean ± s.d. of four measurements). MCH was dried by sparging with argon and then storing over activated 3 Å molecular sieves overnight in a sealed bottle. After bringing into a nitrogen-filled glovebox, the MCH was passed through a 0.2 μm Whatman Anatop 10 syringe filter. The typical water content for dry MCH prepared in this way was <0.1 p.p.m. (that is, below the level of detection of the Karl Fischer titration). Dry samples were prepared in a nitrogen-filled glovebox with dry MCH, taking special care to use oven-dried glassware and Teflon-lined caps for vials. Wet MCH was prepared by layering MCH (around 20 mL) over water (around 1 mL) that was purified with an EMD Millipore Milli-Q Integral Water Purification System. After allowing to set overnight, wet MCH was carefully withdrawn with a syringe from the top layer without disturbing the bottom water phase. Wet samples were prepared on the benchtop;

care must be taken to minimize exposure of the solvent to the atmosphere by quickly sealing the sample vials. Wet MCH transferred in this way contained approximately 60 p.p.m. water.

2.5.2. Synthetic procedures

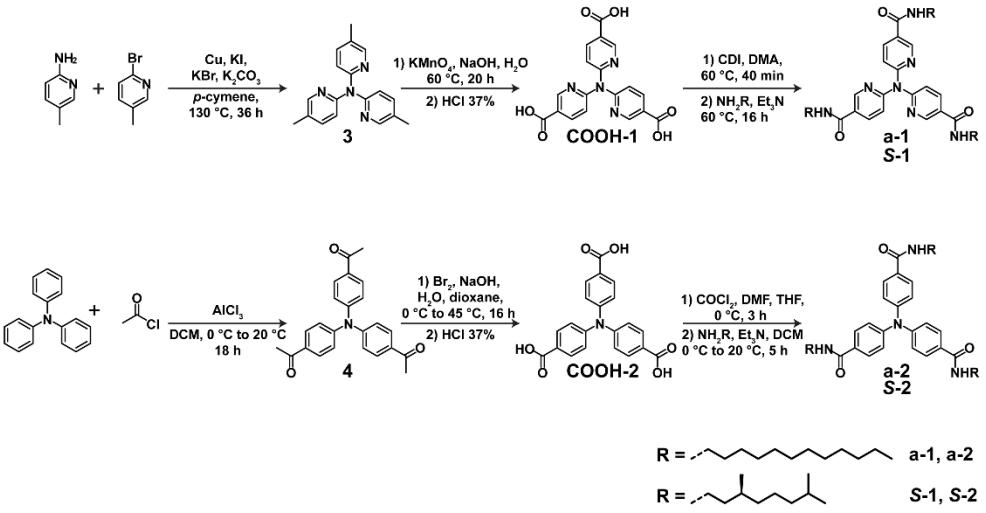

Scheme 3. Synthetic routes for **1** and **2.**

Tris[2-(5-methylpyridyl)]amine (3)

In an oven-dried round bottom flask under argon atmosphere 2-bromo-5-methylpyridine (3.18 g, 18.49 mmol), 5-methylpyridin-2-amine (1.00 g, 9.25 mmol), potassium carbonate (2.94 g, 21.27 mmol), potassium iodide (0.154 g, 0.925 mmol), potassium bromide (0.110 g, 0.925 mmol), and copper powder (0.470 g, 7.40 mmol) were dissolved in p-cymene (15 mL) and refluxed for 3 days under continuous stirring. The mixture was filtered hot over celite, and the solids were washed with ethanol. The filtrate was evaporated in vacuum. The product was purified by SiO_2 column chromatography (CH_2Cl_2/MeOH/DIPA 98/1.6/0.4 v/v/v) and recrystallized from acetone/hexane (2/98 v/v) affording **3** as yellow-green crystalline product (800 mg, 30%).

^{1}H NMR ($CDCl_3$, 200 MHz) δ (ppm): 8.18 (s, 3H,), 7.42 (d, 3H, J = 8 Hz), 6.95 (d, 3 H, J = 8 Hz), 2.28 (s, 9 H); m/z (TOF-MS): Calcd. for $[C_{18}H_{19}N_4]^+$ $[M+H]^+$ 291.16; found 291.16.

Tris(2-nicotinic acid)amine (COOH-1)

In a round bottom flask tris[2-(5-methylpyridyl)]amine **11** (670 mg, 2.307 mmol) was suspended in water (70 mL). A solution of NaOH (831 mg, 20.77 mmol) in water (20 mL) was added to the suspension and stirred, then $KMnO_4$ (3.03 g, 19.15 mmol) was slowly added. The reaction mixture was stirred at 60 °C for 4 h. Then a second portion of $KMnO_4$ (2.50 g, 15.85 mmol) was added. The reaction was continued at 60 °C for 16 h. The reaction mixture was filtered on a paper filter to remove the brown precipitate (MnO_2). The aqueous phase was acidified with concentrated HCl (37%) to pH = 2 and cooled to 5 °C. The resulting white precipitate was filtered and dried under vacuum affording **COOH-1** (750 mg, yield 85%) as a white powder.

^{1}H NMR (MeOD, 200 MHz) δ (ppm): 8.90 (s, 3H), 8.34 (d, 3H, *J* = 8 Hz), 7.27 (d, 3H, *J* = 8 Hz); m/z (ESI$^+$): Calcd. for $[C_{18}H_{13}N_4O_6]^+$ $[M+H]^+$ 381.08; found 381.17; IR (cm^{-1}) 2941, 1741 1727, 1712, 1644, 1585, 1550, 1476 1448, 1414, 1366, 1329, 1301, 1263, 1215, 1188, 1145, 1120, 1023, 962, 946, 899, 873, 849, 761, 673, 656, 619, 551, 531, 520, 494.

General synthesis of 6, 6', 6''-nitrilotris(N-dodecylnicotinamide) (a-1) and 6, 6', 6''-nitrilotris(N-(3,7-dimethyloctyl)nicotinamide) (S-1)

In a round bottom flask under argon atmosphere a solution of **COOH-1** (2.97 mmol) and CDI (1.59 g, 9.81 mmol) were dissolved in dry dimethylacetamide (40 mL) and stirred at 60 °C for 40 min. In a separate round bottom flask under argon atmosphere a solution of the appropriate alkylamine (10.4 mmol) and Et_3N (1.32 g, 13.07 mmol) in dry dimethylacetamide (2 mL) was prepared. Then, the amine solution was collected by a syringe and dropwise added to the CDI activated solution of **COOH-1**. The reaction mixture was stirred and heated at 60 °C for 16 h. The mixture was concentrated (reaching a volume of 5 mL) under reduced pressure and precipitated in acetonitrile (***S*-1**) or directly precipitate in acetonitrile (**a-1**). The crude product was purified by neutral Al_2O_3 column chromatography ($CHCl_3$/MeOH 97/3 v/v) and recrystallized from acetonitrile (***S*-1**) or ethanol (**a-1**) attaining a white solid (yield 35%).

***S*-1**: ^{1}H NMR (400 MHz, $CDCl_3$) δ (ppm): 8.69 (d, 3H, J = 4 Hz), 8.05 (dd, 3H, J_1 = 12 Hz, J_2 = 4 Hz), 7.12 (d, 3H, J = 12 Hz), 6.05 (t, 3H, J = 6 Hz); 3.53-3.44 (m, 6H); 1.66-1.20 (mm, 30H); 0.94 (d, 9H, J = 8 Hz); 0.86 (d, 18H, J = 8 Hz); ^{13}C NMR ($CDCl_3$,100 MHz,) δ (ppm): 165.03, 158.24, 147.30, 137.12, 126.95, 118.33, 39.19, 38.31, 37.11, 36.71, 30.78, 27.93, 24.66, 22.68, 22.57, 19.50; m/z (MALDI-TOF) Calcd. for $[C_{48}H_{76}N_7O_3]^+$ $[M+H]^+$ 798.60 ; found 798.62; IR (cm^{-1}) 3280, 3087, 2953, 2925, 2868, 1628, 1590, 1547, 1470, 1385, 1366, 1307, 1277, 1170, 1145, 1099, 1021, 945, 841, 778, 698, 537, 478. UV-Vis spectra ($CHCl_3$, 50 μM) λ_{max} = 327 nm, Emission spectra ($CHCl_3$, 50 μM) λ_{max} = 372 nm.

a-1: ^{1}H NMR ($CDCl_3$, 400 MHz,) δ (ppm): 8.70 (dd, 3H, J = 2 Hz), 8.07 (dd, 3H, J_1 = 2 Hz, J_2 = 8Hz), 7.15 (d, 3H, J = 8 Hz), 6.05 (t, 3H, J = 6 Hz), 3.49-3.44 (m, 6H), 1.63-1.58 (m, 6H), 1.34-1.17 (mm, 54H,), 0.88 (t, 9H, J = 9 Hz); ^{13}C NMR ($CDCl_3$,100 MHz,) δ (ppm): 165.12, 158.23, 147.35, 137.15, 126.99, 118.34, 40.20, 31.91, 29.65, 29.63, 29.60, 29.57, 29.35, 29.32, 27.00, 22.69, 14.12; m/z (MALDI-TOF) Calcd. for $[C_{54}H_{88}N_7O_3]^+$ $[M+H]^+$ 882.69 ; found 882.71; IR (cm^{-1}) 3279, 2921, 2852, 1629, 1589, 1539, 1470, 1379, 1314, 1276, 1170, 853, 775, 714, 570.

4, 4', 4''-Triacetyltriphenylamine (4)

Triphenylamine (0.5 g, 2.04 mmol) was dissolved in anhydrous CH_2Cl_2 (10 mL) in a three-neck round bottom flask under argon atmosphere. Slowly $AlCl_3$ (0.84 g, 6.32 mmol) was added under stirring, then the whole mixture was cooled to 0 ˚C by ice-water bath. Then acetyl chloride (0.5 g, 6.32 mmol) was added dropwise at 0 ˚C. After the addition was complete, and the reaction was stirred and allowed to reach room temperature overnight. The reaction mixture was poured into ice water (125 mL), the organic layer was extracted with CH_2Cl_2 (3 x 50 mL), dried on $MgSO_4$, collected and evaporated. The yellow green solid was purified by column chromatography (EtOAc/heptane v/v 1/9) to give **4** (700 mg, yield 92%).

^{1}H- NMR (400 MHz, $CDCl_3$) δ (ppm): 7.91 (d, 6H, J = 8 Hz), 7.16 (d, 6H, J = 8 Hz), 2.59 (s, 9H); m/z (ESI MS) Calcd for $[C_{24}H_{21}NO_3]^{\bullet+}$ $[M]^{\bullet+}$, 371.5; found 371.10

4, 4', 4''-Tricarboxyltriphenylamine (COOH-2)

4,4′,4′′-triacetyltriphenylamine **12** (450 mg, 1.21 mmol) was dissolved in 1,4-dioxane (12.5 mL) in a three-neck round bottom flask. Meantime, in a beaker Br_2 (0.62 mL, 12.12 mmol) was added dropwise to an aqueous (7.5 mL) solution of NaOH (1.59 g, 40 mmol) cooled by ice bath. After the addition, the solution was stirred for 20 min at room temperature. The solution was transferred in a dropping funnel and dropped into the solution of **4**. The mixture was stirred and heated at 45 ˚C overnight. Then, the mixture was cooled at 0 ˚C using an ice bath and saturated under stirring with hydroxylamine HCl to deoxidize the excess of formed sub-bromo-sodium ($NaBrO_2$). The solution was acidified by HCl (37%) till pH = 1.5. The pale yellow precipitate was filtered and dried under vacuum. The crude product was recrystallized from acetic acid to afford pure **COOH-2** as a white solid (400 mg, yield 87%).

^{1}H NMR (DMSO-*d6*, 400MHz) δ (ppm): 12.19 (s, 3H), 7.89 (d, 6H, *J* = 8 Hz), 7.12 (d, 6H, *J* = 8 Hz); m/z (ESI MS) Calcd for $[C_{24}H_{16}NO_6]^+$ $[M-H]^+$: 378.10, found 378.08; IR (cm^{-1}): 3183.6, 2984.9, 2826, 2543, 1675, 1592, 1509, 1424, 1314, 1277, 1221, 1174, 1131, 1107, 1016, 932, 852, 801, 770, 697, 669, 661, 628, 548, 521, 479

General synthesis of 4, 4', 4''-nitrilotris(N-dodecylbenzamide) (a-2) and 4,4',4''-nitrilotris(N-((S)-3,7-dimethyloctyl)benzamide) (S-2)

4,4',4"-tricarboxyltriphenylamine **COOH-2** (250 mg, 0.66 mmol) was dissolved in THF (9 mL) in an oven-dried round bottom flask under argon atmosphere and cooled to 0 ˚C with ice-bath. In a second oven-dried round bottom flask oxalylchloride (303 mg, 2.358 mmol) was dissolved in THF (2 mL) with a drop of diluted DMF (1% in THF) under argon atmosphere. The oxalyl chloride solution was collected with a syringe in order to avoid air exposition and added dropwise to the cooled solution of **COOH-2**. The stirred mixture was allowed to reach room temperature. After 3 h, the mixture was checked by IR to assess if the CO vibration of the acid disappeared. The solvent and the excess of oxalyl chloride was evaporated and the acyl chloride derivative dissolved in DCM (7 mL). In a separate round bottom flask under argon atmosphere the appropriate alkylamine (2.186 mmol) was dissolved in DCM (2 mL) with Et_3N (235 mg, 2.31 mmol) and cooled at 0 ˚C by an ice-bath. The solution of triphenylamine tris-acylchloride was collected with a syringe and slowly dropped into the amine. After the addition was complete, the stirred mixture was allowed to reach room temperature and stirred for 5 h. The mixture was diluted in DCM (50 mL), washed with HCl (1 M, 1 x 40 mL) and brine (2 x 40mL). The organic layer was collected, dried over $MgSO_4$, and evaporated. The crude product was purified by silica chromatography ($CHCl_3$/MeOH 98/2 v/v). The product was further recrystallized affording a white powder. Recrystallization with ethanol for **a-2**, (383 mg, yield 66%), and diethylether for ***S*-2** (212 mg, yield 40%).

***S*-2:** ^{1}H NMR $CDCl_3$, 400 MHz) δ (ppm): 7.67 (d, 6H, *J* = 16 Hz), 7.10 (d, 6H, *J* = 16 Hz), 5.98 (t, 3H, *J* = 10 Hz), 3.50-3.43 (m, 6H), 1.66-1.13 (mm, 36H), 0.94 (d, 9H, *J* = 12 Hz), 0.86 (d, 18H, *J* = 16 Hz); ^{13}C NMR ($CDCl_3$, 100 MHz) δ (ppm): 166.65, 149,26, 129,95, 128,33, 123.90, 39.23, 38.27, 37.81, 36.81, 30.81, 27.95, 24.66, 22.70, 22.60, 19.27; m/z (MALDI) Calcd. for $[C_{51}H_{79}N_4O_3]^+$ [M-H]$^+$:795.61 found 795.62; IR (cm^{-1}): 3311, 3071, 2953, 2926, 2868, 1632, 1599, 1548, 1499, 1499, 1467, 1379, 1366, 1297, 1280, 1187, 1146, 1111, 1016, 959, 847, 766, 734, 681, 662, 627, 537. UV-Vis spectra ($CHCl_3$, 50 μM) λ_{max} = 341.5 nm, Emission spectra ($CHCl_3$, 50 μM) λ_{max} = 392 nm.

a-2*:* ^{1}H NMR ($CDCl_3$, 400 MHz) δ (ppm): 7.67 (d, 6H, *J* = 8 Hz), 7.10 (d, 6H, *J* = 8 Hz), 6.01 (t, 3H, *J* = 6 Hz), 3.47-3.42 (m, 6H), 1.60 (q, 6H, *J* = 8Hz), 1.37-1.26 (mm, 54 H), 0.87 (t, 9H, J = 8 Hz); ^{13}C NMR ($CDCl_3$, 100 MHz) δ (ppm): 166.66, 149.24, 129.94, 128.32, 123.88, 40.12, 31.98, 29.72, 29.62, 29.61, 29.57, 29.54, 29.32, 27.00, 22.67, 14.10; m/z (MALDI) Calcd for $[C_{57}H_{91}N_4O_3]^+$ [M-H]$^+$ 879.71, found 879.71; IR (cm^{-1}): 32891, 3073, 2955, 2920, 2851, 1630, 1600, 1539, 1498, 1467, 1368, 1311, 1296, 1277, 1179, 1154, 1108, 1015, 947, 839, 766, 722, 692, 626, 564, 500, 480.

2.5.3. Bulk analysis

Table 1. Bulk analysis of **a-1**, ***S*-1**, **a-2**, ***S*-2**

DSC data[a]			TD-IR vibrations of amide units of ***S*-1** and ***S*-2** in solid and liquid state. [a]		
Molecule	T [K][b]	T_{melt} [K]	ν_{NH} [cm^{-1}]	$\nu_{C=O}$ [cm^{-1}]	$\nu_{NH(II)}$ [cm^{-1}]
a-1	344.6	487.5	3279[e]	1629[e]	1589[e]
***S*-1**	406.2[c]	433.3	3280[f] 3330 (3454) [g]	1627[f] 1641 (1670)[g]	1589[f] 1585[g]
a-2	358.0	474.4	3292[e] 3349 (3456) [g]	1629[e] 1643 (1668)[g]	1598[e] 1594
***S*-2**		391.3	3293[f] 3344 (3456) [g]	1629[f] 1637 (1666) [g]	1598[f] 1594[g]

[a] DSC and TD-IR heating cooling cycles: 10 K min^{-1}. DSC data reported for third cycle, temperature dependent infrared spectroscopy (TD-IR) data reported for first cycle. [b] Transition solid-mesophase. [c] Cold crystallization. [e] Measured at 25 °C for untreated samples. [f] Measured at 25 °C after slow cooling from melted state. [g] Measured in a melted solution.

2.5.4. Computational section

Computational details:

Plane-wave DFT (PW-DFT) electronic-structure calculations were performed for the monomer up to and including the pentamer using the Vienna Ab Initio Simulation Package (VASP). Structures larger than the pentamer were found to be too computationally demanding. All DFT calculations were performed using the PBE exchange-correlation functional that has been shown to reproduce hydrogen-bond lengths and energies with high accuracy. A cutoff energy of 500 eV was used and the VASP precision parameter was set to high. Additional computational details as well as the Cartesian coordinates of the atoms and the unit cell dimensions, are given in the supporting information.

Computational analysis

Supramolecular polymers are rather flexible and small deviations of the geometric parameters were found between the individual discotic and side groups. The geometric flexibility corresponds to a relatively flat potential energy surface (PES) around the conformational minimum as shown for similar benzene tris-amides aggregates (BTAs) earlier. Therefore, the reported values are the average for the abovementioned parameters. Both 3.0 aggregates show the same average interdiscotic distance (d_D) of 4.8 Å (Figures 9, 10). Otherwise, the pyridyl-carbonyl dihedral angle (θ) of **Me-1** was found to be moderately larger (θ = 41°) compared to the phenyl-carbonyl dihedral angle of **Me-2** (θ =30°). The greater rotational mobility of the carbonyl group is rationalized by the deactivation of the conjugated π-system by the presence of the nitrogen in the pyridyl ring. As the pyridyl nitrogen withdraws electronic density from the π-system, less overlap between the latter and the carbonyl group results in an enhanced rotational flexibility. This greater torsion is reflected by the interdiscotic angle (α) and the hydrogen bond length which are both rather smaller for **Me-1** compared to **Me-2**. Therefore, the carbonyl groups of **Me-1** can have a higher out of plane rotation resulting in a more favorable conformation for hydrogen bond formation. This leads to a shorter hydrogen bond lengths (d_H) and, consequently, to a stronger interaction energy. Otherwise, compared to parallel conformation, both systems in the 2:1 fashion show a slightly larger d_D of 5 Å (Figure 10). For **Me-1** the dihedral angle is not affected on the alignment of the three dipole but α results decreased by half and d_H rather longer reaching 1.90 Å. The parallel conformation of **Me-2** shows an increment from 30° to 36° in the out of plane rotation of the carbonyl group (θ) that leads to a smaller interdiscotic angle (α) and a shortened hydrogen bond length (d_H).

Rotation Penalty estimation:

The approximated rotation penalty for one carbonyl in a free **Me-1** monomer and in an assembled stack has been calculated. The "rotation penalty" is defined as the difference between the most stable structure and the most unstable structure while keeping the spatial coordinates of all the other atoms away from the reactive center constant. This rotation penalty is then a rough approximation of the activation energy for rotation.

The rotation penalties measured for a free monomer is 3 kJ mol^{-1}, while for a bound monomer (i.e. inside a chain), the energy barrier is of 46 kJ mol^{-1}. The latter number is in good agreement with the (non-covalent) scission of two hydrogen bonds as the carbonyl rotation results in the elimination of two such hydrogen bonds. Note that within the molecules as studied in this article, the approximated H-bond strength is ~20 kJ mol^{-1}.

Computational settings

All DFT calculations were performed using VASP. The PBE exchange-correlation functional was used in conjunction with the projector augmented wave approach. All structures were optimized to their local minima using the conjugate gradient algorithm as implemented in VASP. Optimization and other electronic settings are given below.

Settings

Parameter	INCAR setting	value
Cutoff energy	ENCUT	500
Precision	PREC	High
Smearing type	ISMEAR	0 (Gaussian mearing)
Smearing width	SIGMA	0.0005
Electronic convergence threshold	EDIFF	1E-5
Ionic relaxation threshold	EDIFFG	1E-4

K-point grid

For all calculations, only the Γ -point was used.

2.6. References

[1] S. T. Hoffmann, F. Jaiser, A. Hayer, H. Bässler, T. Unger, S. Athanasopoulos, D. Neher, A. Köhler, *J. Am. Chem. Soc.* **2013**, 135, 1772–1782.
[2] A. B. Kaiser, *Adv. Mater.* **2001**, 13, 927–941.
[3] A. C. Arias, J. D. MacKenzie, I. McCulloch, J. Rivnay, A. Salleo, *Chem. Rev.* **2010**, 110, 3–24.
[4] A. P. H. J. Schenning, E. W. Meijer, *Chem. Commun.* **2005**, 3245–3258.
[5] A. Jain, S. J. George, *Mater. Today* **2015**, 18, 206–214.
[6] A. P. H. J. Schenning, P. Jonkheijm, F. J. M. Hoeben, J. van Herrikhuyzen, S. C. J. Meskers, E. W. Meijer, L. M. Herz, C. Daniel, C. Silva, R. T. Phillips, et al., *Synth. Met.* **2004**, 147, 43–48.
[7] E. W. Meijer, A. P. H. J. Schenning, *Nature* **2002**, 419, 353–354.
[8] T. Aida, E. W. Meijer, S. I. Stupp, *Science* **2012**, 335, 813–817.
[9] M. Sofos, J. Goldberger, D. a Stone, J. E. Allen, Q. Ma, D. J. Herman, W.-W. Tsai, L. J. Lauhon, S. I. Stupp, *Nat. Mater.* **2009**, 8, 68–75.
[10] J. J. Armao, M. Maaloum, T. Ellis, G. Fuks, M. Rawiso, E. Moulin, N. Giuseppone, *J. Am. Chem. Soc.* **2014**, 136, 11382–11388.
[11] Y. Domoto, E. Busseron, M. Maaloum, E. Moulin, N. Giuseppone, *Chemistry* **2015**, 21, 1938–1948.
[12] V. Faramarzi, F. Niess, E. Moulin, M. Maaloum, J.-F. Dayen, J.-B. Beaufrand, S. Zanettini, B. Doudin, N. Giuseppone, *Nat. Chem.* **2012**, 4, 485–490.
[13] I. Nyrkova, E. Moulin, J. J. Armao, M. Maaloum, B. Heinrich, M. Rawiso, F. Niess, J.-J. Cid, N. Jouault, E. Buhler, et al., *ACS Nano* **2014**, 8, 10111–24.
[14] J. Kim, J. Lee, W. Y. Kim, H. Kim, S. Lee, H. C. Lee, Y. S. Lee, M. Seo, S. Y. Kim, *Nat. Commun.* **2015**, 6, 6959.
[15] P. Jonkheijm, P. van der Schoot, A. P. H. J. Schenning, E. W. Meijer, *Science* **2006**, 313, 80–83.
[16] I. V Baskakov, G. Legname, M. A. Baldwin, S. B. Prusiner, F. E. Cohen, *J. Biol. Chem.* **2002**, 277, 21140–21148.
[17] P. A. Korevaar, T. F. A. de Greef, E. W. Meijer, *Chem. Mater.* **2014**, 26, 576–586.
[18] P. A. Korevaar, S. J. George, A. J. Markvoort, M. M. J. Smulders, P. A. J. Hilbers, A. P. H. J. Schenning, T. F. A. De Greef, E. W. Meijer, *Nature* **2012**, 481, 492–496.
[19] S. Ogi, K. Sugiyasu, S. Manna, S. Samitsu, M. Takeuchi, *Nat. Chem.* **2014**, 6, 188–195.
[20] S. Ogi, V. Stepanenko, K. Sugiyasu, M. Takeuchi, F. Würthner, *J. Am. Chem. Soc.* **2015**, 137, 3300–3307.
[21] R. Rai, A. Saxena, A. Ohira, M. Fujiki, *Langmuir* **2005**, 21, 3957–3962.
[22] D. van der Zwaag, T. F. A. de Greef, E. W. Meijer, *Angew. Chem. Int. Ed.* **2015**, 54, 8334–8336.
[23] A. Aliprandi, M. Mauro, L. De Cola, *Nat. Chem.* **2016**, 8, 10–5.
[24] J. Kang, D. Miyajima, T. Mori, Y. Inoue, Y. Itoh, T. Aida, *Science* **2015**, 347, 646–651.
[25] S. Ogi, V. Stepanenko, J. Thein, F. Würthner, *J. Am. Chem. Soc.* **2016**, 138, 670–678.
[26] Y. Nakano, A. J. Markvoort, S. Cantekin, I. A. W. Filot, H. M. M. ten Eikelder, E. W. Meijer, A. R. A. Palmans, *J. Am. Chem. Soc.* **2013**, 135, 16497–16506.
[27] S. Cantekin, Y. Nakano, J. C. Everts, P. van der Schoot, E. W. Meijer, A. R. A. Palmans, *Chem. Commun.* **2012**, 48, 3803–3805.
[28] R. D. Mukhopadhyay, A. Ajayaghosh, *Science* **2015**, 349, 241–242.
[29] C. K. Song, K. A. Luck, N. Zhou, L. Zeng, H. M. Heitzer, E. F. Manley, S. Goldman, L. X. Chen, M. A. Ratner, M. J. Bedzyk, et al., *J. Am. Chem. Soc.* **2014**, 136, 17762-17773
[30] M. Chen, H. Nie, B. Song, L. Li, J. Z. Sun, A. Qin, B. Z. Tang, *J. Mater. Chem. C* **2016**, 4, 2901–2908.
[31] T. Yamada, H. Kaji, *J. Mol. Struct.* **2009**, 927, 82–87.
[32] Y. T. Tsai, C. T. Lai, R. H. Chien, J. L. Hong, A. C. Yeh, *J. Polym. Sci. Part A Polym. Chem.* **2012**, 50, 237–249.
[33] E. Bacher, M. Bayerl, P. Rudati, N. Reckefuss, C. D. Müller, K. Meerholz, O. Nuyken, *Macromolecules* **2005**, 38, 1640–1647.
[34] H.-J. Yen, G.-S. Liou, *Polym. J.* **2015**, 48, 117–138.
[35] Q. Liu, K. Jiang, L. Wang, Y. Wen, J. Wang, Y. Ma, Y. Song, *Appl. Phys. Lett.* **2010**, 96, 213305.
[36] X. Jiang, K. M. Karlsson, E. Gabrielsson, E. M. J. Johansson, M. Quintana, M. Karlsson, L. Sun, G. Boschloo, A. Hagfeldt, *Adv. Funct. Mater.* **2011**, 21, 2944–2952.
[37] N. Nath Ghosh, A. Chakraborty, S. Pal, A. Pramanik, P. Sarkar, *Phys. Chem. Chem. Phys.* **2014**, 16, 25280–7.
[38] A. Mahmood, *Sol. Energy* **2016**, 123, 127–144.
[39] S. Paek, N. Cho, S. Cho, J. K. Lee, J. Ko, *Org. Lett.* **2012**, 14, 6326–6329.
[40] M. Sonntag, K. Kreger, D. Hanft, P. Strohriegl, S. Setayesh, D. de Leeuw, *Chem. Mater.* **2005**, 17, 3031–3039.
[41] P. J. M. Stals, J. C. Everts, R. de Bruijn, I. A. W. Filot, M. M. J. Smulders, R. Martín-Rapún, E. A. Pidko, T. F. A. de Greef, A. R. A. Palmans, E. W. Meijer, *Chemistry* **2010**, 16, 810–821.
[42] P. J. M. Stals, M. M. J. Smulders, R. Martín-Rapún, A. R. A. Palmans, E. W. Meijer, *Chemistry* **2009**, 15, 2071–2080.
[43] M. M. J. Smulders, A. P. H. J. Schenning, E. W. Meijer, *J. Am. Chem. Soc.* **2008**, 130, 606–611.
[44] K. Wei, J. Ni, Y. Min, S. Chen, Y. Liu, *Chem. Commun.* **2013**, 49, 8220–8222.
[45] H. Szelke, H. Wadepohl, M. Abu-youssef, R. Krämer, *Eur. J. Inorg. Chem.* **2009**, 251–260.
[46] W. Yao, K. Kavallieratos, S. de Gala, R. H. Crabtree, *Inorganica Chim. Acta* **2000**, 311, 45–49.
[47] J. Wang, C. He, P. Wu, J. Wang, C. Duan, *J. Am. Chem. Soc.* **2011**, 133, 12402–12405.
[48] G. Koeckelberghs, L. De Cremer, W. Vanormelingen, W. Dehaen, T. Verbiest, A. Persoons, C. Samyn, *Tetrahedron* **2005**, 61, 687–691.
[49] A. J. Markvoort, H. M. M. ten Eikelder, P. A. J. Hilbers, T. F. A. de Greef, E. W. Meijer, *Nat. Commun*. **2011**, 2, 509.
[50] K. K. Bejagam, G. Fiorin, M. L. Klein, S. Balasubramanian, *J. Phys. Chem. B* **2014**, 118, 5218–28.

[51] I. A. W. Filot, A. R. A. Palmans, P. A. J. Hilbers, R. A. van Santen, E. A. Pidko, T. F. A. de Greef, *J. Phys. Chem. B* **2010**, 114, 13667–13674.
[52] J. van Gestel, P. van der Schoot, M. A. J. Michels, *J. Phys. Chem. B* **2001**, 105, 10691–10699.
[53] M. Roman, C. Cannizzo, T. Pinault, B. Isare, B. Andrioletti, P. van der Schoot, L. Bouteiller, *J. Am. Chem. Soc.* **2010**, 132, 16818–16824.
[54] M. Bellot, L. Bouteiller, *Langmuir* **2008**, 24, 14176–14182.
[55] P. van der Schoot, M. A. J. Michels, L. Brunsveld, R. P. Sijbesma, A. Ramzi, *Langmuir* **2000**, 16, 10076–10083.
[56] P. J. M. Stals, P. A. Korevaar, M. A. J. Gillissen, T. F. A. de Greef, C. F. C. Fitié, R. P. Sijbesma, A. R. A. Palmans, E. W. Meijer, *Angew. Chemie Int. Ed*. **2012**, 51, 11297–11301.
[57] K. K. Bejagam, C. Kulkarni, S. J. George, S. Balasubramanian, *Chem. Commun.* **2015**, 51, 16049–16052.
[58] D. van der Zwaag, P. A. Pieters, P. A. Korevaar, A. J. Markvoort, A. J. H. Spiering, T. F. A. de Greef, E. W. Meijer, *J. Am. Chem. Soc.* **2015**, 137, 12677–12688.
[59] R. Schulman, E. Winfree, *Proc. Natl. Acad. Sci.* **2007**, 104 , 15236–15241.
[60] Mikami, K. , Korenaga, T. , Terada, M. , Ohkuma, T. , Pham, T. and Noyori, R., *Angew. Chem. Int. Ed.* **1999**, 38, 4
[61] Riddick, J. A., Bunger, W. B. & Sakano, T. K. *Organic Solvents, Physical Properties and Methods of Purification,* John Wiley & Sons, New York, **1986.**
[62] Christian, S. D., Taha, A. A. & Gash, B. W. Q., *Rev. Chem. Soc.* **1970**, 24, 20–36.
[63] Wolfenden, R. & Radzicka, A., *Science* **1994**, 265, 936–937.
[64] B. Adelizzi, I. A. W. Filot , A. R. A. Palmans, E. W. Meijer, *Chem. Eur. J.* **2017**, 23 (25), 6103-6110.
[65] N. J. Van Zee, B. Adelizzi, M. F. J. Mabesoone, X. Meng, A. Aloi, R. H. Zha, M. Lutz, I. A.W. Filot, A. R.A. Palmans, E.W. Meijer, *Nature* **2018**, 558, 100-103
[66] T. Mes, R. Van Der Weegen, A. R. a Palmans, E. W. Meijer, *Angew. Chem. Int. Ed.* **2011**, 50, 5085–5089.

3.

Chiral supramolecular polymers suppress hydrogen peroxide formation in water-splitting solar cells

These results are obtained in close collaboration with Ron Naaman's group and are summarized in:

W. Mtangi, F. Tassinari, K. Vankayala, A. R. Vargas Jentzsch, B. Adelizzi, A. R. A. Palmans, C. Fontanesi, E. W. Meijer and R. Naaman
J. Am. Chem. Soc., **2017**, 2794-2798

Abstract: The production of hydrogen through water-splitting in a photoelectrochemical cell suffers from an overpotential that limits the efficiencies. In addition, hydrogen-peroxide formation is identified as a competing process affecting the oxidative stability of photoelectrodes. We propose that a modification of the photoelectrochemical cells with molecules able to exert chiral induced spin-selection reduces these side effects. Here we impose the spin-selectivity by coating the anode with chiral supramolecular polymers which act as sensitizers; Zn-porphyrins and triarylamines. Photoelectrochemical measurements demonstrates that the hydrogen peroxide formation is dramatically suppressed, while the overall current through the cell, related with the water-splitting process, is enhanced. Evidence for a strong spin-selection in the chiral semiconductors is presented by magnetic conducting AFM measurements, in which chiral and achiral Zn-porphyrins are compared. These findings contribute to our understanding of the underlying mechanism of spin selectivity in multiple electron-transfer reactions and pave the way towards better chiral dye-sensitized photoelectrochemical cells

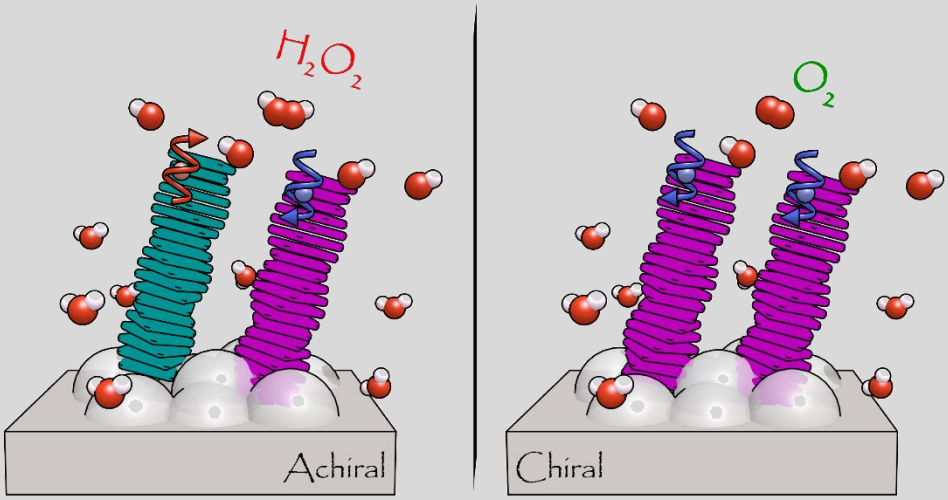

3.1 Introduction

Since it has no carbon, has the highest specific enthalpy of combustion of any chemical fuel, and generates water as its oxidation product, hydrogen has been referred to as the fuel of the future.[1] Although significant progress has been made,[2] the generation of hydrogen by green, sustainable methods on a global scale remains a challenge, both scientifically and technologically.[3-8] Indeed, whereas technologies for the production of H_2 (as electrolysis or photo-electrochemical splitting of water) exist,[9] the processes involve some overpotentials and the formation of peroxides and superoxide radicals. These by-products have the tendency to adsorb onto the photo-catalyst, poisoning it, thereby reducing its stability and lifetime.[10] Although it has been proposed to use specific catalysts which exploit peroxides as intermediates,[11] this solution requires higher voltages. Therefore, a fundamental solution for the off-pathway products is essential.

Water-splitting is a four-electron process that generates hydrogen molecules, which are in singlet ground states, and oxygen molecules, which are in triplet ground states. Commonly, the artificial water-splitting process requires an overpotential of about 0.6 V *vs.* normal hydrogen electrode (NHE), to drive the oxygen evolution reaction.[12-14] The importance of electron-spin correlation of electrons in generating O_2 has been debated for biological photosynthesis. Particularly the chemistry associated with the oxygen evolution reaction in photosystem II has been examined.[15-17] Nevertheless, the details of the mechanism of the O=O bond formation remain unresolved.[18-20]

Although the spin state of the electrons involved is rarely discussed in works exploring artificial photosynthesis, recent theoretical studies suggest that the overpotential required to split water is linked to the restrictions on the electrons' spin in generating a ground state triplet oxygen molecule.[21,22] In recent experimental work, it has been shown that when the anode in the water-splitting cell is coated with chiral molecules, the overpotential is reduced.[23] It has been proposed that the effect is due to spin filtering (obtained through an effect called chiral induce spin selectivity) occurring when electrons are conducted through chiral systems.[24]. However and very importantly, the possible role of the spin control in suppressing the formation of hydrogen peroxide has not been discussed nor experimentally addressed.

3.1.1. Electrons and the chiral induced spin selectivity effect

Before continuing, we briefly describe the underlying physical concepts of the chiral induced spin selectivity (CISS) effect discovered by Ron Naaman and coworkers.[24, 26-28] The CISS effect defines the ability of chiral molecules and molecular layers to filter electrons based on their spin (Figure 1a). In this section we give a general introduction of the effect and some fundamental background, without aiming to demonstrate the operating mechanism in detail.

The spin ($\vec{S}$) is an important quantum mechanical property of electrons, and it is defined as the intrinsic angular momentum of the particle. Its projection along an axis (S_z) is quantized and is given by the product between the quantized angular momentum (m_s), where $-s \leq m_s \leq s$ with s being the spin of the particle (s = ½ for electrons), and the reduced Planck constant ($\hbar$).[F1] As fermions, electrons follow the Pauli exclusion principle, hence two electrons cannot occupy the same quantum state. This means that in order to have two degenerate electrons they have to possess m_s as +1/2 and -1/2, respectively. Moreover, since electrons are negatively charged particles with spin, they possess also a magnetic dipole moment (μ) similarly to a rotating electrically charged body in classical electrodynamics. Due to the spin, electrons have an intrinsic magnetic moment μ directly related to the spin angular momentum ($\vec{S}$) as well as proportional to the ratio between charge and mass of the electron.[F2] Besides the spin angular moment ($\vec{S}$), electrons are in motion within orbitals, thus they have an orbital angular momentum ($\vec{L}$). As a consequence, in addition to the spin magnetic dipole moment (μ_S) an electron has also an orbital magnetic dipole moment (μ_L). For molecules with low symmetry, μ_L is generally negligible and the magnetic behavior can be described just by the intrinsic magnetic moment (μ_S). In some cases, however, the orbital magnetic moment of the electron can be significant and can interact with the spin magnetic momentum in the so-called spin-orbit coupling (SOC). This effect is usually relevant for magnetic materials or systems containing heavy atoms where large spin polarization can occur. Systems with high SOC are often exploited in spintronics for spin-selective transport.

Despite the great success of inorganic-based spintronic devices, the need of working with cheaper and more abundant materials is increasing. Between 1999 and 2011 Naaman and coworkers studied and reported the discovery and the experimental validation that the probability of transmission of electrons through chiral molecules depends on the electrons' spin.[24] They named this effect chiral induced spin selectivity (CISS). Since then, a number of groups are working in creating a complete theoretical framework for describing this effect, however the theories used to describe this effect are multiple, which include for examples tight-binding models to describe the electron transmission through helical molecules and spin-dependent scattering theory.

[F1] $S_z = \hbar m_s$, where m_S is the secondary spin quantum number, $\hbar = h/2\pi = 6.52\ 10^{-16}$ eV·s rad^{-1}

[F2] $\vec{\mu}_s = g\frac{q}{2m}\vec{S}$, where g is the g-factor, a dimensionless number, q the charge and m the mass of the electron

Nevertheless, all the models consider a SOC larger than what is normally reported for organic molecules.[24]

Giving a simplistic description of the CISS effect, the spin selectivity originates by the interaction between the chirality of the system and the spin of the electron transmitted through it.[28] When an electron moves along a chiral molecule it experiences the electrostatic potential of the molecule which is chiral as well (this is strictly related to the electrons and nuclei of the molecules itself). Considering a given position within the traversed path, the transmitted electron is subjected to a magnetic field that depends on the electrostatic potential of the chiral molecule and the Fermi speed of the electron itself.[F3] Because the electron possesses a magnetic dipole which is related to its spin via a SOC relation, the two spin states—degenerated with no magnetic field present—are now split.

The chiral potential causes a significant coupling between the linear momentum and the spin of the electron, and has an important implication for the charge transport in the helix. A freely propagating electron has four states associated with its motions which are related to the direction of the motion and the spin, respectively. This can be denote as $|+,+\rangle, |+,-\rangle, |-,-\rangle, |-,+\rangle$. As a result of the CISS effect, and considering an electron moving in the positive direction through an *M* helix, the state with positive spin $|+,+\rangle$ will be stabilized, while the one with spin down $|+,-\rangle$ will be destabilized (Figure 1b). The opposite stands for an electron moving in the opposite direction. As result, the backscattering of electron with stabilized states (i.e. $|+,+\rangle$ in a *M* helix) is unlikely since it requires a change in both spin and momentum[28]

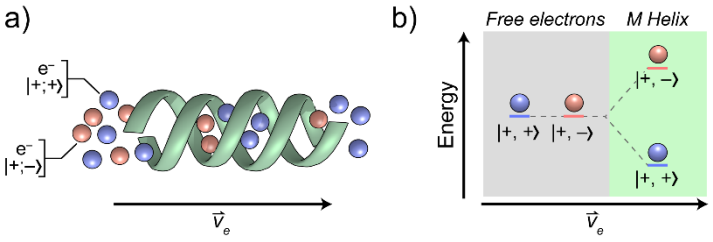

Figure 1. (a) Schematic representation of the CISS effect and (b) the related energy scheme for the states of the electrons, described as |momentum, spin>, moving with a certain speed ($\vec{v_e}$) within a chiral potential. For opposite chirality, or opposite momentum the energy level inverts.

[F3]) $\vec{B} = (\vec{v}/c^2) \times \vec{E}_{chiral}$

$\vec{v}$ is the Fermi velocity, which is normally in the range of 10^5-10^6 m s^{-1};

c is the speed of light: 3 10^8 m s^{-1}

$\vec{E}_{chiral}$ is the potential that confines electrons to move in the helix (estimated in the range of 10^{11} V m^{-1}). It is a property of the molecule and arises from the electron and the nuclei that comprise the chiral molecule.

Although several questions on the mechanism of the CISS effect are still open, numerous experimental proofs have been reported in support of the existence of this effect. Researchers in the field aim both to understand how the CISS effect is operative in the chiral natural world, and to exploit this effect for creating spin-controlled devices made out of organic molecules

Here, we hypothesize that hydrogen peroxide is produced due to uncontrolled spin alignment of the generated radicals[25] and contributes to the high overpotentials. Hence, controlling the spin state of the electronic potential on which the reaction occurs should result in more efficient oxygen production and limited production of hydrogen peroxide. Although, we do not strive to achieve the highest production of hydrogen and oxygen, the results presented show an unprecedented control of chemical kinetics through spin selection.

3.2. Results

3.2.1. Chiral supramolecular polymers

To explore our hypothesis, we investigated the performances of water-splitting solar cells functionalized with two families of molecules able to assemble into helical supramolecular polymers. For this, we selected tri(pyrid-2-yl)amine triamides, chiral, ***S*-1**, and achiral **a-1** (as reported in Chapter 2)[29] and Zinc porphyrins, chiral, ***S*-2**, and achiral **a-2** (Scheme 1).[30] The molecules bearing chiral side chains, ***S*-1** and ***S*-2**, are known to form supramolecular polymers with a preferred handedness defined by the chirality of the side chains. The molecules bearing achiral side chains, **a-1** and **a-2**, instead, are proposed to form racemic supramolecular polymers with an equal population of *P* and *M* helices. The synthesis of **1** is described in Chapter 2, while the Zn porphyrins **2** were synthesized by Helmich *et al.* and described elsewhere.[30,31] To evaluate the effect of the chirality on the water-splitting devices, we functionalized the TiO_2 anode with both chiral and achiral supramolecular polymers based on **1** and **2**.

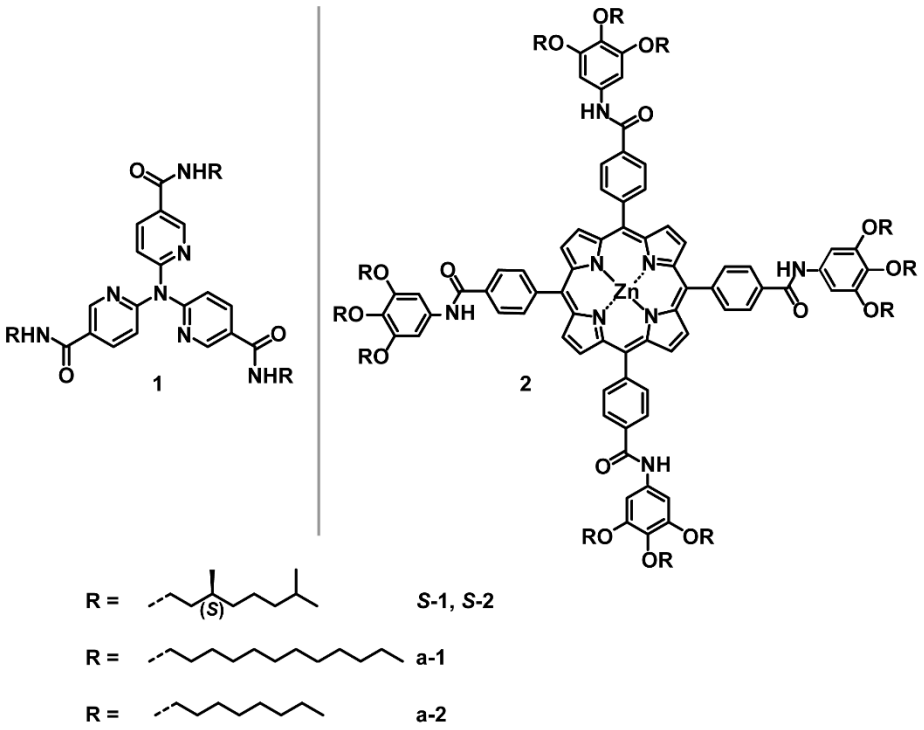

Scheme 1. Molecular structures of the supramolecular monomers used to functionalize the TiO_2 electrodes. Chiral and achiral tripyridylamine triamide, ***S*-1** and **a-1**, and chiral and achiral Zn porphyrins, ***S*-2** and **a-2.** Chiral systems bear enantiopure (*S*)-3,7-dimethyloctyl side chains. Achiral systems bear *n*-dodecyl (**a-1**) or *n*-octyl side chain (**a-2**).

The assembly of both **1** and **2** was evaluated in solution and once deposited on TiO_2 substrate by optical spectroscopy. In the case of **2**, the Soret band at λ = 390 nm confirms the formation of H-aggregated supramolecular structures in solution (Figure 2a),[30,31] which are retained when transferred to the surface (inset of Figure 2a). In a similar manner, the band at λ = 317 nm is indicative of the formation of a supramolecular assembly for **1** (Figure 2b).[29] For both molecules, the chiral analogues show a strong CD response which is not observed for the achiral version (Figures 2c, 2d). UV spectroscopy displays that both chiral and achiral derivatives form supramolecular polymers in alkane solvents and maintain their structure once deposited. Additionally, as expected, CD reveals the presence of supramolecular aggregate with defined handedness for **S-2** and ***S*-1**, and confirms the absence of helical bias for the achiral analogues. This means that electrons are transmitted into the TiO_2 substrate through the same molecular system, which only differs in its molecular organization; either one helical sense (*P* or *M,* for ***S*-1** and ***S*-2**) or a mixture of both (*P* and *M,* for **a-1** and **a-2**).

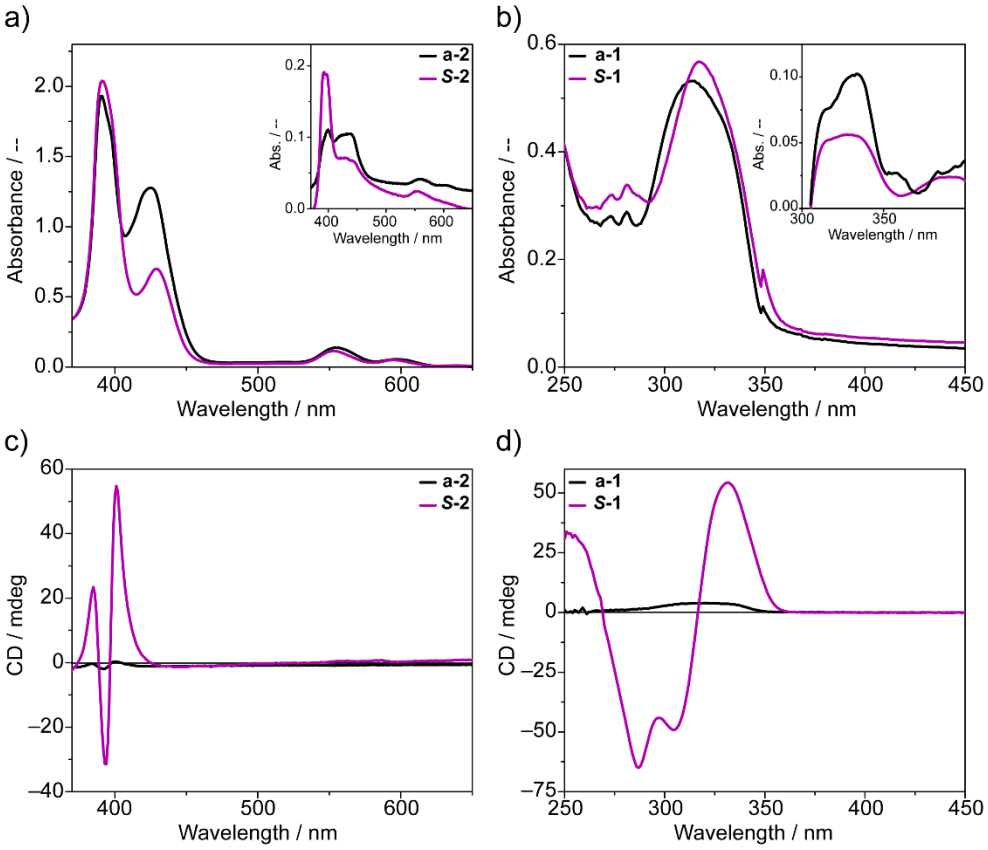

Figure 2. (a, b) Absorption and (c, d) CD spectra of the aggregated state in solution and adsorbed on the surface (inset). (a, c) Spectra of ***S*-2** and **a-2** (c =17 μM in MCH) and (b, d) spectra of ***S*-1** and **a-1** (c =23 μM in MCH). Purple lines for ***S*-2** and ***S*-1**, black lines for the achiral **a-2** and **a-1**.

3.2.2. CISS effect evaluation via magnetic conducting atomic force microscopy

The CISS effect was first evaluated by magnetic conductive probe atomic force microscopy (mc-AFM) by Naaman and coworkers. Samples for mc-AFM measurements were prepared by drop-casting 5 μL solutions of assembled ***S*-2** and **a-2** (c = 17 μM) onto freshly cleaved highly oriented pyrolytic graphite (HOPG) substrate and dried under controlled humidity. The AFM images obtained from dropcasted **2** on HOPG displays micrometer-long, nanometer-thick fibers (Figure 3). By contacting the fibers with the magnetic iron AFM tip, we performed mc-AFM measurements and verified the spin selectivity of electron transmission through the supramolecular polymers (Figure 4a).[32]

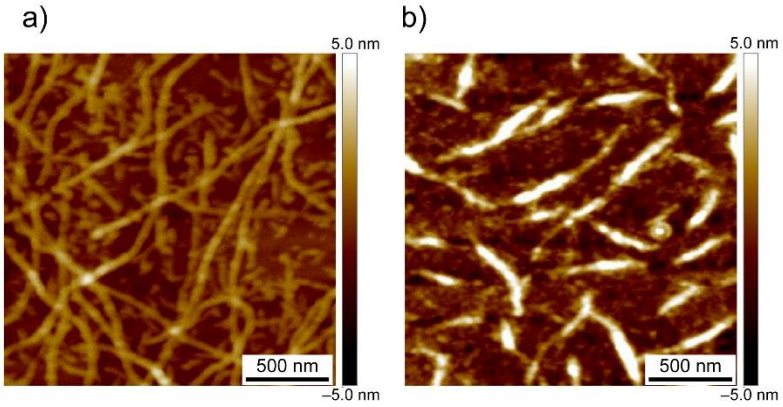

Figure 3. AFM images of (a) ***S*-2** and (b) **a-2** dropcasted on HOPG from MCH (c = 17 μM, MCH)

The current measured contacting ***S*-2** fibers shows dependence on the orientation of the magnetic field at the mc-AFM tip. This signifies that one spin is preferred over the other (Figure 4b). It is important to realize that the ratio between the two spin currents is affected by the non-ideal spin injection from the magnetic tip. Since the spin polarization of the tip is only about 35%, it means that the actual spin filtering of the molecular system is about 4:1, in other words only about 20% of the electrons conducted through the chiral molecular aggregates in this experiment have the "wrong" spin. Mc-AFM on **a-2** (Figure 4c) does not display any preference on the orientation of the magnetic field. The magnitude of the current measured as a function of applied bias does not depend on the orientation of the magnetic field; hence the conduction through this system with equal amount of right and left handed helices is not spin specific.

These results indicate that the supramolecular structures formed from chiral porphyrins can efficiently filter spins. This is consistent with previous reports in which chiral molecules have been observed to be efficient spin filters.[33]

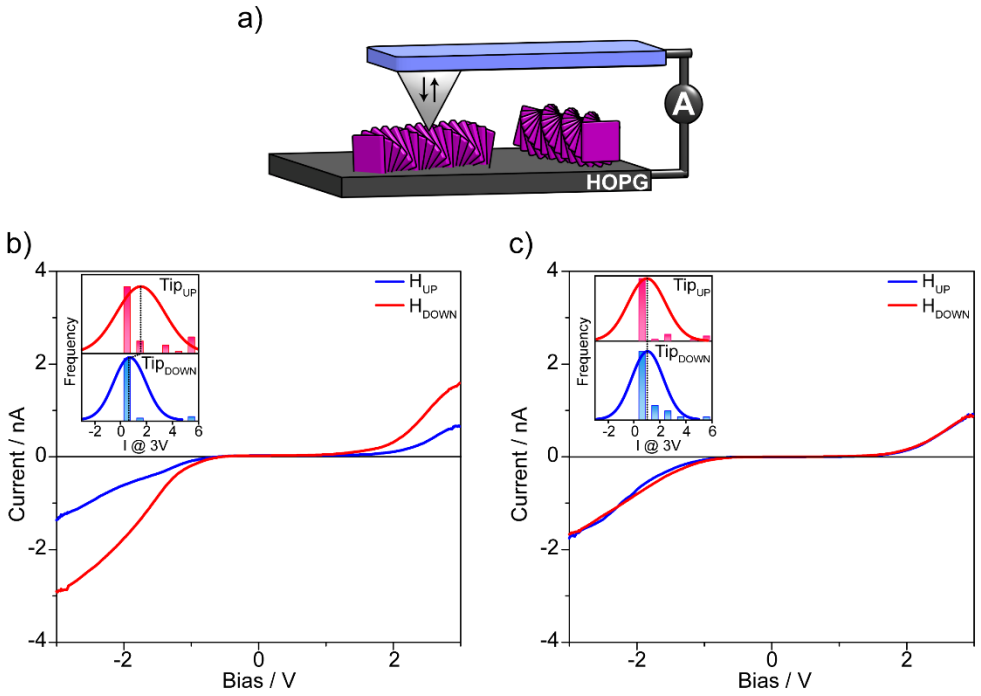

Figure 4. (a) Schematic representation of magnetic conducting atomic force microscopy (mc-AFM) measurements on drop-casted supramolecular polymers. Current as a function of the applied voltage obtained from (b) ***S*-2** and (c) **a-2**. The insets show corresponding histograms of currents obtained at 3 V for the two opposite magnetic orientations of the tip.

3.2.3. Water-splitting photoelectrochemical cells

Next, water-splitting dye-sensitized photoelectrochemical cells (DS-PECs) were assembled to test the CISS effect on the water-splitting process (Figure 5a). To do so, photoelectrochemical measurements were conducted in a three-electrode cell, with Ag/AgCl (saturated KCl) as reference electrode and Pt wire as cathode (Figure 5b). A 0.1 M Na_2SO_4 (pH = 6.56) aqueous solution was used as electrolyte (25mL). TiO_2 anodes were fabricated on FTO/glass substrates using electrophoretic deposition and functionalized with supramolecular polymers (dropcasting from MCH c = 23 μM for **1** and c = 17 μM for **2**). The devices were then tested both in the dark and under irradiation by monitoring the current as a function of the potential. The current is then related with the amount of water split and hence with the production of O_2 at the anode and H_2 at the cathode (Figure 5).[23]

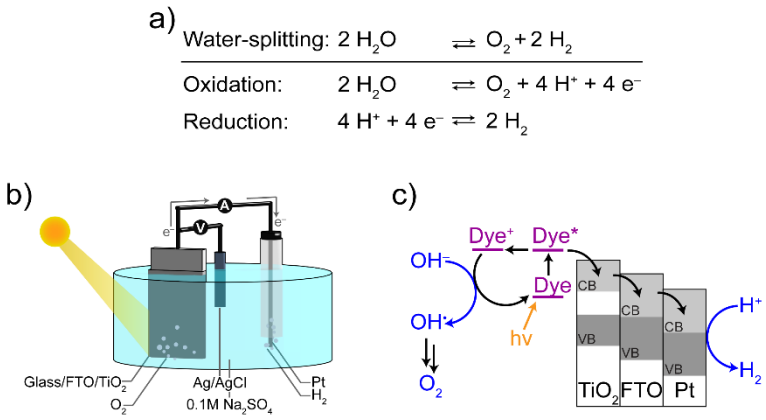

Figure 5. (a) Water-splitting reaction and corresponding semireactions. (b) Schematic representation of a dye sensitized photoelectrochemical cells for water-splitting and (c) the related working mechanism.

I-V curves obtained by varying the voltage and measuring the respective current were performed in dark condition, with light irradiation (Figure 6a, 6c), and by chopping on and off the light (Figure 6b, 6d). Consistently we observed that higher photocurrent densities were recorded for photoelectrodes functionalized with chiral supramolecular polymers, compared to those coated with supramolecular polymers formed by achiral molecules (Figure 6 purple lines *vs*. black lines). This is remarkable, given that the chemical compositions of the chiral and achiral molecules for the two sets used in this study are very similar, except for the stereo-center present in the chiral molecules. In support to the similarity, absorption measurements in solution and in film (Figure 2) display comparable light adsorption for chiral and achiral analogues; Mott Schottky measurements confirm that the analogues have equal electronic properties exhibiting identical flat-band potential for **a-1** and ***S*-1** as well as for **a-2** and ***S*-2** (data not shown).[50] This control confirms that the differences measured in the photocurrents must be attributed only to the chirality of the molecules. It has to be remarked that the photocurrent densities of **1** are reasonably high, since UV light is used for the illumination of the cell (Hg lamp); while the low magnitude of the photocurrents obtained with **2** is typical for porphyrin systems as also been observed by Moore *et al*.[34]

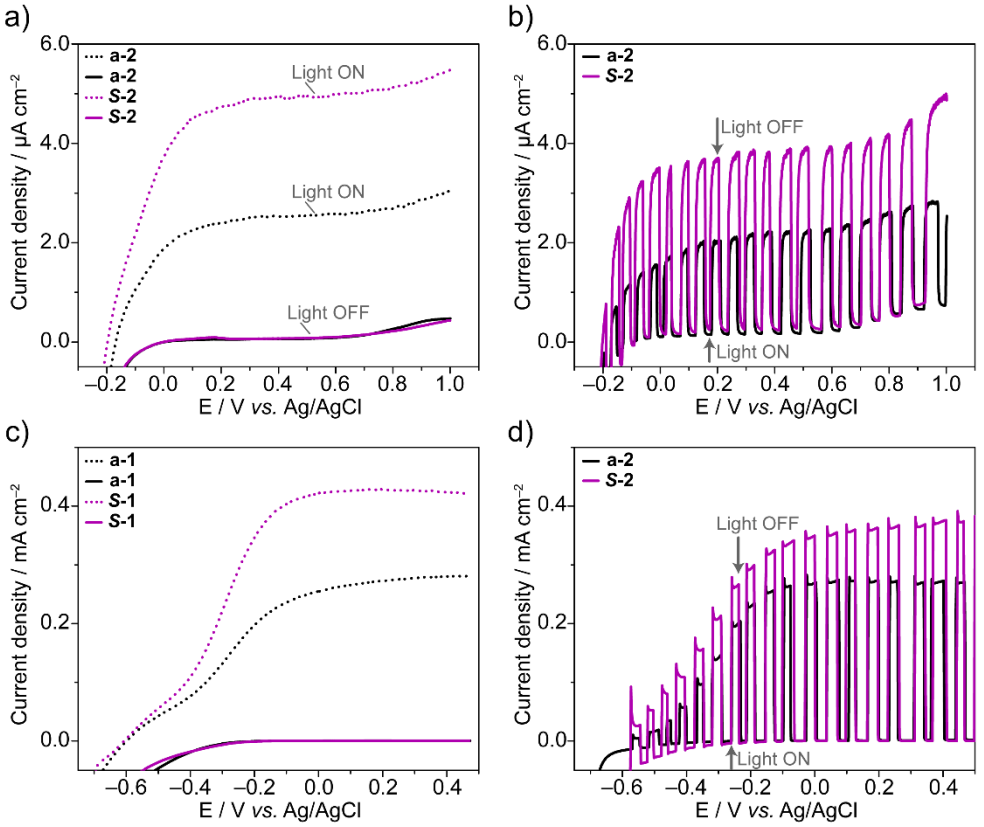

Figure 6. (a, c) I-V curves obtained in the dark (solid lines) and under illumination (dotted lines) for **2** and **1**, respectively. (b, d) I-V curves obtained while chopping the light for **2** and **1**, respectively. All measurements were performed at a scan rate of 10 mV s^{-1}. Purple lines for chiral ***S*-2** and ***S*-1** and black lines for achiral **a-2** and **a-1.** Current densities are measured as $^{i}/_{A}$ where i = measured current and A = active area of the electrode (approximately 1 cm^2).

After showing the difference in water-splitting for the chiral versus racemic aggregates, we tested the beneficial effect of electrons' spin control by evaluating its effect on the H_2O_2 formation. The quantification of the H_2O_2 produced during photoelectrochemical water-splitting was conducted via an indirect spectrophotometric titration of the electrolytes used during the photo-catalyzed water-splitting test. The titrations were performed using *o*-tolidine as redox indicator.[35,36] The amount of peroxide formed was quantified through Ellms-Hauser method calibrating the system with commercial H_2O_2.[37] The presence of H_2O_2 oxidizes the indicator which oxidized product can be monitored by the appearance of an absorption peak at about λ = 436 nm and visually by the change in color of the solution from transparent to yellow. This peak is characteristic for the complete two-electron oxidation product of *o*-tolidine formed by the reaction with hydrogen peroxide.[38]

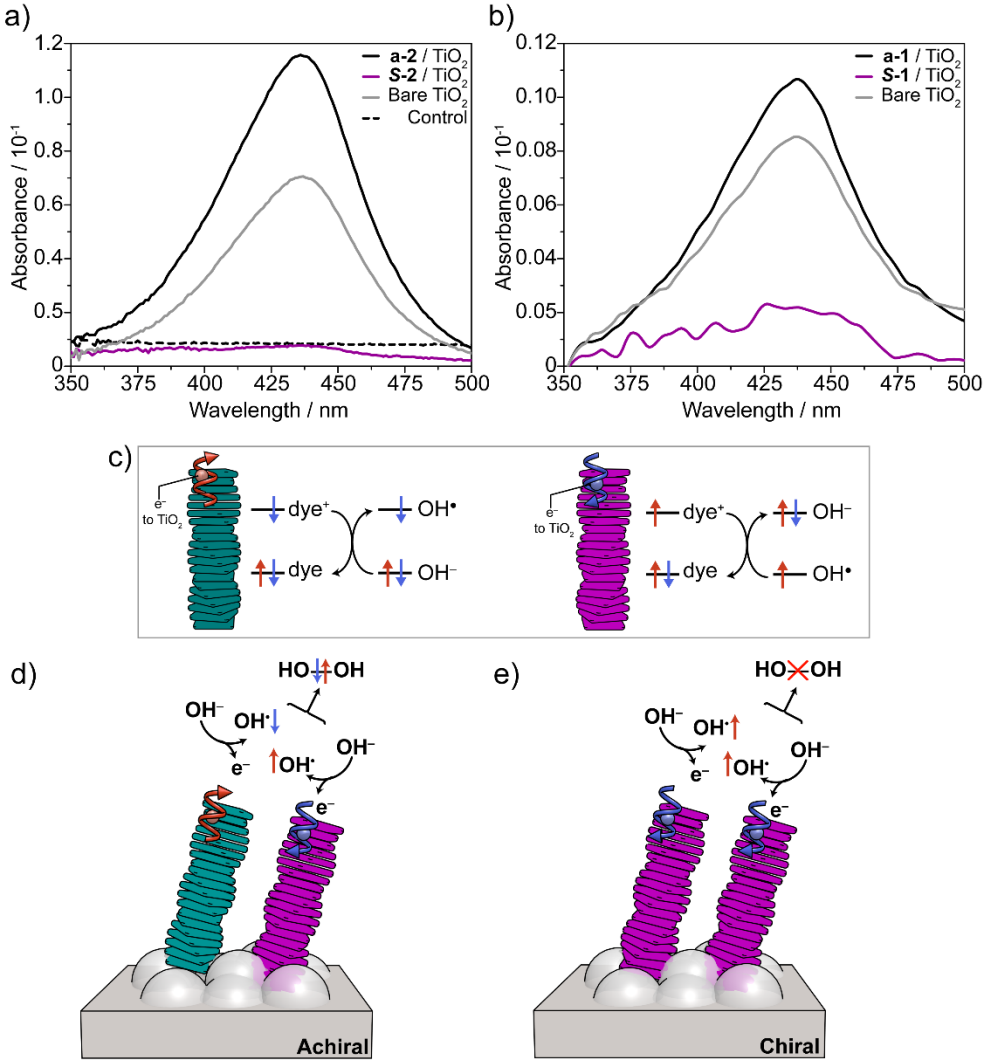

Figure 7. Control of the H_2O_2 production. UV-vis spectra from the titration of the electrolyte after the reaction (0.1 M Na_2SO_4) with *o*-tolidine of bare TiO_2 (grey line) and TiO_2 electrodes functionalized with (a) **a-2** (black line), ***S*-2** (purple line) or with (b) **a-1** (black line), ***S*-1** (purple line). The control (a, black dotted line) refers to the titration of unused Na_2SO_4 with *o*-tolidine. (c) Schematic representation of the CISS effect through the supramolecular polymer with opposite helicity and consecutive oxidation of OH^-. Highest occupied molecular orbital of the species involved displayed for clarity. (d, e) Schematic representation of the CISS effect on photoelectrochemical cells. (d) When the electrons transfer to the anodes though achiral systems the transfer is non spin-specific and the spins of the two $OH^\bullet$ are aligned antiparallel. Their interaction is hence on a singlet surface that correlates with the production of H_2O_2. (e) When the electron transfer to the anode through a chiral system, the transfer is spin specific. The two $OH^\bullet$ interact on a triplet surface that forbids the formation of H_2O_2 and facilitates the production of oxygen in its ground state.

For the measurements for the detection of H_2O_2, chronoamperometry under illumination at 0 V *vs.* Ag/AgCl for 40 minutes is executed. The electrolyte is then collected and titrated with *o*-tolidine. UV-vis measurements of the electrolyte obtained from the bare TiO_2 and from electrodes functionalized with achiral dyes showed the characteristic peak at λ = 436 nm, indicating the production of H_2O_2 during water oxidation (Experimental section, Table 1). Fascinatingly, no detectable amount of hydrogen peroxide was observed for electrodes with the chiral molecules physisorbed (Figure 7a, 7b). Quantitatively, the comparison of H_2O_2 is plausible just considering the amount of absorbed light for each system. Therefore, the amount of produced H_2O_2 obtained from bare TiO_2 cannot be compared with functionalized electrodes, whereas a comparison between analogue molecules can be drawn. Noticeably, after 40 mins of irradiation, 43 ± 5 μM of H_2O_2 have been produced with **a-2** functionalized system, while non-detectable levels of peroxide were found using the chiral analogue ***S*-2**. The electrolyte solutions of the devices functionalized with **1** show low absorbance intensity at λ = 436 nm upon addition of *o*-tolidine. This relatively low level of H_2O_2 in the case of **a-1** may result from performing electrochemistry measurements under illumination with UV light, which might have led to the disproportionation of the peroxide before titration. However, also in this case, much less H_2O_2 is produced with the chiral molecules ***S*-1** than with the achiral **a-1**. Additional evidence is obtained by using achiral 3-mercaptopropionic acid and the chiral oligopeptide [(COOH)-(Ala-Aib)$_7$-NH-$(CH_2)_2$-SH].[50] Only the latter decreases the H_2O_2 production. These results further indicate that the observed elimination of the hydrogen peroxide production is general for all chiral molecules.

3.3. Discussion

The results presented here in the quantification of H_2O_2 production together with the electrochemistry data show a strong correlation between the electrode's activity, the formation of H_2O_2, and the electron's spin alignment. During water-splitting, two OH^- species must combine to form molecular oxygen in its triplet ground state. In the process, an electron from each OH^- is transferred to the anode (Figure 7c-e). This leaves the two $OH^\bullet$ radicals in their doublet ground state, namely each $OH^\bullet$ has one unpaired electron (Figure 7c). When there is no spin control and the interaction electronic potential has a singlet character, the formation of H_2O_2 is possible (Figure 7d). However, when the electron's spins are aligned in a parallel fashion, the two electrons interact on the triplet potential surface which correlates with the formation of the ground state molecular oxygen and on which the formation of H_2O_2 is symmetry forbidden (Figure 7e).

The formation of O_2 and H_2O_2 are anti-correlated; *i.e.*, the formation of one is coming at the expense of the other. This is what the present results indicate. However, it is difficult to draw a quantitative relation between the change in the current and the hydrogen peroxide formation, since the change in the current reflects the change in the

threshold potential for the process while the decrease in the hydrogen peroxide formation is an indication for the extent of spin polarization. Of course, the substrate (the catalyst) may induce spin-orbit coupling that will mix the spin states of the $OH^{\bullet}$ radical. However, for TiO_2 and other relatively light materials, the spins of physisorbed molecules are expected to be conserved, as observed by XPS studies.[39] Note that substrate-induced spin-orbit coupling may explain the low overpotential observed for some oxides,[40-42] magnetic catalysts[43-46] or catalysts made from heavy atoms. For these systems, the side products are not significantly suppressed. Indeed, no investigations were performed in the past aimed at controlling the formation of H_2O_2.

3.4. Conclusions

The experimental results observed in the current study further verify the validity of the CISS effect and demonstrated that spin selection can be achieved with chiral supramolecular polymers. The adaptation of DS-PECs to incorporate chiral supramolecular polymers demonstrated the possibility of applying the CISS effect on functional devices. The functionalization of water-splitting DS-PECs with chiral supramolecular polymer resulted in higher current compared to the achiral analogues and in the depletion of the unwanted production of water peroxide. This proof-of-principle highlights the great potential of exploiting the CISS effect for controlling spin reaction and provide a new path for improving the efficiency of the water-splitting process.

Although the system presented in this chapter is just a primitive model to test the concept, the results obtained are highly promising. For this reason, we propose that a careful optimization of the devices can lead to competitive water-splitting cells and stimulate the interest in implementing spin control in various devices.

3.5. Experimental section

3.5.1 Preparation and characterization of TiO_2 surfaces

TiO_2 electrode fabrication

TiO_2 nanoparticulate films were deposited on fluorine-doped tin oxide, FTO (surface resistivity of ~7 Ω/sq,) coated glass, purchased from Sigma Aldrich Co., using the electrophoretic deposition (EPD) technique. This technique has been used previously to deposit TiO_2 nanoparticles.[47] A suspension of TiO_2 nanoparticles (NPs) was prepared by dispersing 0.4 g TiO_2 NPs (< 25nm in diameter and 99.7% trace metals, purchased from Sigma Aldrich Co.) in 40 mL of de-ionized water. Prior to making dispersions, TiO_2 nanoparticle powders were heated at 570 K for 1 h. The mixture was stirred overnight to ensure homogeneity. Prior to nanoparticle deposition, the FTO substrates were boiled in isopropanol for 15 minutes, followed by 15 minutes of boiling in ethanol, and finally rinsed with de-ionized water. After rinsing, the substrates were dried using nitrogen gas and annealed for 15 minutes at T = 570 K. EPD was then performed with a Princeton potentiostat using the galvanic pulses mode technique with two pulses (Pulse 1 and Pulse 2). Pulse 1 was set to 0 mA for 200 ms for depolarization. Pulse 2 was varied between 0.50 to 0.95 mA to obtain a maximum potential of 10.0 V. Pulse 2 was applied for 1000 ms in each cycle for polarization, and the number of iterations (pulse 1 followed by pulse 2) was set to 1500. Various cycles were used to prepare films of required thicknesses. The samples were annealed in between cycles at 570 K for 15 minutes in air. During EPD, the suspension was continuously stirred using a magnetic stirrer. After completion of the last cycle, the electrodes were annealed again for 8 h at 570 K.

To confirm the surface coverage of the EPD-deposited TiO_2 NP on FTO, high-resolution scanning electron microscope (SEM) measurements were performed using In-lens-detector imaging with a LEO-Supra 55 VP. The SEM image (Figure 8) shows a high surface coverage of the TiO_2 NPs on FTO substrates deposited using the EPD technique. An average film thickness of around 5.0 μm was measured, using a Dektak stylus profilometer.

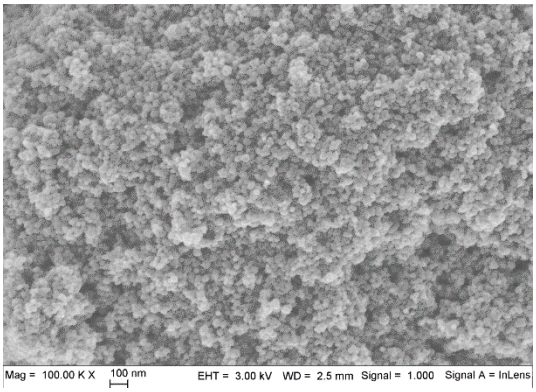

Figure 8. SEM images of EPD TiO_2 nanoparticles on FTO.

Preparation of the solutions and functionalization of the TiO_2 electrodes

The porphyrin solutions were obtained dissolving ***S*-2** or **a-2** in methylcyclohexane (MCH) to a concentration of 17 μM. Dissolution was obtained by multiple cycles of heating-sonicating, and after complete dissolution, the system was let equilibrate overnight to form H-aggregated supramolecular polymers.[30]
The tripyridylamine solutions were prepared by dissolving ***S*-1** or **a-1** in MCH to a concentration of a 23 μM. Dissolution was obtained by multiple cycles of heating-sonicating, and after complete dissolution, the system was brought to 100 °C and cooled to 25 °C (cool rate: 15 °C h^{-1}) to form supramolecular polymers.[29] Absorbance and CD measurements were conducted on all the solutions to confirm the formation of supramolecular structures.
TiO_2 electrodes were functionalized by drop casting 30 μL of the solutions of ***S*-2** or **a-2** on a 1.5 cm^2 area and leaving them to dry overnight under dark and controlled humidity conditions. Structural characterization of the TiO_2 modified electrodes was performed using SEM (Figure 9). **2** form supramolecular structures with lengths of approximately 1 μm on the TiO_2 substrate surfaces. Differently, the functionalization of the TiO_2 electrodes with **1** was performed by dropcasting 150 μL solution on 1.5 cm^2 substrate surfaces and leaving them to dry overnight.

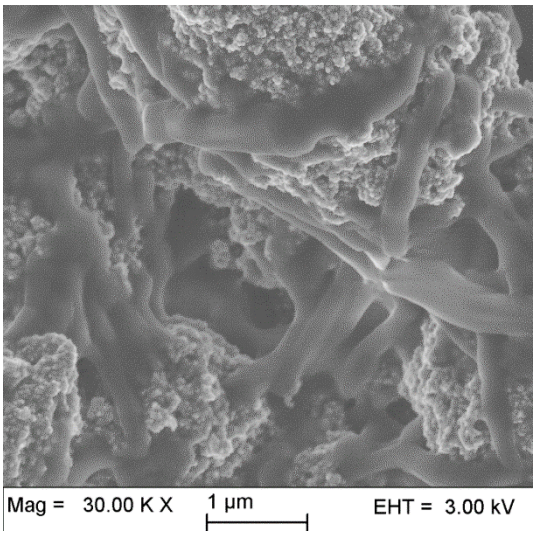

Figure 9. SEM obtained from ***S*-2** functionalized TiO_2 electrode.

Conductive AFM measurements

Naaman and coworkers carried out mc-AFM experiments. Large area topography scans were recorded in PeakForce TUNA (PF-TUNA) mode prior to I-V spectroscopy measurements. I-V measurements were carried out using Multimode AFM with Nanoscope V controller (Bruker-Nano, Santa Barbara, CA, U.S.A.). I-V measurements were performed by recording voltage ramps at an applied force of 12 nN, with which the tip contacts the surface. For each spectroscopy measurement the tip was retracted and placed in a new position, which prevents the damage to the sample by the tip. A total of around 2% of the traces were shorts and 5–8% of the traces show insulating behavior, which were not considered for the analysis. Around 50 I-V traces were recorded and averaged for each magnetic field orientation (magnet UP and DOWN). A magnetic Fe tip (MESP-LC, Bruker) with nominal spring constant 2.8 N/m was used to acquire I-V curves. The tips are magnetized using a permanent magnet.[48,49] The force constant of each probe used was calibrated using the thermal tune procedure of the software.

3.5.2 Photoelectrochemical measurements

Photoelectrochemical measurements were conducted in a three-electrode cell, with an Ag/AgCl (saturated KCl) electrode as the reference and a Pt wire as the cathode. A 0.1 M Na_2SO_4 (pH = 6.56) aqueous solution was used as the electrolyte (25mL). Electrodes were prepared with a total surface area of approximately 1.5 cm^2 and active area is calculated to be approximately 1 cm^2. Areas for each electrode has been recorded (data not shown) and used for calculate the current density (Figure 6). The activity of the photoelectrodes was characterized by measuring the open circuit potential (OCP) in the dark and under illumination at zero current (data not reported). For the measurements on **2**-modified electrodes, a commercial Xe lamp with an intensity of 80 mW cm^{-2} was used. For the measurements on **1**-modified electrodes, a mercury lamp with an intensity of 110 mWcm^{-2} was used. The electrodes show intense response to the illumination confirming their photo-activities.[50] The response of the photoelectrodes was also examined using linear scan voltammetry by switching the light on and off. It is interesting to note that these photoelectrodes have high sensitivity to illumination.[50]

Mott-Schottky measurements

The electronic properties of the photoelectrodes were characterized using Mott-Schottky measurements (data not shown).[50] The measurements were performed in the dark, while sweeping potentials from -0.60 to 0.60 V versus the Ag/AgCl reference electrode. An AC voltage with amplitude of 20 mV was superimposed onto the DC voltages in the defined potential window with frequencies ranging from 200 Hz –200 kHz. 0.1 M Na_2SO_4 was used as the electrolyte with a Pt wire as the counter electrode. The flat band potential of each modified electrode was determined by fitting the lower linear part of the data to the equation,

$$\frac{1}{C^2} = \frac{2}{\varepsilon\varepsilon_0 q N_D}\left(E - V_{bi} - \frac{kT}{q}\right)$$

where C is the capacitance, N_D is the net doping density of TiO_2 which can be calculated from the gradient, E is the applied potential, and V_{bi} is the flat band potential. The flat band potential was obtained as an intercept to the horizontal axis where $^1/_{C^2} = 0$. The flat band potential was obtained as -0.51 V versus Ag/AgCl for both the **a-2** and ***S*-2** modified electrodes, and as -0.70 V versus Ag/AgCl for both the **a-1** and ***S*-1** modified electrodes. This indicates that the electronic properties of the TiO_2 are not affected by molecular organization for each class of molecules used in this study.

Hydrogen peroxide quantification

Seven different sets of electrodes were used during this experiment; bare TiO_2, TiO_2 modified with **a-2**, ***S*-2**, **a-1**, ***S*-1**, mercaptopropionic acid (MPA) and an oligopeptide (Al7). In this case, MPA and Al7 were chosen so as to comprehend the observations obtained with the supramolecular aggregates. Electrochemistry in the chronoamperometry mode was performed under illumination with a 0.1 M Na_2SO_4 aqueous solution as the electrolyte (25mL) and an Ag/AgCl (saturated KCl) reference electrode. A potential was chosen and applied to the bare TiO_2 electrode so that hydrogen and oxygen were evolved on the Pt and working electrodes, respectively. For the functionalized systems potential was set at 0 V *vs*. Ag/AgCl. Bubbles were observed on both the Pt and TiO_2 electrode during the electrochemical measurements. Chronoamperometry measurements were conducted for 40 minutes. The presence of H_2O_2 was verified in a colorimetric test titration experiment of the used electrolyte, with *o*-tolidine as a redox indicator (Scheme 2). For the colorimetric measurements, 0.8 mL of an *o*-tolidine solution prepared according to the Elmms-Hauser method[37] (purchased from Sigma Aldrich Co.) were added to 4 mL of the electrolyte solution obtained from the electrochemical cell and left to react for 30 minutes. In the presence of H_2O_2 a yellow color was observed with an absorption peak at around λ = 436 nm from UV-vis absorption spectroscopy. To estimate the concentration of the hydrogen peroxide produced during electrochemical measurements within a specified period of time, a calibration curve was determined using 30% w/w commercial H_2O_2. Calibration curve has been done following the standard procedure measuring known H_2O_2 concentrations between 10 mM and 0 μM.[47] Results of the calculated concentrations are presented in Table 1. The amount of H_2O_2 for **Al7**, ***S*-2**, ***S*-1**, **a-1** is not reported because the concentration is close or below the detection limit of the method. However qualitative differences can be observed by the absorption measurements (Figure 7). Note that the amount of H_2O_2 produced is related to the current generated which is a function of the absorbed light. Therefore the values of bare TiO_2 cannot be compared with the functionalized devices. Similarly, **1** and **2** cannot be compared since the light source used is different and the molar extinction coefficient of the two families is not comparable.

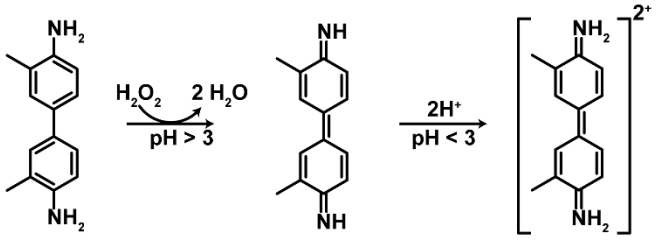

Scheme 2. Reaction scheme between H_2O_2 and *o*-tolidine, spectrophotometric redox indicator.

Table 1: Concentration of H_2O_2 calculated from the electrolyte solutions used in electrochemistry with TiO_2 coated with different molecules.

Molecule	**TiO_2**	**MPA**	**Al7**	**a-2**	***S*-2**	**a-1**	***S*-1**
[H_2O_2] / μM	22.3	2.7	--[a]	42.7	--[a]	--[a]	--[a]

[a] H_2O_2 not quantifiable with the current method applied

3.6. References

[1] Gray, H. B. *Nat. Chem.* **2009**, 1 (1), 7.
[2] Ager, J. W.; Shaner, M. R.; Walczak, K. A.; Sharp, I. D.; Ardo, *S. Energy Environ. Sci.* **2015**, 8 (10), 2811–2824.
[3] Bard, A. J.; Fox, M. A. *Acc. Chem. Res.* **1995**, 28 (3), 141–145.
[4] Blankenship, R. E.; Tiede, D. M.; Barber, J.; Brudvig, G. W.; Fleming, G.; Ghirardi, M.; Gunner, M. R.; Junge, W.; Kramer, D. M.; Melis, A.; Moore, T. A.; Moser, C. C.; Nocera, D. G.; Nozik, A. J.; Ort, D. R.; Parson, W. W.; Prince, R. C.; Sayre, R. T. *Science* **2011**, 332 (6031), 805-809.
[5] Tachibana, Y.; Vayssieres, L.; Durrant, J. R. *Nat Phot.* **2012**, 6 (8), 511–518.
[6] Reece, S. Y.; Hamel, J. A.; Sung, K.; Jarvi, T. D.; Esswein, A. J.; Pijpers, J. J. H.; Nocera, D. G. *Science* **2011**, 334 (6056), 645-648.
[7] Han, Z.; Eisenberg, R. *Acc. Chem. Res.* **2014**, 47 (8), 2537–2544.
[8] Yuhas, B. D.; Smeigh, A. L.; Douvalis, A. P.; Wasielewski, M. R.; Kanatzidis, M. G. *J. Am. Chem. Soc.* **2012**, 134 (25), 10353–10356.
[9] Fujishima, A.; Honda, K. *Nature* **1972**, 238 (5358), 37–38.
[10] Seabold, J. A.; Choi, K.-S. *Chem. Mater.* **2011**, 23 (5), 1105–1112.
[11] Kohl, S. W.; Weiner, L.; Schwartsburd, L.; Konstantinovski, L.; Shimon, L. J. W.; Ben-David, Y.; Iron, M. A.; Milstein, D. *Science* **2009**, 324 (5923), 74-77.
[12] Sivula, K., Le Formal, F. and Grätzel, M. *ChemSusChem* **2011**, 4, 432–449.
[13] Brillet, J.; Cornuz, M.; Formal, F. Le; Yum, J.-H.; Grätzel, M.; Sivula, K. J. *Mater. Res.* **2010**, 25 (1), 17–24.
[14] Mayer, M. T.; Du, C.; Wang, D. *J. Am. Chem. Soc.* **2012**, 134 (30), 12406–12409.
[15] Siegbahn, P. E. M.; Crabtree, R. H. *J. Am. Chem. Soc.* **1999**, 121 (1), 117–127.
[16] McEvoy, J. P.; Gascon, J. A.; Batista, V. S.; Brudvig, G. W. *Photochem. Photobiol. Sci.* **2005**, 4 (12), 940–949.
[17] Tommos, C.; Tang, X.-S.; Warncke, K.; Hoganson, C. W.; Styring, S.; McCracken, J.; Diner, B. A.; Babcock, G. T. *J. Am. Chem. Soc.* **1995**, 117 (41), 10325–10335.
[18] K. Yamaguchi, S. Yamanaka, H. Isobe, K. Tanaka, N. U. *Int J. Quant. Chem.* **2012**, 112, 3849–3866.
[19] Bozoglian, F.; Romain, S.; Ertem, M. Z.; Todorova, T. K.; Sens, C.; Mola, J.; Rodríguez, M.; Romero, I.; Benet-Buchholz, J.; Fontrodona, X.; Cramer, C. J.; Gagliardi, L.; Llobet, A. *J. Am. Chem. Soc.* **2009**, 131 (42), 15176–15187.
[20] Mavros, M. G.; Tsuchimochi, T.; Kowalczyk, T.; McIsaac, A.; Wang, L.-P.; Voorhis, T. Van. *Inorg. Chem.* **2014**, 53 (13), 6386–6397.
[21] Chrétien, S.; Metiu, H. *J. Chem. Phys.* **2008**, 129 (7), 74705.
[22] Torun, E.; Fang, C. M.; de Wijs, G. A.; de Groot, R. A. *J. Phys. Chem. C* **2013**, 117 (12), 6353–6357.
[23] Mtangi, W.; Kiran, V.; Fontanesi, C.; Naaman, R. *J. Phys. Chem. Lett.* **2015**, 6 (24), 4916–4922.
[24] Naaman, R.; Waldeck, D. H. *Annu. Rev. Phys. Chem.* **2015**, 66 (1), 263–281.
[25] Klein, J. H.; Schmidt, D.; Steiner, U. E.; Lambert, C. *J. Am. Chem. Soc.* **2015**, 137 (34), 11011–11021.
[26] Göhler, B.; Hamelbeck, V.; Markus, T. Z.; Kettner, M.; Hanne, G. F.; Vager, Z.; Naaman, R; Zacharias, H *Science* **2011**, 331 (6019), 894-897.
[27] Kettner, M.; Go, B.; Zacharias, H; Mishra, D.; Kiran, V.; Naaman, R.; Waldeck, D. H.; Paw, J.; Juhaniewicz, J.; *J. Phys. Chem. C* **2015**, 119, 14542-14547.
[28] Naaman, R.; Waldeck, D. H.; *J. Phys. Chem. Lett.* **2012**, 3, 2178-2187
[29] Adelizzi, B.; Filot. I. A. W.; Palmans, A. R. A.; Meijer. E. W., *Chem Eur J.* **2017**, 23, 6103-6110.
[30] Helmich, F.; Lee, C. C.; Nieuwenhuizen, M. M. L.; Gielen, J. C.; Christianen, P. C. M.; Larsen, A.; Fytas, G.; Leclère, P. E. L. G.; Schenning, A. P. H. J.; Meijer, E. W. *Angew. Chem. Int. Ed.* **2010**, 49, 3939–3942.
[31] Helmich, F.; Lee, C. C.; Schenning, A. P. H. J.; Meijer, E. W. *J. Am. Chem. Soc.* **2010**, 132 (47), 16753–16755.
[32] Kiran, V., Mathew, S. P., Cohen, S. R., Hernández Delgado, I., Lacour, J. and Naaman, R. *Adv. Mater* **2016**, 28, 1957–1962.
[33] Xie, Z.; Markus, T. Z.; Cohen, S. R.; Vager, Z.; Gutierrez, R.; Naaman, *R. Nano Lett.* **2011**, 11 (11), 4652–4655.
[34] Moore, G. F.; Blakemore, J. D.; Milot, R. L.; Hull, J. F.; Song, H.; Cai, L.; Schmuttenmaer, C. A.; Crabtree, R. H.; Brudvig, G. W. *Energy Environ. Sci.* **2011**, 4 (7), 2389–2392.
[35] Li, Z.; Kong, C.; Lu, G. *J. Phys. Chem. C* **2016**, 120 (1), 56–63.
[36] Gu, B.; Kiwi, J.; Graetzel, M. *In Hydrogen Systems; Pergamon*, **1986**; 1,121–134.
[37] Ellms, J. W.; Hauser, S. J. J. *Ind. Eng. Chem.* **1913**, 5 (11), 915–917.
[38] Hansen, W. N.; Kuwana, T.; Osteryoung, R. A. *Anal. Chem.* **1966**, 38 (13), 1810–1821.
[39] Linsebigler, A. L.; Lu, G.; Yates, J. T. *Chem. Rev.* **1995**, 95 (3), 735–758.
[40] Rossmeisl, J.; Qu, Z.-W.; Zhu, H.; Kroes, G.-J.; Nørskov, J. K. J. *Electroanal. Chem.* **2007**, 607 (1–2), 83–89.
[41] Jirkovský, J.; Makarova, M.; Krtil, P. *Electrochem. commun*. **2006**, 8 (9), 1417–1422.
[42] Nocera, D. G. *Acc. Chem. Res.* **2012**, 45, 767–776.
[43] Hu, A.; Yee, G. T.; Lin, W. *J. Am. Chem. Soc.* **2005**, 127, 12486–12487.
[44] Stevens, P. D.; Fan, J.; Gardimalla, H. M. R.; Yen, M.; Gao, Y. *Org. Lett.* **2005**, 7, 2085–2088.
[45] Ping, Y.; Galli, G.; Goddard, W. A. *J. Phys. Chem. C* **2015**, 119, 11570–11577.
[46] Zhang, B.; Zheng, X.; Voznyy, O.; Comin, R.; Bajdich, M.; Garcıa-Melchor, M.; Han, L.; Xu, J.; Liu, M.; Zheng, L.; Garcıa de Arquer, F. P.; Dinh, C. T.; Fan, F.; Yuan, M.; Yassitepe, E.; Chen, N.; Regier, T.; Liu, P.; Li, Y.; De Luna, P.; Janmohamed, A.; Xin, H. L.; Yang, H.; Vojvodic, A.; Sargent, E. H. *Science* **2016**, 352, 333–337.

[47] Mtangi, W.; Kiran, V.; Fontanesi, C.; Naaman, R. *J. Phys. Chem. Lett.* **2015**, 6 (24), 4916–4922.
[48] Aragonès, A. C.; Aravena, D.; Cerdá, J. I.; Acís-Castillo, Z.; Li, H.; Real, J. A.; Sanz, F.; Hihath, J.; Ruiz, E.; Díez-Pérez, I. *Nano Lett.* **2016**, 16 (1), 218–226.
[49] Chakrabarti, S.; Pal, A. J. *Appl. Phys. Lett.* **2014**, 104 (1), 13305.
[50] Mtangi, W., Tassinari, F., Vankayala, K., Vargas Jentzsch, A. R., Adelizzi, B., Palmans, A. R. A., Fontanesi, C., Meijer, E. W., Naaman, R. *J. Am. Chem. Soc.* **2017**, 139 (7), 2794–2798.

4.

Strategies to improve chiral-functionalized water-splitting solar cells

Part of the results of this work are summarized in:

B. Adelizzi, A. Rösch, A. J. van Rijen, S. R. Martire, S. Esiner, M. Lutz, A. R. A. Palmans, E. W. Meijer,
Submitted

Abstract: Recent developments on water-splitting dye-sensitized photoelectrochemical cells demonstrated that their performance can be improved by exploiting the chiral induced spin selectivity effect (CISS). Functionalization of these cells with chiral supramolecular polymers resulted in higher current and suppression of the water peroxide co-produced during the water oxidation. However, the promising seminal work reported in Chapter 3 was achieved with an embryonal not-optimized system. Improvements on the fabrication and functionalization of the photoelectrode are required to bring chiral functionalized water-splitting solar cells to a competitive level. In this chapter, we address a number of important issues that are required to enhance the photoelectrochemical cell's performance. First, we focus on optimizing the stability and the order of chiral supramolecular polymers used for the electrode functionalization. Hereto, we design anchoring molecules that are capable of covalently binding to the TiO_2 electrode, and non-covalently interact with the supramolecular polymers. A careful selection of the anchoring molecule resulted in greatly improved chiral order in the supramolecular polymer layer. Secondly, we design a novel generation of chiral supramolecular polymers based on molecules frequently used in dye-sensitized solar cells. We exploit their chiral assembly and sun light harvesting properties to obtain water-splitting solar cells able to operate under visible light. The promising results reported here, demonstrate once more the positive effect gained by using chiral systems, and establish the robustness of the CISS effect, which occurs for a variety of molecules and different conditions

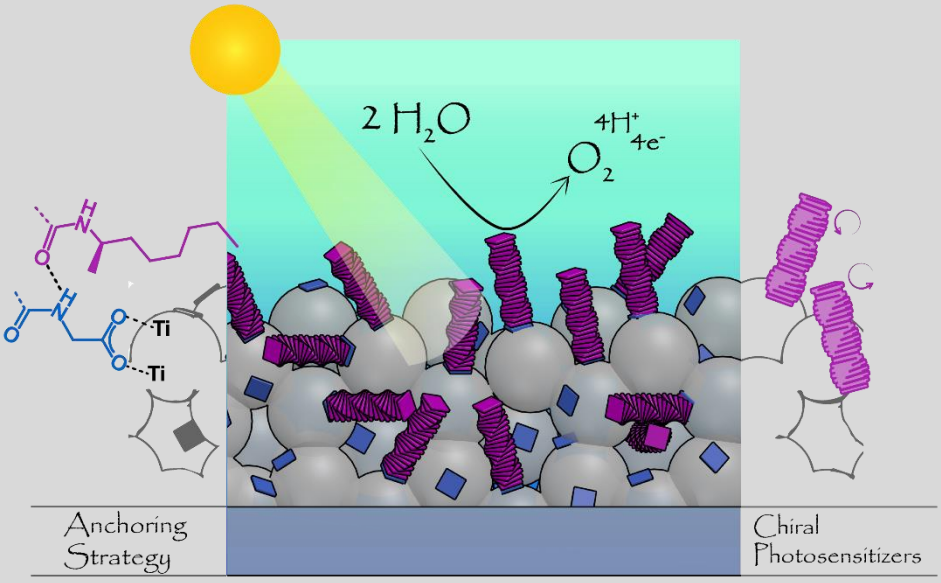

4.1 Introduction

In Chapter 3, we reported the implementation of chiral supramolecular polymers into a water-splitting dye sensitized photoelectrochemical cell (DS-PEC). We found that the chiral induced spin selectivity (CISS) effect induced by chiral supramolecular polymers effectively reduces hydrogen peroxide production,[1] opening the way towards a next-generation of water-splitting solar cells. Although our prototype cells allowed us to rapidly verify the hypothesis that CISS can indeed be exploited to control photoelectrochemical reactions, these cells were not optimized to efficiently harvest solar light nor designed to ensure a high stability of the cell over time. These issues have been tackled in the field of solar cells,[2] and nowadays strategies and procedures to obtain good performances are well-established.

The scope of this chapter is to merge the knowledge previously acquired on spin-filtering with a classic DS-PEC design[3]. In this way, we aim to bring the model device reported in Chapter 3 to a fully operating level. This chapter is therefore divided in two major sections. In first place, we outline methods to increase the order and the stability of the chiral supramolecular polymeric system when absorbed on the TiO_2 electrode. In the second part, we turn our attention to the development of new chiral layer which acts both as spin-filter and photosensitizer for visible light.

4.2 Optimization of order and stability of the chiral supramolecular layer

The photoelectrochemical generation of H_2 is an appealing technique to produce green energy. However, the photoelectrochemical devices used for this scope have to be stable under continuous irradiation and use. During the study reported in Chapter 3, we observed that upon prolonged irradiation time the devices showed decrease in current. We attributed this effect to the lack of an efficient chemisorption of the chiral supramolecular polymers onto the TiO_2. The electrodes were indeed functionalized just via drop-casting and the permanence of the chiral layer on the surface was attributed only to the scarce solubility of the molecules in aqueous solution.

In classic dye-sensitized solar cells (DSSCs) and DS-PEC, the stability problem has been tackled through the use of dyes which can covalently link the TiO_2 via a metal-organic bond.[4] These covalent links, besides increasing the persistency of the dyes on the inorganic surface, can also enhance the electron injection into the TiO_2 layer.[2,4] A wide variety of anchoring groups has been reported in literature such as carboxylic acid, boronic acid, phosphonic acid, sulfuric acid, pyridine, etc.[4,5] Often these groups act both as ligands (able to bind the Ti atoms) as well as electron-withdrawing groups (EWG). In fully conjugated dyes, this ensure an excited state localized on the EWG and hence a direct injection into the TiO_2 conduction band.[2,4,6,] However, for the scope of this section, we aim to introduce the anchoring groups mainly to increase the stability of the system.

We identified carboxylic acids as the most promising anchoring groups. These groups are widely used in DSSCs for good binding properties and good stability. Importantly, they can be easily introduced in the molecular design due to easy synthetic accessibility. However, the design of the chiral supramolecular monomers that we typically apply includes carboxamides to direct the supramolecular polymerization. The incorporation of carboxylic groups in each monomers may bring competition between the amides and the acids and consequent disruption of the chiral order. For this reason, we opt for a multilayer design, in which the anchoring molecules act as bridge between the TiO_2 and the chiral supramolecular polymer layer. Our strategy consists of the introduction of an organic anchoring monolayer that covalently binds to the TiO_2 surface and subsequently non-covalently interacts with the chiral supramolecular polymers (schematic representation in Scheme 1).

In order to ensure good pairing between the anchoring layer and the chiral supramolecular polymers, we utilized the same aromatic core for the two systems. We selected C_3 symmetric tripyridylamine triamide **1** (as reported in Chapter 3) as core, and we optimized the design for the scope of each layer. The anchors were designed to bear both supramolecular units and anchoring groups. Tripyridylamine triamides were hence decorated with peripheral carboxylic acid end groups. In particular, we tested glycine-functionalized tripyridylamine triamide (**Gly-1**) and tripyridylamine triamide functionalized with γ-aminobutirric acid (**BA-1**). Two and four carbon spacers between the supramolecular unit and the anchoring group, respectively (Scheme 1). The length of the spacer between the amide and the anchoring group influences the geometry and the flexibility of the molecules and may result in a different binding geometry to the TiO_2 and a different effect on the organization of the supramolecular layer. The two anchoring molecules were additionally compared with tripyridylamine triacid (**COOH-1**) which has no amide and no peripheral flexibility.

For the chiral supramolecular monomers, we selected a chiral side chain based on 2-aminooctane, with the stereogenic center at the α-position of the amide, because these typically show a reduced solubility compared to side chain based on 3,7-dimethyloctylamine.[7] The introduction of enantiomerically pure 2-octyl chains into the design of tripyridylamine triamides (**2*S*-1** and **2*R*-1**) should further improve the device's stability. As achiral analogue, we maintained the *n*-dodecyl functionalized tripyridylamine triamide, **a-1,** used in Chapter 3.

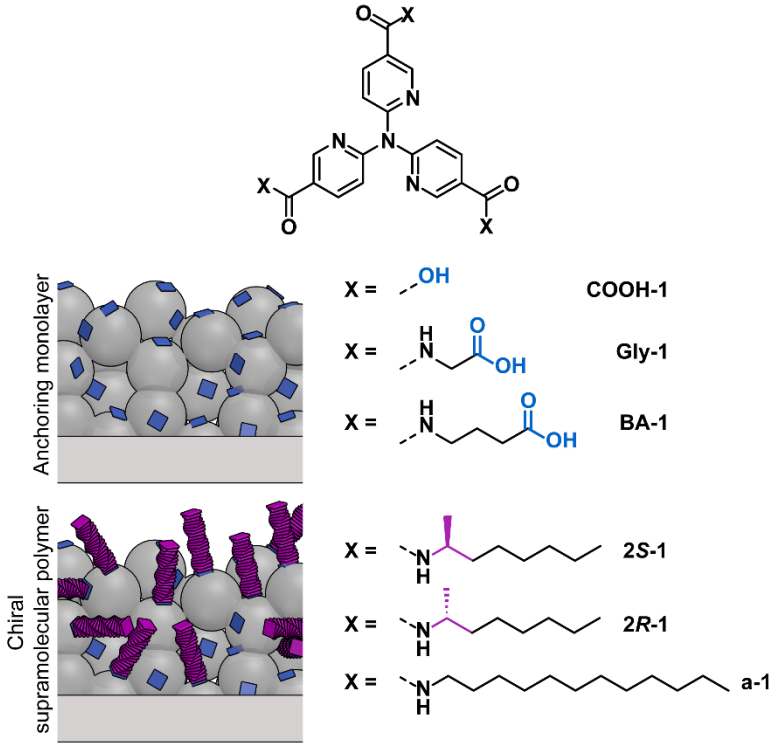

Scheme 1. Molecular structures of the library of **1** designed for the anchoring monolayer (**COOH-1**, **Gly-1**, **BA-1**) and for the chiral supramolecular layer (**2*R*-1**, **2*S*-1**). Analogous achiral molecule (**a-1**) used as reference compound.

4.2.1. Synthesis and characterization in solution

The synthesis of **COOH-1** was performed following the procedure reported in Chapter 2.[8] Conversely, the synthesis of the tripyridylamine triamide has been optimized. This time, amide coupling was performed via activation of the carboxylic acid with pentafluorophenyl trifluoroacetate and consecutive substitution with the required amine (Scheme 2).[9] This route allows the synthesis of all molecules of the library in high yield and purity after recrystallization from acetonitrile. The installation of the side chains for **Gly-1** and **BA-1** was performed with the γ-methylester protected amine giving the methyl-protected products **Me-Gly-1** and **Me-BA-1**. The hydrolysis of the ester was performed with LiOH as it is selective for the ester groups and does not affect the amides.[10,11]

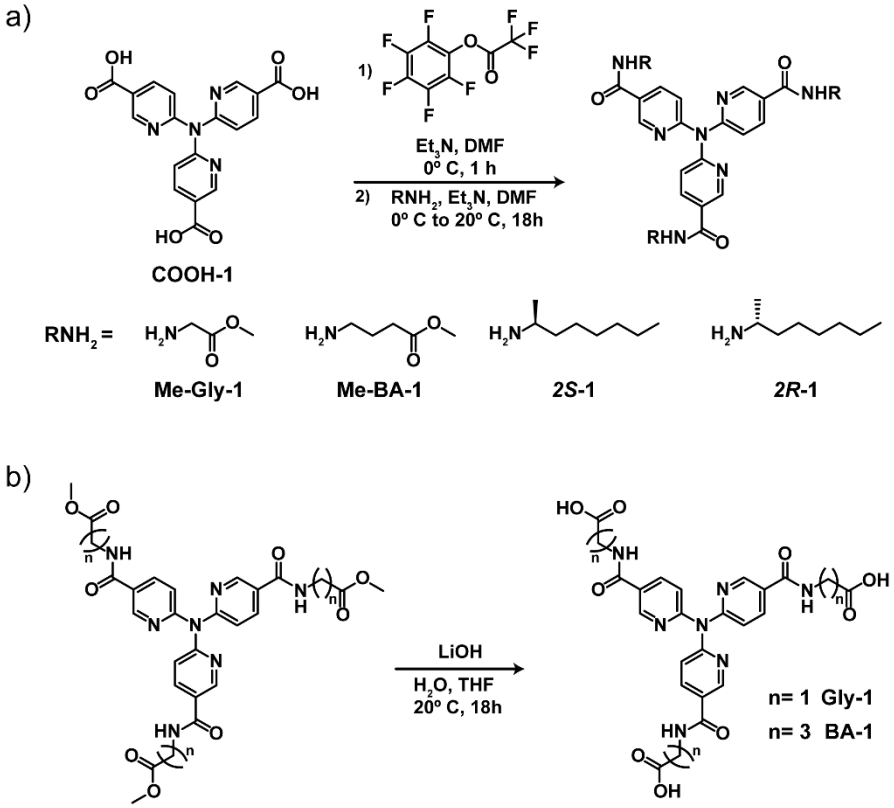

Scheme 2. Synthesis of tripyridyl triamine derivatives **1**. **Gly-1**, **BA-1**, **2*S*-1** and **2*R*-1** were synthesized from **COOH-1** via activation of the acid with pentafluorophenyl trifluoroacetate and consecutive addition of the desired amine to afford the amide. **Gly-1** and **BA-1** were synthesized with methyl ester protected functionalities (**Me-Gly-1**, **Me-BA-1**) which were deprotected by selective hydrolysis with LiOH.

All the molecules synthesized were molecularly characterized via ^{1}H-NMR, ^{13}C-NMR, and mass spectrometry. Bulk and thermal characterization was performed via infrared spectroscopy (FT-IR) and differential scanning calorimetry (DSC). The anchors **BA-1**, **Gly-1** and **COOH-1** decompose, probably by decarboxylation, before melting. **2*S*-1** and **2*R*-1** display bulk properties similar to ***S*-1** (experimental section, Chapter 2).

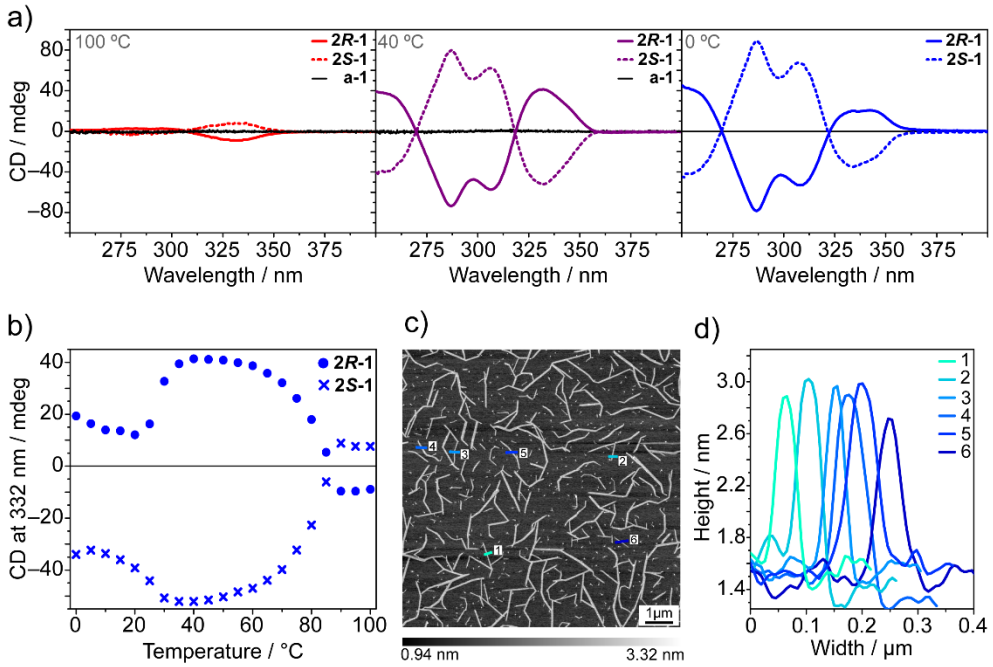

Figure 1. (a) CD spectra of **2*R*-1** (solid line) and **2*S*-1** (dotted line) at 100 °C (left, red lines), 40 °C **state I** (center, purple lines), and 0 °C **state II** (right, blue lines).(b) CD cooling curves recorded at λ = 332 nm for **2*R*-1** (dots) and **2*S*-1** (crosses). (c) AFM height image of **2*R*-1** dropcasted from toluene (c = 50 µM) on mica and (d) relative profile analysis.

In addition, **2*S*-1** and **2*R*-1** were investigated for their self-assembling behavior in organic solvents. The formation of chiral supramolecular polymers was demonstrated in decalin, toluene and *o*-dichlorobenzene (*o*-DCB). Circular dichroism (CD) spectroscopy confirmed that **2*S*-1** and **2*R*-1** form chiral supramolecular polymers, **poly(2*R*-1)** and **poly(2*S*-1)**, with opposite handedness directed by their molecular chirality. In decalin, **poly(2*R*-1)** exhibits supramolecular polymers with the same handedness of **poly(*S*-1)** reported in Chapter 2 and 3 (Figure 1a, comparison with Chapter 2 Figure 6).[8] Variable temperature CD (VT-CD) demonstrated also that **poly(2*R*-1)** and **poly(2*S*-1)** are subject to the same pathway complexity reported for **poly(*S*-1)** (Figure 1b, comparison with Chapter 2 Figure 5). Upon cooling, both **2*S*-1** and **2*R*-1** display the cooperative formation of a first assembled state, which converts to a second state with opposite helicity most probably as consequence of the interaction with co-dissolved water molecules.[12]

Atomic force microscopy (AFM) microscopy on dropcasted **poly(2*R*-1)** onto mica (Figures 1c, 1d) verified the formation of 2-5 μm long, 1.5 nm thick 1D fibers.

4.2.2. Fabrication of TiO_2 electrodes and functionalization with anchors

Often DSSCs and DS-PECs, utilize porous anodes made of sintered TiO_2 nanoparticles.[3] The high porosity permits greater surface area, more coverage of the dyes and a better electron conductance.[13-17] In Chapter 3 instead, we used electrochemically grown TiO_2 which is very compact.[1] In order to improve the performances, here we fabricate standardized Ti-based electrodes adopting the DSSC procedures. The TiO_2 electrodes were prepared on glass/FTO (fluorine doped tin oxide) substrates following the procedure reported for Solaronix T/SP paste® (commercially available TiO_2 paste, anatase 20 nm nanoparticle).[18] Anodes so prepared were then characterized via XRD, ellipsometry and SEM to assess if their crystallinity, thickness and porosity are suitable (experimental section).

Similarly, the functionalization of the TiO_2 electrodes with the anchor molecules was performed by adapting standard procedures from DSSCs.[17] The functionalization was carried out via dip casting the TiO_2 plates in a dry ethanol (EtOH) solution containing the anchoring molecules (c = 0.1 mM) and allowing the plates to equilibrate overnight at 20 °C. The functionalization was done with **COOH-1**, **Gly-1**, **BA-1** and the results were compared with the methyl-protected **Me-Gly-1** and **Me-BA-1** which cannot covalently bind to TiO_2. Because TiO_2 is very hygroscopic,[19] precautions were taken to ensure the absence of water during the functionalization. After the functionalization, the plates were washed with EtOH and dried. This procedure removes physisorbed molecules and ensures the presence of only covalently-bound molecules onto the TiO_2 surface.

The functionalized plates were characterized using FT-IR (Figures 2a, 2b). Carboxylic group can be easily detected by the characteristic stretching band of C=O. Based on the IR signature, it is possible to verify the successful functionalization and to obtain insight into the binding geometry. The IR spectra display C=O stretching band for each tested anchor proving the chemisorption of **COOH-1**, **Gly-1** and **BA-1** (Figure 2a, top). The comparison with methylester protected analogues, **Me-Gly-1** and **Me-BA-1**, shows that the functionalization procedure guarantees the removal of physisorbed molecules. Plates functionalized with **Me-Gly-1** and **Me-BA-1** do not display any signal attributable to the organic molecules (Figure 2a, bottom) and the only vibration peaks detected are attributed to TiO_2, chemisorbed water and EtOH (used for the washing procedure).

Further evidence of the covalent binding of the carboxylic acid groups onto the TiO_2 surface were obtained by comparing the IR spectra of the anchors chemisorbed onto TiO_2 with the ones measured in bulk (Figure 2b). The vibrational frequencies display changes in intensity and energy, in agreement with reported data.[20] For example, the stretching frequency of free C=O of **BA-1** in bulk is recorded at ν =1692 cm^{-1} while upon binding to TiO_2, the band shifts to ν = 1734 cm^{-1} and decreases in intensity (Figure 2a

left, top vs bottom). For **BA-1/TiO_2**, the increase of bands at 1560 cm^{-1} and 1413 cm^{-1} are attributed to the asymmetric and symmetric stretching bands of COO^- due to the splitting of carboxylate groups complexed with surface Ti centers. The distance between these two bands suggests a bidentate binding.[21,22] Similar conclusions can be drawn for **Gly-1/TiO_2** and **COOH-1/TiO_2** (Figure 2b).

Although we achieved successful binding, the presence of just a monolayer of anchors on a 5 µm thick TiO_2 does not permit the use of IR to investigate whether the anchors are bound to the surface with one, two or three carboxylic acid groups. Qualitatively, the presence of the band of free –COOH suggests that not all three carboxylic acids are bound to the surface.[20] **BA-1/TiO_2**, compared to **Gly-1/TiO_2** and **COOH-1/TiO_2**, displays a more intense change between bulk and chemisorbed molecules indicating a better binding.

For more detailed investigations, X-ray photoelectron spectroscopy (XPS) was performed. When comparing Ti 2p and O 1s XPS spectra for functionalized surfaces with the ones of bare TiO_2, we observed that the functionalized systems show lower binding energy and lower intensity (*i.e.,* Ti $2p_{½}$: 459.18 eV for TiO_2 and 456.63 eV for **BA-1/TiO_2**; O 1s: 530.38 eV for TiO_2 and 529.88 eV for **BA-1/TiO_2**;), in agreement with literature reports (Figure 2c, top).[23] This indicates that the TiO_2 surface is more electronrich as a result of chemisorption of the anchors. The effect is larger for **BA-1/TiO_2** supporting the hypothesis that **BA-1** binds more efficiently than **Gly-1** and **COOH-1**. The C 1s spectrum shows peaks for C-C/C=C and C-O/C=O at 285 eV and 289 eV, respectively. The C=O peak is diagnostic for the covalent binding to TiO_2.[23,24] Both **COOH-1** (black line, 288.48 eV) and **BA-1** (blue line, 288.48 eV) display a shift to lower energy compared to bare TiO_2 (gray line, 289.08 eV), while **Gly-1** (green line, 289.08 eV) does not show significant changes. The shift is consistent with the binding reaction of carboxylic groups which are transformed into C-O-Ti units.[23,24]

All taken together, these results indicate that triacids can be chemisorbed to the TiO_2 surface, although presumably not all three carboxylic acids are bound to the surface. In addition, **BA-1** shows the more efficient binding, making it the anchor molecule of choice for further studies.

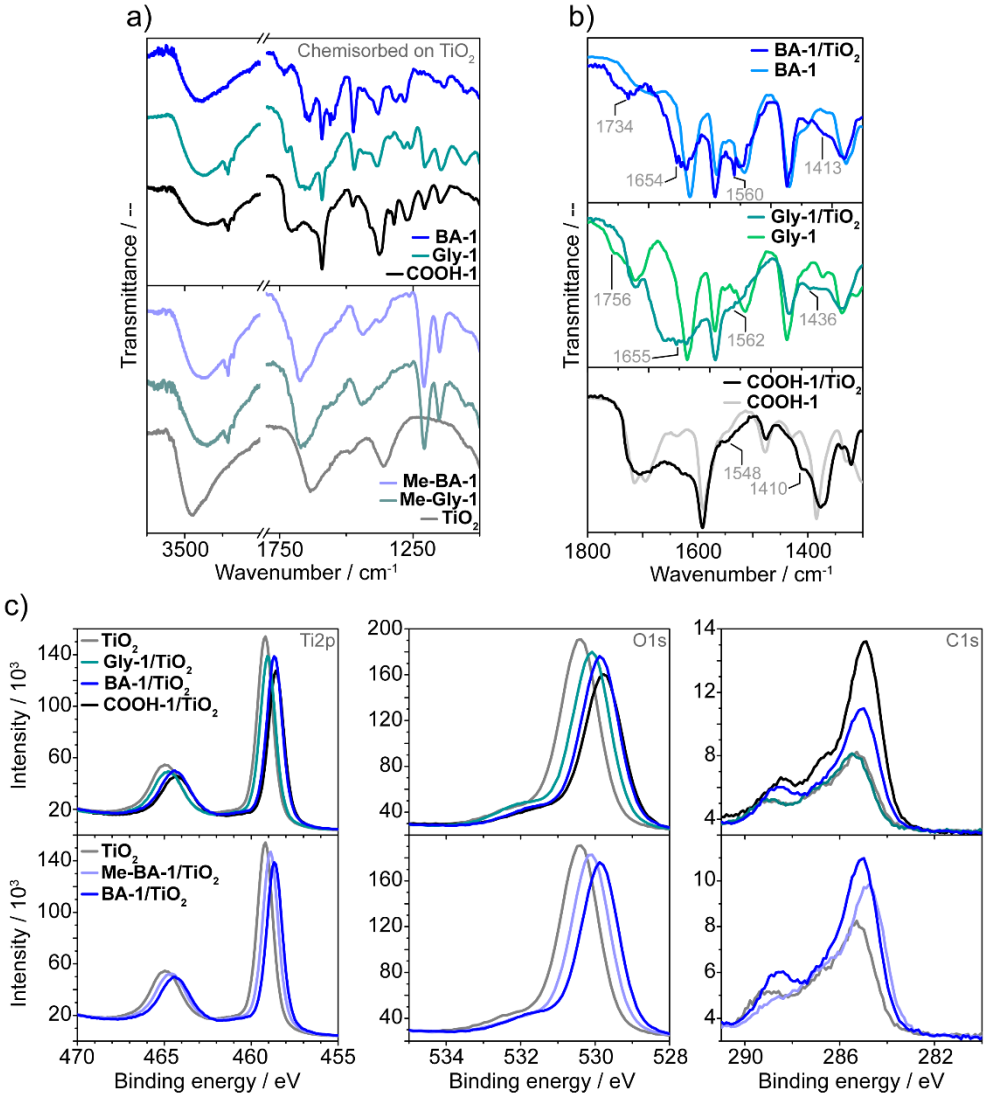

Figure 2. (a) IR spectra, comparison of (a, top) anchors chemisorbed onto TiO_2 and (a, bottom) methyl-protected anchors which cannot bind covalently TiO_2. (b) Comparison of IR spectra of anchors chemisorbed onto TiO_2 and in bulk. (c) XPS spectra for Ti 2p (left), O 1s (center), C 1s (right). Comparison of XPS results for (top) the three anchors and (bottom) for **Me-BA-1** *vs.* **BA-1** *vs.* bare **TiO_2**.

4.2.3. Functionalization with chiral supramolecular polymers

After the successful binding of the anchoring monolayer to the TiO_2, the next step is to functionalize the anchor-TiO_2 electrodes with the supramolecular polymer layer (Figure 3). Energy dispersive X-ray analysis (EDX) and ellipsometry on fully functionalized surfaces demonstrated that both the anchoring monolayer and chiral supramolecular layer penetrate through the entire thickness of the porous TiO_2 (experimental section). The presence of a chiral layer permeated into the TiO_2 layer differs from Chapter 3 (where the chiral supramolecular polymers where deposit on top of compact TiO_2 electrodes) but moves the system closer to classic DS-PECs.

A screening of functionalization procedures varying casting methods, solvents, and annealing steps, was performed to obtain reproducible results and good surface order. The deposition of the supramolecular polymer layer (made with **2*R*-1** or **a-1** monomers) was tested both on bare TiO_2 (giving for example: **2*R*-1/TiO$_2$**), and on anchor functionalized surfaces (giving for example: **2*R*-1/BA-1/TiO$_2$**). The so functionalized systems were then studied by CD spectroscopy, SEM (not shown) and AFM microscopy.

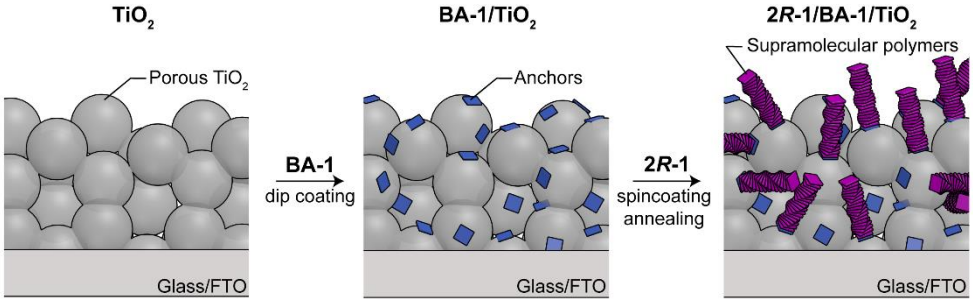

Figure 3. Schematic representation of the functionalization of the TiO_2 electrodes.

To account for small variations in the functionalized electrodes, all CD spectra were measured for n = 5 and the average of the measurements is reported with its standard deviation (Figure 4a-d). Based on the preparation method used, larger or smaller variation of the surfaces were observed. Spincoating **2*R*-1** from $CHCl_3$ (c = 0.5 mM, 1000 rpm) and annealing for 30 minutes (Figures 4b-d) gives the best results in CD intensity and reproducibility. The effect is particularly strikingly when comparing the CD spectra obtained by dropcasting on bare TiO_2 *vs.* spincoating (Figure 4a *vs.* Figure 4b, grey lines). Most important, depositing **2*R*-1** on anchor functionalized TiO_2 instead of bare TiO_2 strongly affects the final result. The nature of the anchoring layer also affects the final CD spectra. The surface **BA-1/TiO$_2$** reproducibly shows the most effective surfaces for increasing CD intensity of the chiral supramolecular layer—in spincoated system the CD is almost doubled compared to bare TiO_2 (Figure 4b). Conversely, surfaces based on **Gly-1/TiO$_2$** and **COOH-1/TiO$_2$** reduce the intensity of the CD (Figure 4b *vs.* Figure 4c).

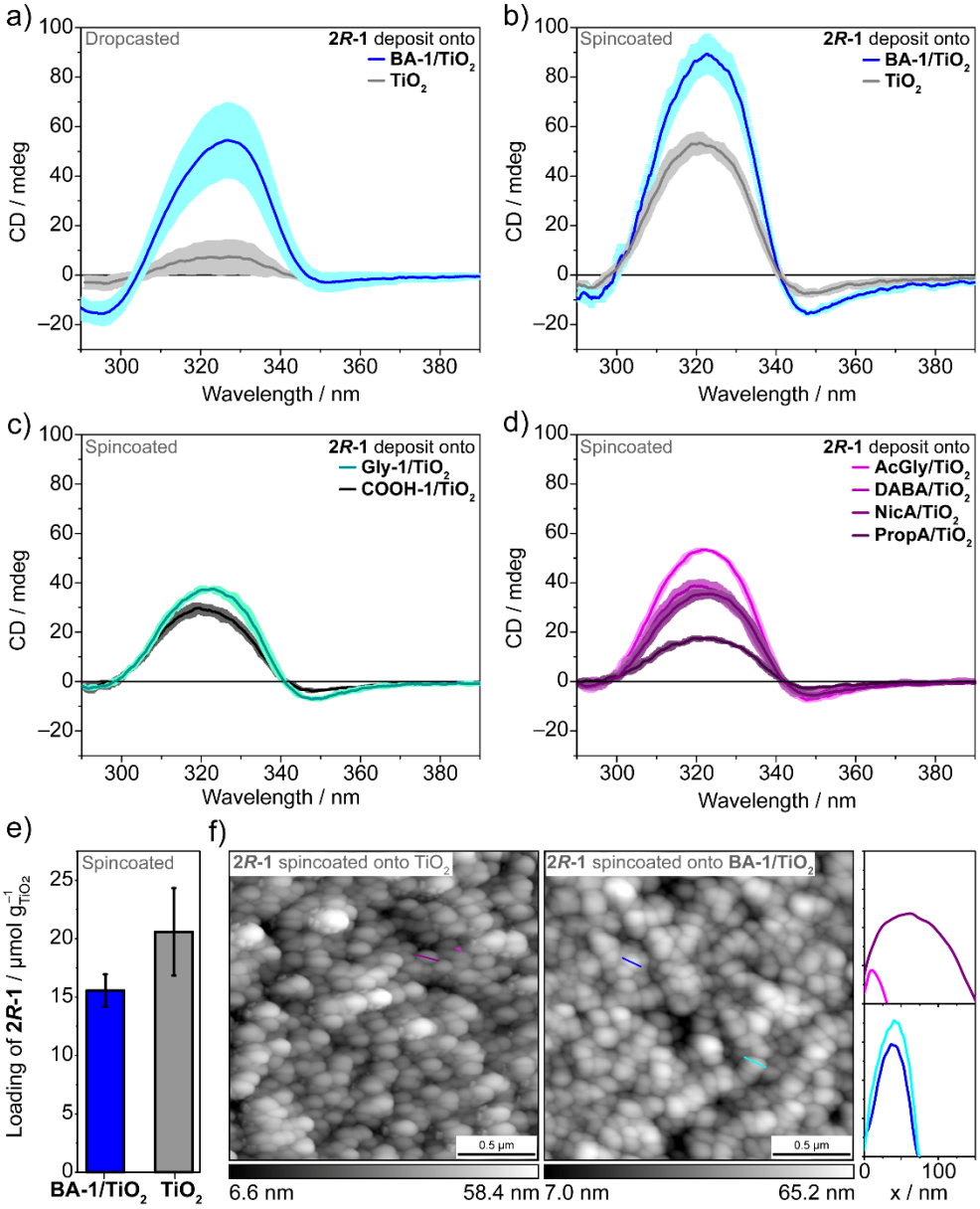

Figure 4. (a-d) CD spectra of **2*R*-1** deposited on bare TiO_2 and on anchors functionalized TiO_2. (a) CD spectra obtained via dropcasting from $CHCl_3$ and annealing (c = 0.5 mM) compared with (b) the ones obtained via spincoating from $CHCl_3$ and annealing (c = 5 mM, 1000 rpm). CD amplified when **2*R*-1** is deposited on **BA-1/TiO₂** (blue line) compared to bare TiO_2 (gray line). (c) CD spectra of **2*R*-1** spincoated on **Gly-1/TiO₂** (green line) and **COOH-1/TiO₂** (black line) and (d) on reference compounds. (e) Loading of **2*R*-1** on bare **TiO₂** and **BA-1/TiO₂** (spincoated, $CHCl_3$, c = 5 mM, 1000 rpm). (f) AFM height images of **2*R*-1** on bare **TiO₂** (left) and **BA-1/TiO₂** (right) and related particles profiles (*y* axis represent high z in nm, scale 0-20nm).

The higher CD intensity signifies either a greater order of the supramolecular polymer layer or a higher loading of the molecules. To evaluate whether the anchor is facilitating the ordering of the surface or the deposition of the chiral layer, we quantified the loading of **2*R*-1**. Interestingly, we noticed that the loading of **2*R*-1** is lower for **BA-1/TiO_2** surfaces compared to bare TiO_2 (Figure 4e). This indicates that the **BA-1** positively affects the order of the **2*R*-1** layer.

Control experiments were performed spincoating **2*R*-1** on TiO_2 functionalized with reference molecules. These reference molecules are selected to represent molecular fragments of the anchor **BA-1** that represent one of the non-covalent interactions. We select N-acetylglycine (**AcGly**) for representing the hydrogen bonding part, 4-(dimethylamino)benzoic acid (**DABA**) and nicotinic acid (**NicA**) for the π-interactions, and propionic acid (**PA**) for van der Waals interactions (Figure 4d). As expected, only **AcGly/TiO_2** showed amplification of the CD intensity confirming that the ability of the surface to form hydrogen bonds is of great importance for the ordering of supramolecular polymers on the surface. However, differently from **BA-1/TiO_2**, **Gly-1** and **COOH-1** do not improve the chiral order of **2*R*-1** even if they bear the same H-bonding units. We propose that careful tuning of the molecular geometry, together with hydrogen bonding, is fundamental to have a positive effect on the supramolecular order. We hypothesize that the rigidity of this two cores does not allow the correct binding geometry on TiO_2 and a favorable angle to interact with **2*R*-1**.

We performed AFM microscopy to further evaluate the enhancement of the supramolecular order. Due to the high porosity of TiO_2 layer, performing AFM proved to be challenging and the resolution of the images does not allow visualization of fibers deposited on the surface. However we noticed that **2*R*-1/BA-1/TiO_2** displays a uniform texture given by the uniform coverage of **2*R*-1/BA-1** on the sintered nanoparticles. In contrast, AFM imaging performed on **2*R*-1/ TiO_2** shows particles of non-uniform sizes, from small hard particles to larger aggregates (Figure 4f).

The positive results obtained by the anchoring strategy can be a fundamental achievement to improve the deposition and the adhesion of supramolecular polymers onto inorganic surfaces. It indeed demonstrates the importance of non-covalent forces at the interface between hard and soft materials and suggests a possible strategy to increase order in hybrid systems.

4.2.4. Device testing

Photoelectrochemical measurements were conducted in a three-electrode cell, with the Ag/AgCl (saturated KCl) as the reference electrode and a Pt plate as the cathode (Figure 5a). A 0.1 M Na_2SO_4 (pH = 6.56) aqueous solution was used as the electrolyte. The devices were tested both in dark conditions (not shown, positive current at 1.75 V *vs.* Ag/AgCl) and under irradiation (LED, 1 A, λ = 365 nm). The magnitude of the measured current, as a function of the potential, is then correlated with the amount of water split hence with the production of O_2 produced at the anode and H_2 at the cathode (Figure 5).[25] The measurements were recorded for chiral, **2*R*-1**, and achiral, **a-1**, supramolecular polymers spincoated (*c* = 5 mM, $CHCl_3$, 100 rpm) both on bare TiO_2 (**2*R*-1/TiO$_2$** and **a-1/TiO$_2$**, respectively) and on the anchoring monolayer (**2*R*-1/BA-1/TiO$_2$**, and **a-1/BA-1/TiO$_2$**, respectively) (Figure 5b).

Current-voltage (I-V) measurements were performed with the aim to test the reproducibility of the effect observed in Chapter 3 and to assess the effect of the anchoring monolayer. Experiments were reproduced 5 times and reported as average with standard deviation. The measurements in the dark do not show any current in the voltage range of interest, while, under LED illumination all the devices display water-splitting. Higher photocurrent densities were consistently recorded for those photoelectrodes functionalized with chiral **2*R*-1** polymers, compared to those coated with achiral **a-1** polymers (Figure 5b left, pink line *vs.* orange line; Figure 5b right, blue line *vs.* green line). This is valid for devices obtained on bare **TiO$_2$** and on **BA-1/TiO$_2$**.

Comparing then the two chiral functionalized cells as a function of the presence of the anchoring monolayer (Figure 5b left, pink line *vs*. Figure 5b right, blue line), we noticed that the presence of the **BA-1** results in lower current densities. A similar trend is observed for the achiral devices **a-1/TiO$_2$** and **a-1/BA-1/TiO$_2$** (Figure 5 left, orange line *vs*. Figure 5b right, green line). While the results for **a-1** are not conclusive as a consequence of the large standard deviation of **a-1/BA-1/TiO$_2$**, the measurements obtained for **2*R*-1** display 0.1 mA cm^{-2} of difference in current density. We speculate that this effect may be due to the fact that the anchoring monolayer is achiral; this can partially interfere with the spin selection effectuated by the chiral layer and worsen the overall performance.

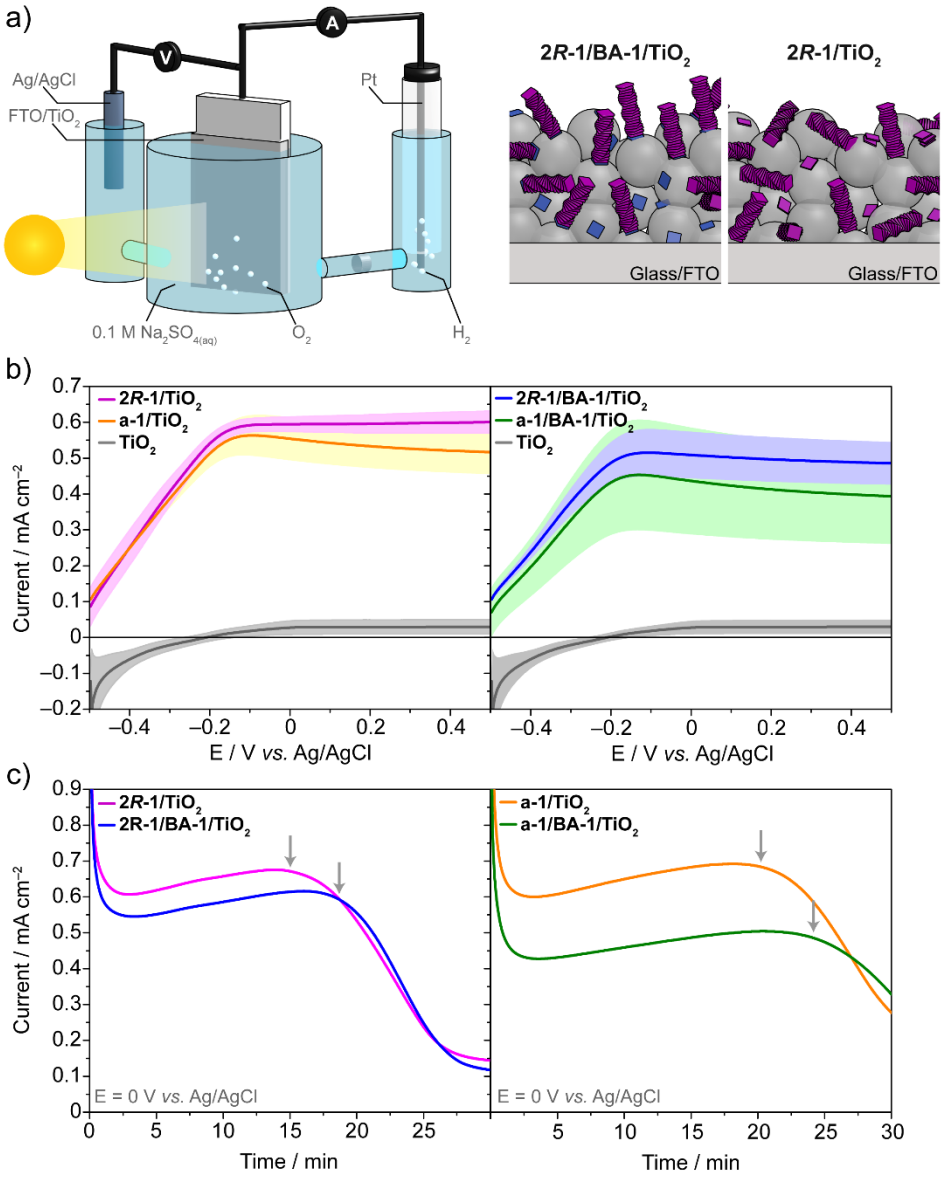

Figure 5. (a) On the left, schematic representation of the three-electrode cell used, on the right, examples of the devices tested, with anchoring monolayer, **2R-1/BA-1/TiO2**, and without, **2R-1/TiO2**. (b) I-V curves obtained under UV illumination with **S-1** and **a-1** deposited on **TiO2** (left) and on **BA-1/TiO2** (right). Comparison of chiral systems (**2R-1/TiO2,** pink line, left, and **2R-1/BA-1/TiO2**, blue line, right) with achiral systems (**a-1/TiO2**, orange line, left, and **a-1/BA-1/TiO2**, green line) and bare TiO_2 (grey line). Curves are reported as average of 4 measurements with their standard deviation. (c) Chronoamperometry, I-time, curves obtained under illumination for chiral (left) and achiral (right) supramolecular layer. Comparison of systems deposit on bare TiO_2 vs. the ones deposited onto **BA-1/TiO2**. Left: **2R-1/TiO2** (pink line) and **2R-1/BA-1/TiO2** (blue line); right: **a-1/TiO2** (orange line) and **a-1/BA-1/TiO2** (green line). Arrows indicate the beginning of the devices' decay.

Secondly, we investigate whether the anchoring monolayer improves the long-term stability of the system. Strong UV light irradiation partially excites the TiO_2 which may provoke the detachment of the polymers from the electrode's surface. We hence measured chronoamperometry (current-time) curves under light irradiation with potential set at 0 V *vs.* Ag/AgCl. When the supramolecular layer is deposited on bare TiO_2 a shorter persistence—noticeable as fast decrease in current— is displayed by the surface compared to the systems deposit on the **BA-1/TiO$_2$** (Figure 5c). The increase in stability is, however, rather limited, around 3 minutes for both chiral (Figure 5c left, pink line *vs*. blue line) and achiral (Figure 5c right, orange line *vs*. green line) systems. Nevertheless, it is worth to notice that **a-1** is more stable than **2*R*-1**. We hypothesize that the different stability is due to the different side chains: long apolar *n*-dodecyl side chains of **a-1** make the molecules highly insoluble in polar media[26] and, as a result, they are less-likely to detach from the surface and diffuse into solution.

4.2.5. Conclusions

In this section we focused on improving the order and stability of the chiral supramolecular layer once deposited on TiO_2. To do so, we introduced an anchoring layer to improve the adhesion of the supramolecular polymers onto the inorganic surface. CD measurements verified that the functionalization of the TiO_2 with anchoring molecules notably modifies the order of the chiral supramolecular layer. We demonstrated that a careful tuning of the design of the anchors is the key to remarkably improve order on the supramolecular layer. However, the improvement of the supramolecular order is not directly translated on the cell's performance as current density. The introduction of the anchoring layer improves the stability of the device by few minutes. Moreover, the achiral molecules, which show a worse solubility than the chiral ones, also showed an improved stability.

This findings suggest that improvements in the stability of the system can be obtained adopting supramolecular polymers with further decreased solubility. The use of chiral anchoring molecules should also be evaluated to increase the efficiency of the CISS effect.

4.3. Chiral supramolecular polymer based on photosensitizers

In the second part of this Chapter, we address the need of using systems able to both induce spin selection and harvest visible light. As established from DSSCs field, the most efficient cells are functionalized with highly absorbing dyes as photosensitizers. We here combine the moieties needed to obtain chiral supramolecular polymers with a classic design used for organic dyes. Organic dyes exploited in solar cells are often asymmetric molecules with a large π core. Usually, to obtain significant light harvesting properties, organic dyes are designed with a donor-π bridge-acceptor structure (D-π-A). However, bulkiness and asymmetry are qualities that may hamper the supramolecular organization.

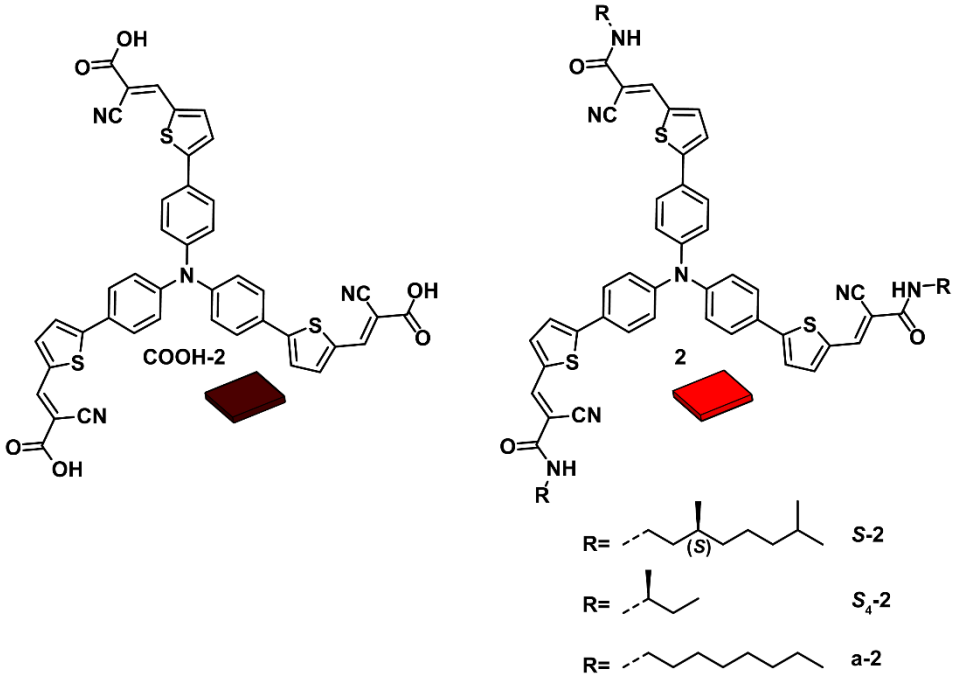

Scheme 3. Molecular structure of triphenylamine-based D-π-A dyes **2**. The reference cyano-acetic, **COOH-2,** and the analogues bearing supramolecular units cyano-acetamide with chiral (*S*)-3,7-dimethyloctyl chains, ***S*-2**, or achiral *n*-octyl chains, **a-2**. An analogue with a short chiral chain is synthesized, ***S*$_4$-2**, for obtaining the crystal structure.

Therefore, we designed a D-π-A dye that maintains C_3 symmetry (which has been proved to be optimal for supramolecular polymerization)[8,27] and that bears carboxamides as supramolecular units. To do so, we selected a branched triphenylamine dye, similar to many reported dyes. [5,28,29] The triphenylamine core is used as donor unit, thiophenes as π bridges, whereas cyanoacetamide units act both as acceptor and as supramolecular units. The molecule, ***S*-2**, bears chiral (*S*)-3,7-dimethyloctyl side chains for imposing chirality to the assembly, while the achiral

analogue, **a-2,** has *n*-octyl chains. In addition, an analogue molecule with short chiral chains, ***S*$_4$-2,** is designed to obtain a crystal structure (Scheme 3). The related cyanoacetic acid molecule, **COOH-2**, previously reported in literature for its optical and electrochemical properties,[30] has also been synthesized (Experimental section).

4.3.1. Synthesis and molecular characterization

***S*-2**, **a-2**, ***S*$_4$-2** were synthesized via amide coupling from **COOH-2**. The synthesis of **COOH-2** was performed following a procedure reported in literature.[30] The amide coupling was then performed as reported for **2*R*-1** (Scheme 2), via activation of **COOH-2** with pentafluorophenyl trifluoroacetate and consecutive substitution with the required amine. SiO_2 gel chromatography and consecutive thin layer chromatography (TLC) yielded to the desired product in high purity. In contrast to **COOH-2**, which is a dark-red solid, ***S*-2**, **a-2**, and ***S*$_4$-2** are bright red-orange powders.

After molecular (^{1}H-NMR, ^{13}C-NMR, Mass) and bulk (DSC, IR, POM) characterization, the optical properties in solution were evaluated. UV and fluorescence measurements in molecularly dissolved state (DMSO c = 20 µM) (Figure 6) were performed to evaluate the spectral range of ***S*-2** and how the latter is affected by the substitution of the cyanoacetic acid group (present in **COOH-2**) with the cyanoacetamides. ***S*-2** displays a broad absorption between 300 and 600 nm and broad emission with the maximum at λ = 505 nm, demonstrating its suitability for harvesting visible light. Compared to **COOH-2**, a general blue-shift of approximately 10 nm is recorded in absorption (Figure 6a), excitation and emission bands (Figure 6b, dashed lines and solid lines, respectively).

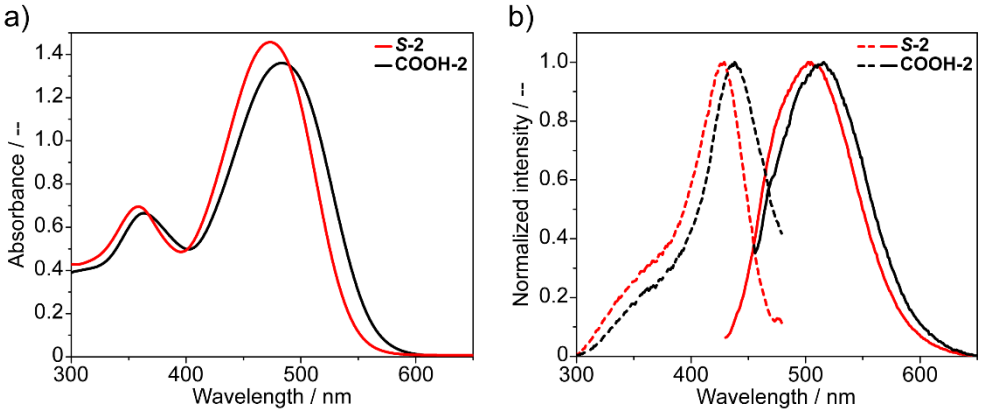

Figure 6. (a) Absorption and (b) excitation-emission spectra for ***S*-2** (red lines) and **COOH-2** (black lines) in molecularly dissolved state (DMSO, c = 20.8 µM). Excitation spectra (b, dashed lines) are recorded for the λ of maximum emission, emission spectra (b, solid lines) are recorded exciting at λ of maximum excitation.

4.3.2. Aggregation in solution and in thin films

We then evaluated the ability of ***S*-2** to form chiral aggregates. To do so, we performed variable temperature UV-vis and CD in methylcyclohexane (MCH). Upon cooling, UV-vis measurements display a decrease in intensity of the main absorption band at λ = 448 nm and the rise of a shoulder at λ = 514 nm (Figure 7a, top). CD spectroscopy reveals a bisignate Cotton effect with a negative maximum at λ = 517 nm (Figure 7a, bottom) verifying the formation of chiral aggregates. The cooling curve was recorded following the evolution of UV and CD intensities at λ = 522 nm as a function of temperature (from 80 °C to 0 °C, cooling rate: 15 °C h^{-1}) (Figure 7b). Upon cooling, the system displays different elongation temperature (T_e) in the UV and in the CD trace. For c = 60 μM, T_e in the UV cooling curve is observed at 46 °C, while in the CD occurs at 39 °C. We attributed this behavior to the formation of two different aggregates, a first which does not display preferred helical organization, and a second that shows preferred handedness. In addition, the shape of both the cooling curves display just a moderate cooperativity showing a gradual increment (in absolute values) of the UV and CD intensities. The isodesmic character is probably due to a π-π driven aggregation rather than a growth by H-bonding.[31,32]

Variable temperature fluorescence measurements confirmed the aggregation observed via CD (Figure 7c). At high temperature, monomerically dissolved ***S*-2** displays an emission band at λ = 505 nm with vibrational structure. This band increases in intensity while cooling from 80 °C to 40 °C. Consecutively, the monomer emission band rapidly decreases in intensity while a broad band at λ = 607 nm grows. This band can be attributed to the aggregate state where an intermolecular charge-transfer between donor and acceptor moieties takes place. The cooling curves obtained by plotting the fluorescence maxima for the monomer (Figure 7d, red open dots) and for the supramolecular aggregate (Figure 7d, blue close dots) display a T_e coincident with the one observed for the CD cooling curves (Figure 7d *vs.* Figure 7b), meaning that the process which gives chirality to the supramolecular aggregates is the same that modifies the emission properties.

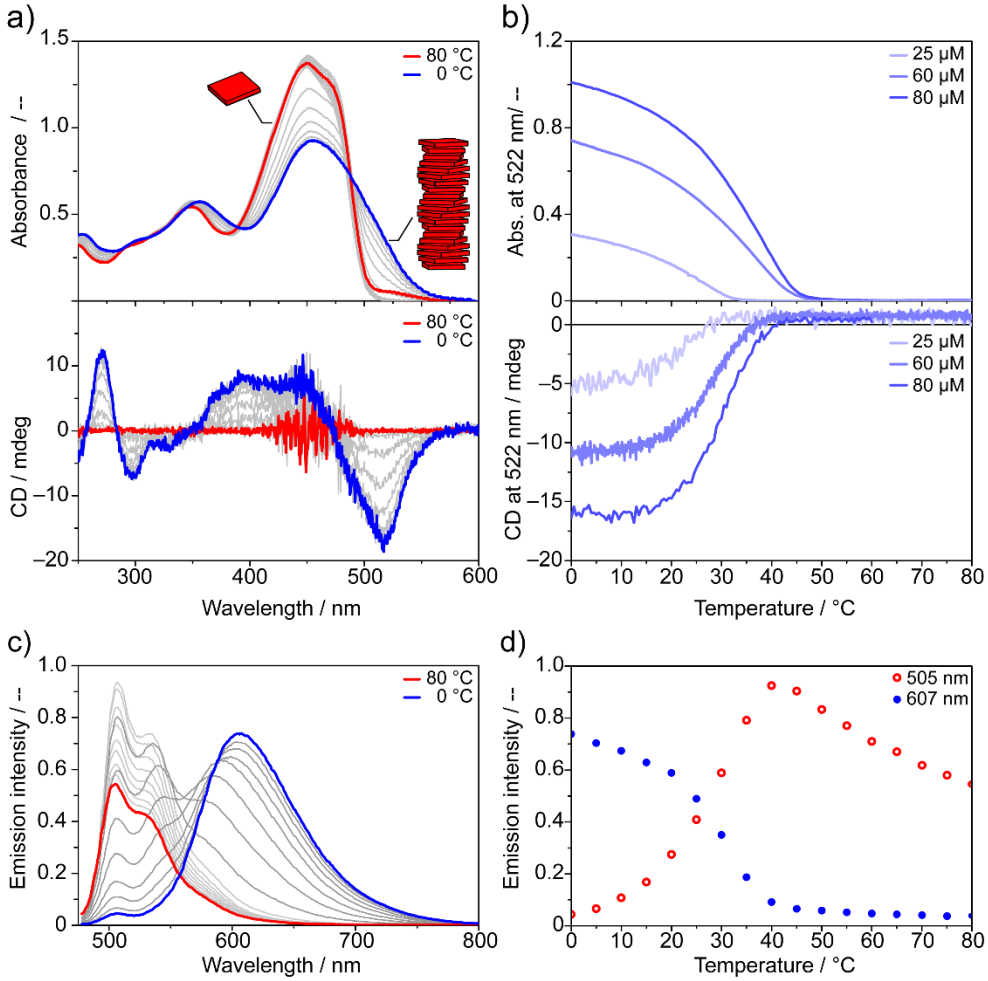

Figure 7. Variable temperature (a, top) absorbance, (a, bottom) CD and (c) emission spectra of ***S*-2** in MCH and (b, d) related cooling curves. (a, top) Absorbance and (a, bottom) CD spectra recorded for c = 25 µM and c = 60 M, respectively (spectra every 5 °C, cooling rate 15 °C h^{-1}). (b) Absorbance and CD cooling curves followed at λ = 522 nm (cooling rate: 15° C h^{-1}, c = 25, 60 and 80 µM). (c) Emission spectra and (d) related cooling curves recorded for c = 60 µM (spectra every 5 °C, cooling rate: 15 °C h^{-1}).

To verify the hypothesis that π-stacking is the driving interaction for assembly of ***S*-2**, we grew crystals of ***S*$_4$-2**. We obtained crystals suitable for single crystal analysis by making a concentrated $CHCl_3$ solution of ***S*$_4$-2** and changing the solvent polarity via slow diffusion of diethyl ether. X-ray analysis shows a crystalline packing consistent with a C2 space group. The molecule lacks C_3 symmetry (Figure 8a) but is able to form an asymmetric unit made of two monomers (Figure 8b). Even though 1D arrays can be observed (Figure 8c, 8d), the crystal structure shows few hydrogen bonding interactions among the molecules and these are not directed between the amide units.

The high conjugation between the donating core and the cyanoacetamides render the molecule particularly planar. This, in combination with the competing –CN groups, hampers the classic hydrogen bonding network of C_3 supramolecular polymers.[7]

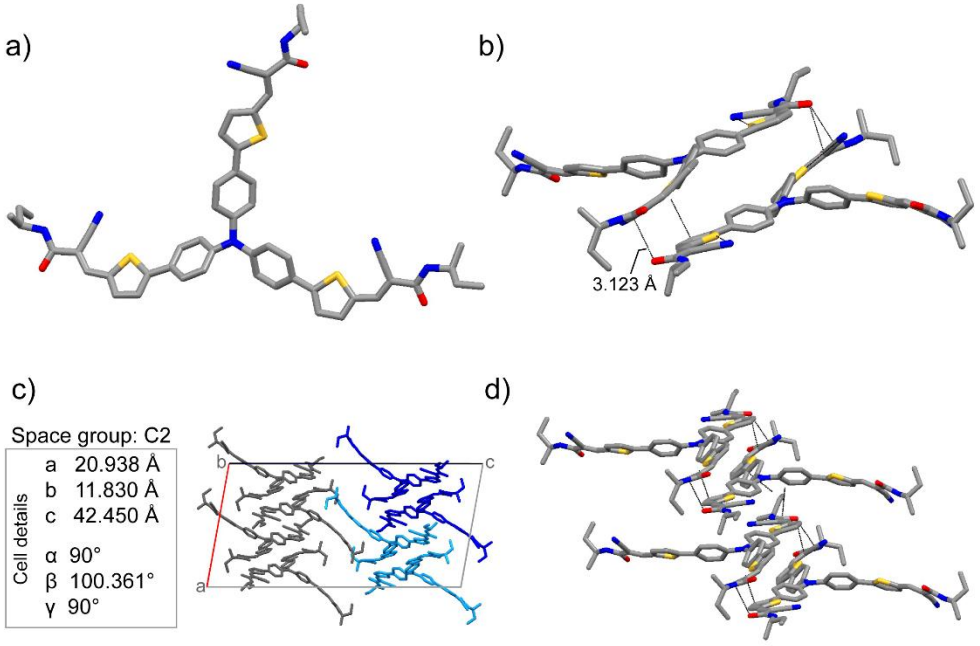

Figure 8. Crystal structure obtain by X-ray crystallography. (a) Monomer of ***S*-2**, (b) asymmetric unit formed by two monomer related by a C2 symmetry. (c) Crystalline packing in a unit cell along b axis. Color coded by symmetry operation (blue, C2 axis, light blue screw axis). (d) Proposed 1D structure in the crystal structure, seen along axis b. (a, b, d)Crystal structures color coded based on the atoms, C are grey, N blue, O red, S yellow. H not displayed.

We then tested the formation of chiral assemblies upon deposition of ***S*-2** both on glass (Figure 9a) and on TiO_2 surfaces (Figure 9b). The dropcasting method was tested on a glass surface (solution of ***S*-2** in MCH, c = 44 μM, annealing 100 °C, 30 min), while dip coating method was tested on the TiO_2 plates (solution of ***S*-2** in 1,2-dichlorobenzene, c = 6 mM) annealing 100 °C, 30 min). The presence of chiral assemblies was verified via UV-Vis and CD spectroscopy. Absorbance measurements displays spectra which resemble the spectrum obtained in MCH solution at 20 °C (Figure 9a top, Figure 9b top). For both the surfaces tested, a weak but present CD signal is also recorded (Figure 9a bottom, Figure 9b bottom). Remarkably, the structure of the chiral assembly on TiO_2 matches well with the aggregates in solution as evidenced by CD (Figure 9b bottom *vs.* Figure 7a bottom).

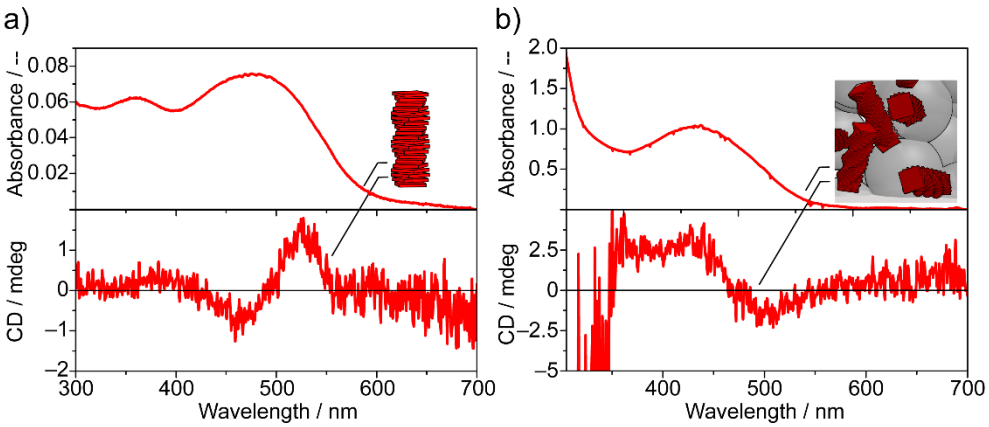

Figure 9. Absorbance (top) and CD (bottom) spectra of ***S*-2** deposited on (a) glass surfaces and (b) porous TiO_2 surface. Note: the absorbance on (b, top) TiO_2 surface is affected by the absorbance of TiO_2 especially in the region $\lambda < 350$ nm.

4.3.3. Device testing

Photoelectrochemical measurements were conducted in a classic three-electrode cell, with Ag/AgCl (saturated KCl) as reference electrode and a Pt plate as cathode (Figure 5a, left). 0.1 M Na_2SO_4 (pH = 6.56) aqueous solution was used as the electrolyte (63 mL). The devices were then tested both in dark conditions (positive current at 0.7 V *vs.* Ag/AgCl) and under shining light (halogen lamp, 12 V, 50 W). The magnitude of the measured current, as a function of the potential, is then correlated with the amount of water split hence with the production of O_2 produced at the anode and H_2 at the cathode (Figure 10).[25] The measurements were performed for chiral, ***S*-2**, and achiral, **a-2**, supramolecular polymers deposited on bare TiO_2, ***S*-2/TiO$_2$** and **a-2/TiO$_2$**, respectively (molecules deposited via spin-coating from $CHCl_3$ c = 5 mM and consequent annealing) (Figure 10a). In line with what is reported in Chapter 3 and in this chapter for **2*R*-1** (Figure 5), these measurements confirm higher current for the chiral device (Figure 10). Chronoamperometry measurements on ***S*-2/TiO$_2$**, **a-2/TiO$_2$**, and on bare TiO_2 (Figure 10b) (molecules deposited via spin-coating from $CHCl_3$ c = 10 mM and consequent annealing) were performed to evaluate the production of H_2O_2. Differently to what is reported in Chapter 3, the concentration of H_2O_2 is determined with the horseradish peroxidase fluorescence test. This test permits higher resolution and detection of extremely small quantities of H_2O_2.

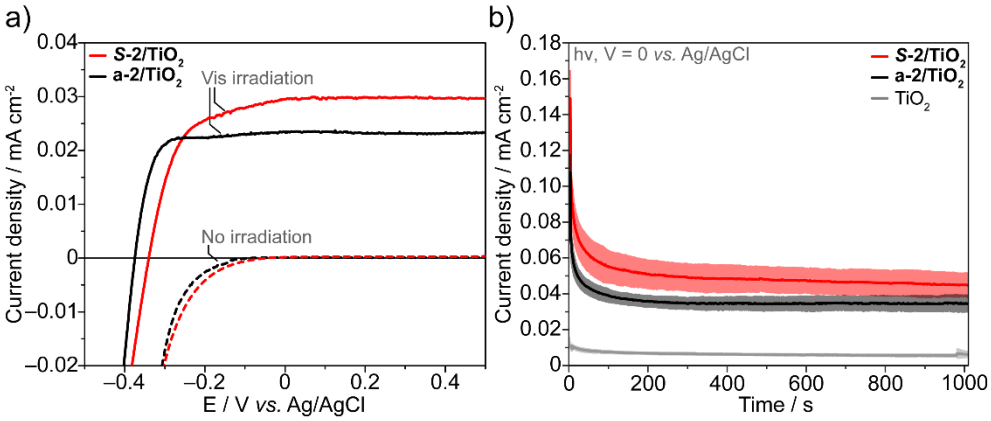

Figure 10. (a) I-V curves obtained in the dark (dashed lines) and under visible light irradiation (solid lines) with ***S*-2** (red lines) and **a-2** (black lines) deposited on bare TiO_2. (b) Chronoamperometry, I-time, curves obtained under illumination for ***S*-2/TiO₂** (red line), **a-2/TiO₂** (black line) and for bareTiO_2 while the voltage is kept at 0 V *vs.* Ag/AgCl. Measurements reported as mean ± s.d. (lines ± solid background).

After 1000 s of constant irradiation and potential kept at 0 V *vs*. Ag/AgCl, an aliquot of the electrolyte was harvested and analyzed for its H_2O_2 content. Similarly to what is observed in Chapter 3, the results show that the H_2O_2 produced with ***S*-2/TiO₂** is on average 37% lower than for **a-2/TiO₂**. Notably, this effect is more accentuated considering that the photocurrent is higher for ***S*-2** than for **a-2.** Calculating the detected H_2O_2 as a function of the photocurrent recorded at 1000 s per each device, we obtained a H_2O_2 production of 9.1 ± 3.7 μM H_2O_2/mA·cm^{-2} for ***S*-2/TiO₂** and 17.5 ± 6.7 μM H_2O_2/mA·cm^{-2} for **a-2/TiO₂**.

4.3.4. Conclusions

The design and synthesis of chiral supramolecular dyes that aggregate and absorb on a broad wavelength range was effective. Both a chiral and achiral version of triphenylamine-based self-assembling dyes was obtained. The chiral dye assembles in apolar solvent, creating chiral structures while the broad conjugated core ensure the absorption in the visible regime.

The tests on chiral-functionalized DS-PEC demonstrates once more the validity of the CISS effect in improving the cell's performances. Experiments on the quantification of the H_2O_2 production confirmed the hypothesis sustained in Chapter 3 on the ability of chiral system to control the spin of the reaction and deplete the production of H_2O_2. We currently plan to quantify the production of H_2 and O_2 to evaluate the cell's efficiency and its connection with the CISS effect.

4.4. Overall conclusions and future directions

This chapter focuses on some of the crucial issues observed in Chapter 3 and addresses the challenge to bring chiral-functionalized water-splitting devices one step closer from an academic curiosity to a working device.

We obtained good results in optimizing and controlling the deposition of chiral supramolecular polymers onto TiO_2 electrodes. Via the use of carefully designed anchoring molecules, we were able to enhance the chiral order of the supramolecular polymer layer. The introduction of the anchor led also to good preliminary results toward increasing the long-term stability of the cells. However further improvements in the design of both the anchoring layer and supramolecular layer are needed.

The parallel development of photosensitizers which can assemble into chiral supramolecular polymers and absorb light in the visible range was successful. Initial device experiments validate once more the presence of the CISS effect.

The encouraging results obtained are, nevertheless, still far from a real exploitation in solar cells. Nevertheless, we are confident that further optimization of the system may result in an effective use of the CISS effect in solar cells.

4.5. Experimental section

4.5.1. Materials and methods

All reagents were purchased from Aldrich and used as received, unless otherwise specified. Copper powder was acquired from Aldrich (< 425 μm, 99.5% trace metals basis). All solvents were purchased from Biosolve and dry solvents were obtained using MBraun solvent purification system (MB SPS-800). Deuterated compounds were obtained from Cambridge Isotopes Laboratories. Reactions were followed by thin-layer chromatography (TLC) using 60-F254 silica gel plates from Merck.

Automated column chromatography was performed on a Grace Reveleris X2 using Reveleris Silica Flash Cartridges. Detail on ^{1}H NMR, ^{13}C NMR, MALDI-TOF-MS, FTIR, DSC, and AFM can be found in the experimental section of Chapter 2.

For all spectroscopic measurements, cells with an optical path length of 1 cm were employed and spectroscopic grade solvents were employed. Solutions were prepared by weighing the necessary amount of compound for the given concentration and dissolved with a weighted amount of solvent based on its density. The stock solutions were heated up, sonicated till complete dissolution and slowly cooled down to room temperature every time before use unless otherwise specified. All the spectroscopic measurement were performed with freshly prepared solutions (max. 1 week after the preparation of the stock solution).

UV/Vis and circular dichroism (CD) measurements were performed on a Jasco J-815 spectropolarimeter, for which the sensitivity, time constants and scan rates were chosen appropriately. Corresponding temperature-dependent measurements were performed with a Jasco PFD-425S/15 Peltier- type temperature controller with a temperature range of 263-393 K and adjustable temperature slope. In all experiments the linear dichroism was also measured and in all cases no linear dichroism was observed. Separate UV/Vis spectra were obtained from a Perkin Elmer UV/Vis spectrometer Lambda 40. Fluorescence spectra were measured with Jasco FMO-427S/15 fluorimeter implemented in the CD spectrometer.

The layer thicknesses were determined on a Veeco Dektak150 profilometer after manually creating scratches with a sharp knife. Doctor blade coating of the TiO_2 layers was performed using an Erichsen Model 360 13mm quadruple film applicator with gap heights of 30, 60, 90 and 120 μm. Atomic force microscopy was performed at room temperature on spincoated or dropcasted films using a Digital Instrument Multimode Nanoscope IV 279 with silicon cantilever tips (PPP-NCH-50, 204 - 497 kHz, 10 - 130 N m^{-1} from Nanosensors) using a tapping regime mode. The roughness of the surface has been measured and images have been processed using Gwyddion software. SEM and EDX was performed on a FEI Nova600i SEM with an EDX detector (136 eV resolution). Ellipsometry was performed using a Sentech 805 SE spectroscopic ellipsometer with a wavelength range 800 - 1700 nm. X-Ray Diffraction (XRD) measurements were performed on a Rigaku Geigerex powder diffractometer with Bragg-Brentano geometry, using copper radiation, wavelength 0.154 nm, at 40 kV and 30 mA. The samples were prepared on a glass substrate and measured from 5° till 80° 2θ with a step size of 0.02° and a dwell time of 15 seconds. The photoelectrochemical cell and the related measurements are described in a following section.

4.5.2. Synthetic procedures

Regarding tripyridylamine-based molecules **1**; **COOH-1** and **a-1** were synthesized as reported in Chapter 2; the synthetic procedures for the other final products are reported in the following. For triphenylamine-base dyes **2**; **COOH-2** was synthesized following the reported procedure[30] (Scheme 4) while amide derivatives (**a-2**, ***S*-2**, ***S*$_4$-2**) were synthesized from **COOH-2** following the procedure optimized for ***2R*-1**.

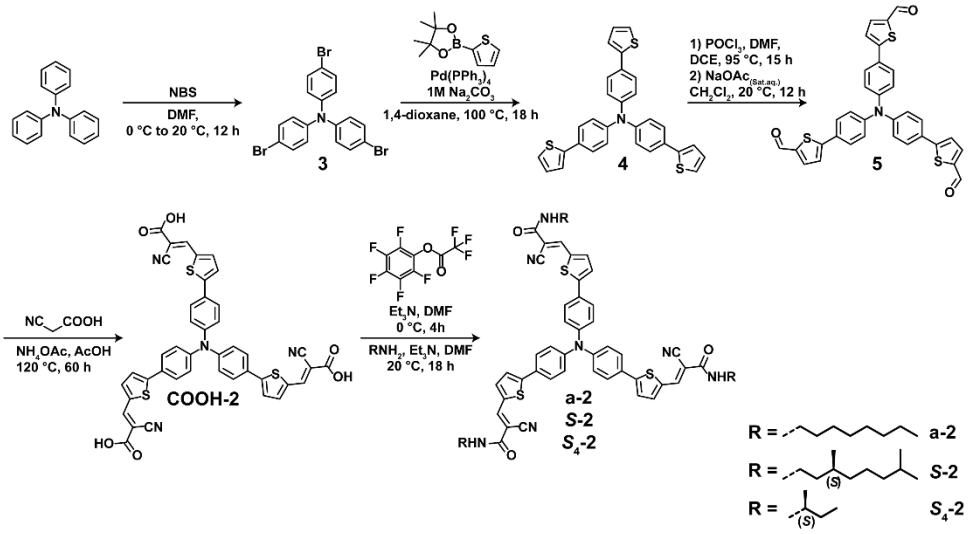

Scheme 4. Synthetic scheme followed for the synthesis of **2** derivatives.

General synthesis of tripyridyl triamides (1)

In a two neck round bottom ask under argon atmosphere **COOH-1** (0.5 g, 1.3 mmol) was dissolved in dry DMF (20 mL) and triethylamine (1.6 mL, 11.7 mmol, 9 eq.). In another round bottom ask under argon atmosphere pentafluorophenol-triuoroacetate (PFP-A) (1 mL, 6 mmol, 4.5 eq.) was dissolved in DMF (2 mL) and triethylamine (0.1 mL) at 0 °C. In another round bottom ask under argon atmosphere the relative amine (4.4 mmol, 3.3 eq.) was dissolved in dry DMF (2 mL). The PFP-A solution was added dropwise to the **COOH-1** solution cooled at 0 °C with ice-bath and stirred at 0 °C for 1 h and at 20 °C for 3 h. Then, the amine solution was added to the reaction mixture and the solution was stirred overnight at 20 °C. The purification is performed differently for each molecule.

6,6',6''-Nitrilotris(N-((S)-octan-2-yl)nicotinamide) (2S-1)
Purification was performed as follows: The mixture was diluted with water and extracted with a solution of 1% Et_3N in $CHCl_3$. The organic phase was collected, dried over $MgSO_4$ and evaporated under reduce pressure. Thus, recrystallization from CH_2Cl_2:CH_3CN (1:4 v/v) yielding to 660 mg (70%) of **2*S*-1** as a white powder.
^{1}H NMR (400 MHz, DMSO) δ 8.72 (d, J = 2.2 Hz, 3H), 8.27 (d, J = 8.3 Hz, 3H), 8.16 (dd, J = 8.6, 2.3 Hz, 3H), 7.17 (d, J = 8.6 Hz, 3H), 4.06-3.94 (m, 3H), 1.50 (d, J = 24.4 Hz, 8H), 1.25 (s, 25H), 1.14 (d, J = 6.6 Hz, 10H), 0.85 (t, J = 6.6 Hz, 9H). ^{13}C NMR (100 MHz, DMSO) δ 164.04, 158.38, 148.26, 137.53, 126.94, 118.50, 45.35, 36.40, 31.72, 29.07, 26.27, 22.53, 21.26, 15.64, 14.42; m/z (MALDI) Calcd. for $[M+H]^+$ 714.50 m/z, found 714.52. IR (cm^{-1}): 3274, 2927, 2855, 1630, 1590, 1541, 1472, 1387, 1352, 1314, 1279, 1171, 1133, 1025, 898, 835, 777, 708, 568, 484. DSC (10 K min^{-1}) T_{melt} : 222 °C.

6,6',6''-Nitrilotris(N-((R)-octan-2-yl)nicotinamide) (2R-1)
Purification was performed as follows: The mixture was diluted with water and extracted with a solution of 1% Et_3N in $CHCl_3$. The organic phase was collected, dried over $MgSO_4$ and evaporated under reduce pressure. Thus, recrystallization from CH_2Cl_2:CH_3CN (1:4 v/v) yielding to 585 mg (69%) of **2*S*-1** as a white powder.
^{1}H NMR (400 MHz, DMSO) δ 8.72 (d, J = 2.2 Hz, 3H), 8.27 (d, J = 8.3 Hz, 3H), 8.16 (dd, J = 8.6, 2.3 Hz, 3H), 7.17 (d, J = 8.6 Hz, 3H), 4.06-3.94 (m, 3H), 1.50 (d, J = 24.4 Hz, 8H), 1.25 (s, 25H), 1.14 (d, J = 6.6 Hz, 10H), 0.85 (t, J = 6.6 Hz, 9H). ^{13}C NMR (100 MHz, DMSO) δ 164.04, 158.38, 148.26, 137.53, 126.94, 118.50, 45.35, 36.40, 31.72, 29.07, 26.27, 22.53, 21.26, 15.64, 14.42; m/z (MALDI) Calcd. for $[M+H]^+$ 714.50, found 714.52. IR (cm^{-1}): 3274, 2927, 2855, 1630, 1590, 1540, 1472, 1387, 1352, 1316, 1279, 1171, 1133, 1024, 897, 835, 777, 708, 568, 484. DSC (ramp: 10 K min^{-1}) T_{melt} : 223 °C.

Trimethyl 2,2',2''-((6,6',6''-nitrilotris(nicotinoyl))tris(azanediyl))triacetate (Me-Gly-1)
The mixture was diluted with water and extracted with ethyl acetate. The organic phase was collected, dried over $MgSO_4$ and evaporated under reduce pressure. The crude product was recrystallized from acetonitrile yielding 150 mg (19%) **Me-Gly-1** as a white powder.
^{1}H NMR (400 MHz, DMSO) δ 9.11 (t, J = 5.9 Hz, 3H), 8.78 (d, J = 2.1 Hz, 3H), 8.20 (dd, J = 8.6, 2.3 Hz, 3H), 7.26 (d, J = 8.5 Hz, 3H), 4.05 (d, J = 5.7 Hz, 6H), 3.67 (s, 9H). ^{13}C NMR (100 MHz, DMSO) δ 170.72, 165.21, 158.68, 148.40, 137.69, 125.89, 118.85, 52.29, 41.62; m/z (MALDI) Calcd. for $[M+H]^+$ 594.19, found 594.17. IR (cm^{-1}): 3259, 3071, 2938, 2857, 1755, 1664, 1637, 1588, 1535, 1514, 1470, 1439, 1414, 1381, 1325, 1289, 1257, 1203, 1174, 1092, 1013, 995, 979, 841, 779, 711, 671, 659, 606, 559, 529, 500, 478.

Trimethyl 4,4',4''-((6,6',6''-nitrilotris(nicotinoyl))tris(azanediyl))tributyrate (Me-BA-1)
The mixture was diluted with water and extracted with ethyl acetate. . The organic phase was collected, dried over $MgSO_4$ and evaporated under reduce pressure. The crude product was recrystallized from acetonitrile yielding 376 mg (42%) **Me-BA-1** as a white powder.
^{1}H NMR (400 MHz, DMSO) δ 8.72 (d, *J* = 2.1 Hz, 3H), 8.60 (t, *J* = 5.0 Hz, 3H), 8.15 (dd, *J* = 6.2 Hz, 3H), 7.18 (d, *J* = 8.9 Hz, 3H), 3.59 (s, 9H), 2.38 (t, *J* = 7.3 Hz, 6H), 1.79 (dt, *J* = 14.3, 7.1 Hz, 6H). ^{13}C NMR (100 MHz, DMSO) δ 173.61, 164.79, 158.42, 148.21, 137.55, 126.67, 118.59, 51.75, 38.94, 31.23, 24.91; m/z (MALDI) Calcd. for $[M+H]^+$ 678.28, found 678.33. IR (cm^{-1}): 3271, 3086, 2950, 1736, 1630, 1588, 1546, 1469, 1443, 1377, 1316, 1276, 1250, 1170, 1095, 1020, 1001, 857, 833, 777, 965, 567, 531, 494.

General hydrolysis of methylester protected anchors
In a round bottom cooled at 0 °C via ice bath **Me-Gly-1** or **Me-BA-1** (0.086 mmol) and $LiOH \cdot H_2O$ (0.0218 g, 0.52 mmol, 6 eq) were dissolved in H_2O:THF (1:2 v/v) (2 mL) and stirred for an hour. The mixture was then allowed to equilibrate to 20 °C overnight. Then, the solution was acidified to pH=3 with 1 M $KHSO_4$ and the product extracted with EtOAc. The organic phase was collected, dried over $MgSO_4$ and evaporated under reduce pressure.

2,2',2''-((6,6',6''-Nitrilotris(nicotinoyl))tris(azanediyl))triacetic acid (Gly-1)
Procedure gives 0.030 g (60%) **Gly-1** as a white powder.
^{1}H NMR (400 MHz, DMSO) δ 8.77 (s, 3H), 8.20 (d, *J* = 10.7 Hz, 3H), 7.24 (d, *J* = 8.9 Hz, 3H), 3.93 (s, 6H). ^{13}C NMR (100 MHz, DMSO) δ 171.64, 165.09, 158.62, 148.37, 137.66, 126.08, 118.79, 41.61; m/z (MALDI) Calcd. for $[M+H]^+$ 552.14, found 552.08. IR (cm^{-1}): 3290, 3057, 2928, 2524, 1725, 1636, 1592, 1542, 1474, 1415, 1383, 1324, 1281, 1246, 1222, 1174, 1130, 1138, 1001, 950, 896, 855, 775, 739, 671, 656, 636, 621, 574, 554, 541, 517, 495, 477.

4,4',4''-((6,6',6''-Nitrilotris(nicotinoyl))tris(azanediyl))tributyric acid (BA-1)
Procedure gives 0.088 g (66%) **BA-1** as a white powder.
^{1}H NMR (400 MHz, DMSO) δ 8.73 (d, *J* = 2.2 Hz, 3H), 8.16 (dd, J = 8.6, 2.4 Hz, 3H), 7.18 (d, *J* = 8.6 Hz, 3H), 2.55 (t, *J* = 5.5 Hz, 6H), 2.29 (t, *J* = 7.3 Hz, 6H), 1.83-1.69 (m, 6H). ^{13}C NMR (100 MHz, DMSO) δ 174.71, 164.76, 158.42, 148.22, 137.55, 126.72, 118.59, 65.39, 39.07, 31.58, 24.97, 15.64; m/z (MALDI), Calcd. for $[M+H]^+$ 636.23, found 636.25. IR (cm^{-1}): 3282, 3072, 2939, 2485, 1693, 1633, 1589, 1545, 1470, 1377, 1316, 1280, 1169, 1140, 1097, 1033, 1022, 960, 936, 910, 851, 806, 776, 678, 614, 569, 530, 495, 456.

Tris(4-bromophenyl)amine (3)
In a two-neck round bottom flask, triphenylamine (2.5 g, 10.0 mmol) was dissolved in anhydrous DMF (25 mL) under argon atmosphere. The solution was cooled to 0 °C by ice-water bath and NBS (5.2 g, 32.0 mmol) in DMF (10 mL) was added drop-wise under stirring. After the addition, the mixture was stirred for 4 h at room temperature. The reaction mixture was then poured into water (400 mL), leading to the formation of a white precipitate. The precipitate was filtered and dried under reduced pressure. The crude product was recrystallized from heptane to afford pure **3** as a white solid (3.8 g, 77 %).
^{1}H-NMR (400 MHz, $CDCl_3$) δ (ppm): 7.36–7.34 (m, 6H), 6.93–6.91 (m, 6H); m/z (APCI) Calcd. for $C_{18}H_{13}Br_3N$ $[M+H]^+$: 481.9, found 482.9.

Tris[4-(2-thienyl)phenyl]amine (4)
In a three-neck round bottom flask, tris(4-bromophenyl)amine (**3**) (3 g, 6.2 mmol), thiophene-2-boronic acid pinacol ester (4.7 g, 22.4 mmol) and tetrakis(triphenylphosphine)palladium(0) (0.36 g, 0.31 mmol) were dissolved in dioxane (100 mL) under argon atmosphere. A 1 M Na_2CO_3 aqueous solution (30 mL) was introduced under stirring. The reaction mixture was heated at 100 °C for 18 h, then cooled to room temperature and diluted with $CHCl_3$ (100 mL). The organic phase was then washed with water (150 mL), 1 M HCl (150 mL) and brine (150 mL), dried over anhydrous $MgSO_4$, filtered and evaporated under vacuum. The crude product was purified via SiO_2 flash column chromatography (CH_2Cl_2/*n*-heptane: 7/3 v/v) to afford **4** as a yellow solid (1.8 g, 57 %).
^{1}H-NMR (400 MHz, $CDCl_3$) δ (ppm): 7.52 (d, *J* = 8.7 Hz, 2H), 7.26 – 7.22 (m, 2H), 7.14 (d, *J* = 8.6 Hz, 2H), 7.07 (dd, *J* = 5.1, 3.6 Hz, 1H); m/z (MALDI) Calcd. for $C_{30}H_{22}NS_3$ $[M+H]^+$: 491.08, found 491.13

Tris[4-(5-formyl-2-thienyl)phenyl]amine (5)
Tris[4-(2-thienyl)phenyl]amine (**4**) (800 mg, 1.63 mmol) was dissolved in 1,2-dichloroethane (50 mL) in a two-neck round bottom flask under argon. DMF (595 mg, 8.14 mmol) and $POCl_3$ (1.25 g, 8.14 mmol) were added dropwise and the solution was stirred and refluxed for 17 h. Next, the reaction mixture was cooled to room temperature; DCM (80 mL) and a saturated aqueous solution of sodium acetate (160 mL) were added. The reaction mixture was then stirred at room temperature for 2 h. The organic phase was washed with water (3 x 150 mL), dried over anhydrous $MgSO_4$, filtered, and evaporated under vacuum, affording **5** as a yellow solid (1.04 g, 99 %).
^{1}H-NMR (400 MHz, $CDCl_3$) δ (ppm): 9.89 (s, 1H), 7.74 (d, *J* = 4.0 Hz, 1H), 7.62 (d, *J* = 8.8 Hz, 2H), 7.36 (d, *J* = 4.0 Hz, 1H), 7.19 (d, *J* = 8.7 Hz, 2H); m/z (MALDI) Calcd. for $C_{33}H_{21}NO_3S_3$ $[M]^+$: 575.07, found 575.12. IR (cm^{-1}): 2793, 1651, 1589, 1528, 1504, 1436, 1385, 1320, 1293, 1269, 1222, 1183, 1113, 1014, 960, 830, 800, 756, 736, 728, 697, 672, 648, 606, 594, 548, 499, 480, 547

3,3',3''-[Nitrilotris(4,1-phenylene-5,2-thiophenediyl)]tris[2-cyano-2-propenoic acid] (COOH-2)
In a two-neck round bottom flask, tris[4-(5-formyl-2-thienyl)phenyl]amine (**5**) (450 mg, 0.78 mmol), cyanoacetic acid (300 mg, 3.51 mmol) and ammonium acetate (42 mg, 0.55 mmol) were dissolved in glacial acetic acid (16 mL). The reaction mixture was refluxed for 40 h under argon atmosphere. After completion, the reaction mixture was cooled to room temperature and the crude product was filtered and washed with $CHCl_3$ (about 50 mL). The crude product was purified by washing in $CHCl_3$ under reflux conditions for 15 h, to afford **COOH-2** as a dark red solid (406 mg, 67 %).
^{1}H-NMR (400 MHz, DMSO-*d*6) δ (ppm): 12.13 (s, 3H), 8.49 (s, 3H), 8.02 (d, *J* = 4.1 Hz, 3H), 7.79 (d, *J* = 8.5 Hz, 6H), 7.73 (d, *J* = 4.0 Hz, 3H), 7.21 (d, *J* = 8.6 Hz, 6H); 13C-NMR (100 MHz, DMSO-*d*6) δ (ppm): 164.13, 152.93, 147.58, 147.05, 142.11, 134.61, 128.24, 128.10, 125.18, 125.10, 117.03, 98.39; m/z (MALDI) Calcd. for $C_{42}H_{24}N_4O_6S_3$ $[M]^+$: 776.09, found 776.09; IR (cm^{-1}): 2920, 2218, 1685, 1567, 1492, 1409, 1321, 1258, 1181, 1060, 936, 801, 734, 683, 608, 582, 503.

General synthesis for (2E,2'E,2''E)-3,3',3''-(5,5',5''-(nitrilotris(benzene-4,1-diyl))tris(thiophene-5,2-diyl))tris(2-cyano-N-alkylamides):
(2E,2'E,2''E)-3,3',3''-(5,5',5''-(nitrilotris(benzene-4,1-diyl))tris(thiophene-5,2-diyl))tris(2-cyano-N-octylacrylamide) (a-2);
(2E,2'E,2''E)-3,3',3''-(5,5',5''-(nitrilotris(benzene-4,1-diyl))tris(thiophene-5,2-diyl))tris(2-cyano-N-((S)-3,7-dimethyloctyl)acrylamide) (S-2);
(2E,2'E,2''E)-3,3',3''-(5,5',5''-(nitrilotris(benzene-4,1-diyl))tris(thiophene-5,2-diyl))tris(N-((S)-sec-butyl)-2-cyanoacrylamide) (S_4-2)
In a two-neck round bottom flask, **COOH-2** (300 mg, 0.39 mmol) and Et_3N (586 mg, 5.79 mmol, 1 ml) were dissolved in dry DMF (10 mL) under argon. The solution was cooled to 0 °C using an ice bath. In a second round bottom flask, pentafluorophenyl trifluoroacetate (487 mg, 1.74 mmol) was dissolved in dry DMF (1.5 mL) under argon atmosphere. This solution was added dropwise to the mixture containing **COOH-2**, stirred at 0 °C for 1 h and then at room temperature for 4 h. Next, a solution of the appropriate alkylamine (1.74 mmol) was prepared in dry DMF (1.5 mL) under argon and then added to the reaction mixture dropwisely. The reaction mixture was stirred for 40 h at room temperature. After completion, the mixture was diluted with $CHCl_3$ (150 mL) and the organic phase was washed with 1N HCl (2 x 200 mL) and water (3 x 200 mL). The organic phase was dried over anhydrous $MgSO_4$, filtered, and evaporated under vacuum, affording a red oil. The crude product was precipitated from the red oil by pouring it in diethyl ether (120 mL) and filtered, affording a red solid. The crude product was first purified via SiO_2 flash column chromatography ($CHCl_3$/EtOAc: 10/0.3 v/v) and then via preparative TLC ($CHCl_3$/EtOAc: 10/0.3 v/v). After recrystallization from acetonitrile, the product was obtained pure as a red solid. The yield was estimated to be about 15 %.

a-2: ^{1}H-NMR (400 MHz, $CDCl_3$) δ (ppm): 8.37 (s, 3H), 7.68 (d, *J* = 4.1 Hz, 3H), 7.62 (d, *J* = 8.7 Hz, 6H), 7.35 (d, *J* = 4.0 Hz, 3H), 7.18 (d, *J* = 8.7 Hz, 6H), 6.24 (t, *J* = 5.8 Hz, 3H), 3.41 (td, *J* = 7.2, 5.8 Hz, 6H), 1.64 – 1.57 (m, 6H), 1.43 – 1.21 (m, 30H), 0.94 – 0.84 (m, 9H); ^{13}C-NMR (100 MHz, CDCl3) δ (ppm): 160.5926, 154.42, 152.54, 147.48, 147.45, 144.41, 138.42, 135.02, 128.32, 127.68, 124.65, 123.74, 99.42, 99.15, 40.63, 31.78, 29.71, 29.48, 29.23, 29.17, 26.87, 22.64, 14.09; m/z (MALDI) Calcd. for $C_{66}H_{75}N_7O_3S_3$ $[M]^+$: 1109.51, found 1109.53. IR (cm^{-1}): 3356, 3027, 2924, 2854, 2205, 1664, 1578, 1521, 1496, 1435, 1354, 1324, 1276, 1226, 1184, 1113, 1065, 940, 831, 802, 734, 734, 689, 609, 545, 504. DSC (ramp: 10 K min^{-1}) T_g: 61.18 °C

S-2: ^{1}H-NMR (400 MHz, $CDCl_3$) δ (ppm): 8.36 (s, 3H), 7.68 (d, *J* = 4.0 Hz, 3H), 7.62 (d, *J* = 8.7 Hz, 6H), 7.35 (d, *J* = 4.0 Hz, 3H), 7.18 (d, *J* = 8.7 Hz, 6H), 6.19 (t, *J* = 5.7 Hz, 3H), 3.44 (dq, *J* = 8.2, 6.1 Hz, 6H), 1.76 – 1.07 (m, 30H), 0.94 (d, *J* = 6.5 Hz, 9H), 0.88 (d, *J* = 0.7 Hz, 18H); ^{13}C-NMR (100 MHz, CDCl3) δ (ppm): 171.15, 160.53, 152.52, 147.43, 144.36, 138.40, 135.00, 128.30, 127.66, 124.63, 123.72, 117.50, 99.15, 60.40, 39.21, 38.76, 37.09, 36.52, 30.70, 27.96, 24.62, 22.70, 22.60, 21.06, 19.50, 14.21; m/z (MALDI) Calcd. for $C_{72}H_{87}N_7O_3S_3$ $[M]^+$: 1193.60, found 1193.63; IR (cm^{-1}): 3355, 3027, 2953, 2924, 2867, 2855, 2205, 1731, 1661, 1579, 1521, 1496, 1464, 1435, 1379, 1365, 1355, 1324, 1275, 1263, 1227, 1184, 1109, 1097, 1065, 1017, 959, 939, 830, 801, 753, 734, 689, 666, 627, 609, 599, 544, 505, 465.

S_4-2: ^{1}H-NMR (400 MHz, $CDCl_3$) δ (ppm): 8.37 (s, 3H), 7.68 (d, *J* = 4.0 Hz, 3H), 7.63 (d, *J* = 8.9 Hz, 6H), 7.35 (d, *J* = 4.0 Hz, 3H), 7.18 (d, *J* = 9.0 Hz, 6H), 5.99 (d, *J* = 8.3 Hz, 3H), 4.08 – 3.99 (m, 3H), 1.56 (d, *J* = 8.2 Hz, 6H), 1.25 (td, *J* = 8.0, 6.3 Hz, 9H), 0.96 (t, *J* = 7.4 Hz, 9H); ^{13}C NMR (100 MHz, $CDCl_3$) δ 159.93, 152.48, 147.43, 144.41, 138.36, 135.03, 128.32, 127.66, 32 124.63, 123.72, 117.50, 99.33, 77.23, 65.86, 47.96, 29.60, 20.35, 15.28, 10.37; IR (cm^{-1}): 3348, 2963, 2929, 2873, 2207, 1663, 1572, 1518, 1493, 1432, 1360, 1323, 1282, 1266, 1242, 1219, 1186, 1157, 1127, 1115, 1090, 1060, 1014, 939, 920, 875, 818, 804, 751, 734, 728, 687, 674, 665, 621, 602, 544, 510, 498, 452, 407.

4.5.3. Surfaces preparation

TiO_2 surfaces

TiO_2 anodes were prepared following the procedure reported for Solaronix T/SP paste® (commercially available TiO_2 paste, anatase 20 nm nanoparticle).[18] TiO_2 surfaces were prepared on glass for optical measurements and on FTO coated glass plates for the water-splitting measurements. Plates of 19 mm x 25 mm were cleaned by sonication in EtOH (15 min) and oven-dried at 140 °C (1 h). The plates were further cleaned with UV-Ozone oven (30 min). TiO_2 Solaronix T/SP paste® is then deposit on the surface and homogenously distributed with a 13 mm wide Doctor Blade. Several blading thicknesses were tested, the optimized thickness used is 60 µm, which give a final sintered TiO_2 layer of 5 µm. After 2 h natural evaporation of the paste, plates were sintered at 450 °C (15' from 20 °C to 450 °C, 45'at 450 °C) for 1 h and let cool (from 450 °C to 250 °C in 30 min followed by cooling to 20 °C in 1 h). At 450 °C the solvent of the paste evaporate and calcination of the paste occurs giving sintered porous TiO_2 anatase layers.

XRD analysis confirmed the crystalline phase, proving full anatase composition (Figure 11a).[33] Film thickness was measured with a profilometer and the reproducibility of thickness was established. Scanning electron microscopy (SEM) was used to image the cross-section of the layer confirming constant thickness of 5 µm and showing the nanoporous character of the layer (Figure 11c). The elemental composition of the layers via energy-dispersive X-ray spectroscopy (EDX) confirmed the presence of TiO_2 and SiO_2 in the two region imaged by SEM (Figure 11d).

Via ellipsometry the porosity of the layer was calculated based on its refractive index. The interference pattern indicates a constant and defined layer thickness. The fitting of the experimental data (at θ = 65°) report a thickness of 5.1 µm and a calculated refractive index of n = 1.46. Based on reported refractive index for bulk TiO_2 (n = 2.56)[34] we concluded that the sintered layer of TiO_2 is highly porous and roughly half of the volume is free (Figure 11b).

Quality control and selection of the plates was finally done by eye and by UV-Vis measurements. Defected plates and plates with outlying transmissions were discarded. Selected plates (5 µm TiO_2) present transmission at 330 nm between 7.5-12.5% and 3-6% for glass and glass/FTO, respectively.

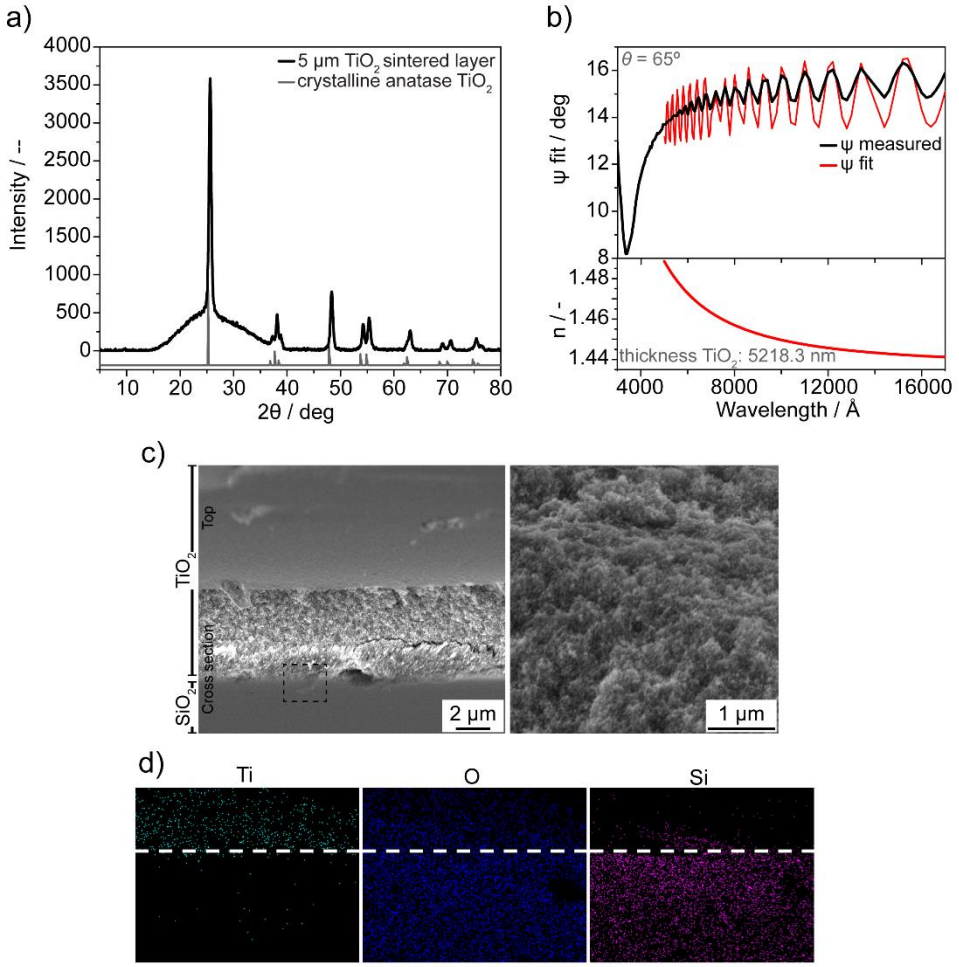

Figure 11. (a) XRD spectra of sintered TiO_2 layer (5 µm) on glass. (b, top) Ellipsometry results on of sintered TiO_2 layer for angles of incident θ = 65 ° (black line) and fitting with Cauchy function. (b, bottom) The fitting confirms the thickness of TiO_2, 5.1 µm, and calculates a refractive index much lower compare to bulk TiO_2 indicating porosity. (c) SEM imaging of TiO_2 on glass and (d) EDX analysis further determines the porosity of the electrode and the composition. SEM detail: HV: 5.00 kV, Current 26.6 pA, mode SE. EDX performed on the window dashed in SEM image.

Anchor deposition

Anchor molecules were dissolved in dry EtOH (c = 0.1 mM) and sonicated to ensure full dissolution. TiO_2 plates were fired again before usage to remove adsorbed water and other contaminants (450 °C, 30 min). Anchor solution were transferred in brown sealable container, TiO_2 plates (at 60 °C to minimize water absorption) were immerse in the solution with TiO_2 side facing the solution, and the container sealed to avoid water diffusion. Plates were let in the anchor solution overnight at 20 °C, then cleaned with clean ethanol solution by immersion (3 x 5 min, 25 mL of EtOH per plate). Consequently, plates were ambient dried (30 min) and vacuum–dried (60 °C, 2 h).

Supramolecular layer deposition for 1

Solution of ***2R-1***, ***2S-1*** or ***a-1*** were prepared in $CHCl_3$ (c = 5 mM) via cycles of sonication and heating to ensure full dissolution. The supramolecular polymer layer was deposit on TiO_2 plates (or on anchor-functionalized TiO_2 plates) spincoating 100 µL of solution (1000 rpm, 60 sec). Plates are then annealed at 100 °C for 30 min and let cool down to room temperature (20 min-30min). Note: Supramolecular monomers are molecularly dissolved in $CHCl_3$ and the aggregation occurs via spincoating and consequent annealing. Different annealing procedure were tested, and the optimum was selected based on the obtained CD spectra of the surfaces.

SEM and EDX and ellipsometry demonstrated the penetration of the organic layers through the thickness of TiO_2 (Figure 12).

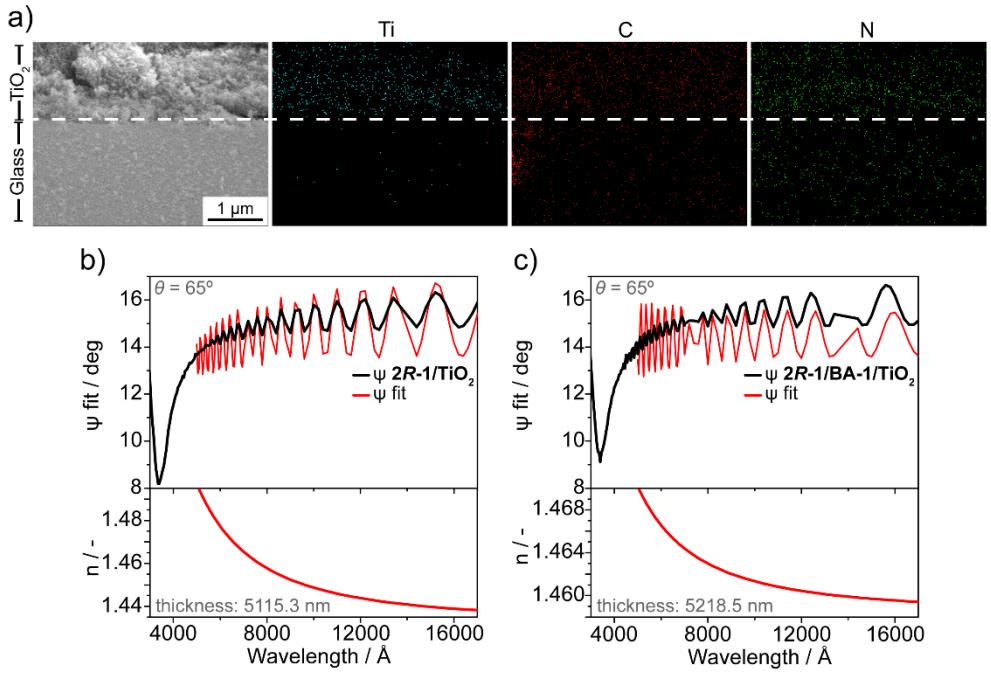

Figure 12. (a) SEM image and EDX analysis of the system **2*R*-1/BA-1/TiO$_2$**. Ellipsometry result for incident angle θ = 65 ° for (b) **2*R*-1/TiO$_2$** and (c) **2*R*-1/BA-1/TiO$_2$**.

Supramolecular layer deposition for 2

For the photoelectrochemical measurements of ***S*-2/TiO$_2$** and **a-2/TiO$_2$**, an accurate selection of the TiO_2 plates was done in order to ensure the reproducible quality of each individual substrates. I-V curves were recorded for each TiO_2 photoanode, and a set of anodes with equal electrochemical behavior was chosen for functionalization with **2**. Before functionalization, the anodes were reheated to 450 C , cooled down to 50 C and stored in water-free atmosphere. The plates were then functionalized as follow. Solution of ***S-2*** or ***a-2*** were prepared in $CHCl_3$ (c = 10 mM for I-V curves and c = 2.5 mM for chronoamperometry measurements) via cycles of sonication and heating to ensure full dissolution. The supramolecular polymer layer was deposit on TiO_2 plates spincoating 100 µL of solution (1000 rpm, 60 sec). Plates are then annealed at 100 °C for 30 min and let cool down to room temperature (20 min-30min). Note: Supramolecular monomers are molecularly dissolved in $CHCl_3$ and the aggregation occurs via spincoating and consequent annealing.

4.5.4. Photoelectrochemical cell and measurements

Photoelectrochemical cells were tested in custom-made glassware consisting of three connected chambers, the chamber set for the working electrode is provided with a flat quartz window for illumination. A glass filter separates the electrolyte solution of the counter electrode with the one of the working and reference electrodes. The cell was set with TiO_2 plate as working electrode, (description of the plate below), Ag/AgCl (Sigma Aldrich©) as reference electrode, and Pt plate as counter electrode. Wires to connect the electrodes were copper. The cell was filled with 63 mL of 0.1 M Na_2SO_4 aqueous solution (pH = 6.56). The potential applied between the reference and the working electrode can be referred to reversible hydrogen electrode (RHE) via the following equation:

$$E_{RHE} = E_{Ag/AgCl} + 0.059 \cdot pH_{solution} + E^0_{g/AgCl}$$

For example: 0 V *vs.* Ag/AgCl = 0.597 *vs.* RHE.

Experiments under illumination are performed with Philips Brilliantline halogen lamp, 12 V 50 W or with a LED 1A, 365 nm. The light is positioned 7 cm afar from the TiO_2 electrode for all the measurements except for chronoamperometry on ***S*-2/TiO$_2$** and **a-2/TiO$_2$** which has the LED at 8 cm distance. Electrical measurements were taken with an Autolab PGstat12. I-V measurements were performed with linear scans from -0.5 to +0.5 V (scan rate 0.01 V min^{-1}) or with 3 cycles from -0.5 to +0.5 V (scan rate 0.1 V min^{-1}). In case of cycles the first run was used, if not otherwise specified. After every measurement the solution was refreshed and a sample was taken to determine the hydrogen peroxide content. Chronoamperometry measurements were performed under illumination with potential set at 0 V *vs*. Ag/AgCl, and the current recorded for 20-30minutes.

4.6 References

[1] Mtangi, W.; Tassinari, F.; Vankayala, K.; Vargas Jentzsch, A.; Adelizzi, B.; Palmans, A. R. A.; Fontanesi, C.; Meijer, E. W.; Naaman, R. *J. Am. Chem. Soc.* **2017**, 139 (7), 2794–2798.

[2] Hagfeldt, A.; Boschloo, G.; Sun, L.; Kloo, L.; Pettersson, H. *Chem. Rev.* **2010**, 110 (11), 6595–6663.

[3] Nazeeruddin, M. K.; Kay, A.; Rodicio, I.; Humphry-Baker, R.; Mueller, E.; Liska, P.; Vlachopoulos, N.; Graetzel, M. *J. Am. Chem. Soc.* **1993**, 115 (14), 6382–6390.

[4] Zhang, L.; Cole, J. M. *ACS Appl. Mater. Interfaces* **2015**, 7 (6), 3427–3455.

[5] Cecconi, B.; Manfredi, N.; Montini, T.; Fornasiero, P.; Abbotto, A. European *J. Org. Chem.* 2016, **2016** (31), 5194–5215.

[6] Wang, J.; Liu, K.; Ma, L.; Zhan, X. *Chem. Rev.* **2016**, 116 (23), 14675–14725.

[7] Stals, P. J. M.; Everts, J. C.; de Bruijn, R.; Filot, I. A. W.; Smulders, M. M. J.; Martín-Rapún, R.; Pidko, E. A.; de Greef, T. F. A.; Palmans, A. R. A.; Meijer, E. W. *Chemistry* **2010**, 16 (3), 810–821.

[8] Adelizzi, B.; Filot, I. A. W.; Palmans, A. R. A.; Meijer, E. W. *Chem. A Eur. J.* **2017**, 23 (25), 6103–6110.

[9] Chen, S.; Xu, J. *Tetrahedron Lett.* **1991**, 32 (46), 6711–6714.

[10] Ghosh, A. K.; Liu, C. *Org. Lett.* **2001**, 3 (4), 635–638.

[11] Hartwig, S.; Nguyen, M. M.; Hecht, S. *Polym. Chem*. **2010**, 1 (1), 69–71.

[12] Van Zee, N. J.; Adelizzi, B.; Mabesoone, M. F. J.; Meng, X.; Aloi, A.; Zha, R. H.; Lutz, M.; Filot, I. A. W.; Palmans, A. R. A.; Meijer, E. W. *Nature* **2018**, 558 (7708).

[13] Ito, S.; Murakami, T. N.; Comte, P.; Liska, P.; Grätzel, C.; Nazeeruddin, M. K.; Grätzel, M. *Thin Solid Films* **2008**, 516 [14), 4613–4619.

[14] Tricoli, A.; Wallerand, A. S.; Righettoni, M. *J. Mater. Chem.* **2012**, 22 (28), 14254–14261.

[15] Chen, D.; Huang, F.; Cheng, Y.-B.; Caruso, *R. A. Adv. Mater.* **2009**, 21 (21), 2206–2210.

[16] Ding, X.; Gao, Y.; Ye, L.; Zhang, L.; Sun, L. *ChemSusChem* **2015**, 8 (23), 3992–3995.

[17] Manfredi, N.; Boldrini, C. L.; Abbotto, A. *ChemElectroChem* **2018**, 5 (17), 2395–2402.

[18] Choi, H.; Baik, C.; Kang, S. O.; Ko, J.; Kang, M. S.; Nazeeruddin, M. K.; Grätzel, M. *Angew. Chem. Int. Ed.* **2008**, 47 (2), 327–330.

[19] Diebold, U. *Surf. Sci. Rep.* **2003**, 48 (5), 53–229.

[20] Zhang, F.; Ma, W.; Jiao, Y.; Wang, J.; Shan, X.; Li, H.; Lu, X.; Meng, S. *ACS Appl. Mater. Interfaces* **2014**, 6 (24), 22359–22369.

[21] Qu, Q.; Geng, H.; Peng, R.; Cui, Q.; Gu, X.; Li, F.; Wang, M. *Langmuir* **2010**, 26 (12), 9539–9546.

[22] Chesalov, Y. A.; Chernobay, G. B.; Andrushkevich, T. V. J. Mol. *Catal. A Chem*. **2013**, 373, 96–107.

[23] Lee, K. E.; Gomez, M. A.; Regier, T.; Hu, Y.; Demopoulos, G. P. *J. Phys. Chem. C* **2011**, 115 (13), 5692–5707.

[24] Schnadt, J.; O'Shea, J. N.; Patthey, L.; Schiessling, J.; Krempaský, J.; Shi, M.; Mårtensson, N.; Brühwiler, P. A. *Surf. Sci.* **2003**, 544 (1), 74–86.

[25] Mtangi, W.; Kiran, V.; Fontanesi, C.; Naaman, R. J. Phys. *Chem. Lett.* **2015**, 6 (24), 4916–4922.

[26] Adelizzi, B., Aloi, A., Van Zee, N. J., Palmans, A.R.A., Meijer, E.W., Voets, I. K. *ACS Nano* **2018**, 12 (5), 4431–4439, .

[27] Stals, P. J. M.; Smulders, M. M. J.; Martín-Rapún, R.; Palmans, A. R. A.; Meijer, E. W. *Chem. A. Eur. J.* **2009**, 15 (9), 2071–2080.

[28] Mahmood, A. *Sol. Energy* **2016**, 123, 127–144.

[29] Manfredi, N.; Cecconi, B.; Abbotto, A. *Eur. J. Org. Chem.* **2014** (32), 7069–7086.

[30] Shang, H.; Luo, Y.; Guo, X.; Huang, X.; Zhan, X.; Jiang, K.; Meng, Q. *Dye. Pigment.* **2010**, 87 (3), 249–256.

[31] Kulkarni, C.; Meijer, E. W.; Palmans, A. R. A. Acc. *Chem. Res.* **2017**, 50 (8), 1928–1936.

[32] Mabesoone, M. F. J.; Markvoort, A. J.; Banno, M.; Yamaguchi, T.; Helmich, F.; Naito, Y.; Yashima, E.; Palmans, A. R. A.; Meijer, E. W. *J. Am. Chem. Soc*. **2018**, 140 (25), 7810–7819.

[33] Downs, R. T.; Bartelmehs, K. L.; Gibbs, G.; Boisen Jr, M. B. *Am. Mineral.* **1993**, 78, 1104–1107.

[34] Miyauchi, M.; Tokudome, H. *Thin Solid Films* **2006**, 515 (4), 2091–2096.

5.

Supramolecular block copolymers under thermodynamic control

The results of this work are summarized in:

B. Adelizzi, A. Aloi, A. J. Markvoort, H. M. M. Ten Eikelder, I. K. Voets, A. R. A. Palmans, E. W. Meijer
J. Am. Chem. Soc. **2018**, 140 (23), 7168-7175

B. Adelizzi‡, A. Aloi‡, N. J. Van Zee, A. R. A. Palmans, E. W. Meijer, I. K. Voets
ACS Nano, **2018**, 12 (5), 4431-4439
‡ The authors equally contributed to the work

Abstract: Supramolecular block copolymers are becoming attractive materials in nascent optoelectronic and catalytic technologies. However, their dynamic nature precludes the straightforward tuning and analysis of the copolymer's microstructure. Here we report the elucidation of the microstructure of triarylamine triamide-based supramolecular block copolymers through a comprehensive battery of spectroscopic, theoretical, and super-resolution microscopic techniques. Via spectroscopic analysis we demonstrate that the direct mixing of pre-assembled homopolymers and the copolymerization induced by slow cooling of monomers lead to the formation of the same copolymer's architecture. The small but pronounced deviation of the experimental spectra from the linear combination of the homopolymers' spectra hints to the formation of block copolymers. A mass balance model is introduced to further unravel the microstructure of the copolymers formed and it confirms that stable multi-block supramolecular copolymers can be accessed from different routes. The multi-block structure of the supramolecular copolymers originates from the fine balance between favorable hydrogen bonding interactions in combination with a small mismatch penalty between two different monomers. Finally, we visualized the formation of the supramolecular block copolymers by adapting a recently developed super resolution microscopy technique, interface point accumulation for imaging in nanoscale topography (iPAINT), for visualizing the architectures formed in organic media. Combining multiple techniques is crucial to unveil the microstructure of these complex dynamic supramolecular systems.

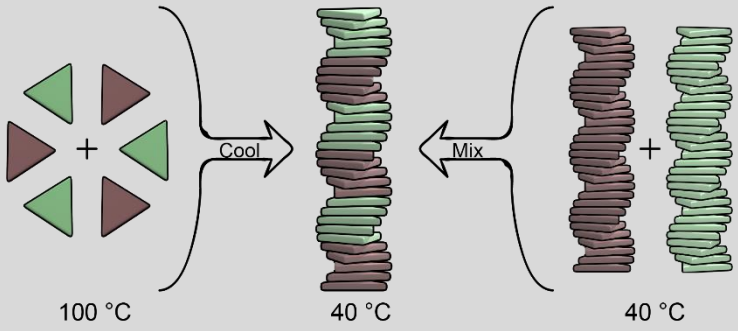

5.1. Introduction

The widespread employment of nanotechnologies has stimulated the development of high-performance, nano-ordered materials.[1-6] Supramolecular polymers are a compelling platform for introducing diverse functionalities and long-range order.[7-10] Their intrinsic self-organizing properties offer the possibility of creating finely tuned dynamic microstructures that are simply not possible with conventional covalent polymers. As mentioned in Chapter 1, this potential has motivated rapid progress in developing fundamental principles for designing one-dimensional supramolecular polymers, such as "sergeant and soldiers" chirality amplification[11] and supramolecular living polymerization.[12-16] Concurrently, theoretical models have been developed to describe supramolecular (co)-polymerization[17-22] and pathway complexity[23-25] of these systems. A crucial step toward competitive functional materials requires control over the sequence of different monomers held together through non-covalent hetero-interactions in a supramolecular copolymer. Such control may represent an easy strategy to achieve *p*-*n* junctions,[26] FRET systems,[27] and bio-sensors.[28] Recently, kinetically controlled supramolecular block copolymers have been reported with different microstructures from Aida[26] Takeuchi[29] and Manners' group.[30,31] However, these systems are obtained with supramolecular polymers which exhibit really slow monomer exchange (or absent in case of Manners' co-micelles) and the control over the block microstructure is achieved via subsequent feeding with different monomers, and are thus kinetically trapped. Hereinbefore, synthesis and characterization of well-defined block structures under thermodynamic control has been elusive.

Based on our previous studies in Chapter 2, we hypothesized that a promising couple for obtaining functional supramolecular block copolymers may be found in triarylamine triamide-based monomers, ***S*-1** and ***S*-2** (Scheme 1)[32]. In the last years, the exploitation of the intrinsic functionality of these aromatic cores in supramolecular polymers led to versatile and switchable semi-conductive supramolecular materials.[33-36] For example, as described in Chapter 3 and Chapter 4, the exploitation of the supramolecular chirality of **poly(*S*-1)** and analogues in water-splitting solar cells resulted in improved performances and depletion of unwanted side-reactions.[37]

The selection of ***S*-1** and ***S*-2** as co-monomers is due the similar molecular geometry and to the analogous behavior upon polymerization which make the two monomers promising candidates for copolymerization. Additionally, we expect that the small conformational difference (Chapter 2, Figure 9)[32] between the supramolecular homopolymers **poly(*S*-1)** and **poly(*S*-2)** will result in a modest mismatch penalty upon copolymerization. Together with a hydrogen bond directionality in the polymer formed, we anticipate that the copolymer **poly[(*S*-1)$_x$-*co*-(*S*-2)$_{(1-x)}$]** can exhibit a multi-block architecture as a result of the balanced H-bonding interactions between preferred homopolymer segments and a limited number of hetero monomer couplings in the polymer.

In this Chapter, we report the non-covalent synthesis of triarylamines triamide-based supramolecular copolymers. Through a combination of spectroscopic, theoretical, and super-resolution microscopic techniques, we unambiguously demonstrate that these copolymers exhibit a thermodynamically stable multi-block architecture.

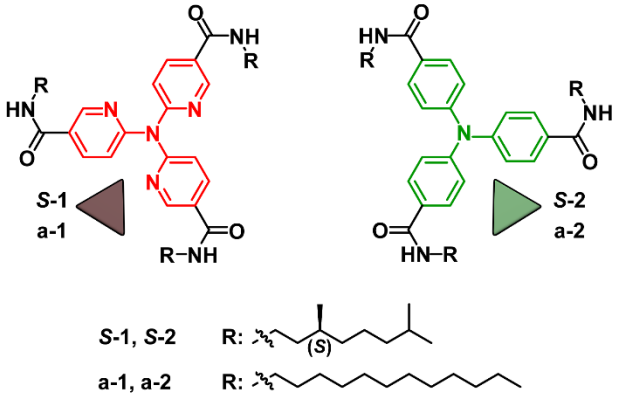

Scheme 1. Chemical structures of tri(pyrid-2-yl)amine triamide (**1**) and triphenylamine triamide (**2**), with chiral (*S*)-3,7-dimethyloctyl chain (***S*-1**, ***S*-2**) and achiral dodecyl chain (**a-1**, **a-2**).

5.2. Results and discussion

5.2.1. Spectroscopic study of the supramolecular copolymers

The supramolecular copolymerization between ***S*-1** and ***S*-2** was first evaluated by recording the spectroscopic variations upon mixing pre-assembled homopolymers, **poly(*S*-2)** to **poly(*S*-1)**. As reported in Chapter 2,[32] both **poly(*S*-1)** and **poly(*S*-2)** form via a cooperative mechanism two assembled states with opposite helicity, **state I** and **state II**, as a function of temperature. Both the homopolymers **poly(*S*-1)** and **poly(*S*-2)** display two states characterized by opposite Cotton effect at λ = 333 nm and λ = 350 nm, respectively) (Chapter 2, Figures 5, 6). Our studies revealed that the transition of **state I** into **state II**, which occurs at $T < 20$ °C, is allowed by the great flexibility of the monomers and caused by the interaction of supramolecular polymers with co-dissolved water in alkanes (Chapter 2, Figure 13).[38] To avoid the complexity that arises from this additional interaction, we performed the copolymerization under thermodynamic control in **state I** above 20 °C in decalin.

First, we added **poly(*S*-2)** to **poly(*S*-1)** at 40 °C in a stepwise manner, leading to **poly[(*S*-1)$_x$-*co*-(*S*-2)$_{(1-x)}$]**, where x and (1-x) are the feed ratios of ***S*-1** and ***S*-2**, respectively (Figure 1a). After each addition, followed by equilibration of the solution (30 min, 40 °C), we recorded UV-vis,[51] CD, and fluorescence spectra (Figures 1b, 1c). The resulting CD spectra display a linear transition from **poly(*S*-1)** to **poly(*S*-2).** The linear combination of the two CD spectra of the homopolymers—calculated assuming no interaction between the two homopolymers—is similar but not identical to the experimental curves. A small but clear deviation at λ = 297 nm (Figure 1d) is observed.

To investigate if the deviation between the experimental and the calculated CD spectra of **poly[(*S*-1)$_{0.5}$-*co*-(*S*-2)$_{0.5}$]** is related to an interaction between the two homopolymers, fluorescence (Figures 1c, 1e) and ^{1}H NMR experiments (Figures 2) were performed. The fluorescence measurements, performed during the stepwise addition of **poly(*S*-2)** to **poly(*S*-1)** in decalin at 40 °C, display a sharp change in the emission band already for **poly[(*S*-1)$_{0.8}$-*co*-(*S*-2)$_{0.2}$]** (Figure 1c, lightest grey curve). In this case, the comparison of the measured emission with the linear combination of the emission of the homopolymers reveals the absence of the shoulder at λ = 360 nm (attributed to **poly(*S*-1)**) and the dominance of **poly(*S*-2)** emission features (Figures 1c, 1e). This indicates the presence of supramolecular interactions between the two homopolymers, which affect the electronic levels involved in the emission.

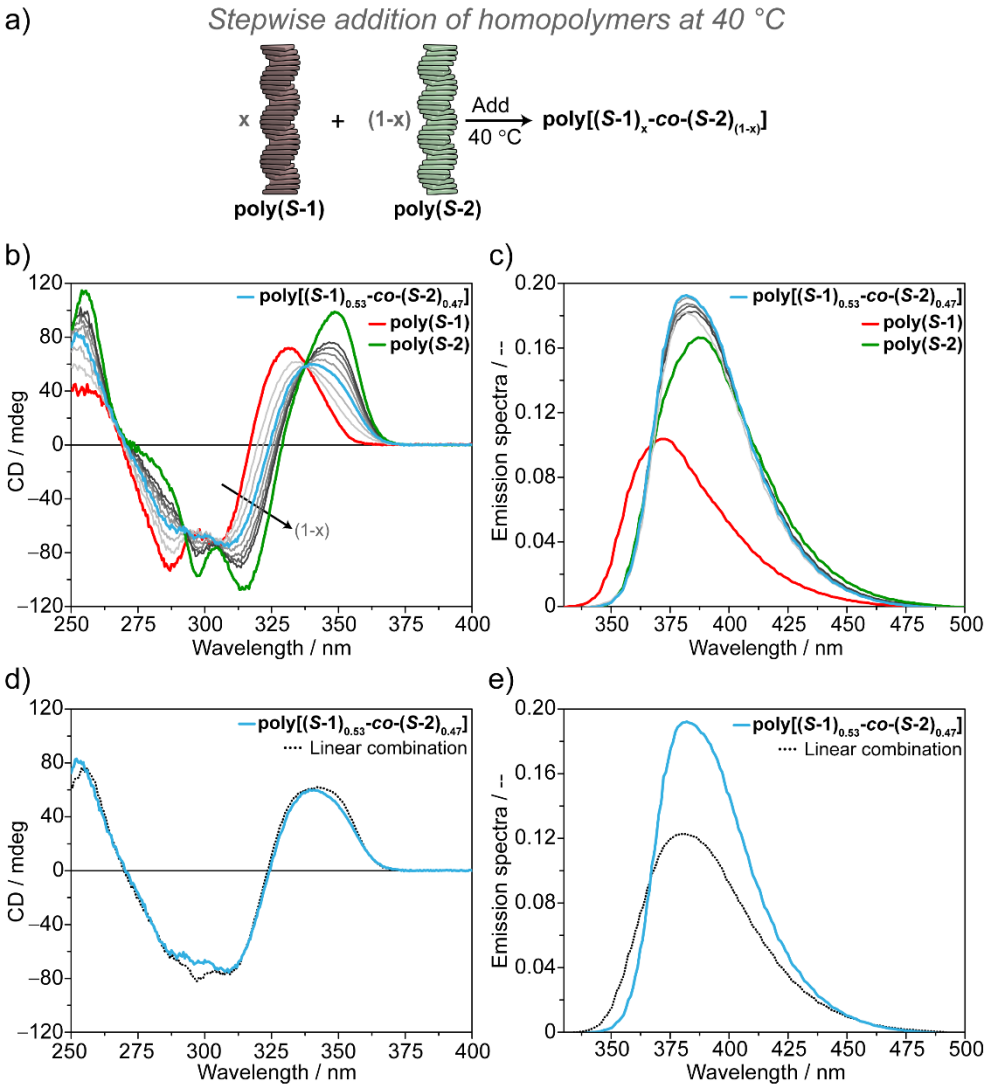

Figure 1. Spectroscopic analysis of the copolymerization achieved via stepwise addition of supramolecular homopolymers. (a) Schematic representation of the experiment performed. (b) CD and (c) emission spectra of **poly[(*S*-1)$_x$-*co*-(*S*-2)$_{(1-x)}$]** obtained by stepwise addition of **poly(*S*-2)** (green lines) to **poly(*S*-1)** (red lines) at 40 °C (decalin, $c_{S\text{-}1} = c_{S\text{-}2}$ = 50 μM). The grey lines represent the different steps performed with different percentage of **poly(*S*-2)** added, from **poly[(*S*-1)$_{0.8}$-*co*-(*S*-2)$_{0.2}$]** (lightest grey) to **poly[(*S*-1)$_{0.24}$-*co*-(*S*-2)$_{0.76}$]** (darkest grey). **Poly[(*S*-1)$_{0.53}$-*co*-(*S*-2)$_{0.47}$]** reported as light blue line. (d,e) Comparison of the experimental results of **poly[(*S*-1)$_{0.53}$-*co*-(*S*-2)$_{0.47}$]** (light blue lines) with the linear combination obtained assuming no interaction as **[0.53 x poly(*S*-1) + 0.47 x poly(*S*-2)]** (black dotted lines) for (d) CD and (e) emission spectra.

^{1}H NMR spectra were recorded in deuterated chloroform ($CDCl_3$). Because H-bond-driven assembly in chloroform is weaker than in alkane solvents, the experiments were performed at −40 °C. The shift of the aromatic and amide peaks in the copolymer, compared to the ones recorded for separate **poly(*S*-1)** and **poly(*S*-2)** (Figures 2a), is indicative for co-aggregation of ***S*-1** and ***S*-2.** In addition, the ^{1}H NOE spectra of the mixed ***S*-1** and ***S*-2** solution, acquired under the same conditions, showed the presence of a non-covalent hetero-interaction, which is revealed by a negative Overhauser effect of both molecules while irradiating at specific signals of one of the two monomers[39] (Figures 2b).

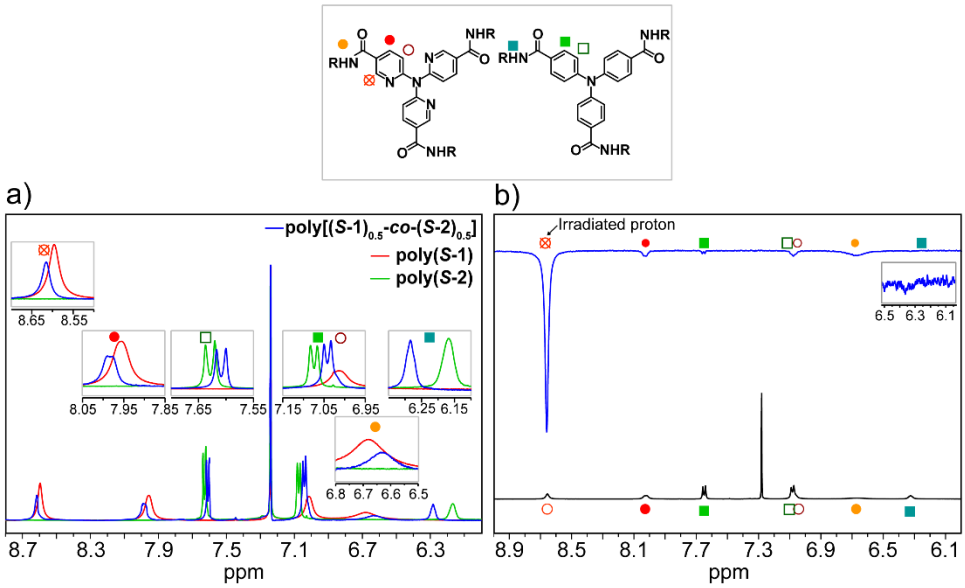

Figure 2. (a) ^{1}H NMR in $CDCl_3$ of **poly(*S*-1)**, **poly(*S*-2)** and **poly[(*S*-1)$_{0.5}$-*co*-(*S*-2)$_{0.5}$]** at -40 °C. (b) NOE spectrum of **poly[(*S*-1)$_{0.5}$-*co*-(*S*-2)$_{0.5}$]**, proton irradiated indicated by blue arrow.

Since the conditions of ^{1}H NMR are not fully comparable with the ones used for the spectroscopic measurements, we further tested the co-interaction between the two monomers performing a "mixed" sergeant and soldier experiment (Figures 3a).[40] This time, we mixed achiral **poly(*a*-2)** to **poly(*S*-1)** in a 1:1 ratio at 40 °C in decalin and recorded the resulting CD spectra. Although the kinetics are slow compared to the ***S*-1**: ***S*-2** couple, the mixed sergeant and soldiers experiment reveals chirality transfer from **poly(*S*-1)** to **poly(a-2)** (Figures 3b, 3c). Since ***S*-1** and **a-2** have different spectroscopic features, the increase of the CD band related to **a-2** is symptomatic for a co-interaction, indicating the presence of both monomers in the same aggregate.

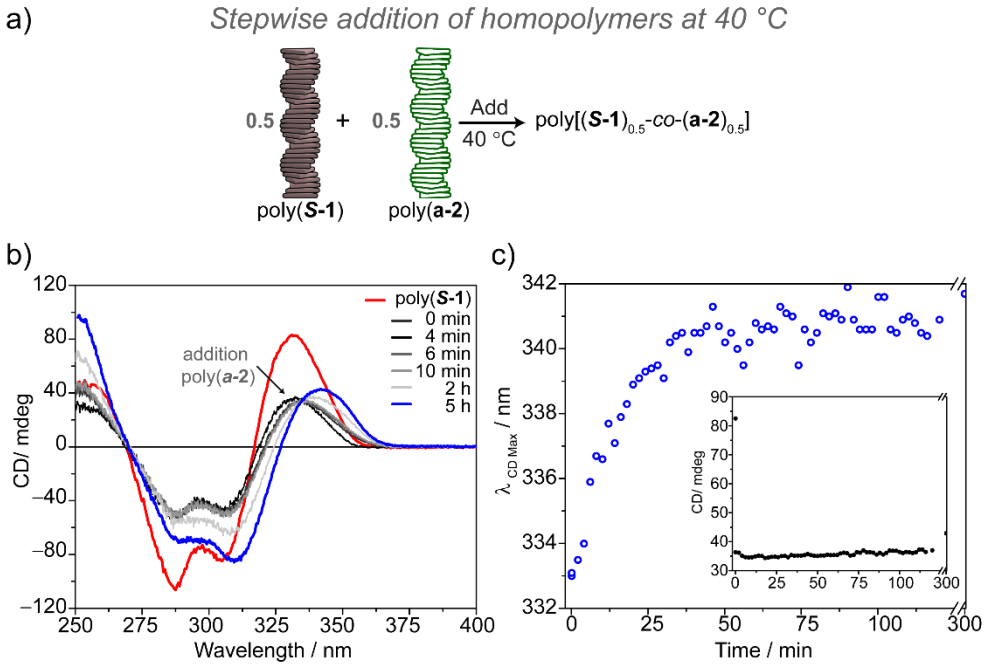

Figure 3. Spectroscopic analysis of the "mixed" sergeant and soldier copolymerization achieved via addition of supramolecular homopolymers. (a) Schematic representation of the experiment performed. (b) Evolution of the CD spectrum of **poly[(*S*-1)$_{0.5}$-*co*-(a-2)$_{0.5}$]** (grey and blue lines) in time obtained by addition of **poly(a-2)** to **poly(*S*-1)** (red line) at 40 °C (decalin, $c_{S\text{-}1} = c_{a\text{-}2}$ = 50 μM). (c) Evolution of the wavelength of maximum CD ($\lambda_{CD\,Max}$) in time after the addition of **poly(a-2)** to **poly(*S*-1)** at 40 °C, inset CD intensity at the maximum wavelength.

From the results above, it becomes clear that a co-interaction occurs upon mixing pre-assembled homopolymers, excluding the possibility of self-sorting.[41] However its effect on the CD spectra is subtle. This means that the interaction does not significantly interfere with the supramolecular structure of the original homopolymers, excluding both the possibility of an alternate as well as a random organization.

To further investigate the mechanism of formation of copolymers, we performed the copolymerization via slow cooling of monomers (Figures 4). ***S*-1** and ***S*-2** were mixed in a 1:1 ratio and monomerically dissolved at 100 °C. Subsequently slow cooling (cooling rate = 15 °C h^{-1}) of the solution induces the supramolecular copolymerization of **poly[(*S*-1)$_{0.50}$-*co*-(*S*-2)$_{0.50}$]** under thermodynamic control (Figure 4a). The variation of the CD value at λ = 341 nm (CD maximum of **poly[(*S*-1)$_{0.50}$-*co*-(*S*-2)$_{0.50}$]** at 40 °C) as a function of temperature permits to elucidate the mechanism of copolymerization (Figure 4b).[42] During cooling and copolymerization, full UV-vis, emission, and CD spectra are registered every 5 degrees (Figure 4c).[51] This allows to have an overview of the thermal effect on the CD spectrum of the copolymer.

The cooling curve recorded discloses the formation of the copolymer displaying a cooperative mechanism and the elongation temperature (T_e) at 85 °C. Interestingly, the T_e of **poly[(*S*-1)$_{0.5}$-*co*-(*S*-2)$_{0.5}$]** (c_{tot} = 50 μM, $c_{S\text{-}1}$ = $c_{S\text{-}2}$ = 25 μM) coincides with the T_e of **poly(*S*-1)** ($c_{S\text{-}1}$ = 25 μM) (Figure 4b, blue line *vs*. red line). This indicates that the nuclei of **poly[(*S*-1)$_{0.5}$-*co*-(*S*-2)$_{0.5}$]** coincide with the nuclei of **poly(*S*-1)**. The presence of one single T_e is a clear indication of the interaction occurring between ***S*-1** and ***S*-2**. Indeed, in case of independent formation of **poly(*S*-1)** and **poly(*S*-2)** (estimated by the linear sum of the individual cooling curves of **poly(*S*-1)** and **poly(*S*-2)** at c = 25 μM), two transitions with different T_e would be present in the cooling curve (Figure 4b, black dotted line). The single T_e and the coincidence of it with the T_e of **poly(*S*-1)** reveals that the copolymer nucleates from ***S*-1** nuclei, and elongates copolymerizing ***S*-1** with ***S*-2** monomers.

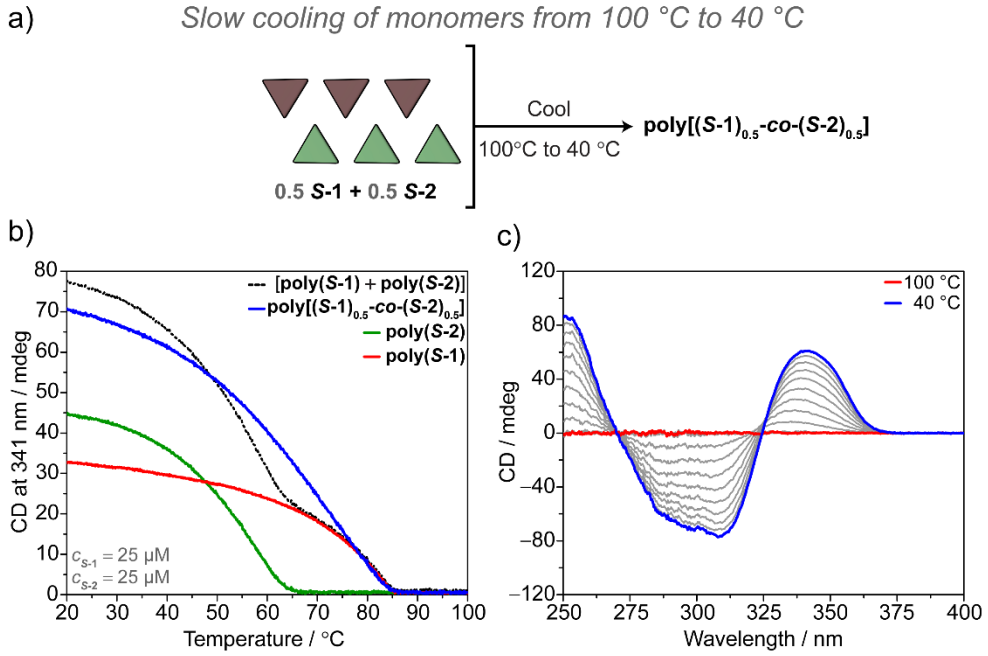

Figure 4. Spectroscopic analysis of the copolymerization achieved via slow cooling monomers. (a) Schematic representation of the experiment performed. (b) CD cooling curves (λ = 341 nm, cooling rate = 15 °C h^{-1}) of **poly[(*S*-1)$_{0.5}$-*co*-(*S*-2)$_{0.5}$]** (decalin, c_{tot} = 50 μM) (blue line), **poly(*S*-1)** (red line), **poly(*S*-2)** (green line) and the linear sum as **[poly(*S*-1) + poly(*S*-2)]** assuming no interaction (decalin, $c_{S\text{-}1}$ = $c_{S\text{-}2}$ = 25 μM) (black dotted line). (c) CD spectra of **poly[(*S*-1)$_{0.5}$-*co*-(*S*-2)$_{0.5}$]** recorded while cooling (cooling rate = 15 °C h^{-1}) and copolymerizing. Spectra acquired every 5 degrees from 100 °C (red line) to 40 °C (blue line).

We performed the same cooling experiment on **poly[(*S*-1)$_{0.5}$-*co*-(*a*-2)$_{0.5}$]** (Figure 5). The cooling curve and the T_e = 85 °C were matching those of **poly[(*S*-1)$_{0.5}$-*co*-(*S*-2)$_{0.5}$]**, further supporting the hypothesis that ***S*-1** oligomers act as nuclei for the copolymerization with ***S*-2** or **a-2**.

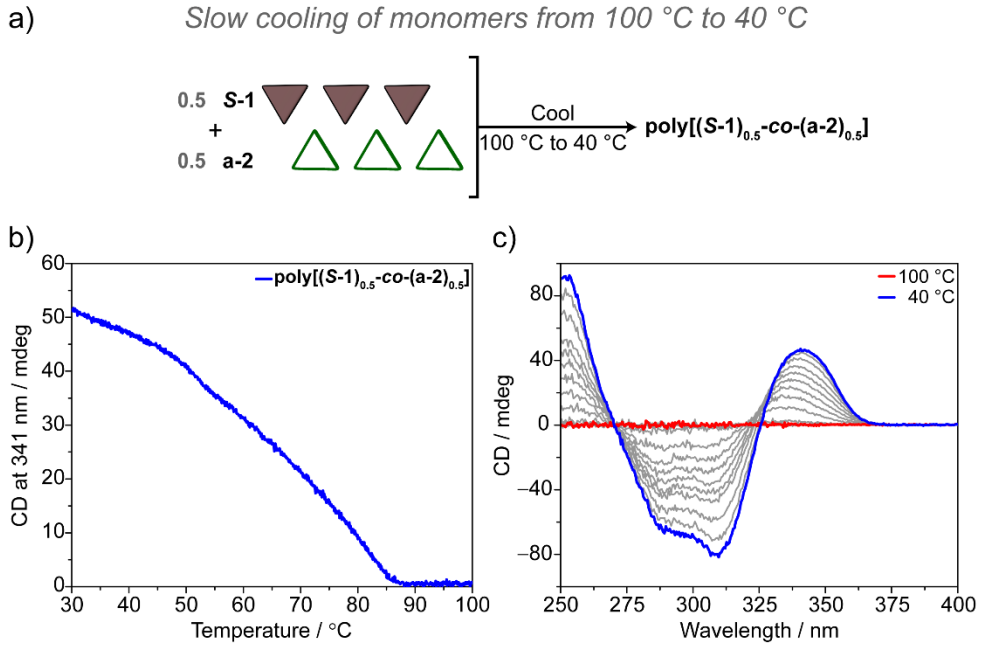

Figure 5. Spectroscopic analysis of the mixed sergeant and soldiers copolymerization achieved via slow cooling monomers. (a) Schematic representation of the experiment performed. (b) CD cooling curves (λ = 341 nm, cooling rate = 15 °C h^{-1}) of **poly[(*S*-1)$_{0.5}$-*co*-(a-2)$_{0.5}$]** (decalin, c_{tot} = 50 μM). (c) CD spectra of **poly[(*S*-1)$_{0.5}$-*co*-(a-2)$_{0.5}$]** recorded while cooling (cooling rate = 15 °C h^{-1}) and copolymerizing. Spectra acquired every 5 °C from 100 °C (red line) to 40 °C (blue line).

To understand whether the copolymerization strategies used play a role in the resulting microstructure, we compared the CD and the emission spectra of **poly[(*S*-1)$_{0.5}$-*co*-(*S*-2)$_{0.5}$]** obtained at 40 °C via the addition of homopolymers with the ones measured under thermodynamic control via slow cooling (Figures 6). Strikingly, both the CD (Figure 6b) and the fluorescence (Figure 6c) spectra perfectly overlap indicating that the same copolymer can be formed via different pathways and is stable over time. The single elongation temperature and the CD spectrum, similar but not identical to the linear combination of the homopolymers, support the hypothesis of the formation of a block-like copolymer structure. This is analogous to covalent block copolymers, where some spectroscopic features of the homopolymers are conserved and linearly combined in the corresponding block copolymer.[43]

According to this hypothesis, we speculate that the small deviation observed at λ = 297 nm (Figure 6b) from the CD spectrum of the linear combination is the result of small conformational changes required for the co-interaction of ***S*-1** with ***S*-2**.

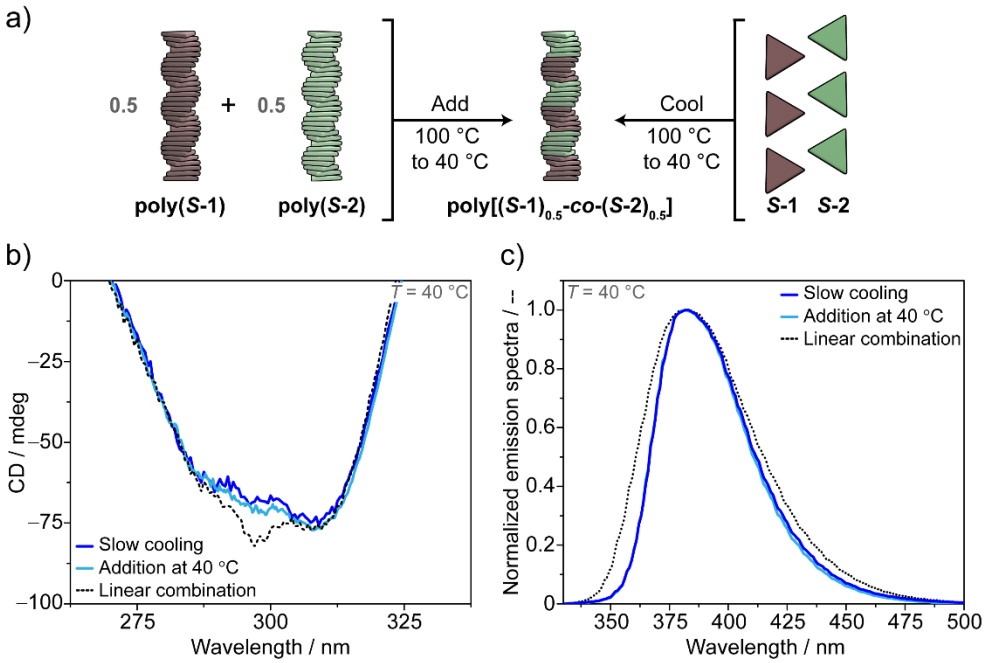

Figure 6. Comparison of the spectroscopic features of the copolymers obtained via the two copolymerization strategies (decalin, 40 °C, c_{tot} = 50 μM). (a) Schematic representation of the proposed copolymerization model, (b) CD diagnostic band and (c) normalized emission spectra. The CD and the emission spectra obtained by addition of homopolymers at 40 °C (light blue lines) coincides with the ones recorded via cooling of monomers (blue lines). The experimental spectra deviate from the linear combination of the homopolymers' spectra (black dotted lines) in the CD band at 297 nm and in the fluorescence band at 360 nm (linear combination spectra obtained assuming no interaction as **[0.5 x poly(*S*-1) + 0.5 x poly(*S*-2)]** with $c_{S\text{-}1} = c_{S\text{-}2}$ = 50 μM).

To get more insight into how the two monomers are incorporated in the copolymers, we simultaneously analyzed the variation of the CD intensities at multiple wavelengths of **poly(*S*-1)**, **poly(*S*-2)** and **poly[(*S*-1)$_{0.5}$-*co*-(*S*-2)$_{0.5}$]** while cooling (Figure 7a). Following the CD intensities at λ = 333 nm and 350 nm (*i.e.* corresponding to the CD maxima of **poly(*S*-1)** and **poly(*S*-2)**, respectively) (Figure 7a top) allows to decompose the CD cooling curve of **poly[(*S*-1)$_{0.5}$-*co*-(*S*-2)$_{0.5}$]** (Figure 7a bottom) intensities into contributions of **poly(*S*-1)** and **poly(*S*-2)** and thus calculate the amounts of ***S*-1** and ***S*-2** in the copolymer chain as a function of temperature (Figure 7b, solid dots). As expected, at higher temperatures the copolymer consists primarily of ***S*-1** units, while at 20 °C the effective ratio of the monomers in **poly[(*S*-1)$_{0.5}$-*co*-(*S*-2)$_{0.5}$]** equilibrates to 0.5:0.5, in line with the feed ratio. Additionally, we observe that the incorporation of ***S*-1** occurs rapidly while ***S*-2** incorporates in a more gradual manner but it starts to copolymerize at higher temperatures (Figure 7b, green dots) compared to its homopolymer **poly(*S*-2)** (Figure 7b, green line). This further provides evidence that the ***S*-1** and ***S*-2** do not polymerize independently of each other.

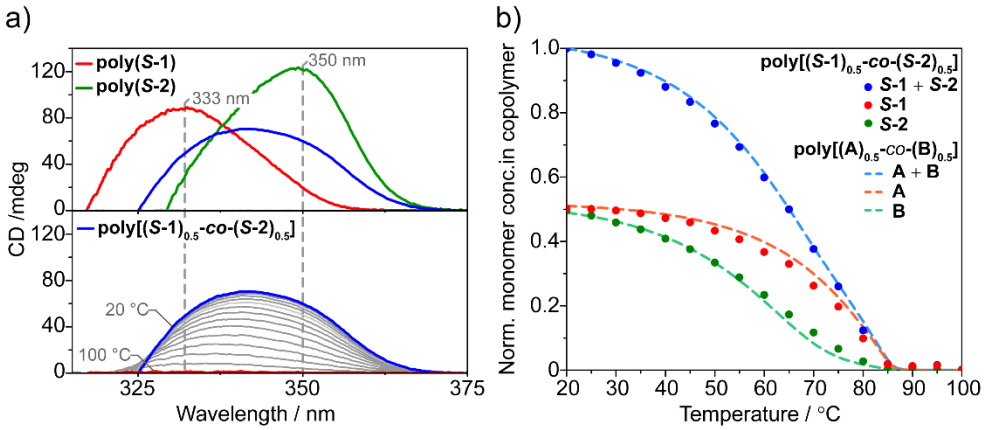

Figure 7. (a, top) CD spectra of **poly(*S*-1)** (red line), **poly(*S*-2)** (green line) and **poly[(*S*-1)$_{0.5}$-*co*-(*S*-2)$_{0.5}$]** (blue line) at 20 °C and (bottom) CD spectra (grey lines) of **poly[(*S*-1)$_{0.5}$-*co*-(*S*-2)$_{0.5}$]** from 100 °C to 20 °C (blue line). Vertical dashed lines for λ = 333 nm and 350 nm (CD maxima of **poly(*S*-1)** and **poly(*S*-2)**, respectively), wavelengths used for the decomposition of the CD spectra of **poly[(*S*-1)$_{0.5}$-*co*-(*S*-2)$_{0.5}$]** upon cooling. (b) Normalized concentration of monomers in the copolymers (computed via CD spectra decomposition) for **poly[(*S*-1)$_{0.5}$-*co*-(*S*-2)$_{0.5}$]** (solid dots) and the simulation for **poly[(A)$_{0.5}$-*co*-(B)$_{0.5}$]** with ΔH_{AB} = −37 kJ mol^{-1} (dashed lines).

5.2.2. Modeling of supramolecular block copolymer formation

Recently Das *et al.*[40] demonstrated that theoretical modeling integrated in the study of spectroscopic data helps understanding the composition in supramolecular copolymers. In collaboration with Markvoort and ten Eikelder, the copolymerization model there reported[40] was expanded to take into account copolymerization of monomers that individually form distinctly cooperative aggregates (the modelling has been developed by Markvoort and ten Eikelder). The main idea of the model is that homo-bonds (*i.e.*, non-covalent bonds between two equal monomers) in the copolymer behave equal to those in their respective homopolymer, and that the copolymerization can thus be fully described by the free energy gain of the formation of a hetero-bonds (*i.e*, non-covalent bond between two different monomers).

Since it was not possible to reliably fit the CD cooling curves of the homopolymers **poly(*S*-1)** and **poly(*S*-2)** over a wide concentration range, we used hypothetical polymers poly(*A*) and poly(*B*) as simulated systems. Thermodynamic parameters, including different cooperativities as nucleation penalties (NP), (ΔH_{AA} = −53 kJ mol^{-1}, NP$_A$ = −40 kJ mol^{-1}, ΔH_{BB} = −50 kJ mol^{-1}, NP$_B$ = −20 kJ mol^{-1}, ΔS = −0.06 kJ mol^{-1}), were then selected to give rise to calculated homopolymerization curves that resemble the experimental curves of **poly(*S*-1)** and **poly(*S*-2)**, respectively (Figure 8a). Next, we generated a series of theoretical copolymerization curves by varying the enthalpic interaction between subsequent A and B units (ΔH_{AB}) in the copolymer (Figures 8b).

For a weak *A*-*B* interaction (ΔH_{AB} = −25 kJ mol^{-1}), the cooling curve resembles the linear combination of cooling curves of the homopolymers (Figure 8b, black line), while for a relatively strong *A*-*B* interaction (ΔH_{AB} = −47 kJ mol^{-1}), the elongation temperature

increases significantly (Figure 8b, orange line). For an intermediate *A*-*B* interaction of ΔH_{AB} = −37 kJ mol^{-1} the cooling curve shows the typical linear dependence (Figure 8b, blue line) that was also observed experimentally (Figure 4b, blue line). For every ΔH_{AB}, it is possible to determine the copolymer composition as a function of temperature, as concentration of polymerized monomers (Figure 8c). Less negative ΔH_{AB} values give independent incorporation of *A* and *B*: *A* polymerizes first and *B* polymerizes at lower temperatures (Figure 8c, left). Highly favorable ΔH_{AB} values result in a *quasi*-coincident incorporation of the two monomers, meaning that *B* copolymerizes at higher temperature compared to its homopolymerization (Figure 8c, right).

Based on selected ΔH_{AB} values, stochastic simulation predicts the length and the microstructure of the related copolymers.[44] Zoomed regions of the microstructures obtained with increasingly favorable ΔH_{AB} values (Figure 8d) display how weak co-interactions give self-sorted polymers, (Figure 8d, left) and strong co-interactions results in alternated microstructures (Figure 8d, right).

In addition, the stochastic simulation allows to investigate the evolution of the fraction of *A*-*B* bonds in time (namely the number of *A*-*B* contacts in the copolymer over the total number of contacts) starting from different scenarios. We simulated the fraction of *A*-*B* bonds during the copolymerization starting either from supramolecular homopolymers (fraction *A*-*B* bond = 0 at *t* = 0.0 s Figure 8e, light blue crosses) or from molecularly-dissolved monomers (fraction *A*-*B* bond = 0.22 at *t* = 0.0 s, Figure 8e, blue crosses). In line with the spectroscopic data (*vide supra*), the stochastic simulations highlight the convergence of the curves starting from two different points to the same value of *A*-*B* bonds. This occurs for all the different copolymerization scenarios in a reasonable amount of time. The fraction of *A*-*B* bonds converges to ≈ 0.002 (Figure 8e, left) for self-sorted systems, to ≈ 0.5 for random systems, and to ≈ 0.75 for systems with an alternate predominance (Figure 8e, right).

Comparing the simulated cases with the experimental cooling curve of **poly[(*S*-1)$_{0.5}$-*co*-(*S*-2)$_{0.5}$]**, it is possible to identify the case corresponding to ΔH_{AB} = −37 kJ mol^{-1} as the simulation which best resembles the experimental curve (Figure 8b, blue curve *vs.* Figure 4b, blue curve). The selected simulated case (ΔH_{AB} = −37 kJ mol^{-1}) shows also similar dependence of monomers composition as a function of temperature (Figure 7b). Based on the stochastic simulation, this case exhibits a multi-block structure (Figures 8d, 8e, second to left), which agrees remarkably well with the hypothesis of the formation of supramolecular multi-block copolymers under thermodynamic equilibrium conditions. This evidence further supports the possibility of achieving stable supramolecular block architectures under thermodynamic control.

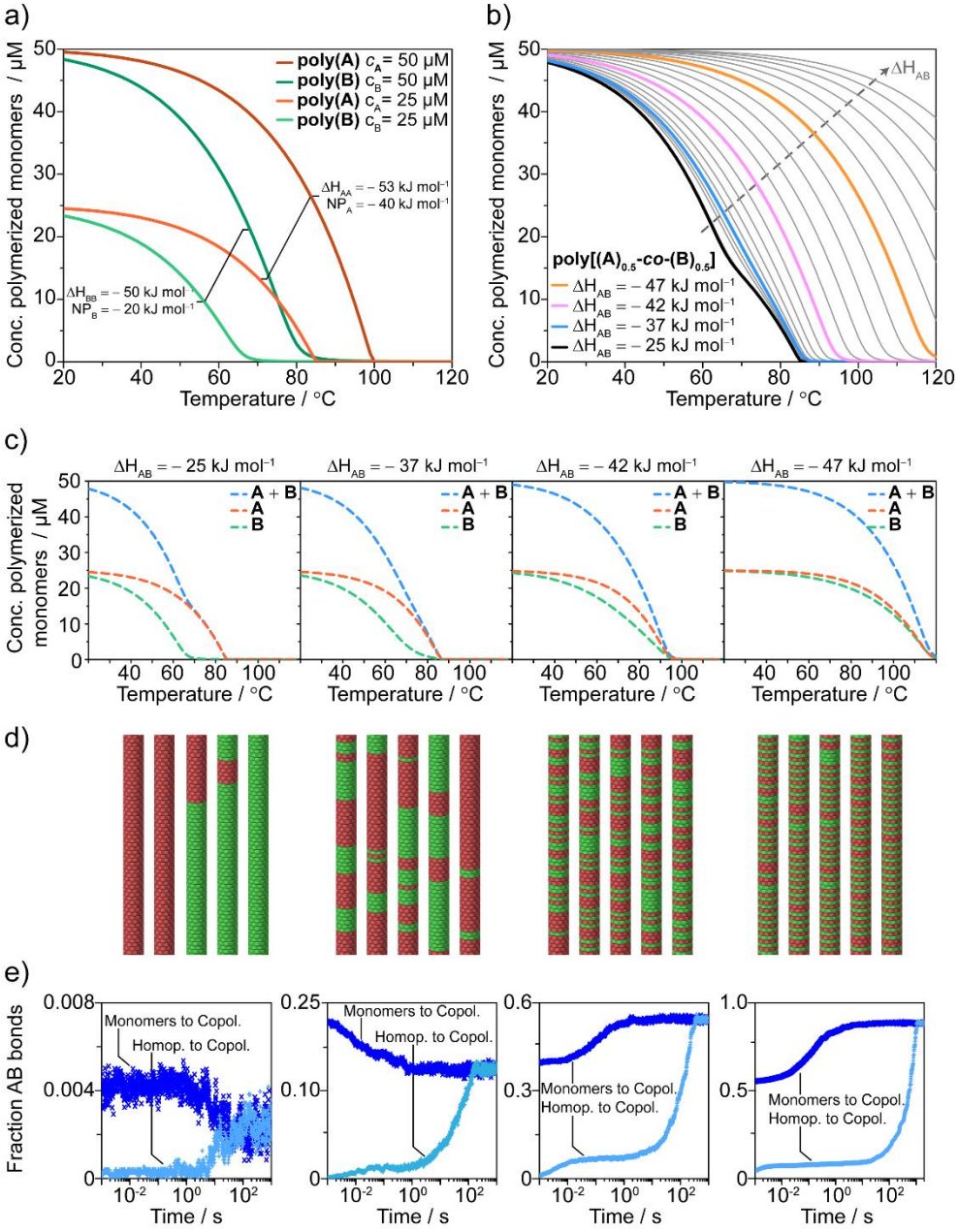

Figure 8. Simulated cooling curves of (a) **poly(A)** (orange lines) and **poly(B)** (green lines) and (b) related copolymers **poly[(A)$_{0.5}$-*co*-(B)$_{0.5}$]** (c_{tot} = 50 µM) while varying ΔH_{AB}. (c) Concentration of polymerized monomers in the copolymer as a function of temperature. (d) Section of the copolymer's microstructure obtained via stochastic simulation from ΔH_{AB} -25 to -47 kJ mol^{-1}. (e) Related evolution in time of the fraction of A-B bonds, from homopolymers (light blue crosses) and from the monomerically dispersed state (blue crosses).Simulation at 50 °C for $c_A = c_B$ = 25 µM.

5.2.3. Visualization of supramolecular block copolymers by iPAINT

Spectroscopic measurements and simulation indicated the presence of multi-block structure. To further support this hypothesis, we employed a recently developed super resolution microscopy technique, interface point accumulation for imaging in nanoscale topography (iPAINT),[45-47] to visualize the copolymer obtained.

iPAINT allows imaging in organic solvent by single molecule localization with a spatial resolution on the order of 20 nm. The technique exploits the spontaneous physisorption of the photoactivated caged-rhodamine dyes to the 1D supramolecular polymers,[45] and does not require the synthesis of *ad-hoc* dye-functionalized monomers. Caged-rhodamine dyes are photoactivated with UV light and require the attack from nucleophiles in solution to form the fluorescent state. For this reason, the measurement in apolar organic solvents (required to have the assembly) are performed in presence of 1% of *iso*-propanol (*i*-PrOH).

Differently from water-based iPAINT[47] (where probes are freely diffusing in solution and the imaging is obtained via a temporary physisorption of the dyes on the interface) the solubility of the dyes in MCH is poor and the physisorption of the dyes on the polymers' interface is more stable. The technique has been tested on diverse H-bonded supramolecular homopolymers and then applied on **poly(*S*-1)-*co*-(*S*-2)**.[46]

The deposition of the probes is non-covalent and non-specific and it has been demonstrated that does not hamper the free exchange of monomers. In addition, the hindered exchange of dyes between the stained interface and the reservoir, as well as the hampered migration of dyes along the fibers, grants the dye–polymer correspondence imposed by pre-staining the supramolecular homopolymers before mixing. This ensures the investigation of the arrangement of the copolymer microstructure with a two-color imaging.

Although the measurements are performed in conditions which render a direct comparison with the spectroscopic data difficult, iPAINT microscopy can provide visual evidence for the blocky character of the copolymer. The supramolecular homopolymers were assembled in MCH and stained individually with photoactivatable caged dyes: Cage-635 for **poly(*S*-1)** giving **poly(*S*-1)$^{C\text{-}635}$**, and Cage-552 for **poly(*S*-2)** giving **poly(*S*-2)$^{C\text{-}552}$**. Successively, the pre-stained homopolymers **poly(*S*-1)$^{C\text{-}635}$** and **poly(*S*-2)$^{C\text{-}552}$** are mixed in a 1:1 ratio at 40 °C (Figure 9a). The low solubility of the dyes in MCH ensures the dye-polymers correspondence imposed by pre-staining (which is fundamental for the experiment) without hampering the intrinsic dynamicity of the supramolecular fibers.[46] The solution is then injected in the sample chamber and the imaging is performed once the fibers are physisorbed on the coverslip. At this point the dynamicity is suppressed and no further exchange occurs.

Remarkably, iPAINT revealed the presence of red and green bi- and tri-block fibers, confirming our hypothesis of formation of supramolecular block copolymers. Differently from what we observed when mixing the same homopolymer oppositely stained (e.g.: **poly(*S*-1)$^{C\text{-}552}$+ poly(*S*-1)$^{C\text{-}635}$**), in which a full reconstruction of the fiber

in the two channels is obtained,[46] the addition of **poly(*S*-2)$^{C\text{-}552}$** to **poly(*S*-1)$^{C\text{-}635}$** confirmed the formation of supramolecular block copolymers **poly[(*S*-1)$^{C\text{-}635}{}_{0.5}$-*co*-(*S*-2)$^{C\text{-}552}{}_{0.5}$]** in alkane solvents (Figure 9b) and the capability to discern between random aggregates and block architectures.[46]

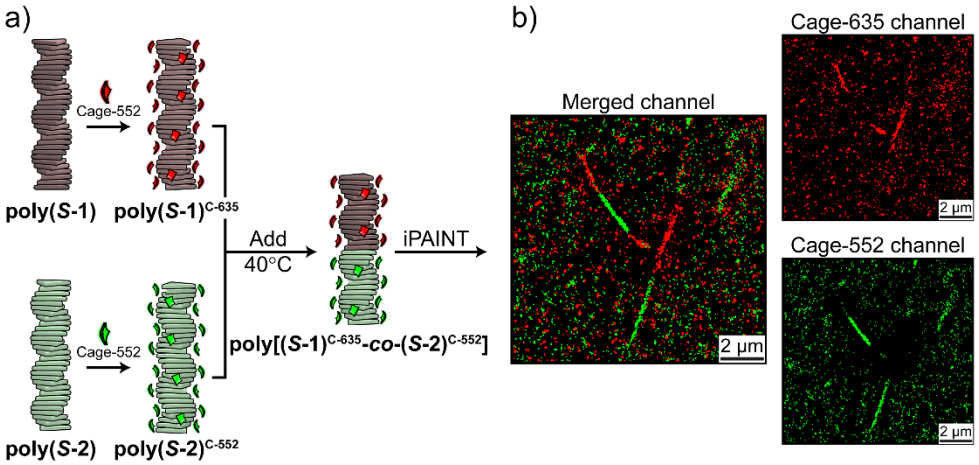

Figure 9. (a) Schematic representation of staining (**poly(*S*-1)** with Cage-635 giving **poly(*S*-1)$^{C\text{-}635}$** and **poly(*S*-2)** with Cage-552 giving **poly(*S*-2)$^{C\text{-}552}$**) and mixing at 40 °C ($c_{S\text{-}1}$ = $c_{S\text{-}2}$ = 200 µM in MCH, 0.5% v/v Cage-dye c = 10 mM in DMSO, 1% *i*-PrOH). (b) iPAINT images of supramolecular copolymers, reconstructed images of merged channels and single Cage-635 and Cage-552 channels.

We noticed that the block-length observed in the iPAINT experiments differs from the one estimated by the model. This discrepancy likely results from the different conditions used between spectroscopic and microscopy experiments. iPAINT is performed in more concentrated conditions and in the presence of 1% of isopropanol (*i*-PrOH), 0.5% of dimethylsulfoxide (DMSO) and the dye. The imaging is then acquired on the fibers physisorbed on a glass coverslip, which is fundamental to achieve well-resolved reconstructed images.[48]

To evaluate the impact of *i*-PrOH and DMSO on the fiber assembly, we performed CD spectroscopy on the supramolecular polymers in the same conditions as used for iPAINT imaging (c = 200 µM in MCH, 0.5% DMSO, 1% *i*-PrOH v/v) (Figure 10). For **poly(*S*-1)** and **poly(*S*-2)** the shape of the CD spectrum (Figures 10a, 10b) was unaltered, although the CD intensity was reduced. This indicates a partial denaturation of the assemblies upon addition of the polar solvents.[42,49]

The stepwise addition of **poly(*S*-2)** to **poly(*S*-1)** in iPAINT conditions performed at 40 °C was also evaluated by CD spectroscopy and **poly[(*S*-1)$_{0.5}$-*co*-(*S*-2)$_{0.5}$]** displayed the same CD features as those obtained in pure MCH (Figure 10b). It is worth to notice that the presence of *i*-PrOH seems to affect the copolymer more than the homopolymers. The spectrum recorded in absence of polar solvents displays a CD maximum at the same wavelength (λ = 341 nm) at intensity of the crossing point of the

homopolymers' CD curves as expected (Figure 10a). Conversely, the copolymer's CD spectrum recorded in presence of DMSO and *i*-PrOH is partially decreased in intensity (Figure 10b). This indicates that the denaturing effect of *i*-PrOH/DMSO is enhanced in the copolymer when compared to the relative homopolymers. This result is consistent with the data obtained with the mass balance model, where the enthalpic gain of hetero-interactions ($\Delta H_{\mathbf{AB}}$) is less favorable than the homo-interactions (ΔH_{AA} and ΔH_{BB}) (Figure 8).

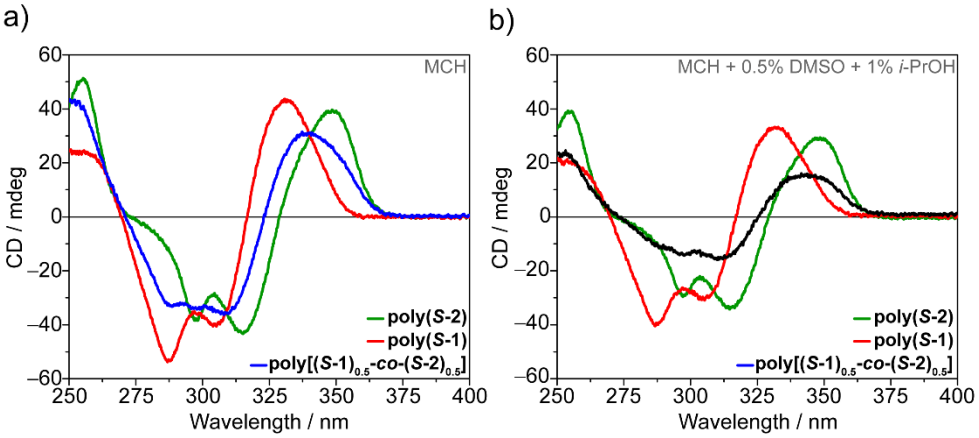

Figure 10. CD spectra in (a) MCH and (b) MCH + 0.5 % DMSO, 1% *i*-PrOH of **poly(*S*-1)** (red line), **poly(*S*-2)** (green line) and **poly[(*S*-1)$_{0.5}$-*co*-(*S*-2)$_{0.5}$]** (blue and black lines, respectively) (40 °C, *c* = 200 μM).

This means that the *A*-*B* contacts are easier to break than *A*-*A* or *B*-*B* and more affected by *i*-PrOH and DMSO. Based on this, we speculate that the addition of 0.5% DMSO of and 1% *i*-PrOH (v/v) partially favors the homo-interactions making bi- or tri- blocks copolymers more stable than multi-block copolymers. Despite the differences induced by the denaturing effect, the system is still stable enough to copolymerize, demonstrating once more the reproducible tendency of the system to form block copolymers under different conditions.

5.2.4. Kinetic spectroscopic and iPAINT studies

Finally, we explored the kinetics involved in the formation of **poly[(*S*-1)$_{0.5}$-*co*-(*S*-2)$_{0.5}$]** by adding **poly(*S*-2)** to **poly(*S*-1)** at 20 °C (Figure 11a). The addition at this temperature resulted in a CD spectrum perfectly superimposable with the linear combination of the homopolymers, also in the diagnostic band (Figure 11b, left). Subsequent heating to 40 °C led to a transition visible in the CD diagnostic band as a flattening (Figure 11b, right) and in the heating curve as an additional transition at ≈ 27 °C (Figure 11c). Subsequently, in the emission spectra a loss of the shoulder at λ = 360 nm and an increase in emission intensity was observed (data not shown).[51]

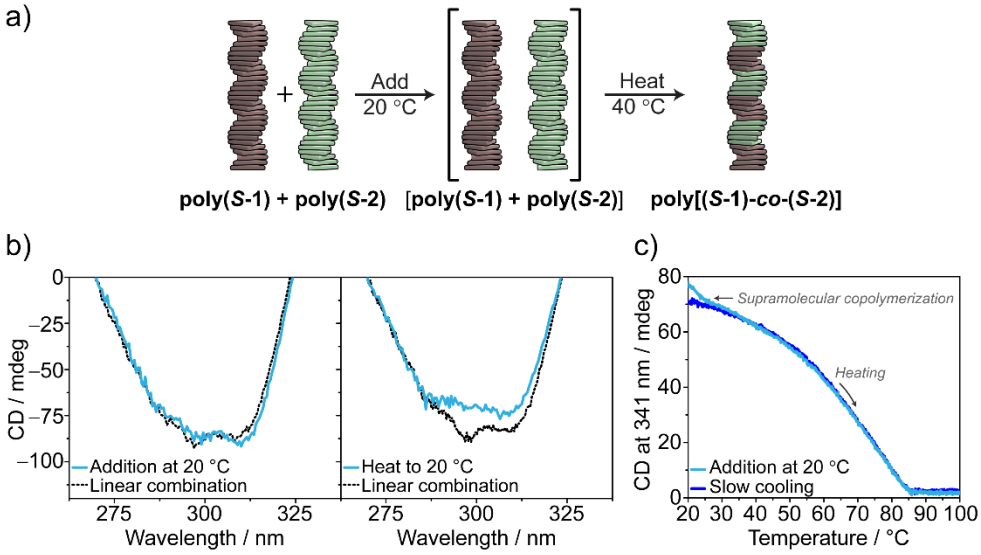

Figure 11. (a) Addition at 20 °C, kinetic trap of self-sorted homopolymers and consequent evolution to **poly[(*S*-1)$_{0.5}$-*co*-(*S*-2)$_{0.5}$]** by heating. (b) CD diagnostic band of (left) self-sorted trapped state at 20 °C and evolution to **poly[(*S*-1)$_{0.5}$-*co*-(*S*-2)$_{0.5}$]** (right) at 40 °C (decalin c_{tot} = 50 μM). Comparison of the experimental results (light blue lines) with the linear combination spectra (black dotted lines) (c) CD heating curves followed at λ= 341 nm for the originally self-sorted solution **[0.5 × poly(*S*-1) + 0.5 × poly(*S*-2)]** (light blue curve) and for the supramolecular copolymer **poly[(*S*-1)$_{0.5}$-*co*-(*S*-2)$_{0.5}$]** (blue curve).

The CD spectrum recorded at 40 °C perfectly overlaps with the one recorded via slow cooling of monomers. We attribute this to the possibility to kinetically trap the "self-sorted" homopolymers by mixing at 20 °C. Subsequently, giving thermal energy to the system, or equilibrating, the metastable mixed state [0.5 × **poly(*S*-1)** + 0.5 × **poly(*S*-2)**] transforms into **poly[(*S*-1)$_{0.5}$-*co*-(*S*-2)$_{0.5}$]** block copolymers. To confirm this hypothesis, we imaged with iPAINT the evolution of the mixture prepared at 20 °C at different time-lapses. By mixing the stained supramolecular homopolymer at 20 °C (Figure 12a) and directly imaging them, we verified the self-sorting at low temperatures (Figure 12b). By repeating the imaging on the mixed solution equilibrated for one hour at 20 °C, we confirmed the occurred copolymerization (Figure 12c).

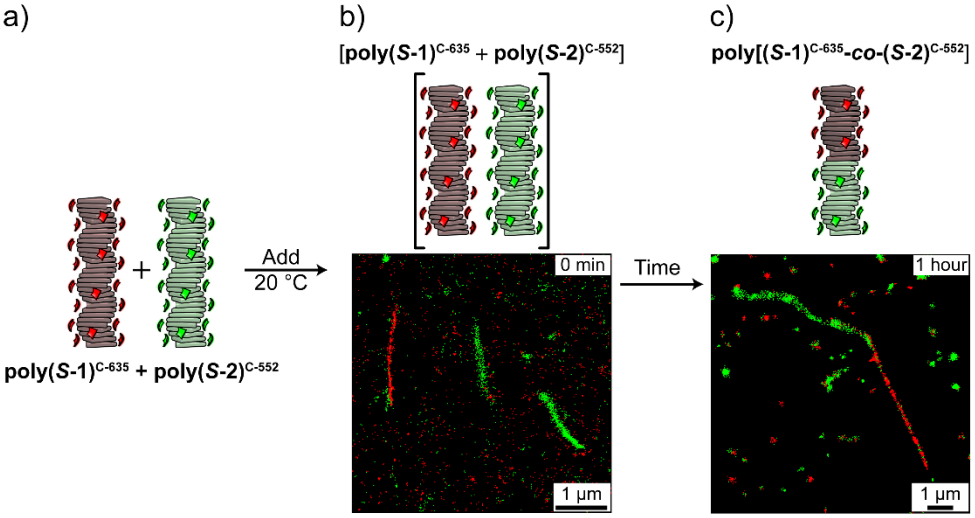

Figure 12. (a, b) Addition at 20 °C, kinetic trap of self-sorted homopolymers and consequent evolution to (c) **poly[(*S*-1)$^{C\text{-}635}{}_{0.5}$-*co*-(*S*-2)$^{C\text{-}552}{}_{0.5}$]** by equilibration at 20 °C. iPAINT image at (b) t = 0 min and (c) 1 hour after the addition. ($c_{S\text{-}1}$ = $c_{S\text{-}2}$ = 200 µM in MCH, 0.5% v/v Cage-dye c = 10 mM in DMSO, 1% v/v *i*-PrOH).

5.3. Conclusions

Taken all together, the results presented clearly indicate the formation of supramolecular block copolymers under thermodynamic equilibrium conditions. The strategy applied here is generally applicable to create supramolecular block copolymers. This approach takes advantage of the balance between the mismatch penalty that hampers the complete mixing and the enthalpic cost of the chain-ends that drives to co-interactions. In a similar way that propagation of errors in olefin polymerization occurs,[50] blocky structures can be formed.

Based on the above, we can list (some of) the requirements needed for monomer' couples to obtain multi-block supramolecular copolymers. Besides the symmetry prerequisite needed to achieve successful interactions among the different monomers, such as H-bonding, the couple of monomers has to display a similar cooperative homopolymerization and a moderately small enthalpic gain. This last factor, unique for every couple, is a combination of multiple energies involved. For example, the mismatch penalties paid for the conformational change required to interact with the other type of monomers as well as positive contributions (*e.g.*, H-bonding formation, donor-acceptor interactions). The enthalpic gain defines the formation of a certain microstructure (from alternate to self-sorted). The more negative the value, the more favorable the interaction, which drives to random or alternated structure. Oppositely, multi-blocks and block copolymers are formed when ΔH_{AB} is much less negative than the enthalpy for the relative homopolymers ($|\Delta H_{AB}| << |\Delta H_{AA}|$ and $|\Delta H_{AB}| << |\Delta H_{BB}|$). Moreover, since the cooperativity plays a fundamental role in the homopolymers and copolymers growth, the difference between the two cooperativities will define the length of the respective blocks.

The application of this strategy allows the formation of stable non-covalent block copolymers. The use of co-assembling monomers with diverse optoelectronic properties would lead to new, unexpected functionalities in the field of supramolecular electronics.

5.4. Experimental section

5.4.1. Methods

All solvents were obtained from Biosolve, Acros or Aldrich and used as received. 6,6',6"-Nitrilotris(*N*-(3,7-dimethyloctyl)nicotinamide) (***S*-1**), 6,6',6"-Nitrilotris(*N*-dodecylnicotinamide) (**a-1**), 4,4',4"-nitilotris(*N*-dodecylbenzamide) (**a-2**) and 4,4',4"-nitrilotris(*N*-((*S*)-3,7-dimethyloctyl)benzamide) (***S*-2**) were synthesized as reported in Chapter 2[32] and vacuum-oven dried before use. Cage-dyes were obtained from Abberior®[52] and used as received.

^{1}H-NMR measurements were conducted on a 500 MHz Bruker five-channel liquid-state spectrometer equipped with a high sensitivity QXI cryoprobe with cooled proton channel. Proton chemical shifts are reported in ppm downfield from tetramethylsilane (TMS).

UV/Vis and circular dichroism (CD) measurements were performed on a Jasco J-815 spectropolarimeter, for which the sensitivity, time constants and scan rates were chosen appropriately. Corresponding temperature-dependent measurements were performed with a Jasco PFD-425S/15 Peltier- type temperature controller with a temperature range of 263–393 K and adjustable temperature slope. In all experiments the linear dichroism was also measured and in all cases no linear dichroism was observed. Fluorescence spectra were measured with Jasco FMO-427S/15 fluorimeter implemented in the CD spectrometer. For spectroscopic measurements spectroscopic grade solvents were employed and different cells were employed. For CD, UV/Vis and fluorescence measurements a sealable quartz cuvette with optic path of 1 cm × 1 cm was used. Fluorescence was tested also with a fluorescence cuvette with 1 cm x 1 mm path, the results obtained with the two cuvettes are comparable. Solutions (50 μM) were prepared by weighing the necessary amount of compound for the given concentration and dissolved with a weighted amount of solvent based on its density. The stock solutions were heated up, sonicated till complete dissolution and slowly cooled down to room temperature every time before use unless otherwise specified. All the spectroscopic and microscopy measurement were performed with freshly prepared solutions (max. 1 week after the preparation of the stock solution).

iPAINT images were acquired using a Nikon N-STORM system equipped with ~158.3 mW cm^{-2} (λ = 405 nm), ~488 mW/cm^2 (λ = 561 nm) and ~1335 mW cm^{-2} (λ = 647 nm) laser lines configured for total internal reflection fluorescence (TIRF) imaging. The angle at which the inclined excitation was performed was finely tuned to maximize the signal-to-noise ratio. The fluorescence emission was collected by means of an oil immersion objective (Nikon 100x, 1.4NA) A quad-band pass dichroic filter (97335 Nikon) was used to separate the excitation light from the fluorescence emission. Time lapses of 15 × 10^3 frames were recorded onto a 256 × 256 pixel region (pixel size 170 nm) of an EMCCD camera (ixon3, Andor) at a rate of 47 f s^{-1}. Two different photo-activated dyes were used to perform two-color iPAINT measurements: Cage-552 and Cage-635 (Abberior®). These caged rhodamines reside in a dark, non-fluorescent state; upon UV irradiation (λ = 405 nm) the photolysis of the photo-activated moiety is carried out, leading to an open-fluorescent form through the Wolff rearrangement.[52] Upon excitation with the proper wavelength (λ = 561 nm for Cage-552, λ = 647 nm for Cage-635), the fluorescence of the dyes was collected. To perform single-molecule experiments, a low UV laser light power (< 1% power) was used. In this way a small amount of dyes per frame is uncaged, ensuring statistically a spatial separation greater than the diffraction limit of light $\left(\frac{\lambda}{2NA} \sim 200\ nm\right)$. Subsequently, the sample was irradiated with a 100 % power laser at the proper wavelength to achieve both excitation and bleaching of the single molecules previously photo-activated. In such a way the excited and bleached molecules are no longer contributing to the reconstruction of the super-resolved image. The iPAINT image was analyzed with NIS-element Nikon software. The sample chamber used to perform iPAINT imaging was made from a cover slide and a coverslip held together by double-side tape, creating a chamber volume of ~30 μL. Prior assembly of the sample chamber, the coverslip was cleaned by piranha etching, followed by rinsing and sonication in acetone, isopropanol, MQ-water (18.2 MΩ) and finally blown-dry with nitrogen. To perform super-resolution imaging in organic solvents, a protocol based on adding a small amount of an alcohol to the sample solution was followed, to achieve the uncaging of the caged dyes.[44] Hence, iPAINT polymers (c = 200 μM) was carried out in methylcyclohexane (MCH), adding 1% v/v of isopropanol (*i*-PrOH) to the solution, and 0.5% v/v of the cage-dyes (c = 10 mM in DMSO). Further insight on the techniques are published elsewhere.[46]

5.4.2. Sample preparation

The supramolecular copolymerizations were performed with tri(pyrid-2-yl)amine tricarboxyamide (**1**) and triphenylamine tri-*p*-carboxamide (**2**). In detail: 6,6',6"-nitrilotris(*N*-((*S*)3,7-dimethyloctyl)nicotinamide) (***S*-1**), 6,6',6"-nitrilotris(*N*-dodecylnicotinamide) (**a-1**), 4,4',4"-nitilotris(*N*-dodecylbenzamide) (**a-2**) and 4,4',4"-nitrilotris(*N*-((*S*)-3,7-dimethyloctyl)benzamide) (***S*-2**).[32]

The techniques used to supramolecularly copolymerize **1** and **2** were developed taking inspiration from classical copolymerization techniques as stepwise addition and random polymerization. The two techniques used in this work are: "addition of self-assembled homopolymers" and "slow cooling of monomers".

We investigated the supramolecular copolymerization of the following couples of monomers, ***S*-2:a-1** (**poly[(*S*-2)$_x$-*co*-(a-1)$_{(1-x)}$]**), ***S*-1:a-2** (**poly[(S-1)$_x$-*co*-(a-2)$_{(1-x)}$]**), and ***S*-1:*S*-2** (**poly[(*S*-1)$_x$-*co*-(*S*-2)$_{(1-x)}$]**), where x and (1-x) are the respective feed ratios.

Copolymerization in state I, under thermodynamic control

As reported in Chapter 2, both the homopolymers are subject to pathway complexity. In MCH both **poly(*S*-1)** and **poly(*S*-2)** show two different assembled states with opposite handedness.[32] **State I**, with positive CD signal, is formed at high temperatures from a molecularly dissolved solution via a nucleation-elongation mechanism. **State II**, is formed below room temperature through a sharp transition from the first assembled **state I**. We reported that, applying a slow cooling-heating cycle on the systems, the CD curves display hysteresis in the temperature window below room temperature. Besides, out of the hysteresis region, the CD reports the same value while heating and cooling, meaning that above room temperature the system is under thermodynamic equilibrium in the state previously identified as **state I**.[38]

In the previous work the necessity of analyzing the polymerization of ***S*-1** in decalin isomer mixture for increasing the solubility was addressed. **Poly(*S*-1)** shows the same assembling path in decalin and MCH: in ambient condition in decalin the transition **state I** to **state II** occurs at 0 °C.[32] For this reason, we chose to perform the supramolecular copolymerization in decalin isomer mixture and for completeness we investigated the assembling behavior of ***S*-2** in decalin isomers mixture. We confirmed the analogous behavior observed in MCH[51]. Thus, in order to perform all the copolymerization under thermodynamic control in **state I**, all the measurements were performed at temperatures higher that 20 °C. The solutions were prepared in ambient conditions and stored in sealable vials or cuvettes.

Stepwise addition of self-assembled homopolymers

Poly(*S*-1) and **poly(*S*-2)** were assembled in decalin isomer mixture (c = 50 μM) from the monomerically dissolved state (100 °C) via slow cooling (cooling rate = 15 °C h^{-1}). **Poly(*S*-1)**, was placed in a cuvette and **poly(*S*-2)** was stepwisely added at a fixed temperature of 40 °C. The system was equilibrated for 5-10 minutes after every addition in order to stabilize the signal. Spectra were recorded after the equilibration time. Based on the stage of the stepwise addition, the ratio between ***S*-1** and ***S*-2** is expressed as **poly[(*S*-1)$_x$-*co*-(*S*-2)$_{(1-x)}$]** while the total concentration of the mixed solution is kept at 50 μM.

The same procedure was performed at 20 °C to kinetically trap the self-sorted state. The self-sorted solution eventually evolves into the supramolecular copolymer via equilibration or heating.

Slow cooling of monomerically dissolved state

The supramolecular copolymerization via slow cooling was performed in decalin isomers mixture combining monomers ***S*-1** and ***S*-2** in a 1:1 ratio to obtain **poly[(*S*-1)$_{0.5}$-*co*-(*S*-2)$_{0.5}$]**. Slow cooling of monomers was performed at c_{tot} = 50 μM, meaning a concentration per each monomer of 25 μM. The solution was heated to 100 °C to reach the molecularly dissolved state and slowly cooled down (cooling rate of 15 °C h^{-1}) leading to the formation of the copolymer under thermodynamic control.

Mixed sergeant and soldiers experiment

Mixed sergeant and soldiers experiments were performed to investigate the possibility of interaction between different supramolecular monomers or polymers and were measured for the couples ***S*-1:a-2**, **poly[(*S*-1)$_x$-*co*-(a-2)$_{(1-x)}$]**, and ***S*-2:a-1**, **poly[(*S*-2)$_x$-*co*-(a-1)$_{(1-x)}$]**.
Mixed sergeant and soldiers experiments were performed via "stepwise addition at 40 °C" and "slow cooling of monomers" and prepared as described before for ***S*-2:*S*-1** couple.
The achiral molecules show **state I** to **state II** transition at higher temperatures compared to the chiral analogues. Therefore, all the measurements were performed at T > 30 °C, preventing in this way, the transition to **state II**.

5.4.3. iPAINT solution

The solutions for iPAINT were prepared in MCH since previous work showed the possibility to do super resolution imaging in MCH.[45] As previously reported in Chapter 2,[32] the self-assembling properties of triarylamines in MCH and in decalin are comparable. **Poly(*S*-1)** and **poly(*S*-2)** were polymerized individually under thermodynamic control (cooling rate 15 °C h^{-1}) in MCH (c = 200 μM). Then, at 20 °C **poly(*S*-1)** was stained with 0.5% v/v of Cage-635 (c = 10 mM in DMSO) and 1% of *i*-PrOH. **Poly(*S*-2)** was stained with 0.5% v/v Cage-552 (c = 10 mM in DMSO) and 1% of *i*-PrOH. Both solutions were vortexed and brought to the temperature required for the mixing.

Addition at 40 °C:

The stained solutions of **poly(*S*-1)** and **poly(*S*-2)** were brought to 40 °C in a water bath, equilibrated for 5 minutes, then mixed in a 1:1 ratio. The mixed solution was injected in the sample chamber and consequently imaged.

Addition at 20 °C:

Stained **poly(*S*-1)** and **poly(*S*-2)** were mixed in a 1:1 ratio at 20 °C, one aliquot was injected in the sample chamber to be imaged directly after the mixing. Another aliquot was kept at 20 °C and then imaged one hour after the mixing.

5.4.4. Decomposition of the variable temperature copolymer CD spectra

The homopolymers **poly(*S*-1)** and **poly(*S*-2)** do not present shift in the wavelength of CD spectra during the polymerization: the maximum of the CD stays constant during the polymerization process. Besides, the copolymer CD spectra (and the related wavelengths where the CD maximum falls) are temperature dependent. This effect is due to the change in the effective composition of the copolymer while cooling the system. In order to estimate the effective composition of **poly[(*S*-1)$_{0.5}$-*co*-(*S*-2)$_{0.5}$]** while cooling and polymerizing, we analyzed the changes in the CD spectrum as a function of temperature.
From the variable temperature CD spectra of **poly(*S*-1)**, **poly(*S*-2)** and **poly[(*S*-1)$_{0.5}$-*co*-(*S*-2)$_{0.5}$]**, we extracted the values of CD at three wavelengths (λ = 333 nm, 338 nm, and 350 nm). λ = 350 nm is **poly(*S*-2)** CD maximum, λ = 333 nm is **poly(*S*-1)** CD maximum, and λ = 338 nm corresponds to the wavelength where the intensities of **poly(*S*-1)** and **poly(*S*-2)** are similar. The cooling curves obtained were normalized such that the area under the curves for all three wavelengths is the same, and the CD signal at λ = 338 nm at the lowest temperature equals 1.

In standard one-component system (assuming the formation of a single supramolecular species in solution) the CD spectrum of the supramolecular polymer should vary just in intensity while cooling and polymerizing. Thus, their normalized cooling curves followed at multiple wavelengths should overlaps. As expected, the normalized cooling curves for the three wavelengths reasonably overlap both for **poly(*S*-1)** and **poly(*S*-2)**. Nevertheless, for **poly[(*S*-1)$_{0.5}$-*co*-(*S*-2)$_{0.5}$]** this does not happen; between 85 °C and 50 °C the CD at λ = 333 nm is more intense, while below 50 °C the CD at λ = 350 nm is more intense. This effect can be attributed to the composition (ratio ***S*-1** to ***S*-2**) of the copolymer that is temperature dependent.
We then used the non-normalized cooling curves at the two wavelengths where the CD intensities of **poly(*S*-1)** and **poly(*S*-2)** are maximal, i.e., λ = 333 nm and 350 nm respectively, to analyze this temperature dependence of the copolymer composition based on the assumption that the measured CD signal of **poly[(*S*-1)$_{0.5}$-*co*-(*S*-2)$_{0.5}$]** is the linear combination of the signals of the two monomer types:

$$CD^{\lambda}_{\mathrm{poly}[(\boldsymbol{S}\text{-}\mathbf{1})-co-(\boldsymbol{S}\text{-}\mathbf{2})]} = \alpha CD^{\lambda}_{\mathrm{poly}(\boldsymbol{S}\text{-}\mathbf{2})} + \beta CD^{\lambda}_{\mathrm{poly}(\boldsymbol{S}\text{-}\mathbf{1})} \quad \text{(S5.1)}$$

$CD^{\lambda}_{\mathrm{poly}[(\boldsymbol{S}\text{-}\mathbf{1})-co-(\boldsymbol{S}\text{-}\mathbf{2})]}$ is the CD signal of **poly[(*S*-1)$_{0.5}$-*co*-(*S*-2)$_{0.5}$]** at a certain temperature T and wavelength λ. This coincides with the amount (in μM) of polymerized ***S*-2** (α) at that temperature multiplied by the CD signal of **poly(*S*-2)** (per μM) at that wavelength ($CD^{\lambda}_{\mathrm{poly}(\boldsymbol{S}\text{-}\mathbf{2})}$) plus the amount (in μM) of polymerized ***S*-1** (β) at the same temperature multiplied by the CD signal of **poly(*S*-1)** (per μM) at that wavelength ($CD^{\lambda}_{\mathrm{poly}(\boldsymbol{S}\text{-}\mathbf{1})}$). Note that α and β may depend on the temperature, but are independent of λ. The CD signals per polymerized ***S*-1** and ***S*-2** ($CD^{\lambda}_{poly(\boldsymbol{S}\text{-}\mathbf{1})}$ and $CD^{\lambda}_{\mathrm{poly}(\boldsymbol{S}\text{-}\mathbf{2})}$) were extract from the homopolymer CD spectra at the lowest temperature (20 °C) assuming that all material (50 μM) is polymerized at that temperature.
For the wavelengths λ = 333 nm and λ = 350 nm we thus have:

$$CD^{333}_{\mathrm{poly}[(\boldsymbol{S}\text{-}\mathbf{1})-co-(\boldsymbol{S}\text{-}\mathbf{2})]} = \alpha CD^{333}_{\mathrm{poly}(\boldsymbol{S}\text{-}\mathbf{2})} + \beta CD^{333}_{\mathrm{poly}(\boldsymbol{S}\text{-}\mathbf{1})} \quad \text{(S5.2)}$$

$$CD^{350}_{\mathrm{poly}[(\boldsymbol{S}\text{-}\mathbf{1})-co-(\boldsymbol{S}\text{-}\mathbf{2})]} = \alpha CD^{350}_{\mathrm{poly}(\boldsymbol{S}\text{-}\mathbf{2})} + \beta CD^{350}_{\mathrm{poly}(\boldsymbol{S}\text{-}\mathbf{1})} \quad \text{(S5.3)}$$

Together, these Equations (S5.2) and (S5.3) constitute two equations with two unknown, *i.e.*, α and β, which can be rewritten as:

$$\alpha = \left(CD^{350}_{\mathrm{poly}(\boldsymbol{S}\text{-}\mathbf{1})} \cdot CD^{333}_{\mathrm{poly}[(\boldsymbol{S}\text{-}\mathbf{1})-co-(\boldsymbol{S}\text{-}\mathbf{2})]} - CD^{333}_{\mathrm{poly}(\boldsymbol{S}\text{-}\mathbf{1})} \cdot CD^{350}_{\mathrm{poly}[(\boldsymbol{S}\text{-}\mathbf{1})-co-(\boldsymbol{S}\text{-}\mathbf{2})]}\right)/Q \quad \text{(S5.4)}$$

$$\beta = \left(-CD^{350}_{\mathrm{poly}(\boldsymbol{S}\text{-}\mathbf{2})} \cdot CD^{333}_{\mathrm{poly}[(\boldsymbol{S}\text{-}\mathbf{1})-co-(\boldsymbol{S}\text{-}\mathbf{2})]} + CD^{333}_{\mathrm{poly}(\boldsymbol{S}\text{-}\mathbf{2})} \cdot CD^{350}_{\mathrm{poly}[(\boldsymbol{S}\text{-}\mathbf{1})-co-(\boldsymbol{S}\text{-}\mathbf{2})]}\right)/Q \quad \text{(S5.5)}$$

with:

$$Q = CD^{333}_{\mathrm{poly}(\boldsymbol{S}\text{-}\mathbf{2})} \cdot CD^{350}_{\mathrm{poly}(\boldsymbol{S}\text{-}\mathbf{1})} - CD^{350}_{\mathrm{poly}(\boldsymbol{S}\text{-}\mathbf{2})} \cdot CD^{333}_{\mathrm{poly}(\boldsymbol{S}\text{-}\mathbf{1})} \quad \text{(S5.6)}$$

The temperature dependence of α and β (i.e. equivalent concentration of ***S*-2** and ***S*-1** in polymers, respectively) can be determined via above equations from $CD^{333}_{\mathrm{poly}[(\boldsymbol{S}\text{-}\mathbf{1})-co-(\boldsymbol{S}\text{-}\mathbf{2})]}$ and $CD^{350}_{\mathrm{poly}[(\boldsymbol{S}\text{-}\mathbf{1})-co-(\boldsymbol{S}\text{-}\mathbf{2})]}$ at different temperatures.

Given α and β, the CD signal can be recalculated via Equation (S5.1). At λ = 333 nm as well as at λ = 350 nm, the so calculated CD signal exactly matches the experimental curve for the copolymer. This is expected since these wavelengths were used to determine α and β. At other wavelengths, *e.g.* λ = 338 nm, the match is not necessarily perfect.

Deviations can be explained by the three assumptions made on the model:

- $CD^{\lambda}_{\mathrm{poly}(\boldsymbol{S}\text{-}\mathbf{1})}$ and $CD^{\lambda}_{\mathrm{poly}(\boldsymbol{S}\text{-}\mathbf{2})}$ are estimates based on the assumption that at 20 °C all material is polymerized;
- The shape of the CD spectra of ***S*-1** and ***S*-2** are completely temperature independent;
- The CD signal of the copolymer is the exact linear combination of the signals of the two homopolymers.

However, the differences are acceptable and the resulting concentrations of copolymerized material seem reasonable. These results clearly show that at high temperature ***S*-1** is the majority copolymer constituent, while at 20 °C the copolymers balance at 50:50 ratio.

5.4.5. Simulations

Brief discussion on the mass balance model

The goal of the simulation is to compute an equilibrium situation with given total concentrations of A and B monomers. To do that, a complex mass balance model developed by Markvoort and ten Eikelder is exploited (model not shown).[53-55] The mass balance is designed to consider the growth of the copolymer just as a function of the last polymerized monomer and of the monomer which is being added (*e.g.* the reaction PA +A ⇌ PAA, where P is the polymer chain, is considered just based on the thermodynamic values related to AA interaction).

Upon a fixed overall concentrations of monomers A and B, the simulation of the cooling curves is then based on the equilibrium constants of the different reactions (PA +A ⇌ PAA; PB-B ⇌ PBB; PA +B ⇌ PAB; PB +A ⇌ PBA). Each equilibrium constant can be written as $K = \mathrm{e}^{(-\Delta G^0/RT)}$, with ΔG^0 the standard free energy differences of the corresponding reaction. The homopolymerization reactions are described with a single entropy term and two enthalpy terms per system (*i.e.*, ΔS_{AA}, ΔH_{AA} and NP_A for A and ΔS_{BB}, ΔH_{BB} and NP_B for B). Thus:

$K_{PA-A} = e^{-(\Delta H_{AA} - T\Delta S_{AA})/RT}$ and $\sigma_A = e^{NP_A/RT}$, for A;

$K_{PB-B} = e^{-(\Delta H_{BB} - T\Delta S_{BB})/RT}$ and $\sigma_B = e^{NP_B/RT}$ for B;

$K_{PB-A} = e^{-(\Delta H_{AB} - T\Delta S_{AB})/RT}$ for the extra equilibrium constant for the copolymerization.

The copolymerization is thus described using the two additional energy terms ΔH_{AB} and ΔS_{AB}.
In the current manuscript we took all entropy terms equal: $\Delta S_{AA} = \Delta S_{AB} = \Delta S_{BB} = \Delta S$.

Settings used in the simulation

In order to simulate systems similar to **poly(*S*-1)** and **poly(*S*-2)**, we used hypothetical polymers poly(A) and poly(B) and selected the related thermodynamic parameters in order to resemble **poly(*S*-1)** and **poly(*S*-2).** To do so, we set the same entropic term for the two homopolymerizations and varied just the enthalpy of elongation (ΔH), to account for the difference in elongation temperature between **poly(*S*-1)** and **poly(*S*-2)**, and the nucleation penalties (NP), to account for the difference in shape of the cooling curves of **poly(*S*-1)** and **poly(*S*-2)** around their respective elongation temperatures. The values selected are the following:

poly(A): $\Delta H_{AA} = -53\ kJ\ mol^{-1}, \Delta S_{AA} = -0.06\ kJ\ mol^{-1}, NP_A = -40\ kJ\ mol^{-1}$

poly(B): $\Delta H_{BB} = -50\ kJ\ mol^{-1}, \Delta S_{BB} = -0.06\ kJ\ mol^{-1}, NP_B = -20\ kJ\ mol^{-1}$

The resulting homopolymer cooling curves for c = 25 μM reasonably match the cooling curves of respectively **poly(*S*-1)** and **poly(*S*-2)** at that same concentration. The copolymerization cooling curve and the concentration of polymerized monomers units are simulated by varying the value of ΔH_{AB} between $-53\ kJ\ mol^{-1} \leq \Delta H_{AB} \leq -25\ kJ\ mol^{-1}$ (while keeping $\Delta S_{AB} = \Delta S_{AA} = \Delta S_{BB}$).

Stochastic analysis

Stochastic simulations of a set of copolymers poly[$(A)_{0.5}$-*co*-$(B)_{0.5}$] with different ΔH_{AB}values ($\Delta H_{AB} = -25\ kJ\ mol^{-1}$; $\Delta H_{AB} = -37\ kJ\ mol^{-1}$; $\Delta H_{AB} = -42\ kJ\ mol^{-1}$ and $\Delta H_{AB} = -47\ kJ\ mol^{-1}$) were run to visualize the copolymer microstructures. The simulations were performed from two different starting points, free monomer, and pre-assembled homopolymers. 10000 monomers (5000 A and 5000 B) were followed during 1011–1012 reaction steps. The assumption of diffusion-controlled association rate constants (1010 $M^{-1}\ s^{-1}$) was considered for all monomer association and dimer formation reactions. The simulations were performed for c = 50 μM at 50 °C. The simulation's temperature, 50 °C, has been chosen to have avoid working with longer polymers which would require longer computation time. However, the ratio of $A-B$ contact is not highly influenced by the temperature of these simulations. The fraction $A-B$ bonds is shown from t = 0.001 s for computational reason, the formation of the first contacts (*e.g.,* $A-A$, $A-B$, $B-B$) are necessary to get a value of the fraction of $A-B$ bonds for the molecularly-dissolved case.

The simulations give distributions of lengths of copolymers with different microstructures based on ΔH_{AB}. The evolution of the system was followed monitoring the fraction of $A-B$ contacts in the copolymers as a function of time (e.g., for a copolymer $AABBBBBBA$ the fraction of $A-B$ contact is 0.25, *i.e.,* 2 out of 8 contacts are $A-B$, while 1 is $A-A$ and 5 are $B-B$). It is important to note that the fraction of $A-B$ contacts as a function of time displays that both starting from monomers and from assembled homopolymers the system reaches the same copolymer microstructure rapidly, indicating that the equilibrium is reached well within the time scale of the simulations.

5.5. References

[1] Schumer J., *Nat. Nano.* **2016**, 11 (10), 828–834.
[2] Zhang, L.; Zhong, X.; Pavlica, E.; Li, S.; Klekachev, A.; Bratina, G.; Ebbesen, T. W.; Orgiu, E.; Samorì, P. *Nat. Nano.***2016**, 11 (10), 900–906.
[3] Baroncini, M.; d'Agostino, S.; Bergamini, G.; Ceroni, P.; Comotti, A.; Sozzani, P.; Bassanetti, I.; Grepioni, F.; Hernandez, T. M.; Silvi, S.; Venturi, M.; Credi, A. *Nat. Chem.* **2015**, 7, 634.
[4] Borges, J.; Rodrigues, L. C.; Reis, R. L.; Mano, J. F. *Adv. Funct. Mater.* **2014**, 24 (36), 5624–5648.
[5] Guo, P.; Weimer, M. S.; Emery, J. D.; Diroll, B. T.; Chen, X.; Hock, A. S.; Chang, R. P. H.; Martinson, A. B. F.; Schaller, R. D. *ACS Nano* **2017**, 11 (1), 693–701.
[6] Chen, F.; Zhu, Y.J. *ACS Nano* **2016**, 10 (12), 11483–11495.
[7] Aida, T.; Meijer, E. W.; Stupp, S. I. *Science* **2012**, 335 (6070), 813–817.
[8] Würthner, F.; Saha-Möller, C. R.; Fimmel, B.; Ogi, S.; Leowanawat, P.; Schmidt, D. *Chem. Rev.* **2016**, 116 (3), 962–1052.
[9] López-Andarias, J.; Rodriguez, M. J.; Atienza, C.; López, J. L.; Mikie, T.; Casado, S.; Seki, S.; Carrascosa, J. L.; Martín, N. *J. Am. Chem. Soc.* **2015**, 137 (2), 893–897.
[10] Bakker, M. H.; Lee, C. C.; Meijer, E. W.; Dankers, P. Y. W.; Albertazzi, L. *ACS Nano* **2016**, 10 (2), 1845–1852.
[11] Smulders, M. M. J.; Schenning, A. P. H. J.; Meijer, E. W. *J. Am. Chem. Soc.* **2008**, 130 (2), 606–611.
[12] Mukhopadhyay, R. D.; Ajayaghosh, A. *Science* **2015**, 349 (6245), 241–242.
[13] Kang, J.; Miyajima, D.; Mori, T.; Inoue, Y.; Itoh, Y.; Aida, T. *Science* **2015**, 347 (6222), 646–651.
[14] Ogi, S.; Sugiyasu, K.; Manna, S.; Samitsu, S.; Takeuchi, M. *Nat. Chem.* **2014**, 6 (3), 188–195.
[15] Ogi, S.; Stepanenko, V.; Sugiyasu, K.; Takeuchi, M.; Würthner, F. *J. Am. Chem. Soc.* **2015**, 137 (9), 3300–3307.
[16] Aliprandi, A.; Mauro, M.; De Cola, L. *Nat. Chem.* **2016**, 8 (1), 10–15.
[17] Markvoort, A. J.; ten Eikelder, H. M. M.; Hilbers, P. A. J.; de Greef, T. F. A.; Meijer, E. W. *Nat. Commun.* **2011**, 2, 509.
[18] Korevaar, P. A.; Grenier, C.; Markvoort, A. J.; Schenning, A. P. H. J.; de Greef, T. F. A.; Meijer, E. W. *Proc. Natl. Acad. Sci.* **2013**, 110 (43), 17205–17210.
[19] Jabbari-Farouji, S.; van der Schoot, P. *J. Chem. Phys.* **2012**, 137 (6), 64906.
[20] Gestel, J. van; van der Schoot, P.; Michels, M. A. J. *J. Chem. Phys.* **2004**, 120 (17), 8253–8261.
[21] Buchelnikov, A. S.; Evstigneev, V. P.; Evstigneev, M. P. *Chem. Phys.* **2013**, 421, 77–83.
[22] ten Eikelder, H. M. M.; Markvoort, A. J.; de Greef, T. F. A.; Hilbers, P. A. J. *J. Phys. Chem. B* **2012**, 116 (17), 5291–5301.
[23] Korevaar, P. A.; George, S. J.; Markvoort, A. J.; Smulders, M. M. J.; Hilbers, P. A. J.; Schenning, A. P. H. J.; De Greef, T. F. A.; Meijer, E. W. *Nature* **2012**, 481 (7382), 492–496.
[24] Ogi, S.; Fukui, T.; Jue, M. L.; Takeuchi, M.; Sugiyasu, K. *Angew. Chem. Int. Ed.* **2014**, 53 (52), 14363–14367.
[25] van der Zwaag, D.; Pieters, P. A.; Korevaar, P. A.; Markvoort, A. J.; Spiering, A. J. H.; de Greef, T. F. A.; Meijer, E. W. *J. Am. Chem. Soc.* **2015**, 137 (39), 12677–12688.
[26] Zhang, W.; Jin, W.; Fukushima, T.; Saeki, A.; Seki, S.; Aida, T. *Science* **2011**, 334 (6054), 340–343.
[27] Ajayaghosh, A.; Vijayakumar, C.; Praveen, V. K.; Babu, S. S.; Varghese, R. *J. Am. Chem. Soc.* **2006**, 128 (22), 7174–7175.
[28] Adler-Abramovich, L.; Gazit, E. *Chem. Soc. Rev.* **2014**, 43 (20), 6881–6893.
[29] Sugiyasu, K.; Jung, S. H.; Bochicchio, D.; Pavan, G. M.; Takeuchi, M.; Sugiyasu, K. *J. Am. Chem. Soc.* **2018**, 140 (33), 10570–10577
[30] Rupar, P. A.; Chabanne, L.; Winnik, M. A.; Manners, I. *Science* **2012**, 337 (6094), 559–562.
[31] Qiu, H.; Hudson, Z. M.; Winnik, M. A.; Manners, I. *Science* **2015**, 347 (6228), 1329–1332.
[32] Adelizzi, B.; Filot, I. A. W.; Palmans, A. R. A.; Meijer, E. W. *Chem. A Eur. J.* **2017**, 23 (25), 6103–6110.
[33] Moulin, E.; Niess, F.; Maaloum, M.; Buhler, E.; Nyrkova, I.; Giuseppone, N. *Angew. Chem. Int. Ed.* **2010**, 49, 6974–6978.
[34] Faramarzi, V.; Niess, F.; Moulin, E.; Maaloum, M.; Dayen, J.-F.; Beaufrand, J.-B.; Zanettini, S.; Doudin, B.; Giuseppone, N. *Nat. Chem.* **2012**, 4, 485–490.
[35] Haedler, A. T.; Kreger, K.; Issac, A.; Wittmann, B.; Kivala, M.; Hammer, N.; Köhler, J.; Schmidt, H.-W.; Hildner, R. *Nature* **2015**, 523, 196.
[36] Ellis, T. K.; Galerne, M.; Armao IV, J. J.; Osypenko, A.; Martel, D.; Maaloum, M.; Fuks, G.; Moulin, E.; Gavat, O.; Giuseppone, N. *Angew. Chemie Int. Ed.* **2018**, 57, 15749-15753
[37] Mtangi, W.; Tassinari, F.; Vankayala, K.; Vargas Jentzsch, A.; Adelizzi, B.; Palmans, A. R. A.; Fontanesi, C.; Meijer, E. W.; Naaman, R. *J. Am. Chem. Soc.* **2017**, 139 (7), 2794–2798.
[38] Van Zee, N. J.; Adelizzi, B.; Mabesoone, M. F.J.; Meng, X.; Aloi, A.; Zha, R. H.; Lutz, M.; Filot, I. A.W.; Palmans, A. R.A.; Meijer, E.W. *Nature* **2018**, 558, 100-103
[39] Claridge, T. D. W.; Claridge, T. D. W. *High-Resolution NMR Techniques in Organic Chemistry* **2016**; 315–380.
[40] Das, A.; Vantomme, G.; Markvoort, A. J.; ten Eikelder, H. M. M.; Garcia-Iglesias, M.; Palmans, A. R. A.; Meijer, E. W. *J. Am. Chem. Soc.* **2017**, 139 (20), 7036–7044.
[41] Onogi, S.; Shigemitsu, H.; Yoshii, T.; Tanida, T.; Ikeda, M.; Kubota, R.; Hamachi, I. *Nat. Chem.* **2016**, 8 (8), 743–752.
[42] De Greef, T. F. A.; Smulders, M. M. J.; Wolffs, M.; Schenning, A. P. H. J.; Sijbesma, R. P.; Meijer, E. W. *Chem. Rev.* **2009**, 109 (11), 5687–5754.
[43] Lee, I.; Bates, F. S. *Macromolecules* **2013**, 46 (11), 4529–4539.
[44] Markvoort, A. J.; Eikelder, H. M. M. ten; Hilbers, P. A. J.; de Greef, T. F. A. *ACS Cent. Sci.* **2016**, 2 (4), 232–241.
[45] Aloi, A.; Vargas Jentzsch, A.; Vilanova, N.; Albertazzi, L.; Meijer, E. W.; Voets, I. K. *J. Am. Chem. Soc.* **2016**, 138 (9), 2953–2956.
[46] Adelizzi, B., Aloi, A., Van Zee, N. J., Palmans, A.R.A., Meijer, E.W., Voets, I. K. *ACS Nano* **2018**, 12 (5), 4431–44392017.
[47] Aloi, A.; Vilanova, N.; Albertazzi, L.; Voets, I. K. *Nanoscale* **2016**,8, 8712-8716

[48] Albertazzi, L.; van der Zwaag, D.; Leenders, C. M. A.; Fitzner, R.; van der Hofstad, R. W.; Meijer, E. W. *Science* **2014**, 344 (6183), 491-495.
[49] Korevaar, P. A.; Schaefer, C.; de Greef, T. F. A.; Meijer, E. W. *J. Am. Chem. Soc.* **2012**, 134 (32), 13482–13491.
[50] Coates, G. W. *Chem. Rev.* **2000**, 100 (4), 1223–1252.
[51] Adelizzi, B.; Aloi, A.; Markvoort, A. J.; Ten Eikelder, H. M. M.; Voets, I. K.; Palmans, A. R. A.; Meijer, E. W. *J. Am. Chem. Soc.* **2018**, 140 (23), 7168-7175.
[52] Belov, V. N.; Mitronova, G. Y.; Bossi, M. L.; Boyarskiy, V. P.; Hebisch, E.; Geisler, C.; Kolmakov, K.; Wurm, C. A.; Willig, K.; Hell, S. W. *Chem. A Eur. J.* **2014**, 20 (41), 13044.
[53] ten Eikelder, H. M. M.; Markvoort, A. J.; de Greef, T. F. A.; Hilbers, P. A. J. *J. Phys. Chem. B* 2012, 116 (17), 5291–5301
[54] Markvoort, A. J.; Eikelder, H. M. M. ten; Hilbers, P. A. J.; de Greef, T. F. A. *ACS Cent. Sci.* 2016, 2 (4), 232–241
[55] Markvoort, A. J.; Eikelder, H. M. M. ten; Hilbers, P. A. J.; de Greef, T. F. A. Meijer, E. W. **2011**, *Nature Commun.,* 2, 509–518.

6.

Boron and boron-nitrogen supramolecular (co)polymers

These results are obtained in collaboration with Shigehiro Yamaguchi's group and summarized in:

B. Adelizzi, N. Tanaka, S. C. J. Meskers, A. R. A. Palmans, S. Yamaguchi and E. W. Meijer
(Manuscript in preparation)

Abstract: The rapid growth of the field of supramolecular copolymers is generating a fertile playing field for developing functional, multicomponent, dynamic systems. Fundamental studies to determine how to control supramolecular copolymers have revealed the prerequisites to achieve emerging properties upon non-covalent copolymerization. Here, we report the development of bridged triphenylborane-based monomers, their supramolecular polymerization, and copolymerization with tri(biphenyl)amine-based monomers. Because of the Lewis base character of the tri(biphenyl)amine and the Lewis acid character of the triphenylborane, we anticipate on the formation of 1D supramolecular B-N copolymers may show unforeseen optoelectronic properties. Bridged triphenylboranes and tri(biphenyl)amine monomers were synthesized and their homopolymerization in apolar solvents was studied via variable temperature spectroscopic analysis. After selection of the most promising B-N couple, their supramolecular copolymerization was evaluated. Absorbance and circular dichroism measurements on the copolymerization mixture suggest self-sorting of the system. In contrast, emission studies reveal the emergence of a green emission with a remarkably long lifetime. Combination of circular polarized luminescence, oxygen-free lifetime measurements, and variable temperature emission spectra demonstrate the presence of B-N couples within the supramolecular copolymers chain. Kinetic studies demonstrate the increase over time of B-N interactions suggesting a slow formation of copolymers upon aging. Although the creation of an alternating B-N supramolecular copolymer cannot be concluded or excluded from the experiments, the results demonstrate the great potential of this interaction for optoelectronic materials.

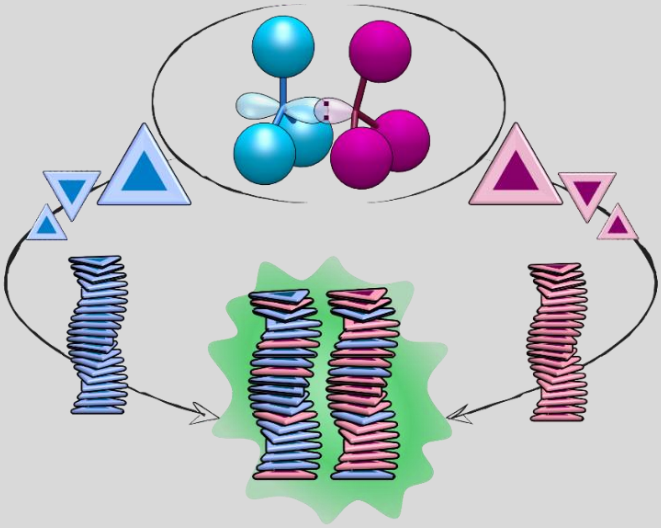

6.1. Introduction

The growing interest in the field of 1D supramolecular copolymers is generating an intense activity directed to create new copolymers with precise microstructure and interesting properties. The field is currently expanding to develop new functional systems and methods for characterizing them. In the last few years supramolecular copolymers with defined structures have been reported by several groups. For example, alternating architectures have been reported by Besenius' group,[1,2] periodic structures by Würthner and coworkers,[3,4] and block copolymers by Aida,[5] Manners,[6,7] Takeuchi[8] and our group.[9,10] In the block copolymer field, apart from our contribution (Chapter 5),[9] the strategy used to control the structure is to apply a kinetic control over the fiber's growth in a way similar to a living copolymerization. Contrarily, alternating copolymer structures are often obtained carefully tailoring the cores, or the side chains, to promote complementary interaction, such as Coulombic attractions or charge-transfer systems.

Intrigued by the possibility to further widening the field, we aimed to complement the copolymerization with an additional interaction. To do so, we evaluated frustrated Lewis pairs as a possible driving interactions. Frustrated Lewis pairs are non-covalent adducts classically formed between a strong Lewis acid (LA) and a strong Lewis base (LB) that, due to their steric congestion, cannot create a covalent dative adduct.[11] Using a simplification, the empty p_z of the boron interacts with the lone-pair of the Lewis base via a non-covalent interaction. Typically, frustrated Lewis pairs are formed by triphenylboranes derivatives, as the LA, and triphenylphosphines[12] or bulky amines,[11,13] as the LB, and often exploited for their peculiar properties as catalyst.[14-16] Recently, researchers have been pushing the boundaries of these adducts toward responsive materials,[17,18] gels,[19] and polymers[20,21] modulating the dynamics and the stability of the Lewis adducts.[22]

Based on this, we here evaluated the possibility to go further and convert these systems from a dimeric[23] to a truly polymeric form including B-N non-covalent interactions in 1D supramolecular copolymers. However, the classic boron-based molecules used, triphenylborane and tri(pentafluorophenyl)borane, are highly reactive and not stable to air. We therefore opted for a more stabilized system such as the ones reported by the outstanding work of Yamaguchi and coworkers.[24-26] Bridged or partially bridged triphenylboranes developed by Yamaguchi's group, present enhanced stability to air and nucleophiles. This is due to firstly, an electrodonating conjugated environment and secondly, to a geometrical constraint which partially hampers the conformation change from the trigonal planar conformation of the acid and the tetrahedral conformation of the adduct.[24,25] As Lewis base partner molecules, we selected triphenylamine cores which have proved their potential as supramolecular monomers[27] and ability to create radical cations under specific conditions.[28,29]

Here we report the preliminary results on the design, synthesis and characterization of boron-based supramolecular polymers and their copolymerization with

triphenylamine-based monomers. Our hypothesis is that, if boron-nitrogen 1D supramolecular copolymers can be obtained, new fascinating electronic properties may emerge from these systems, in which the lone-pair of the nitrogen is shared with the empty orbitals of the boron in a 1D fashion. The work has been carried out in close collaboration with the group of Shigehiro Yamaguchi.

6.2. Design and synthesis

The chemistry related to triphenylboranes is particularly complex and delicate and often limits the functionalization of these cores. However, bridged triphenylboranes, which present increased stability, can be functionalized with boronic acid pinacolesters or with bromides. Kushida *et al.* reported a C_3 symmetric carbon-bridged triphenylboranes which is stable under Suzuki conditions and display interesting electronic properties in liquid crystalline state.[24,25] Similarly, Hirai *et al.* demonstrated that partially oxygen-bridged triphenylboranes are stable and display peculiar optical properties.[30]

After selecting these cores as suitable boron building blocks, we designed a library of triphenylboranes and analogous triphenylamine-based monomers (Scheme 1). The design is based on C_3 symmetric molecules (expect for the B cores which display a C_2 symmetry) bearing a B or N core, carboxamides as H-bonding units, and solubilizing chains at the periphery. The design includes H-bonding units to direct the assembly. We anticipated that the strength of these B-N couples maybe be not enough to drive the copolymerization. Bridged triphenylboranes are indeed more electronrich compared to non-bridged analogues and so may form less strong interactions compared to classic frustrated Lewis pairs. Nevertheless, we speculated that these interactions maybe be sufficient to promote hetero-interactions between the two types of monomers.

Due to the need of functionalizing the B cores via Suzuki reactions, we designed different peripheries which both allow their installation via cross-coupling and bear the H-bonding units with the solubilizing chains. For the O-bridged triphenylborane core, the two peripheries designed are phenylamides bearing either a single chiral (*S*)-3,7-dimethyloctyl chain (***S*-B1**) or a gallic moiety bearing 3 chiral chains per branch (***S*-B2**). In contrast, the C-bridged triphenylborane core was designed to bear 3 chiral gallic moieties and no amides (***S*-B3**), creating in this way the chiral analogue of the boron molecules previously reported by Kushida *et al.*[24]

The N analogues were designed in accord to the B molecules using, this time, classic C_3 symmetric unbridged triphenylamine as core. Therefore, ***S*-N1** corresponds to ***S*-B1**, while ***S*-N2** to ***S*-B2.** For the version with no amide groups, the N analogue of ***S*-B3** has been designed with achiral *n*-dodecyl chains, **a-N3.**

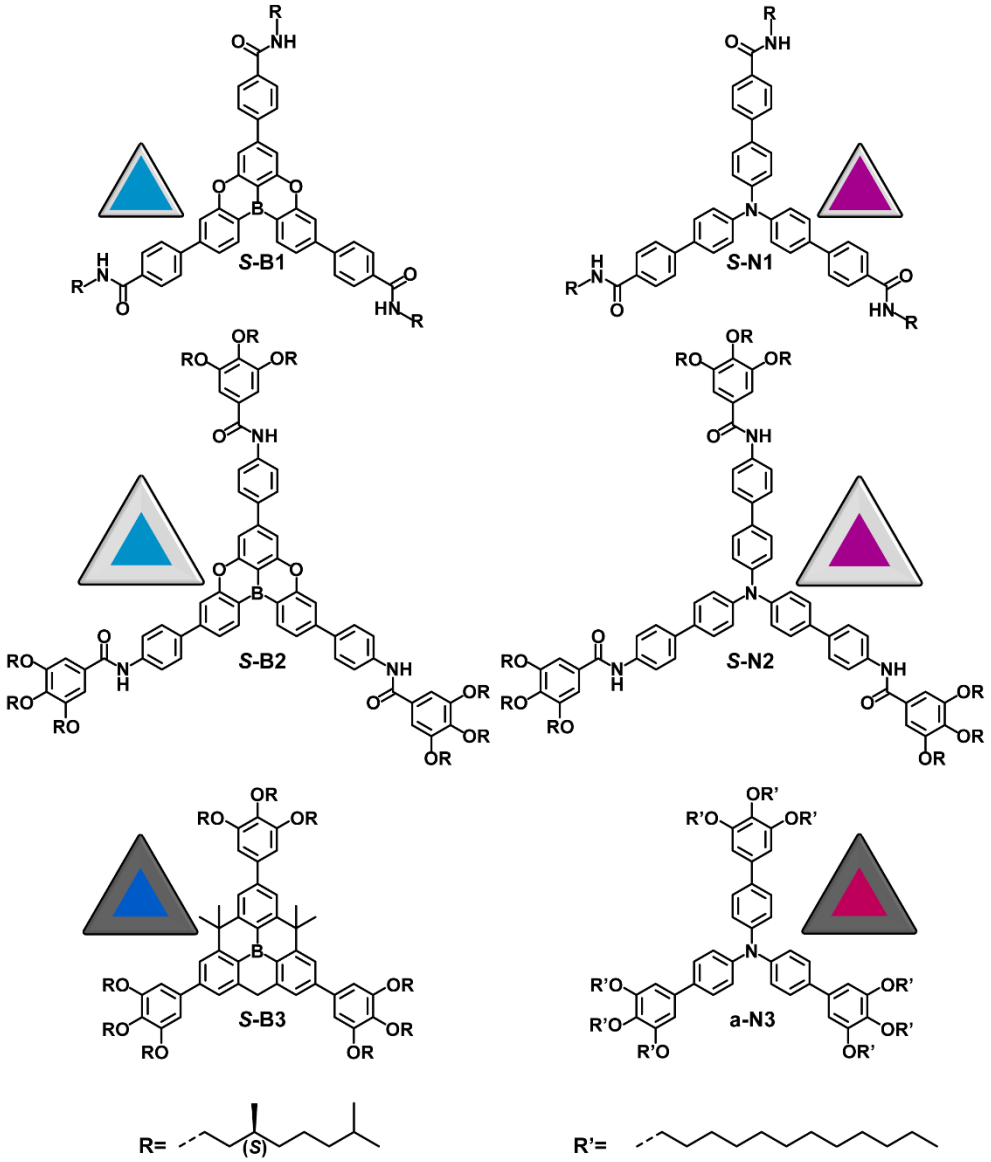

Scheme 1. Molecular structures of boron-based and nitrogen-based supramolecular monomers.

The synthesis of all the supramolecular monomers is achieved via a final Suzuki cross-coupling between the boron (or nitrogen) core and the solubilizing wedges (Scheme 2). The bridged triphenylborane cores **BBr** and **BPin** have been previously synthesized by Yamaguchi's group,[24] while the synthesis of the solubilizing wedges is reported in the experimental section. The Suzuki cross-coupling reaction for the boron cores were performed according to the procedure previously published by Yamaguchi's group,[24] while for the nitrogen core, standard cross-coupling conditions with $Pd(PPh_3)_4$ and K_2CO_3 were used.

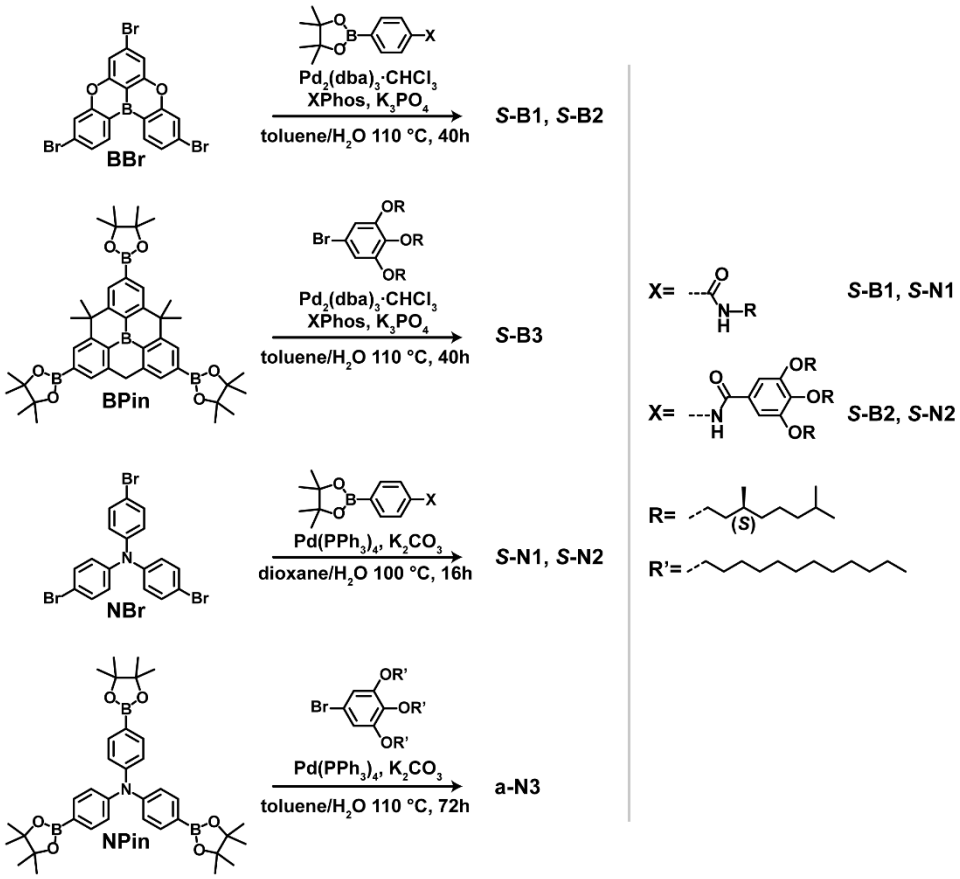

Scheme 2. Synthetic scheme of Suzuki cross couplings performed.

Purification of ***S*-B1**, ***S*-B2** and ***S*-B3** was performed via SiO_2 chromatography and multiple cycles of recycling gel-permeation chromatography and high performance liquid chromatography. ***S*-B1** and ***S*-B2** were so obtained in high purity in 58% to 45% yield, respectively. Conversely, pure ***S*-B3** was isolated in a small quantities only. Purifications of ***S*-N1** and ***S*-N2** were achieved by SiO_2 chromatography and recrystallization in acetonitrile resulting in 60 % yield. **a-N3** was obtained in moderate yield but the purification via SiO_2 chromatography caused oxidation of the product similarly to ***S*-B3**. As a results, the pure product was obtained in a small quantities.

All molecules were molecularly characterized by ^{1}H-NMR, ^{13}C-NMR, mass spectrometry and IR. IR measurements for ***S*-B1**, ***S*-B2**, ***S*-N1**, ***S*-N2** display –NH stretching and –C=O stretching consistent with hydrogen-bonding similarly to what we reported for the triphenylamines in Chapter 2. Further analysis on supramolecular homopolymerization and copolymerization were performed with ***S*-B1**, ***S*-B2**, ***S*-N1**, and ***S*-N2**.

6.3. Optical characterization of B and N monomers

Due to the highly conjugated cores, the molecules designed may display interesting properties already in the monomerically dissolved state.[31] For this reason, optical characterization of ***S*-B1**, ***S*-B2**, ***S*-N1**, and ***S*-N2** was performed in diluted condition ($c \leq$ 30 μM) in 1,2-dichloroethane (DCE).

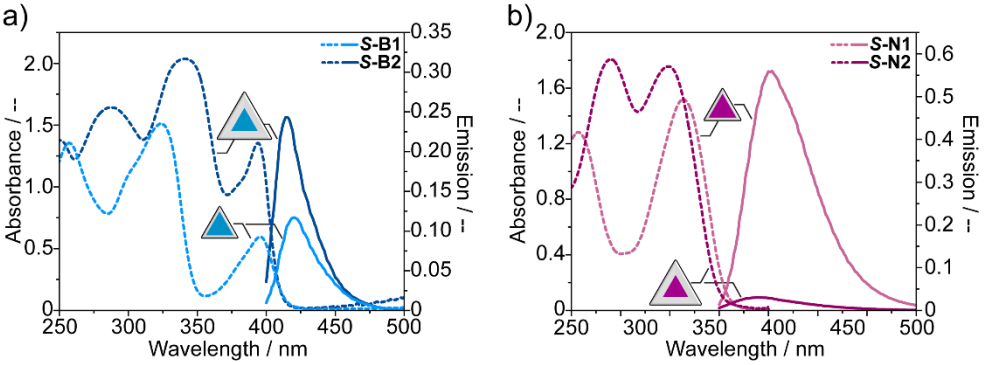

Figure 1. Absorbance (dashed lines) and emission spectra (solid lines) of molecularly dissolved (a) boron monomers: ***S*-B1** (light blue lines) and ***S*-B2** (dark blue lines) and (b) nitrogen monomers: ***S*-N1** (rose lines) and ***S*-N2** (purple lines). Measurements performed in DCE, c = 30 μM, 20 °C. Emission spectra performed exciting in the excitation maximum, parameter maintained as 400 V, 2 nm emission slit for (a) the boron molecules and as 500 V, 4 nm emission slit for (b) the nitrogen molecules.

In DCE the absorbance spectra of the boron-based molecules show three main bands between λ = 420 nm and 250 nm. The low energy absorption band at λ = 395 nm presumably belongs to the oxygen-bridged core, as previously reported.[30] Both ***S*-B1** and ***S*-B2** are highly fluorescent and display emission bands at λ = 420 nm and λ = 414

nm, respectively (Figure 1). Both ***S*-N1** and ***S*-N2**, display two absorption bands between λ = 375 nm and 250 nm. ***S*-N1** shows the core absorption band at λ = 363 nm and emission at λ = 453 nm, remarkably similar to its ester analogue reported by Zhang *et al*.[32] Conversely, ***S*-N2** exhibits a blue-shifted core absorption at λ = 349 nm and a less intense fluorescence.

6.4. Homopolymerization of bridged triphenylboranes

Supramolecular homopolymerizations of ***S*-B1** and ***S*-B2** were tested in apolar solvents via optical spectroscopy. UV-vis, circular dichroism (CD) and emission measurements were hence performed in decalin and compared with the molecularly dissolved state previously characterized in DCE. The formation of supramolecular homopolymers in decalin was monitored via variable temperature optical measurements (100 °C to 20 °C, cooling rate: 15 °C h^{-1}).

***S*-B1**, which bears just three side chains, displays poor solubility in decalin and homogenously dissolved solutions are only obtained at $c \leq 20$ μM. Variable temperature (VT) measurements of ***S*-B1** ($c = 10$ μM) show aggregation upon cooling (Figure 2). Both UV-vis and emission spectra of ***S*-B1** display a decrease of the main peaks belonging to the monomer and a general red-shift in absorption and emission bands indicative of the formation of aggregates (Figures 2a and 2b, respectively). Especially, the emission measurements show a decrease in intensity of one order of magnitude compared to the monomer peak (λ = 409 nm for ***S*-B1**) and the growth of a broad red-shifted emission peak related to the polymers (λ = 500 nm for **poly(*S*-B1)**). VT-CD spectra exhibit the growth of negative CD signal upon cooling indicating the formation of chiral supramolecular polymers, **poly(*S*-B1)** (Figure 2c). The CD of **poly(*S*-B1)** displays three intense negative bands at λ = 410 nm, 345 nm, and 274 nm and a positive band below 250 nm (Figure 2c).

Due to the low absorbance and intense CD, the related g_{ASB} is remarkably high (g_{ABS} = 0.03 at λ = 470 nm). In line with this value, circularly polarized luminescence (CPL) in the aggregated state (20 °C, decalin, $c = 10$ μM) displays g_{LUM} in the order of $-2\ 10^{-2}$ in the emission band (spectra not shown). Usually organic molecules[33-35] and supramolecular polymers[36] show g values in the order of 10^{-3}.[37] This high asymmetry can be due to a higher degree of order, extremely long fibers,[36] to the boron cores in a chirally locked conformation,[30,38,39] or to artifacts.

Following the evolution of UV and CD intensity, at a fixed λ, as a function of temperature it is possible to retrace the cooling curves and analyze the supramolecular polymerization mechanism. As visible both in the absorbance (not shown) and CD cooling curves, ***S*-B1** shows a cooperative polymerization with elongation temperature T_e at 90 °C for $c = 10$ μM (Figure 2d). Comparing the cooling curves obtained for different concentration of ***S*-B1**, it is noticeable that the cooling curves for $c = 10$ μM and 15 μM display almost the same T_e, whereas the cooling curve of $c = 5$ μM shows a much lower

T_e. In addition, the CD intensity does not scale linearly with the concentration. The solution at c = 10 µM shows a more intense CD than the one recorded for c = 15 µM, whereas the solution at c = 5 µM has a CD intensity four times smaller than the one for c = 10 µM (Figure 2d). The absence of linear scaling between concentration and the magnitude of the CD effect, and the ln(c) with the inverse T_e is remarkable and in stark contrast to the observations made in previously studied cooperative systems.[40]

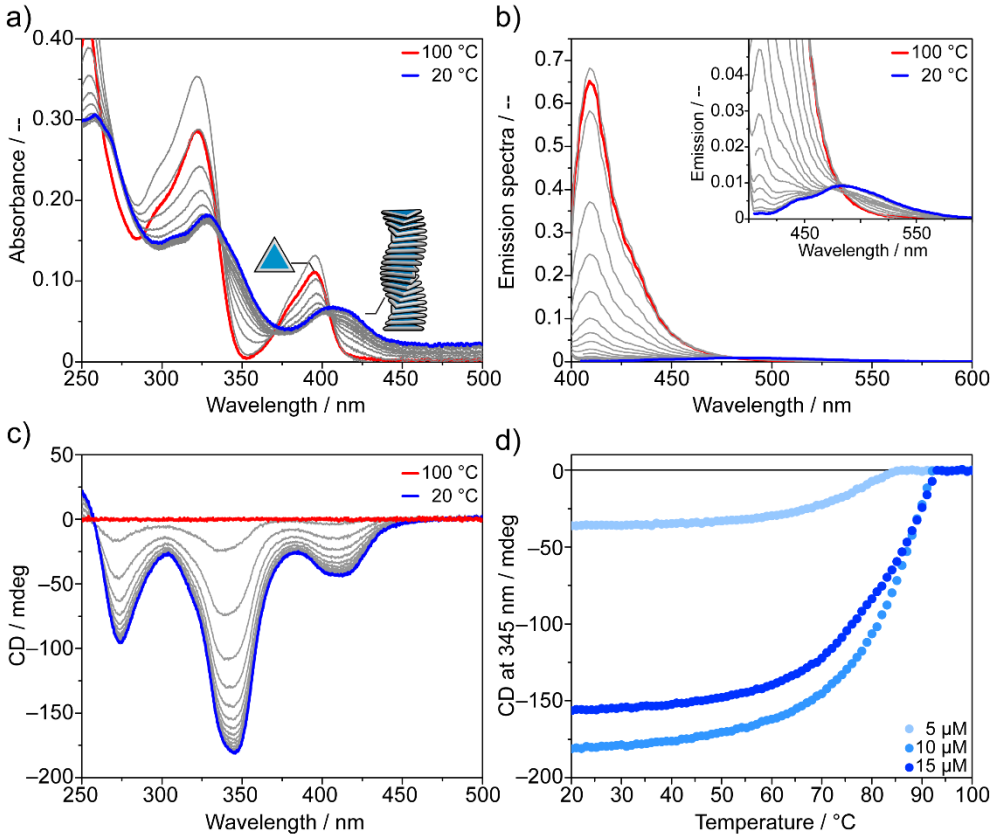

Figure 2. Variable temperature spectroscopic measurements of ***S*-B1**. (a) Absorbance, (b) emission and (c) CD spectra from 100 °C (red lines) to 20 °C (blue lines) and (d) related cooling curves. CD cooling curve measured at 345 nm, from 100 °C to 20 °C for different concentrations. Measurements performed in decalin, cooling rate 15 °C h^{-1}, spectra reported for c = 10 µM.

These effects hint to the presence of some uncontrolled mechanism in solution. A similar behavior has been observed in assembling systems that undergo heterogeneous nucleation.[41] This process occurs when supramolecular polymers grow from nuclei caused by external agents which are present in traces amount in solution or when some aggregates are still present at high temperature and act as nuclei during the cooling procedure. Alternatively, another explanation can be found in the low solubility of the

system causing the formation of higher order aggregates or uncontrolled crystallization rather than supramolecular polymerization.[42]

In contrast with ***S*-B1**, ***S*-B2**—the extended analogue with gallic wedges—shows good solubility properties in decalin. Similarly to ***S*-B1,** variable temperature measurements show aggregation upon cooling. UV-vis (Figure 3a) and emission spectra (Figure 3b) display a reduction of the intensity of the monomer's peaks (monomer's absorbance λ = 390 nm, and emission λ = 408 nm for ***S*-B2**) and a growth of red-shifted bands both in the absorption (shoulder at λ = 410 nm) and emission (λ = 475 nm) spectra which can be attributed to the formation of aggregates. The presence of isosbestic points indicates that just two species are existing in solution, the monomer and the growing polymer chains.

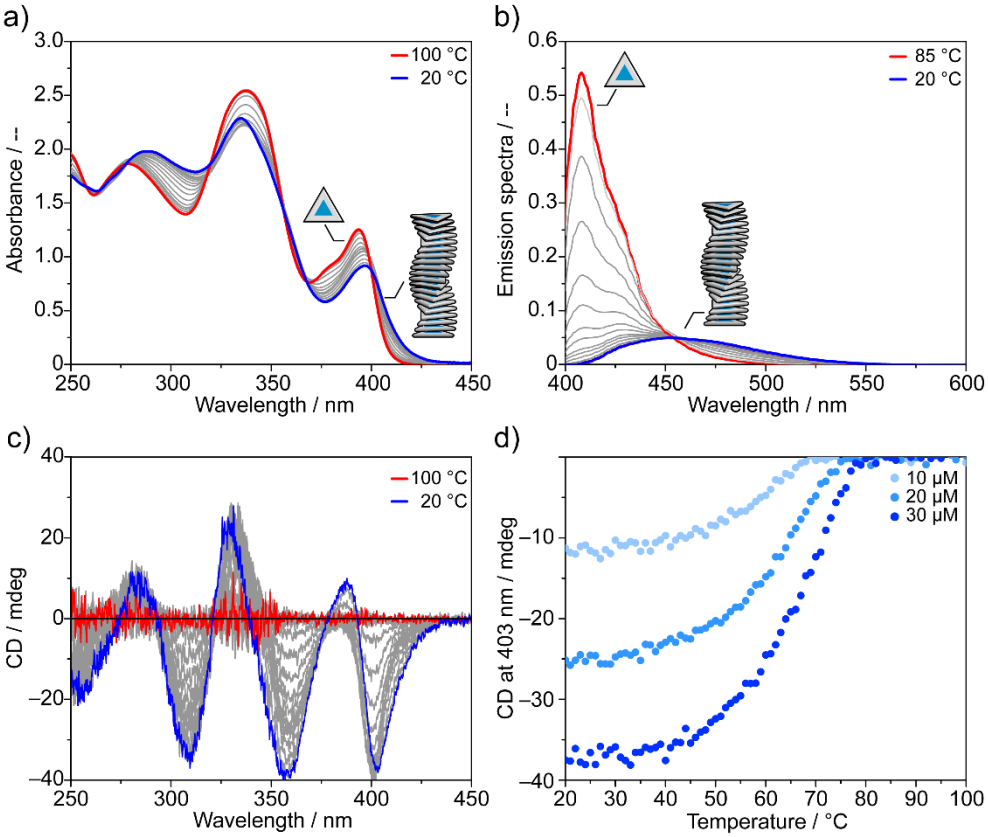

Figure 3. Variable temperature spectroscopic measurements of ***S*-B2.** (a) Absorbance, (b) emission and (c) CD spectra from 100 °C (red lines) to 20 °C (blue lines) and (d) related CD cooling curve measured at λ = 403 nm, from 100 °C to 20 °C for different concentrations. Measurements performed in decalin, cooling rate 15 °C h^{-1}, spectra reported for *c* = 30 μM.

Via VT-CD measurements recorded upon cooling, a negative cotton effect is observed and the formation of chiral supramolecular polymers, **poly(*S*-B2)**, is attested (Figure 3c). The CD cooling curves recorded at λ = 403 nm show cooperative polymerization with elongation temperature T_e at 75 °C for c = 30 μM (Figure 3d). Differently from ***S*-B1**, ***S*-B2** display a classic linear dependence on the concentration as expected by standard cooperative systems.[40]

Circular polarized luminescence (CPL) and emission lifetime measurements were then recorded in the aggregated state at 20 °C. In line with the recorded CD, **poly(*S*-B2)** displays negative CPL (Figure 4a). However, in clear contrast to **poly(*S*-B1)**, **poly(*S*-B2)** has values of g_{LUM} and g_{ABS} (measurable from the CD spectra) in the order of 10^{-3}, as often reported for organic molecules and assemblies.[36]

The emission lifetime (τ) of a molecule strongly depends on the environments of the fluorophore. This means that monomers and supramolecular polymers have different lifetimes. For this reason, the measurements recorded at 20 °C display two-component decay, one defined by a short (τ ≈ 3 ns) and one by a longer decay time (τ ≈ 16 ns) (Figure 4b). Measurements performed at two different wavelengths permit to assign the short decay time to the monomers (since that component contributes more at shorter λ) (Figure 4b top) and the long decay time to the polymer (since that component contributed more at longer wavelengths (Figure 4b bottom). A longer decay for supramolecular aggregates compared to their monomers has already been reported for other systems[43-46] and it can be attributed to several factors, such as the formation of H aggregates,[47-48] which may be related to the presence of excimers[49] or charge transfer interactions[50] in the aggregate, or to aggregation-induced inter system crossing.[51]

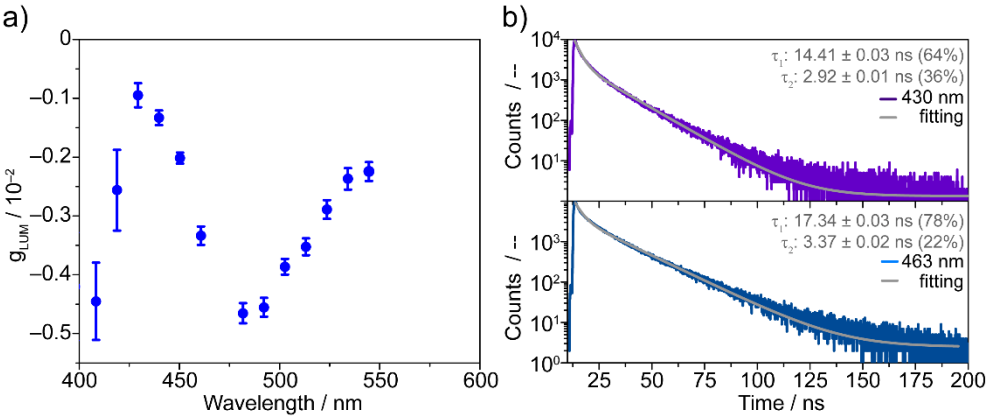

Figure 4. (a) Circularly polarized luminescence and (b) emission lifetime of **poly(*S*-B2)** for (top, violet line) monomer and (bottom, blue line) polymer's wavelengths. Measurements performed in decalin, at 20 °C after proper polymerization procedure. Spectra reported for c = 30 μM.

To confirm the 1D structure, we performed atomic force microscopy (AFM) measurements on **poly(*S*-B2)**. Samples were prepared by dropcasting an assembled solution of **poly(*S*-B2)** onto mica (c = 30 μM, decalin). AFM imaging revealed the presence of linear aggregates ≈ 2 μm long and 1.5 nm thick, confirming the formation of 1D linear supramolecular polymers (Figure 5).

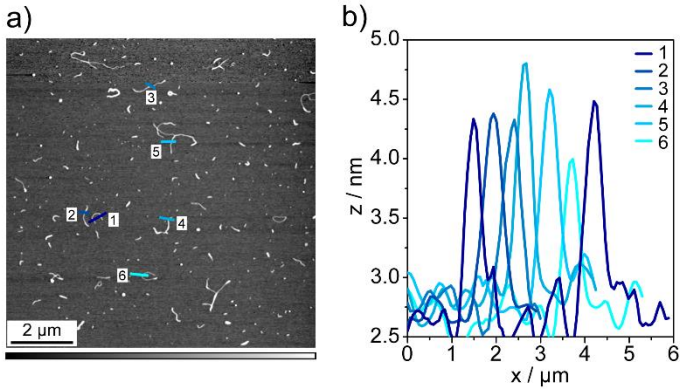

Figure 5. (a) AFM height measurements of **poly(*S*-B2)** on mica dropcasted from decalin (c = 30 μM) and (b) related profile analysis. Grey bar from 1.52 nm (black) to 5.62 nm (white).

6.5. Homopolymerization of tri(biphenyl)amines

Similarly, the supramolecular homopolymerizations of the nitrogen-based supramolecular polymers were investigated. Variable temperature UV-vis and CD studies of ***S*-N1** in decalin (c = 10 μM) displayed aggregation (Figure 6). However, the solution did not show full disaggregation at 100 °C, as visible from the presence of a positive CD signal at 100 °C (Figure 6b, red line). In addition, measurements recorded upon slow cooling from 100 °C to 20 °C displayed uncontrolled assembly as visible by some UV curves, which do not follow a clear trend (Figure 6a, grey curves), and from the CD cooling curve measured at λ =384 nm as a function of temperature (Figure 6d).

These results are probably related to the presence of an intense linear dichroism (LD) (Figure 6c). LD effects are usually caused by alignment of fibers in a preferred direction[52,53] and can interfere with the CD measurements causing artifacts. Several attempts to remove the LD and to obtain a controlled polymerization were tested. Stirring or shaking the solution resulted in an increased LD value. Polymerization in decalin with 5% $CHCl_3$, or in toluene, did not improve the control over the assembly. Considering all the results of ***S*-N1**, and comparing them with the ones obtained for ***S*-B1**, we conclude that this particular molecular design does not allow a full control over the polymerization. The ratio between the large conjugated cores and the few solubilizing chains is probably not adequately balanced.

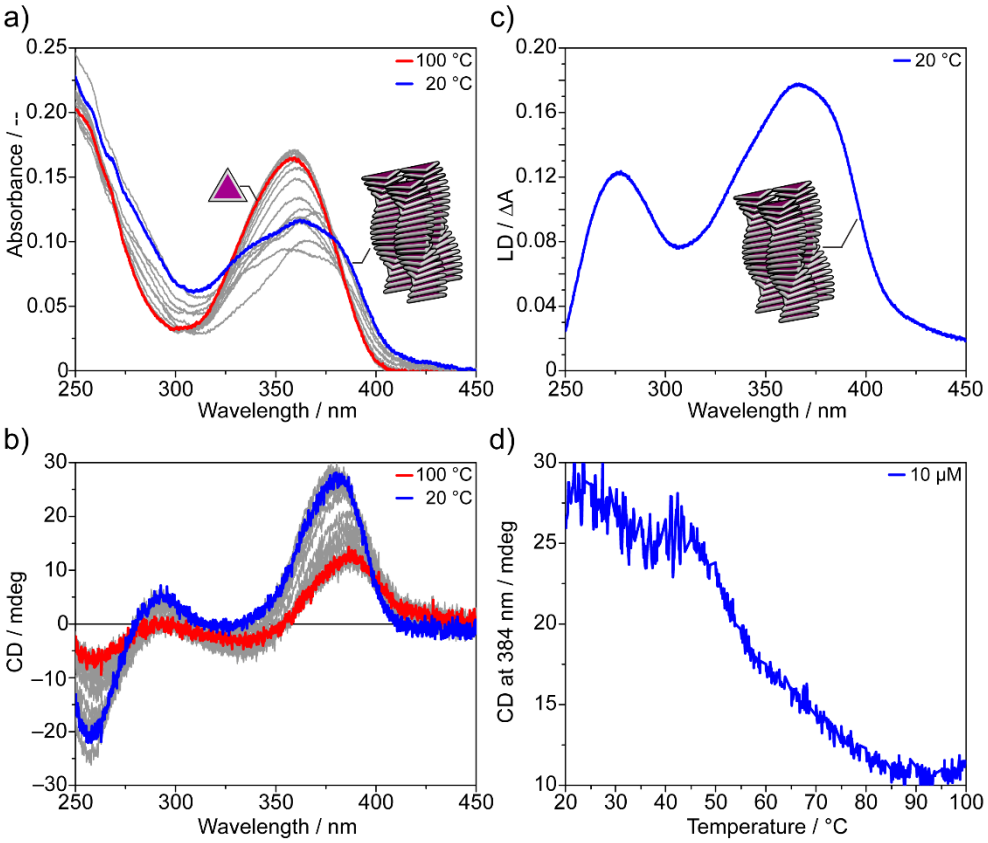

Figure 6. Variable temperature (a) absorbance and (b) CD spectra of ***S*-N1** in decalin (c = 10 μM). Measurements performed from 100 °C (red lines) to 20 °C (blue lines) with a cooling rate of 15 °C h^{-1}. (c) LD spectra recorded at 20 °C and (d) CD cooling curve followed at λ = 384 nm (cool rate = 15 °C h^{-1} , c = 10 μM).

In support of this, ***S*-N2**, which bear larger solubilizing units than ***S*-N1**, displays a controlled cooperative supramolecular polymerization in decalin. VT-UV, VT fluorescence, and VT-CD spectra recorded upon cooling the solution from 80 °C to 20 °C display aggregation (Figures 7a-c). The absorption spectra show small variation as blue-shift of the main peak and the rise of a small shoulder at λ = 380 nm (Figure 7a). CD spectra exhibit the formation of an aggregated state with negative bisignated Cotton effect at λ = 370 nm (Figure 7c). UV and CD cooling curves recorded at λ = 370 nm verify the formation of chiral supramolecular polymers **poly(*S*-*N*2)** in a cooperative fashion (Figure 7d).

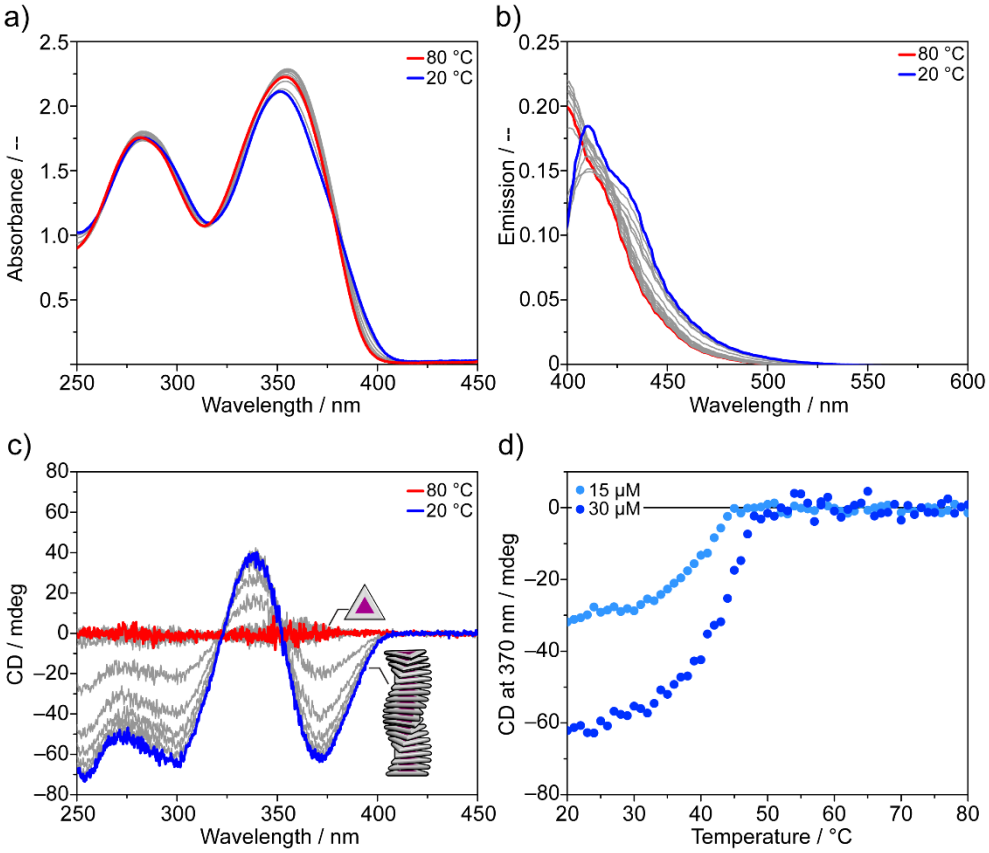

Figure 7. Variable temperature spectroscopic measurements of ***S*-N2.** (a) Absorbance, (b) emission, and (c) CD spectra from 80 °C (red lines) to 20 °C (blue lines). (d) CD cooling curves measured at λ = 370 nm, from 80 °C to 20 °C for different concentrations. Measurements performed in decalin, cooling rate 15 °C h^{-1}, spectra reported for c = 30 μM.

Variable temperature emission measurements display a red shift in the emission band and a small decrease in intensity of the main peak (Figure 7b) upon assembly. Between 80 °C and 50 °C the increase in emission intensity is probably due to a decrease in the non-radiative relaxation decays of the monomer. Below 50 °C the rise of the emission band at λ = 410 nm is assigned to the polymers. CPL measurement displays a negative g_{LUM} (Figure 8a), and emission lifetime measurement (Figure 8b) shows a fast fluorescence decay for both monomer, ***S*-N2,** and aggregated state, **poly(*S*-N2)**. However, the two components of the fluorescence decay show very similar lifetime (τ = 1.29 ns ***S*-N2** and τ = 2.15 ns **poly(*S*-N2)**).

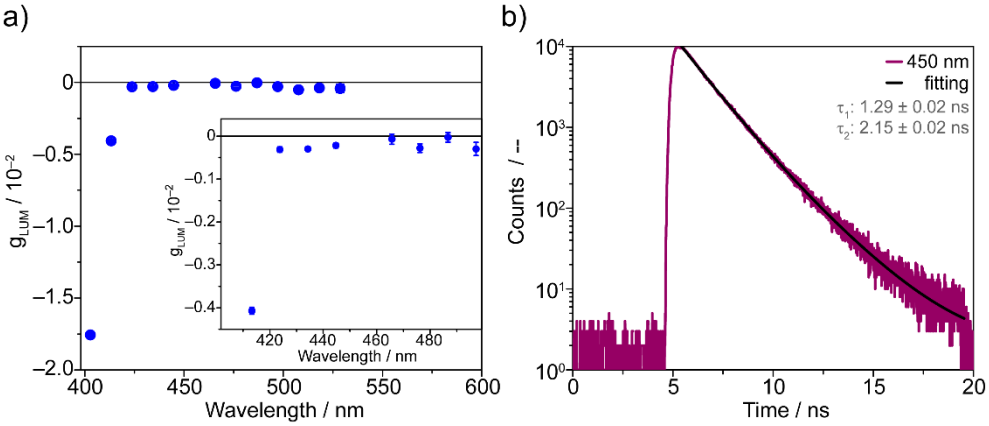

Figure 8. (a) Circular polarized emission spectra and (b) fluorescence lifetime of **poly(*S*-N2)** recorded in the aggregated state at 20 °C. Measurements performed in decalin *c* = 30 μM.

6.6. Supramolecular copolymerization of B-N monomers

Due to their similar cooperative behavior in the homopolymerizations, we selected ***S*-B2** and ***S*-N2** as monomers of choice to investigate the formation of copolymers. The supramolecular copolymerization was performed by mixing solution of ***S*-B2** (decalin, c = 30 μM) with one of ***S*-N2** (decalin, c = 30 μM) in a 1:1 ratio. The mixed solution was heated to 100 °C to reach the molecularly dissolved state and cooled to 20 °C to favor the polymerization (30 °C h^{-1}). Similar to Chapter 5,[54] the supramolecular copolymerization was investigated via variable temperature UV-vis, CD and emission measurements. VT-CD measurements display the formation of a negative CD signal upon cooling, indicative for the formation of chiral supramolecular polymers in solution (Figure 9a). However, the CD spectrum obtained at 20 °C for the mixture (c_{tot} = 30 μM, ratio 1:1 ***S*-B2**: ***S*-N2**) remarkably overlaps with the linear sum of the spectra of **poly(*S*-B2)** and **poly(*S*-N2)** at half of the concentration ($c_{S\text{-}B1}$ = $c_{S\text{-}B2}$ = 15 μM, linear sum calculated as: [$CD_{poly(S\text{-}B2)}$ + $CD_{poly(S\text{-}N2)}$]) (Figure 9b). This hints to self-sorting of the two homopolymers, where **poly(*S*-B2)** and **poly(*S*-N2)** are not interacting and their CD features are simply summed.[54,55] The CD cooling curve measured at λ = 363 nm upon slow cooling (30 °C h^{-1}) further sustains this hypothesis (Figure 9c).

Differently from the copolymerization reported in Chapter 5,[54] this time the cooling curve shows two independent transitions, a first one at 75 °C and a second one at 45 °C (Figure 9c, green line). Comparing this cooling curve with the cooling curve of **poly(*S*-B2)** (Figure 9c, blue line) and **poly(*S*-N2)** (Figure 9c, purple line), it is possible to correlate the two transitions found in the mixture to the T_e of each homopolymer. When comparing the linear sum of the cooling curve of the homopolymers at 15 μM, with the cooling curve of the mixture (c_{tot} = 30 μM, $c_{S\text{-}B1}$ = $c_{S\text{-}B2}$ = 15 μM) a clear overlap is observed (Figure 9c, green *vs.* black line). The two transitions observed in this cooling curve are further analyzed by evaluating the full CD spectra upon cooling. The shape of the CD effect is different in the two regions and coincides with the CD of **poly(*S*-B2)** above 45 °C (Figure 9a dark grey line) and to the sum of the two homopolymers below that transition. VT-UV spectra display the same behavior (data not shown) and the UV spectrum recorded at 20 °C after slow cooling largely coincides with the linear sum of the homopolymers (Figure 9d). Again, all the data are indicating the complete lack of interaction between the two supramolecular homopolymers. However, as shown in Chapter 5, a detailed analysis is required to confirm this conclusion.

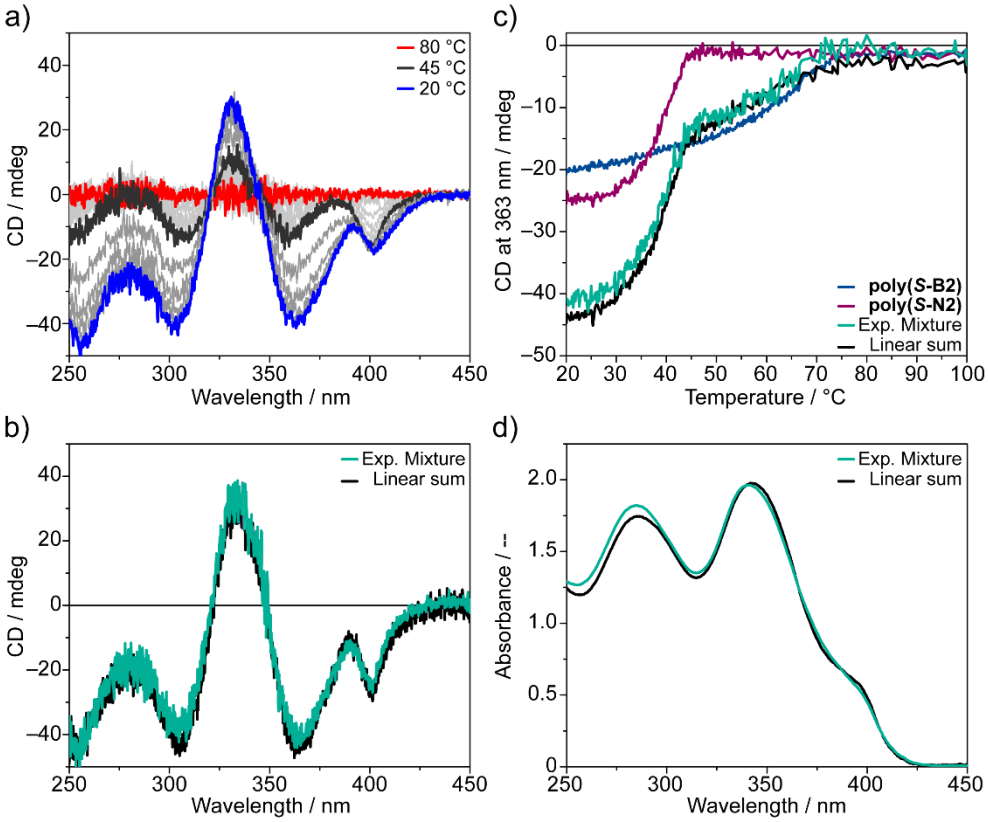

Figure 9. (a) Variable temperature CD spectra of the mixture 1:1 of ***S*-B2:*S*-N2** from 100 °C (red line) to 20 °C (blue line) (Cooling rate 30 °C h^{-1}, spectra recorded every 5 degrees). (b) Comparison of experimental CD spectrum of the 1:1 mixture (green line) (c_{tot} = 30 μM, $c_{S\text{-}B1}$ = $c_{S\text{-}B2}$ = 15 μM) and the linear sum of the CD **poly(*S*-B2)** and **poly(*S*-N2)** ($c_{S\text{-}B1}$ = $c_{S\text{-}B2}$ = 15 μM). (c) CD cooling curve followed at λ = 363 nm, for the 1:1 mixture (green line) (c_{tot} = 30 μM, $c_{S\text{-}B1}$ = $c_{S\text{-}B2}$ = 15 μM), **poly(*S*-B2)** (blue line), **poly(*S*-N2)** (purple line) and the linear sum of the homopolymers (black line) ($c_{S\text{-}B1}$ = $c_{S\text{-}B2}$ = 15 μM). (d) Comparison of experimental CD spectrum of the 1:1 mixture (green line) (c_{tot} = 30 μM, $c_{S\text{-}B1}$ = $c_{S\text{-}B2}$ = 15 μM) and the linear sum of the CD **poly(*S*-B2)** and **poly(*S*-N2)** ($c_{S\text{-}B1}$ = $c_{S\text{-}B2}$ = 15 μM). Measurements performed in decalin.

Variable temperature emission spectroscopy displays a decrease of the monomer emission at λ = 410 nm upon cooling and the growth of a broad emission band at λ = 430 nm with a shoulder at λ = 530 nm (Figure 10a, red line *vs.* blue line). In this case, we observed that the shoulder at λ = 520 nm grows non-linearly upon cooling and displays a sudden growth between 45 °C and 40 °C (Figure 10a inset, dark grey line). Following the emission intensity at λ = 530 nm upon cooling (Figure 10b) this double trend is clear and seems analogous to what observed in the CD cooling curve (Figure 9c). However, this time the emission cooling curve deviates remarkably from the linear sum of **poly(*S*-B2)** and **poly(*S*-N2)** (Figure 10b, green *vs.* black line).The homopolymers' emission of **poly(*S*-B2)** and **poly(*S*-N2)** at λ = 530 nm is just minimal

and belongs to the tail of the emission band of the supramolecular homopolymer's which occur at λ = 450 nm and λ = 410 nm, respectively (Figure 11a, top). Comparing the emission spectra of the mixture with that of both the homopolymers (Figure 11a, top) and the linear sum of the emission of the homopolymers (Figure 11a, bottom), we noticed that the deviation of the mixture is remarkable and large enough to be observed by eye (Figure 11c).

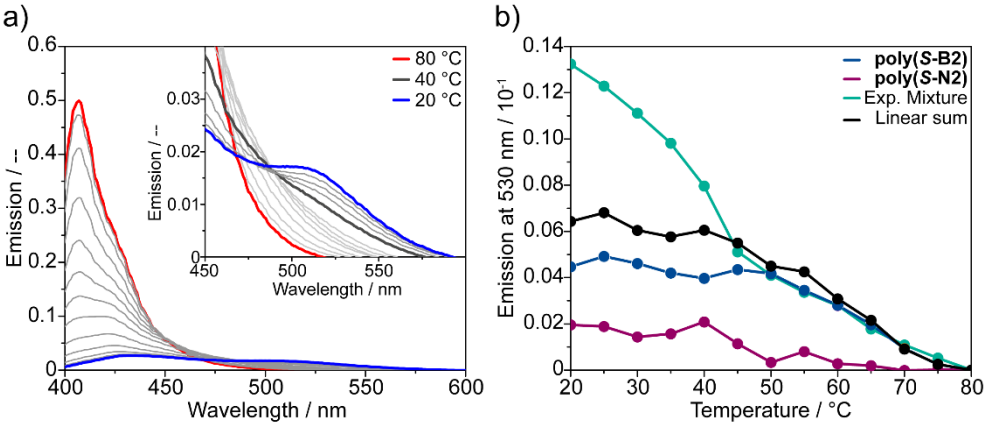

Figure 10. (a) Emission spectra of the 1:1 mixture **poly(*S*-B2):poly(*S*-N2)** from 80 °C (red line) to 20 °C (blue line) and (b) emission cooling curve followed at λ = 530 nm for the 1:1 mixture **poly(*S*-B2):poly(*S*-N2)** (green line) (c_{tot} = 30 μM, $c_{S\text{-}B1}$ = $c_{S\text{-}B2}$ = 15 μM), **poly(*S*-B2)** (blue line) **poly(*S*-N2)** (purple line) and the linear sum of the homopolymers (black line) ($c_{S\text{-}B1}$ = $c_{S\text{-}B2}$ = 15 μM). Measurements performed in decalin, cooling rate = 30 °C h^{-1}.

Moreover, the mixture of **poly(*S*-B2)** and **poly(*S*-N2)** exhibits circularly polarized emission both in the band at λ = 460 nm, attributable to the homopolymers emission, and in the emerging band at λ = 530 nm. The CPL intensity of the band at λ = 460 nm is in the order of g_{LUM} 2 10^{-3}, comparable with the one of **poly(*S*-B2)** and **poly(*S*-N2)** (Figure 11b *vs.* Figure 4a and Figure 8a), whereas the intensity at λ = 530 nm is about half of the magnitude. The lifetime of the emission at λ = 430 nm is moderately longer than **poly(*S*-B2)** but in the same order of magnitude (Figure 11d). Conversely, the excited state belonging to the transition at λ = 530 nm displays a dramatically longer lifetime compared to the homopolymers (Figure 11e). An accurate fitting of the decay is not possible due to the large number of components, however it is visible a fast decay, approximately of 15 ns, attributable to the homopolymers (inset Figure 11e, approximately first 15 ns) and a long-lived excited state which fully decays in 1μs. Such long decays are often attributed to some non-permitted transitions, *e. g.* charge-transfer interactions,[56] exciplexes[49,57] and excited triplet states.[58]

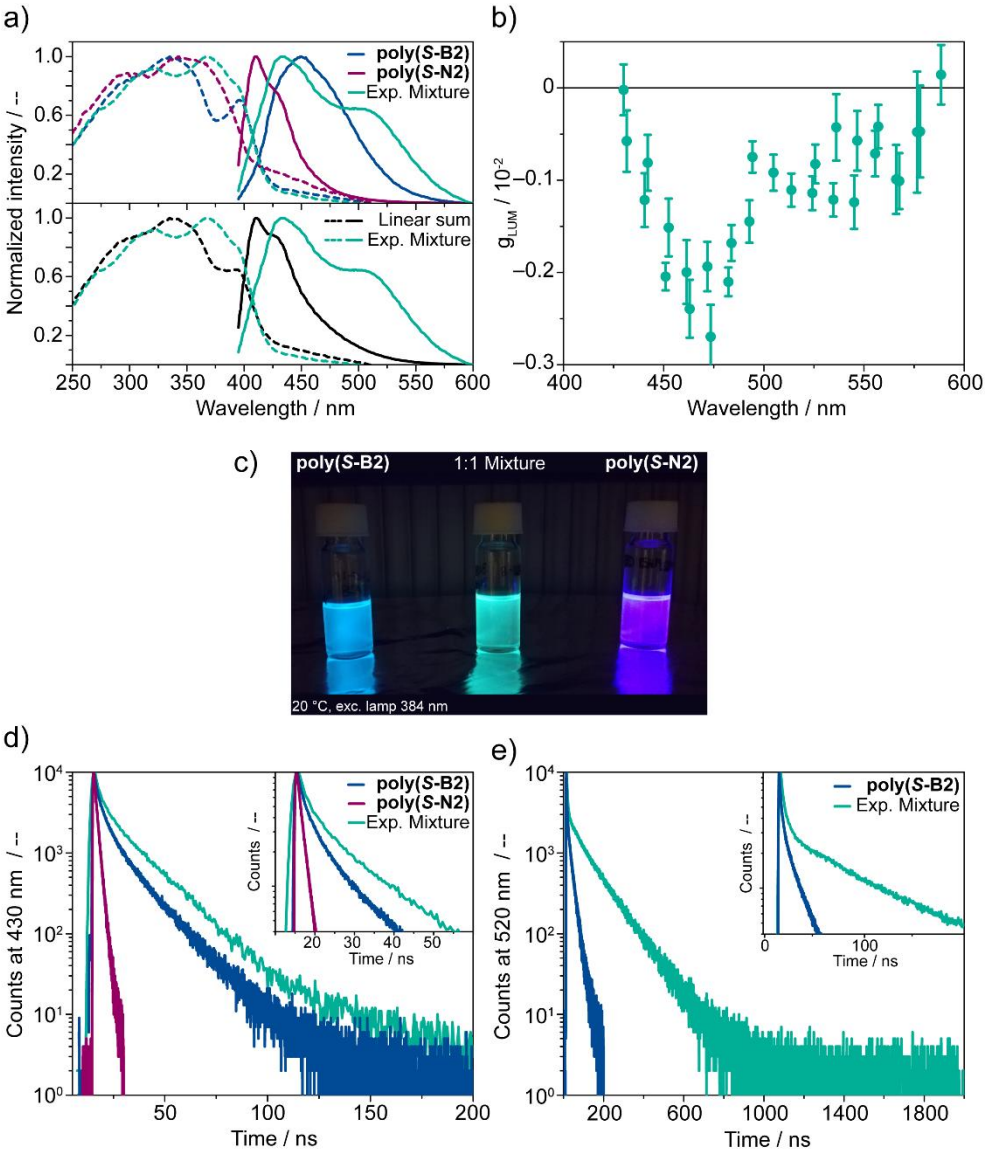

Figure 11. (a) Normalized excitation (dashed lines) and emission (solid lines) spectra of the 1:1 mixture **poly(*S*-B2):poly(*S*-N2)** (green lines), **poly(*S*-B2)** (a top, blue line), **poly(*S*-N2)** (a top, purple line), and the linear sum of the homopolymer spectra (a, bottom, black line). (b) CPL measurement of the 1:1 mixture **poly(*S*-B2):poly(*S*-N2)**. (c) Picture of **poly(*S*-B2)** (left)**, poly(*S*-B2):poly(*S*-N2)** (center), **poly(*S*-N2)** (right) under UV light (λ = 384 nm). (d, e) Emission lifetime at (d) λ = 430 nm and (e) λ = 520 nm. Decay of the mixture (green line), compared with **poly(*S*-B2)** (blue line) and **poly(*S*-N2)** (purple line, decay not possible for 530 nm). Measurements performed in decalin (c_{tot} = 30 µM, $c_{S\text{-}B2}$ = $c_{S\text{-}B1}$ = 15 µM) at 20° C.

To verify whether the long-lived excited state is due to a triplet state, we repeated the measurements in oxygen free conditions. The triplet ground state of O_2, can interact with the triplet excited state of organic emitters and decay via different paths by which the emission of the organic molecules is quenched.[59-62] Solutions of **poly(*S*-B2)** and **poly(*S*-N2)** were prepared in a N_2-equilibrated glovebox with anhydrous degassed decalin. The 1:1 mixture was obtained by addition of **poly(*S*-B2)** to **poly(*S*-N2)** at 20 °C. CD and emission spectra were recorded and compared with the spectra obtained for the 1:1 mixture prepared in the same way but in ambient condition (benchtop prepared, anhydrous not-degassed decalin). Whereas CD and CPL spectra display superimposable spectra of O_2-free and ambient-equilibrated samples (not shown), the emission exhibits a notable variation in the region of λ = 520 nm (Figure 12a). The degassed sample clearly presents two emission band of almost equal intensity (Figure 12a, green line), while the mixture in ambient condition shows just a minor shoulder in the same region (Figure 12a, dark grey line). Moreover, as visible from lifetime measurements (Figure 12b *vs.* Figure 11e), the lifetime of the excited state is largely affected by the presence of O_2. Degassed samples present an extraordinary long-lived excited state which fully decays in 3 μs (transition related to the band at λ =520 nm). This experiment is a further evidence of the formation of charge separated excited state, possibly in a triplet state.

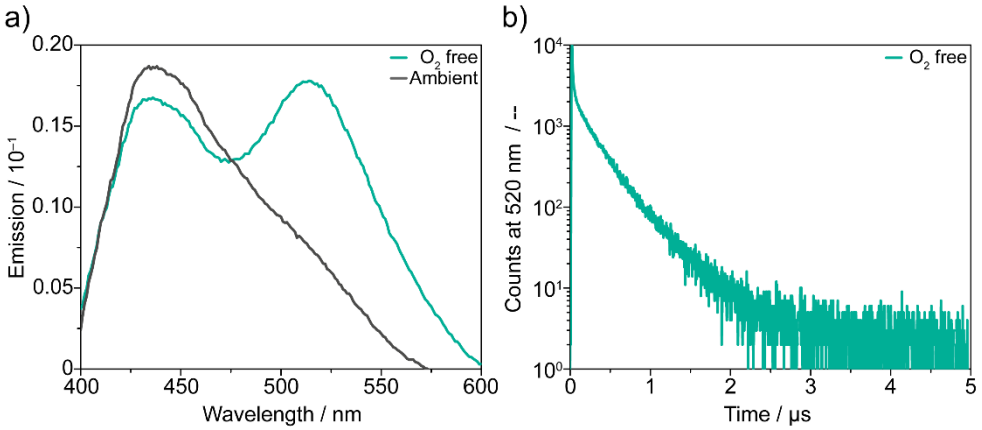

Figure 12. Oxygen free measurements of the 1:1 mixture of **poly(*S*-B2):poly(*S*-B1).** (a) Comparison of the emission spectra of the sample prepared in O_2 free (green line) and ambient (grey line) conditions. (b) Emission lifetime at λ = 520 nm of the sample prepared in O_2 free condition. Measurements performed in decalin (c_{tot} = 30 μM, $c_{S\text{-}B2}$ = $c_{S\text{-}B1}$ = 15 μM) at 20 °C.

In addition, we observed that the emission spectra of the 1:1 mixture of **poly(*S*-B2):poly(*S*-B1)** prepared by mixing **poly(*S*-B2)** to **poly(*S*-B1)** at 20 °C in presence of O_2 gives a moderate difference in the emission at λ = 530 nm compared to the sample treated by heating and slow-cooling (Figure 12a, grey line, direct mixing *vs.* Figure 11a, green line, measurement after slow cooling). To further investigate this, we followed spectroscopically the O_2 free mixture over a period of time. Between the measurements, the sample was kept at 20 °C, in light- and O_2-free conditions to avoid any possible interference. We observed that over a period of 10 days the system evolves in all its spectroscopic features. Absorbance (Figure 13a) and CD measurements (Figure 13b) display subtle, but visible, variation upon aging. Emission measurements display a decay of the band at λ = 420 nm and an increase of the band at λ = 530 nm (Figure 13c).

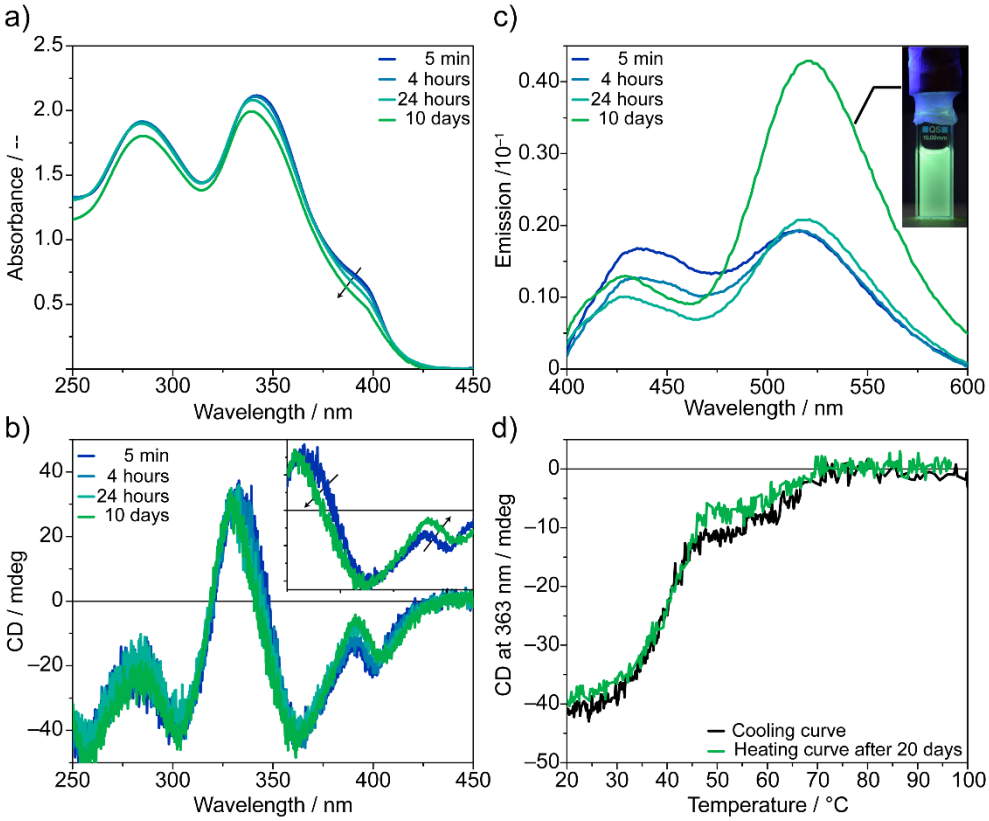

Figure 13. Evolution in time of the spectra of the 1:1 mixture of **poly(*S*-B2):poly(*S*-B1)** obtained upon mixing homopolymers at 20 °C in O_2 free condition and let equilibrate in at 20 °C in dark, O_2 free condition. (a) Absorbance, (b) CD, and (c) emission spectra. (d) CD heating curve (green light) recorded after 20 days of equilibration compared with CD cooling curve (black line). Measurements performed in decalin (c_{tot} = 30 μM, $c_{S\text{-}B2} = c_{S\text{-}B1}$ = 15 μM) at (a,b,c) 20 °C or (d) cooling heating rate = 30 °C h^{-1}.

Measurements recorded after 20 days do not display further changes in the spectroscopic features (not shown). We then performed a heating curve from 20 °C to 100 °C (heat rate: 30 °C h^{-1}) on the sample equilibrated for 20 days at 20 °C and compared it with the cooling curve recorded from monomerically dissolved state form 100 °C to 20 °C (heat rate: 30 °C h^{-1}) (Figure 13d). Although also the depolymerization curve displays two transitions as the polymerization curve, they do not coincide. The largest deviation is recorded between 45 °C and 70 °C where the heating curves displays a CD reduced by one third compared to the cooling curve. Since the CD in that region is mainly attributed to **poly(*S*-B2)** (Figures 9a, 9c), we speculate that the lower intensity recorded upon heating is related to less polymerized ***S*-B2** in that specific temperature section. This can be explained by the following hypothesis: upon mixing **poly(*S*-B2)** with **poly(*S*-N2)** and equilibration, some ***S*-B2** monomers are incorporated in the **poly(*S*-N2)**. Then, when the heating curve is performed and **poly(*S*-N2)** disaggregates, the ***S*-B2** monomers hosted in **poly(*S*-N2)** get depolymerized as well causing a less intense CD above 45 °C.

6.7. Discussion

The mixture between **poly(*S*-B2)** and **poly(*S*-N2)** displays ground state properties, such as absorbance and CD, which could be directly related to the homopolymer mixture suggesting self-sorting of **poly(*S*-B2)** and **poly(*S*-N2)**. However, emission studies reveals the insurgence of a green emission which presents remarkably long lifetime and sensitivity to O_2. This feature can be assigned to the presence of B-N excimers or Lewis pairs.[17] This emission band presents circular polarization and is found just in conditions in which the system is fully aggregated (measurements in DCE c = 5 mM do not show emission at $\lambda \geq 500$ nm, data not shown). These characteristics indicates that the B-N excimers (or Lewis pairs) are incorporated in the chiral supramolecular polymer structures. [19,21]

However, it has to be considered that UV-vis and CD are techniques that measure the whole system, while emission measurements represent only the emitting species in a weighted average based on their relative quantum yield. Combining all the results, we hypothesize that the ***S*-B2**:***S*-N2** mixture can mainly be described by self sorting and the polymerization of the two systems occurs independently. Upon cooling, between 75 °C and 45 °C, **poly(*S*-B2)** is formed and ***S*-N2** is still molecularly dissolved; below 45 °C ***S*-N2** begins to polymerize into **poly(*S*-N2)** while **poly(*S*-B2)** grows into longer polymers**.** However, due to the intrinsic reversibility of supramolecular systems, monomers can exchange in and out the main chain. This exchange causes a few ***S*-B2** to insert in **poly(*S*-N2)** (or *vice versa*). This effect, which causes the rise of the emitting properties, is reminiscent to the doping effect in semiconductors. These doping units within the supramolecular polymers have a charge-separated excited state and give the green emission (Figure 14a).

We also observed that in time the mixture displays a more intense green emission and subtle deviations in UV and CD spectra indicating a more intimate mixing of ***S*-B2** and ***S*-N2**, so probably more B-N couples are formed (Figure 14b). This hypothesis, is sustained by the heating curve measured after 20 days of equilibration and can be related to the kinetic profile of the mixing process which appears to be rather slow. Slow dynamics in supramolecular polymers are occasionally observed and are often coupled with the presence of a competitive aggregation pathways.[63,64]

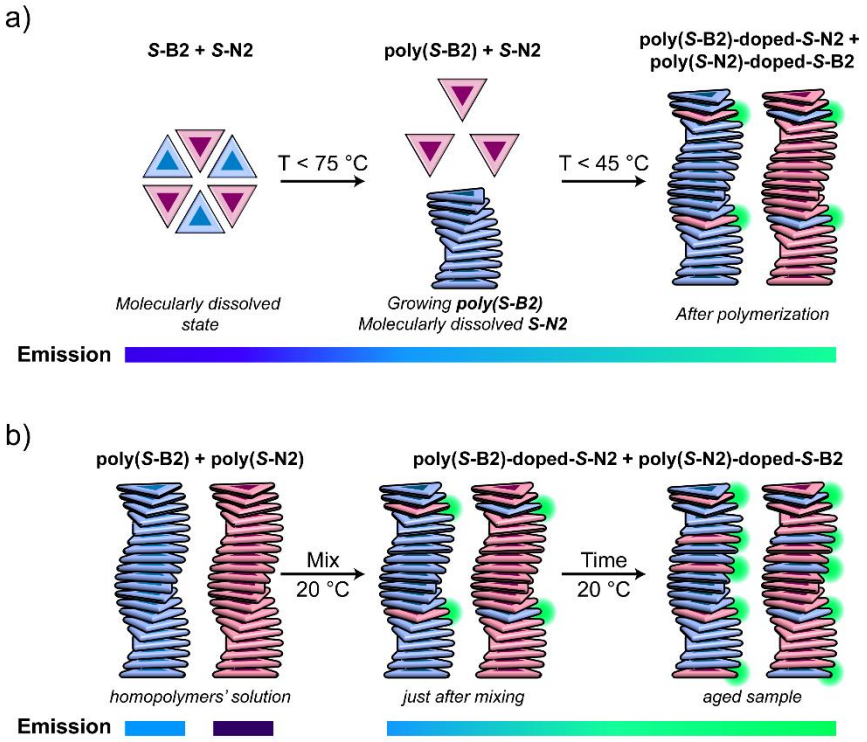

Figure 14. Schematic representations of some of the possible mechanisms for self-sorting and partial copolymerization of **poly(*S*-B2)** and **poly(*S*-N2)** from (a) molecularly dissolved state and (b) from homopolymers.

6.8. Conclusions

In conclusion, we reported on the synthesis and the supramolecular polymerization of bridged triphenylboranes and their copolymerization with tri(biphenyl)amine-based monomers. A first study on the homopolymerization of the boron and nitrogen monomers highlighted the possibility of obtaining controlled chiral supramolecular homopolymers for both O-bridged triphenylborane and tri(biphenyl)amine-based monomers bearing nine solubilizing side chains. Both B- and N-based molecules show interesting emission properties in assembled state as circularly polarized luminescence and lifetime emission in the order of 15 ns for the boron molecules and 2 ns for the nitrogen analogues.

We then investigated whether a 1:1 mixture of O-bridged triphenylborane and tri(biphenyl)amine-based monomers could copolymerize and generate new emergent properties. Although ground state optical measurements evidenced the occurrence of self-sorting, emission spectroscopy highlighted the presence of a charge-separated excited state which can be addressed to a B-N interaction in an aggregated state. This emergent characteristic originating from the B-N mixture displays circularly polarized emission and an incredibly long excited state lifetime, which could be of high interest for new functional materials. We speculate that this feature originates from the presence of a few B molecules in the N stack (and *vice versa*) and acts similarly to a *p*-*n* doping effect.

The results presented here are the first demonstration of B-N supramolecular couples that can interact and give rise to new emerging properties. We propose that this interaction can be exploited both in solution and in the bulk state. However, these molecules show just a partial interaction, which we speculate is due to their difference in geometry. The rigid bridged B core and the flexible N core influence the thermodynamics involved in the related homopolymerization and therefore cause a large difference in the elongation temperatures (T_es). We maintain that by tuning the two homopolymerization T_es we may obtain a more efficient co-interaction. We are currently testing this hypothesis by applying two strategies. Firstly, modifying the feed ratio of ***S*-B2:*S*-N2** in order to shift the two T_es closer together, and secondly, re-designing the B and N monomers to further improve the hetero-interactions. We anticipate that these adjustments may lead to outstanding optical and conductive properties.

6.9 Experimental section

6.9.1 Materials and methods

All solvents were obtained from Biosolve, Acros or Aldrich. All other chemicals were obtained from Aldrich. Dry DCM, THF, and DMF were tapped off a distillation setup which contained molsieves. $CHCl_3$ was dried over molsieves and triethylamine was stored on KOH pellets. (*S*)-(-)-Citronellol was purchased from Aldrich and converted into the corresponding (*S*)-3,7-dimethyloctan-1-amine according to a described procedure. All other chemicals were used as received. Septum-sealed anhydrous decalin used as solvent was purchased by Aldrich and used as received for preparing the solutions (unless otherwise mentioned). Synthesized compounds were vacuum-oven dried before use.

Detail on ^{1}H NMR, ^{13}C NMR, MALDI-TOF-MS, FTIR and AFM can be found in the experimental section of Chapter 2. UV/Vis and circular dichroism (CD) measurements were performed on a Jasco J-815 spectropolarimeter, for which the sensitivity, time constants and scan rates were chosen appropriately. Corresponding temperature-dependent measurements were performed with a Jasco PFD-425S/15 Peltier-type temperature controller with a temperature range of 263–393 K and adjustable temperature slope. The Spectrophotometer is equipped with a multi-cells holder for 6 samples and the temperature controlled was set on the holder station. In all experiments the linear dichroism was also measured, unless otherwise mentioned, no linear dichroism was observed. Separate UV/Vis spectra were obtained from a Perkin–Elmer UV/Vis spectrometer Lambda 40. Fluorescence spectra were measured with Jasco FMO-427S/15 fluorimeter implemented in the CD spectrometer. CPL measurements were carried out using a custom built setup equipped with a photo-elastic modulator and a 16-channel photomultuplier array possessing a photon counting detection method. The excitation wavelength was selected from a Hg lamp using appropriate interference and bandpass filters (λ = 365 nm). The excitation light was depolarized by passing it through a bundle of optical fibers. The direction of the excitation was normal to the surface of the film and in line with the direction of emission collection. Time resolved photoluminescence spectra were recorded on an Edinburgh Instruments LifeSpec-PS spectrophotometer.

For all spectroscopic measurements, cells with an optical path length of 1 cm were employed and spectroscopic grade solvents were employed. Solutions were prepared by weighing the necessary amount of compound for the given concentration and dissolved with a weighted amount of solvent based on its density. The stock solutions were heated up, sonicated till complete dissolution and slowly cooled down to room temperature every time before use unless otherwise specified. The stock solutions were heated up and sonicated till complete dissolution every time before the preparation of diluted sample solutions. Unless otherwise mentioned, all the spectroscopic measurement were performed with freshly prepared solutions (max. 1 week after the preparation of the stock solution). CD experiments related to the oxygen effects were performed using special precaution to control the humidity and O_2. Cuvettes equipped with a screw cap and a Teflon-lined septum were found to be best suited for these measurements. The preparation of the solution and the filling of the cuvette was done in N_2 equilibrate glovebox and degassed anhydrous decalin was used.

6.9.2 Synthetic procedures

The synthesis of all the molecules consist in a final Suzuki cross-coupling step between the bridged triphenylborane, or triphenylamine, core and the solubilizing wedge. The cores were previously synthesized by Yamaguchi's group (for ***S*-B1**, ***S*-B2**, ***S*-B3**) or by us (see Chapter 4, experimental section for tris(4-bromophenyl)amine). The solubilizing wedges were synthesized as follow (Scheme 3). The peripheries which bear an amide group as supramolecular unit, **4** and **5**, were synthesized with the classic amino acid coupling agent, EDC (1-Ethyl-3-(3-dimethylaminopropyl)carbodiimide). The wedges that do not bear any amide, **6** and **7** were obtained by nucleophilic substitution with chiral mesylate (**6**) or 1-bromododecane (**7**). All chiral reagents required: (*S*)-3,7-dimehtyloctlyamine, (*S*)-3,4,5-tris((3,7-dimethyloctyl)oxy)benzoic acid and (*S*)-3,7-dimethyloctyl 4-mesilate were previously synthesized in the group as described in literature.[65,66,67]

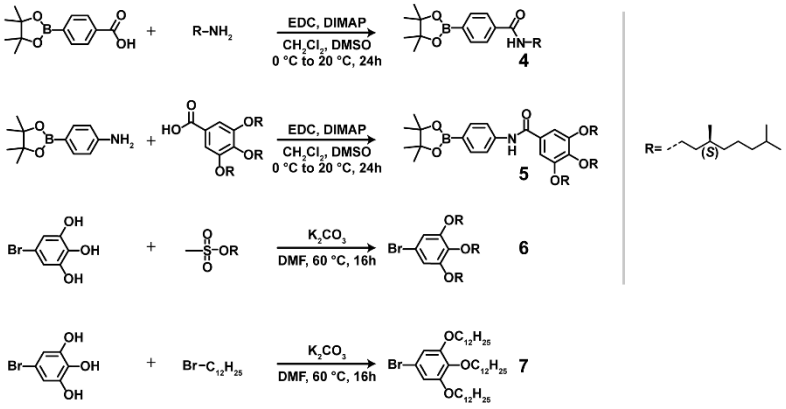

Scheme 3. Synthetic scheme for the synthesis of the chiral solubilizing wedges.

(S)-N-(3,7-Dimethyloctyl)-4-(4,4,5,5-tetramethyl-1,3,2-dioxaborolan-2-yl)benzamide (4)

In a three neck round bottom flask 4-carboxylphenylboronic acid pinacol ester (3 g, 12.09 mmol), EDC (2.78 g, 14.51 mmol) and 4-dimethylaminopyridine (DIMAP) (1.92 g, 17.72 mmol) were dissolved in dry CH_2Cl_2 (100 mL) and DMSO (2.6 mL) at 0 °C and stirred under Argon for 15 minutes. Then, (*S*)-3,7-dimethyloctylamine (2.85 g, 18.14 mmol) was slowly added and the reaction let reach 20 °C and stirred for 24 h. After completion, the reaction was washed with 1 M HCl (3 x 100 mL) and with water (2 x 100 mL). The organic fraction was collected, dried over $MgSO_4$, and evaporated under reduced pressure affording to **4** as transparent highly viscous liquid (3.53 g, 9,12 mmol), 75% yield.

^{1}H-NMR ($CDCl_3$, 400 MHz) δ (ppm): 7.85 (d, 2H, *J* = 8 Hz), 7.73 (d, 2H, *J* = 8Hz), 6.05 (s, 1H), 3.51-3.42 (m, 2H), 1.68-1.14 (mm, 22H), 0.94 (d, 3H, *J* = 6.5 Hz), 0.86 (d, 6H, *J* = 6.5); ^{13}C-NMR ($CDCl_3$, 100 MHz) δ (ppm): 167.34, 137.09, 134.95, 125.93, 84.11, 39.23, 38.29, 37.15, 36.76, 30.82, 27.95, 24.88, 24.65, 22.69, 22.56, 19.57; m/z (MALDI) Calcd. for $[C_{23}H_{39}BNO_3]^+$ $[M-H]^+$ 388.29, found 388.34; FT-IR (cm^{-1}) 3313, 3073, 2954, 2927, 2869, 1636, 1615, 1542, 1509, 1466, 1398, 1358, 1324, 1270, 1214, 1166, 1142, 1089, 1021, 692, 858, 830, 815, 771, 710, 654, 633, 578, 521, 461

3,4,5-tris(((S)-3,7-Dimethyloctyl)oxy)-N-(4-(4,4,5,5-tetramethyl-1,3,2-dioxaborolan-2-yl)phenyl)benzamide (5)

In a three neck round bottom flask 3,4,5-tris(((*S*)-3,7-dimethyloctyl)oxy)benzoic acid (3 g, 5.08 mmol), EDC (1.17 g, 6.10 mmol) and 4-dimethylaminopyridine (DIMAP) (806 mg, 6.60 mmol) were dissolved in dry CH_2Cl_2 (41 mL) and DMSO (1.1 mL) at 0 °C and stirred under Argon for 15 minutes. Then, 4-aminophenylboronic acid pinacol ester (1.67 g, 7.62 mmol) was slowly added and the reaction let reach 20 °C and stirred for 24 h. After completion, the reaction was washed with 1 M HCl (3 x 100 mL) and with water (2 x 100 mL). The organic fraction was collected, dried over $MgSO_4$, and evaporated under reduced pressure. The product was then purified with SiO_2 chromatography (Heptane/EtOAc gradient from 100% heptane to v/v 5:5) affording to **5** as white solid (2.19 g, 2.76 mmol) 54% yield.

^{1}H-NMR ($CDCl_3$, 400 MHz) δ (ppm): 7.82 (d, 2H, *J* = 8.4 Hz), 7.73 (s, 1H), 7.65 (d, 2H, *J* = 8.4 Hz), 7.05 (s, 2H), 4-11-3.99 (m, 6H), 1-92-1.47 (mm, 16H), 1.35 (s, 12H), 1.29-1.15 (mm, 16H), 0.96-0.92 (m, 9H), 0.87 (d, 18H, *J* = 6.6 Hz); ^{13}C-NMR ($CDCl_3$, 100 MHz) δ (ppm): 165.51, 153.30, 141.64, 140.68, 135.89, 135.89, 129.85, 118.85, 105.81, 83.78, 71.81, 67.82, 39.37, 39.27, 37.51, 37.34, 36.38, 29.85, 29.67, 29.85, 29.67, 27.66, 24.89, 24.74, 24.89, 24.74, 22.71, 22.60, 19.60; m/z (MALDI) Calcd. for $[C_{49}H_{83}BNO_6]^+$ [M-H]$^+$ 792.62, found 792.64; FT-IR (cm^{-1}) 3269, 2954, 2926, 2869, 1647, 1583. 1527, 1498, 1467, 1427, 1396, 1356, 1335, 1285, 1272, 1211, 1144, 1114, 1088, 1047, 995, 962, 918, 860, 842, 737, 672, 655, 635, 614, 579, 521

5-Bromo-1,2,3-tris(((S)-3,7-dimethyloctyl)oxy)benzene (6)

In a three neck round bottom flask 5-bromobenzene-1,2,3-triol (1.24 g, 6.07 mmol) and K_2CO_3 (7.97 g, 50.40 mmol) were dissolved in dry DMF (10 mL). The mixture was stirred at 20 °C for 30 min, then (*S*)-3,7-dimethyloctyl methanesulfonate (6 g, 25.38 mmol) was added and the reaction heated to 60 °C for 18 h. The reaction mixture was then diluted with Et_2O (120 mL) and washed with water (3 x 100 mL). The organic fraction was collected, dried over $MgSO_4$ and evaporated under reduced pressure. SiO_2 chromatography (Heptane/CH_2Cl_2 gradient from 100% Heptane to 100% CH_2Cl_2) afforded to **6** as transparent liquid (1.2 g, 1.91 mmol) Yield 31%.

^{1}H-NMR ($CDCl_3$, 400 MHz) δ (ppm): 6.68 (s, 2H), 4.01-3.88 (m, 6H), 1.88-1.456 (mm, 12H), 1.37-1.13 (mm, 20H), 0.94-0.90 (m, 9H), 0.87 (d, 12H, *J* = 6.6 Hz), 0.86 (d, 6H, *J* = 6.6 Hz); ^{13}C-NMR ($CDCl_3$, 100 MHz) δ (ppm): 153.83, 137.42, 115.56, 110.07, 71.68, 67.60, 39.37, 39.27, 37.52, 37.32, 37.29, 36.26, 29.80, 29.67, 27.99, 24.73, 22.71, 22.62, 22.60, 19.56; FT-IR (cm^{-1}) 2953, 2927, 2870, 1587, 1493, 1468, 1422, 1383, 1224, 1115, 810

5-Bromo-1,2,3-tris(dodecyloxy)benzene (7)

In a three neck round bottom flask 5-bromobenzene-1,2,3-triol (1. 4 g, 6.83 mmol) and K_2CO_3 (7.83 g, 56.7 mmol) were dissolved in dry DMF (12 mL). The mixture was stirred at 20 °C for 30 min, then 1-Bromo dodecane (7.49g, 30 mmol) was added and the reaction heated to 60 °C for 18 h. The reaction mixture was poured into water (200 mL) and extracted with Et_2O (3 x 100 mL). The organic fraction was collected, dried over $MgSO_4$ and evaporated under reduced pressure. SiO_2 chromatography (Heptane/CH_2Cl_2 gradient from 100% Heptane to 100% CH_2Cl_2) afforded to **7** as transparent liquid (2.67 g, 3.76 mmol) Yield 55%.

^{1}H-NMR ($CDCl_3$, 400 MHz) δ (ppm): 6.66 (s, 2H), 3.95-3.86 (m, 6H), 1.77-1.66 (m, 6H), 1.35-1.20 (m, 14H), 0.87 (t, 9H).

4,4',4''-(5,9-dioxa-13b-boranaphtho[3,2,1-de]anthracene-3,7,11-triyl)tris(N-((S)-3,7-dimethyloctyl) benzamide) (S-B1)

In a Schlenk tube under argon, **BBr** (100 mg, 0.20 mmol), **4** (382 mg, 0.99mmol), XPhos (61 mg, 0.13 mmol), K_3PO_4 (439 mg, 2.07 mmol) and $Pd_2(dba)_3$-$CHCl_3$ (32.68 mg, 0.03 mmol) were introduced and dissolved in dry toluene (7.9 mL). The reaction was stirred and heated to 110 °C under argon for 48h. The reaction mixture was then diluted in with $CHCl_3$ (80 mL) and washed with water (3 x 100 mL). The organic fraction was collected, dried over $MgSO_4$ and evaporated under reduced pressure. The product was first purified with SiO_2 chromatography ($CHCl_3$:EtOAc, v/v = 9:1), then with GPC (hexane) and finally with HPLC (CH_2Cl_2:EtOAc v/v =8:2) affording to ***S*-B1** as yellow solid (120mg, 0.11 mmol) yield 58%.

^{1}H-NMR ($CDCl_3$, 400 MHz) δ (ppm): 8.34 (d, 2H, *J* = 7.44 Hz), 7-74-7.70 (mm, 6H), 7-58-7.54 (mm, 8H), 7.34 (d, 2H, *J* = 7,2 Hz), 7.20 (s, 2H), 6.54 (s, 3H), 3.60-3.49 (m, 6H), 1.78-1.57 (mm, 7H), 1.42-1.16 (mm, 23H), 1.00 (d, 9H, *J* = 6.4 Hz), 0.89 (d, 18H, *J* = 6.6 Hz); ^{13}C-NMR ($CDCl_3$, 100 MHz) δ (ppm): 168.25, 156.69, 147.65, 134.58, 134.00, 129.82, 127.41, 127.34, 126.33, 99.99, 39.33, 38.55, 37.36, 36.76, 31.08, 28.02, 24.80, 22.78, 22.66, 19.66 m/z (MALDI) Calcd. for $[C_{69}H_{87}BN_3O_5]^+$[M-H]$^+$, 1047.67 found 1048.63; FT-IR (cm^{-1}) 3285, 2953, 2925, 2868, 1632, 1608, 1577, 1540, 1510, 1464, 1422, 1395, 1384, 1347, 1301, 1213, 1164, 1108, 1069, 1016, 940, 839, 819, 764, 692, 572.

N,N',N''-(5,9-dioxa-13b-boranaphtho[3,2,1-de]anthracene-3,7,11-triyltris(benzene-4,1-diyl))tris(3,4,5-tris(((S)-3,7-dimethyloctyl)oxy)benzamide) (S-B2)

In a Schlenk tube under argon, **BBr** (100 mg, 0.20 mmol), **5** (781 mg, 0.99 mmol), XPhos (61 mg, 0.13 mmol), K_3PO_4 (439 mg, 2.07 mmol) and $Pd_2(dba)_3$-$CHCl_3$ (32.68 mg, 0.03 mmol) were introduced and dissolved in dry toluene (7.9 mL). The reaction was stirred and heated to 110 °C under argon for48 h. The reaction mixture was then diluted with $CHCl_3$ (80 mL) and washed with water (3 x 100 mL). The organic fraction was collected, dried over $MgSO_4$ and evaporated under reduced pressure. The product was first purified with SiO_2 chromatography (Hexane: CH_2Cl_2, v/v = 3:6), then with HPLC ($CHCl_3$) and finally with GPC (hexane) affording to ***S*-B2** as yellow solid (200mg, 0.09mmol) yield 45%.

^{1}H-NMR ($CDCl_3$, 400 MHz) δ (ppm): 8.69(d, 2H, *J* = 8.2 Hz), 7.84 (s, 3H), 7.79-7.78 (m, 14H), 7.63 (d, 2H, *J* = 8.2 Hz), 7.14 (s, 2H), 7.13 (s, 6H), 4.14-4.07 (m, 18H), 1.94-1.18 (mm, 90H), 0.99-0.95 (mm, 27H), 0.90-0.89 (mm, 54H) ^{13}C-NMR ($CDCl_3$, 100 MHz) δ (ppm): 166.45, 156.78 141.32, 134.59, 128.09, 127.44, 126.26, 126.39, 113.41, 104.66, 99.97, 99.77, 84.95, 39.32, 38.54, 37.32, 36.77, 31.06, 28.01, 24.79, 22.76, 22.65, 19.64 m/z (MALDI) Calcd. for $[C_{147}H_{219}BN_3O_{14}]^+$[M-H]$^+$, 2261.65 found 2261.44; FT-IR (cm^{-1}) 3303, 2953, 2926, 2865, 2842, 1676, 1649, 1610, 1596, 1583, 1567, 1520, 1494, 1468, 1423, 1396, 1383, 1365, 1332, 1268, 1237, 1210, 1185, 1163, 1113, 1068, 1016, 992, 938, 835, 816, 765, 753, 710, 575, 526.

4,4,12,12-Tetramethyl-2,6,10-tris(3,4,5-tris(((S)-3,7-dimethyloctyl)oxy)phenyl)-8,12-dihydro-4H-3a2-boradibenzo[cd,mn]pyrene (S-B3)

In a Schlenk tube under argon, **BPin** (50 mg, 0.08mmol), **6** (248 mg, 0.39 mmol), XPhos (26 mg, 0.054 mmol), K_3PO_4 (172 mg, 0.81 mmol) and $Pd_2(dba)_3$-$CHCl_3$ (14 mg, 0.01 mmol) were introduced and dissolved in dry toluene (3 mL). The reaction was stirred and heated to 110 °C under argon for 48 h. The reaction mixture was then diluted with $CHCl_3$ (40 mL) and washed with water (3 x 30 mL). The organic fraction was collected, dried over $MgSO_4$ and evaporated under reduced pressure. The product was first purified with SiO_2 chromatography (hexane:EtOAc v/v = (8:2), then with GPC (hexane) and finally with HPLC (hexane;EtOAc v/v = 9:1) affording to a dark-yellow viscous liquid (20mg, 0.01 mmol) yield 13 %.

^{1}H-NMR ($CDCl_3$, 400 MHz) δ (ppm): 8.50 (s, 2H0, 8.12 (s, 2H), 7.84 (s, 2H), 6.94 (s, 4H), 6.89 (s, 2H), 4.16-4.04 (mm, 18H), 2.01-1.16 (mm, 48H), 1.45-1.68 (mm, 66H), 0.99-0.86 (mm, 81 H); ^{13}C-NMR ($CDCl_3$, 100 MHz) δ (ppm): 160.24, 156.87, 153.60, 146.6, 145.54, 139.19, 136.34, 129.89, 125.60, 123.71, 122.82, 122.70, 107.58, 106.93, 71.91, 71.82, 68.21, 67.80, 67.69, 39.39, 39.29, 37.57, 37.42, 36.54, 33.74, 30.45, 29.86, 29.77, 28.00. 24.76, 22.72, 22.62, 19.64 m/z (MALDI) Calcd. for $[C_{133}H_{216}BO_9]^+$[M-H]$^+$, 1698.65 found 1968.81; FT-IR (cm^{-1}) 2953, 2926, 1969, 1657, 1583, 1558, 1504, 1463, 1435, 1384, 1347, 1235, 1114, 1045, 999, 902, 830, 735, 700, 669, 619.

4',4''',4'''''-Nitrilotris(N-((S)-3,7-dimethyloctyl)-[1,1'-biphenyl]-4-carboxamide) (S-N1)

In a three neck round bottom flask under argon, **NBr** (1 g, 2.07 mmol), **4** (3.97 g, 10.24 mmol), K_2CO_3 (2.3 g, 16.5 mmol), and $Pd_2(PPh_3)_4$ (120 mg, 0.104 mmol) were introduced and dissolved in dioxane (38 mL) and water was then added (1.3 mL). The reaction was stirred and heated to 100 °C under argon for 36 h. The reaction mixture was then diluted with $CHCl_3$ (100 mL) and washed with water (3 x 80 mL). The organic fraction was collected, dried over $MgSO_4$ and evaporated under reduced pressure. The product was first purified with SiO_2 chromatography ($CHCl_3$/MeOH v/v = 98:4), then recrystallized from acetonitrile affording to ***S*-N1** as a white solid (1.3g, 1.27 mmol) yield 61%.

^{1}H-NMR ($CDCl_3$, 400 MHz) δ (ppm): 7.82 (d, 6H, *J* = 8.3 Hz), 7.64 (d, 6H, *J* = 8.3 Hz), 7.55 (d, 6H, *J* = 8.6 Hz), 7.24 (d, partially hidden by $CHCl_3$ signal), 6.07 (t, 3H, *J* =4.8 Hz), 3.54-3.47 (m, 6H), 1.67-1.62 (m, XXH), 1.53-1.15 (mm, XXH), 0.96 (d, 9H, *J* = 6.5 Hz), 0.87 (d, 18H, *J* = 6.6 Hz); ^{13}C-NMR ($CDCl_3$, 100 MHz) δ (ppm): 167.13, 147.19, 143.36, 134.66, 133.18, 128.10, 127.41, 126.69, 124.55, 39.24, 38.29, 37.17, 36.81, 30.83, 27.67, 24.68, 22.70, 22.60, 19.58; m/z (MALDI) Calcd. for $[C_{69}H_{90}N_4O_3]^{\bullet+}$ $[M]^{\bullet+}$, 1022.70 found 1022.72; FT-IR (cm^{-1}) 3305, 3034, 2958, 2924, 2867, 1366, 1599, 1537, 1489, 1381, 1366, 1314, 1296, 1281, 1198, 1146, 1005, 859, 823, 770, 723, 683, 637, 530.

N,N',N''-(Nitrilotris([1,1'-biphenyl]-4',4-diyl))tris(3,4,5-tris(((S)-3,7-dimethyloctyl)oxy) benzamide) (S-N2)

In a three neck round bottom flask under argon, **NBr** (150 mg, 0.31 mmol), **5** (1.15 g, 0.1.46 mmol), K_2CO_3 (149 mg, 2.49 mmol), and $Pd_2(PPh_3)_4$ (18 mg, 0.015 mmol) were introduced and dissolved in dioxane (5 mL) and water was then added (0.2 mL). The reaction was stirred and heated to 100 °C under argon for 36 h. The reaction mixture was then diluted with $CHCl_3$ (80 mL) and washed with water (3 x 80 mL). The organic fraction was collected, dried over $MgSO_4$ and evaporated under reduced pressure. The product was first purified with SiO_2 plug in $CHCl_3$ (50mL) and precipitation from $CHCl_3$ into CH_3CN, affording to a beige solid (365 mg, 0.185 mmol) yield 60%.

^{1}H-NMR ($CDCl_3$, 400 MHz) δ (ppm): 7.73-7.69 (mm, 9H), 7.61 (d, 6 H, *J* = 8.04 Hz), 7.53 (d, 6H, *J* = 8.44 Hz), 7.24 (d partially covered by $CHCl_3$ signal), 7.07 (s, 6H), 4.09-4.02 (mm, 18H), 1.91-1.55 (mm, 30H), 1.34-1.17 (mm, 60 H), 0.96-0.93 (mm, 27H), 0.87 (d, 54H, *J* = 6.6 Hz) ^{13}C-NMR ($CDCl_3$, 100 MHz) δ (ppm): 165.32, 153.32, 146.71, 141.60, 136.95, 136.73, 134.92, 129.94, 127.62, 127.22, 1224.47, 120.45, 105.81; 71.82, 67.83, 39.37, 39.27, 37.51, 37.34, 36.38, 29.86, 29.67, 27.99,24.76, 22.72, 22.61, 19.30; FT-IR (cm^{-1}): 3300, 2955, 2926, 2870, 2845, 1675, 1644, 1601, 1582, 1522, 1494, 1469, 1426, 1400, 1384, 1366, 1333, 1290, 1267, 1236, 1208, 1180, 1113, 1043, 1005, 850, 819, 755, 710, 589, 552, 522.

Tris(3',4',5'-tris(dodecyloxy)-[1,1'-biphenyl]-4-yl)amine (a-N3)

In a three neck round bottom flask under argon, **NPin** (700 mg, 1.12 mmol), **7** (2.63 g, 3.71 mmol), K_2CO_3 (14.2 mg, 135 mmol), and $Pd_2(PPh_3)_4$ (260 mg, 0.225 mmol) were introduced and dissolved in toluene (90 mL) and water was then added (5 mL). The reaction was stirred and heated to 100 °C under argon for 72 h. The reaction mixture was then diluted with $CHCl_3$ (80 mL) and washed with water (3 x 80 mL). The organic fraction was collected, dried over $MgSO_4$ and evaporated under reduced pressure. The product was first purified with SiO_2 chromatography in (Heptane: CH_2Cl_2 v/v 5:5) affording to a viscous amber oil mg however the product oxidized and just traces of the pure product were observed.

^{1}H-NMR ($CDCl_3$, 400 MHz) δ (ppm): 7.44 (d, 6H, *J* = 8.6 Hz), 7.18 (d, 6H, *J* = 8.6 Hz), 6.74 (s, 6H), 4.002 (t, 12H, *J* = 4.5 Hz), 3.98 (t, 6H, *J* = 6.4 Hz), 1.85-1.73 (mm, 18 H), 1.51-1.25 (180 H), 0.90-0.85 (mm, 27H), m/z (MALDI) Calcd. for $[C_{144}H_{24}NO_9]^{\bullet+}$ $[M]^{\bullet+}$, 2131.86 found 2131.90.

6.10 References

[1] Frisch, H.; Unsleber, J. P.; Lüdeker, D.; Peterlechner, M.; Brunklaus, G.; Waller, M.; Besenius, P. *Angew. Chemie Int. Ed.* **2013**, 52 (38), 10097–10101.

[2] Frisch, H.; Fritz, E. C.; Stricker, F.; Schmüser, L.; Spitzer, D.; Weidner, T.; Ravoo, B. J.; Besenius, P. *Angew. Chemie - Int. Ed.* **2016**, 55 (25), 7242–7246.

[3] Görl, D.; Zhang, X.; Stepanenko, V.; Würthner, F. *Nat. Commun.* **2015**, 6, 7009.

[4] Yagai, S.; Hamamura, S.; Wang, H.; Stepanenko, V.; Seki, T.; Unoike, K.; Kikkawa, Y.; Karatsu, T.; Kitamura, A.; Würthner, F. *Org. Biomol. Chem.* **2009**, 7 (19), 3926–3929.

[5] Zhang, W.; Jin, W.; Fukushima, T.; Saeki, A.; Seki, S.; Aida, T. *Science* **2011**, 334 (6054), 340–343.

[6] Boott, C. E.; Leitao, E. M.; Hayward, D. W.; Laine, R. F.; Mahou, P.; Guerin, G.; Winnik, M. A.; Richardson, R. M.; Kaminski, C. F.; Whittell, G. R.; Manners, I. *ACS Nano* **2018**, 12 (9), 8920–8933.

[7] Hudson, Z. M.; Lunn, D. J.; Winnik, M. A.; Manners, I. *Nat. Commun.* **2014**, 5, 1–8.

[8] Sugiyasu, K.; Jung, S. H.; Bochicchio, D.; Pavan, G. M.; Takeuchi, M.; Sugiyasu, K. *J. Am. Chem. Soc.* **2018**, 140 (33), 10570–10577.

[9] Adelizzi, B.; Aloi, A.; Markvoort, A. J.; Ten Eikelder, H. M. M.; Voets, I. K.; Palmans, A. R. A.; Meijer, E. W. J. *Am. Chem. Soc.* **2018**, 140 (23), 7168–7175.

[10] Adelizzi, B.; Aloi, A.; Van Zee, N. J.; Palmans, A. R. A.; Meijer, E. W.; Voets, I. K. *ACS Nano* **2018**, 12 (5), 4431–4439.

[11] Sumerin, V.; Chernichenko, K.; Schulz, F.; Leskelä, M.; Rieger, B.; Repo, T. In Frustrated Lewis Pairs I: Uncovering and Understanding; Springer Berlin Heidelberg: Berlin, Heidelberg, **2013**; 111–155.

[12] Stephan, D. W. *Science* **2016**, 354 (6317).

[13] Geier, S. J.; Stephan, D. W. *J. Am. Chem. Soc.* **2009**, 131 (10), 3476–3477.

[14] Meng, W.; Feng, X.; Du, H. *Acc. Chem. Res.* **2018**, 51 (1), 191–201.

[15] Paradies, J. *Eur. J. Org. Chem.* **2018**, doi.org/10.1002/ejoc.201800944

[16] Chapman, A. M.; Haddow, M. F.; Wass, D. F. *J. Am. Chem. Soc.* **2011**, 133 (45), 18463–18478.

[17] Hou, Q.; Liu, L.; Mellerup, S. K.; Wang, N.; Peng, T.; Chen, P.; Wang, S. *Org. Lett.* **2018**, 20 (20), 6467–6470.

[18] Cao, Y.; Nagle, J. K.; Wolf, M. O.; Patrick, B. O. *J. Am. Chem. Soc.* **2015**, 137 (15), 4888–4891.

[19] Wang, M.; Nudelman, F.; Matthes, R. R.; Shaver, M. P. *J. Am. Chem. Soc.* **2017**, 139 (40), 14232–14236.

[20] Welch, G. C.; Bazan, G. C. *J. Am. Chem. Soc.* **2011**, 133 (12), 4632–4644.

[21] Wang, J.; Wang, N.; Wu, G.; Wang, S.; Li, X. *Angew. Chem. Int. Ed.* **2018**, doi: 10.1002/anie.201812210

[22] Dou, C.; Liu, J.; Wang, L. Sci. *China Chem.* **2017**, 60 (4), 450–459.

[23] Gao, F.-W.; Zhang, F.-Y.; Zhong, R.-L.; Xu, H.-L.; Sun, S.-L.; Su, Z.-M. *Dye. Pigment.* **2017**, 145, 21–28.

[24] Kushida, T.; Shuto, A.; Yoshio, M.; Kato, T.; Yamaguchi, S. Angew. Chem. Int. Ed. Engl. **2015**, 54 (23), 6922–6925.

[25] Kushida, T.; Camacho, C.; Shuto, A.; Irle, S.; Muramatsu, M.; Katayama, T.; Ito, S.; Nagasawa, Y.; Miyasaka, H.; Sakuda, E.; Kitamura, N.; Zhou, Z.; Wakamiya, A.; Yamaguchi, *S. Chem. Sci.* **2014**, 5 (4), 1296–1304.

[26] Lorbach, A.; Hübner, A.; Wagner, M. *Dalton Trans.* **2012**, 41 (20), 6048–6063.

[27] Adelizzi, B.; Filot, I. A. W.; Palmans, A. R. A.; Meijer, E. W. *Chem. A Eur. J.* **2017**, 23 (25), 6103–6110.

[28] Ellis, T. K.; Galerne, M.; Armao IV, J. J.; Osypenko, A.; Martel, D.; Maaloum, M.; Fuks, G.; Moulin, E.; Gavat, O.; Giuseppone, N. *Angew. Chem. Int. Ed.* **2018**, 57,14749-15753.

[29] Faramarzi, V.; Niess, F.; Moulin, E.; Maaloum, M.; Dayen, J.-F.; Beaufrand, J.-B.; Zanettini, S.; Doudin, B.; Giuseppone, N. *Nat. Chem.* **2012**, 4, 485–490.

[30] Hirai, H.; Nakajima, K.; Nakatsuka, S.; Shiren, K.; Ni, J.; Nomura, S.; Ikuta, T.; Hatakeyama, T. *Angew. Chemie Int. Ed.* **2015**, 54 (46), 13581–13585.

[31] Yamaguchi Shigehiro; Wakamiya Atsushi. *Pure and Applied Chemistry* . **2006**, 1413.

[32] Zhang, Y.; Feng, Y.-Q.; Wang, J.-H.; Han, G.; Li, M.-Y.; Xiao, Y.; Feng, Z.-D. *RSC Adv.* **2017**, 7 (57), 35672–35680.

[33] Longhi, G.; Castiglioni, E.; Koshoubu, J.; Mazzeo, G.; Abbate, S. *Chirality* **2016**, 28 (10), 696–707.

[34] Richardson, F. S.; Riehl, J. P. *Chem. Rev.* **1977**, 77 (6), 773–792.

[35] Riehl, J. P.; Richardson, F. S. *Chem. Rev.* **1986**, 86 (1), 1–16.

[36] Kumar, J.; Nakashima, T.; Kawai, T. *J. Phys. Chem. Lett.* **2015**, 6 (17), 3445–3452.

[37] Sánchez-Carnerero, E. M.; Agarrabeitia, A. R.; Moreno, F.; Maroto, B. L.; Muller, G.; Ortiz, M. J.; de la Moya, *S. Chem. A Eur. J.* **2015**, 21 (39), 13488–13500.

[38] Kumar, J.; Nakashima, T.; Tsumatori, H.; Mori, M.; Naito, M.; Kawai, T. *Chem. A Eur. J.* 2013, 19 (42), 14090–14097.

[39] Kumar, J.; Nakashima, T.; Tsumatori, H.; Kawai, T. *J. Phys. Chem. Lett.* **2014**, 5 (2), 316–321.

[40] De Greef, T. F. A.; Smulders, M. M. J.; Wolffs, M.; Schenning, A. P. H. J.; Sijbesma, R. P.; Meijer, E. W. *Chem. Rev.* **2009**, 109 (11), 5687–5754.

[41] Wolffs, M.; Korevaar, P. A.; Jonkheijm, P.; Henze, O.; Feast, W. J.; Schenning, A. P. H. J.; Meijer, E. W. *Chem. Commun.* **2008**, 38, 4613–4615.

[42] Louis, M.; Sethy, R.; Kumar, J.; Katao, S.; Guillot, R.; Nakashima, T.; Allain, C.; Kawai, T.; Métivier, R. *Chem. Sci.* **2019**.

[43] Haedler, A. T.; Kreger, K.; Issac, A.; Wittmann, B.; Kivala, M.; Hammer, N.; Köhler, J.; Schmidt, H.-W.; Hildner, R. *Nature* **2015**, 523, 196.

[44] García, F.; Buendía, J.; Ghosh, S.; Ajayaghosh, A.; Sánchez, L. *Chem. Commun.* **2013**, 49 (81), 9278–9280.

[45] Basak, S.; Nandi, N.; Bhattacharyya, K.; Datta, A.; Banerjee, A. *Phys. Chem. Chem. Phys.* **2015**, 17 (45), 30398–30403.

[46] Shao, H.; Nguyen, T.; Romano, N. C.; Modarelli, D. A.; Parquette, J. R. *J. Am. Chem. Soc.* **2009**, 131 (45), 16374–16376.

[47] Más-Montoya, M.; Janssen, R. A. *J. Adv. Funct. Mater.* **2017**, 27 (16), 1605779.

[48] Kumar, M.; George, S. J. *Nanoscale* **2011**, 3 (5), 2130–2133.

[49] Shih, C.-J.; Lee, C.-C.; Yeh, T.-H.; Biring, S.; Kesavan, K. K.; Amin, N. R. Al; Chen, M.-H.; Tang, W.-C.; Liu, S.-W.; Wong, K.-T. *ACS Appl. Mater. Interfaces* **2018**, 10 (28), 24090–24098.

[50] Mallia, A. R.; Hariharan, M. *J. Phys. Chem. C* **2017**, 121 (9), 4778–4788.
[51] Zhang, J.; Sharman, E.; Yang, L.; Jiang, J.; Zhang, G. *J. Phys. Chem. C* **2018**, 122 (45), 25796–25803.
[52] Hannon, M. J.; Moreno, V.; Prieto, M. J.; Moldrheim, E.; Sletten, E.; Meistermann, I.; Isaac, C. J.; Sanders, K. J.; Rodger, A. *Angew. Chemie Int. Ed.* **2001**, 40 (5), 879–884.
[53] Rodger, A.; Dorrington, G.; Ang, D. L. *Analyst* **2016**, 141 (24), 6490–6498.
[54] Adelizzi, B.; Aloi, A.; Markvoort, A. J.; Ten Eikelder, H. M. M.; Voets, I. K.; Palmans, A. R. A.; Meijer, E. W. *J. Am. Chem. Soc.* **2018**, 140 (23).
[55] Onogi, S.; Shigemitsu, H.; Yoshii, T.; Tanida, T.; Ikeda, M.; Kubota, R.; Hamachi, I. *Nat Chem* **2016**, 8 (8), 743–752.
[56] Verhoeven, J. W. J. Photochem. Photobiol. C *Photochem. Rev.* **2006**, 7 (1), 40–60.
[57] Dimitriev, O. P.; Piryatinski, Y. P.; Slominskii, Y. L. J. Phys. *Chem. Lett.* **2018**, 9 (9), 2138–2143.
[58] Hoffmann, S. T.; Schrögel, P.; Rothmann, M.; Albuquerque, R. Q.; Strohriegl, P.; Köhler, A. *J. Phys. Chem. B* **2011**, 115 (3), 414–421.
[59] Ware, W. R. J. *Phys. Chem.* **1962**, 66 (3), 455–458.
[60] Gijzeman, O. L. J.; Kaufman, F.; Porter, G. J. *Chem. Soc. Faraday Trans. 2 Mol. Chem. Phys.* **1973**, 69 (0), 708–720.
[61] Gorman, A. A.; Rodgers, M. A. J. *J. Am. Chem. Soc.* **1986**, 108 (17), 5074–5078.
[62] Nau, W. M.; Scaiano, J. C. *J. Phys. Chem.* **1996**, 100 (27), 11360–11367.
[63] Chen, H.; Huang, Z.; Wu, H.; Xu, J.-F.; Zhang, X. *Angew. Chem. Int. Ed.* **2017**, 56 (52), 16575–16578.
[64] Tantakitti, F.; Boekhoven, J.; Wang, X.; Kazantsev, R. V; Yu, T.; Li, J.; Zhuang, E.; Zandi, R.; Ortony, J. H.; Newcomb, C. J.; Palmer, L. C.; Shekhawat, G. S.; de la Cruz, M. O.; Schatz, G. C.; Stupp, S. I. *Nat. Mater.* **2016**, 15, 469.
[65] Mes, T.; Van Der Weegen, R.; Palmans, A. R. a; Meijer, E. W. *Angew. Chem. Int. Ed.* **2011**, 50, 5085–5089.
[66] Helmich, F.; Smulders, M. M. J.; Lee, C. C.; Schenning, A. P. H. J.; Meijer, E. W. *J. Am. Chem. Soc.* **2011**, 133 (31), 12238–12246.
[67] Li, X.; Shi, Z. J. *Org. Chem. Front.* **2016**, 3 (10), 1326–1330.

Some general conclusions and future perspectives

With the consolidation of supramolecular chemistry and the development of many fundamental tools to control the supramolecular polymerization, it is now time to exploit this knowledge into real materials and applications. To enable this transition, the field of supramolecular polymers needs to be expanded towards multicomponent supramolecular systems and merged with material science and technology. This broadening requires, *inter alia*, the acquisition of the knowledge to control the complexity of these systems and the use of functional building blocks.

This thesis present our efforts in this direction. We developed supramolecular homopolymers and copolymers based on building blocks commonly used in optoelectronics. The behavior of the supramolecular homopolymers was studied in solution and used to establish a first rationalization of the dynamics involved in the supramolecular copolymers and their structure. We then exploited these systems in water-splitting solar cells to demonstrate that mastering the organization of a material's nanostructure is crucial to improve its performance.

However, bringing supramolecular polymers into action highlights the necessity of further enhancing the performance of these systems. As introduced in Chapter 4, to achieve so, it is necessary to work on improving the interaction between the supramolecular polymers and inorganic interfaces, and via the development of systems with enhanced optoelectronic properties. We believe that the strategies used in Chapter 4, although primitive, are promising to create an optimized platform to link supramolecular and inorganic materials. In addition, the direct application of supramolecular strategies on established organic electronic materials may enhance both ordering and performance.

We also sustain that properties that are still not achievable with current monomers, covalent polymers, and supramolecular polymers, can be attained via carefully designed supramolecular copolymers. Our efforts in Chapter 6 describe a promising strategy to find new systems that may result in unexpected properties once supramolecularly copolymerized. The promising early results achieved in that chapter display a possible direction for future functional supramolecular copolymers.

Summary

Functional supramolecular materials

Fundamentals, copolymers and application

At the beginning of this century, the great potential and complexity of supramolecular polymers have emerged. Recent progress in the fundamental understanding of supramolecular polymerization has pushed the field towards a real exploitation of these systems into applications. However, the combination of both structural control and functionality in supramolecular polymers is still an open challenge. Supramolecular polymers with controlled size and structure are often achieved using monomers which lack functionality, whereas functional monomers often display complex polymerization profiles which renders their control less straightforward. In this thesis, we aim to study functional supramolecular polymers and copolymers and to exploit them in opto-electronic applications. This research encompasses both fundamental studies on the control of the (co)polymerization and the exploitation of these system in solar cells.

In Chapter 1, an introduction of the field of supramolecular polymerization and copolymerization is given. By constructing parallels with their covalent counterpart, an analytical perspective on supramolecular copolymers is presented. A classification of supramolecular copolymers based on their microstructure and thermodynamic parameters is conveyed along with the current state of the art of the field. We additionally comment on the strategies so far used to analyze the supramolecular copolymers sequence and the possible application of these multicomponent systems.

In Chapter 2, two families of C_3-symmetrical triarylamine-triamides comprising a triphenylamine- or a tri(pyrid-2-yl)amine-core are presented. Both families undergo supramolecular polymerization in apolar solvents via a cooperative mechanism, which involves the formation of hydrogen-bonding interactions as evidenced by spectroscopic measurements and validated by DFT calculations. The introduction of stereocenters in the side chains biases the helical sense of the supramolecular polymers formed. Compared to other typical C_3-symmetrical monomers, triarylamine-based systems display a richer assembly landscape. Two assembled states of opposite handedness are accessed by tuning the temperature of the system. This complexity is attributed to two different conformations in the assembled state which are the origin of the polymer's helicity. Moreover, spectroscopic measurements varying the water-content of the solutions demonstrate that co-dissolved water in alkanes plays a fundamental role in the transition between the two states. In fact, we find that other supramolecular

polymers that possess conformational flexibility also show a high sensitivity to the amount of co-dissolved water.

In Chapter 3, the functional supramolecular polymers are exploited as spin filters in water-splitting solar cells. In a collaborative work with prof. dr. Ron Naaman and coworkers at the Weizmann Institute of Science (IL), we studied the impact of chiral supramolecular polymers in the context of water-splitting dye-sensitized photoelectrochemical cells (DS-PEC). The study includes spectroscopic analyses of the assembled polymers in solution, to verify the formation of chiral polymers, and magnetic atomic force microscopy, to measure the spin selection due to a physical effect called chiral induced spin selectivity (CISS effect). The effect of the functionalization of TiO_2 anodes with chiral supramolecular polymers was evaluated in DS-PEC under illumination. The chiral functionalization results not only in an increase of device's current but also in the depletion of the water peroxide formed as byproduct of the reaction, demonstrating the possibility of controlling the spin in the reaction exerting spin selection with supramolecular polymers.

Research within this field is continued in Chapter 4. In this section we report on improvements to chiral-functionalized water-splitting devices by implementing a more classical design of dye sensitized solar cells (DSSCs). The chapter is focused on confirming the reproducibility of the effect and improving the efficiency and stability of the cells. A standardized procedure for the fabrication of porous TiO_2 anodes is introduced along with an improved procedure for the deposition of supramolecular polymers. Supramolecular anchors are also examined to improve the device's stability. A library of anchoring tripyridylamine monomers is designed and synthesized to covalently link to the TiO_2 surface and non-covalently interact with the chiral supramolecular polymers made with the same core. A careful selection of the anchoring molecule results in great improvement of the chiral order and a modest improvement in time-stability. Finally, the study on a chiral supramolecular polymers based on classic donor–π bridge–acceptor (D-π-A) design of dyes is reported. We exploit its chiral assembly to obtain water-splitting solar cells able to operate under visible light while exerting spin-selection. C_3-symmetric triphenylamine-based dyes bearing a chiral periphery were synthesized and their supramolecular polymerization studied. Supramolecular characterization and initial testing displayed promising results confirming the advantage of using chiral systems.

In Chapter 5, our interest returns to fundamental research exploring multicomponent supramolecular systems in solution. Here, the study of the microstructure of triarylamine triamides-based supramolecular copolymers through a comprehensive battery of spectroscopic, theoretical, and super-resolution microscopic techniques is described. We demonstrate via spectroscopic analysis that the supramolecular copolymerization obtained by mixing tripyridylamine-based and triphenylamine-based monomers leads to a microstructure that is independent of the copolymerization protocol. The small but pronounced deviation of the experimental spectra from the linear combination of the homopolymers' spectra hints to the formation of block

copolymers. A mass balance model is introduced to further unravel the microstructure of the copolymers. The simulated data confirm that stable multi-block supramolecular copolymers can be accessed from different routes and that the multi-block structure originates from the fine balance between favorable hydrogen bonding interactions in combination with a small mismatch penalty between two different monomers. Finally, we visualize the formation of the supramolecular block copolymers by adapting a recently developed super resolution microscopy technique, interface point accumulation for imaging in nanoscale topography (iPAINT), for visualizing the architectures formed in organic media. The combination of multiple techniques is crucial to unveil the polymer sequence of these complex dynamic supramolecular systems.

Finally, Chapter 6 aims to develop and study supramolecular copolymers with new emerging functionalities. In collaboration with prof. dr. Shigehiro Yamaguchi's group at Nagoya University (JP), we aimed to study boron-nitrogen supramolecular copolymers. A library of bridged-triarylborane supramolecular monomers and triphenylamine analogues is designed and synthesized. The formation of homopolymers in apolar solvents is studied via variable temperature spectroscopic analysis. After selection of the most promising B-N couple, we report on preliminary supramolecular copolymerization experiments. Although absorbance and circular dichroism studies do not show features that can be assigned to the formation of copolymers (suggesting self-sorting of the system) emission studies reveal the emergence of a green fluorescence with remarkably long lifetime. Combination of circular polarized luminescence, oxygen-free lifetime measurements, and variable temperature emission spectra demonstrate the presence of B-N couples within the supramolecular copolymers chain. Kinetic studies demonstrate the growth of B-N interactions over time, suggesting a slow copolymerization of the system upon aging.

The thesis ends with a comprehensive conclusion on this research field aiming to highlight the strength and potential of exploiting functional supramolecular polymers and copolymers and possible future directions.

Curriculum Vitae

Beatrice Adelizzi was born on November 11, 1988 in Monza (Italy). After finishing her secondary education in 2007 and concluding her career in the Italian national team of synchronized swimming in 2009, she studied Chemical Science and Technology at the University of Milano Bicocca (Italy). During her bachelor studies she performed the graduation internship in the group of prof. dr. Alessandro Abbotto where she worked on the synthesis and characterization of conjugated dyes for dye-sensitized solar cells. In 2012 she graduated *cum laude*. During her master program, she was awarded with an Erasmus Exchange scholarship and performed an internship of 7 months in the group of prof. Luisa De Cola at the Institut de Science et d'Ingenierie Supramoléculaires in Strasbourg (France) where she worked on the synthesis and characterization of iridium complexes for photo-induced water-splitting. After graduating *cum laude* under the supervision of prof. dr. Alessandro Abbotto and prof. Luisa De Cola in 2014, she started her PhD project in 2015 at the Technical University of Eindhoven (The Netherlands). Supervised by prof. dr. E. W. Meijer and dr. ir. A. R. A. Palmans in the research group of Macromolecular and Organic Chemistry, she investigated the dynamic structure of functional supramolecular polymers and copolymers and their exploitation in water-splitting devices. During her PhD studies, she visited the groups of prof. dr. Ron Naaman at the Weizmann institute of Science (Israel), prof. dr. David A. Leigh at The University of Manchester (UK), and prof. dr. Shigehiro Yamaguchi at Nagoya University (Japan) for fruitful collaborations. The most significant results of her research are presented in this dissertation.

List of publications

H. M. M. Ten Eikelder, A. J. Markvoort, B. Adelizzi, A. R. A. Palmans, E. W. Meijer, Modeling supramolecular copolymerization: insight into the effect of solvent on the block length. *Manuscript in preparation*

X. Meng, T.Putzeys, B. Adelizzi, I. Urbanavičiūtė, S. C. J. Meskers, A. R. A. Palmans, M. Kemerink, E. W. Meijer, M. Wübbenhorst, R. P. Sijbesma, Polar switching in a hydrogen-bonded tripyridyl-amine, *Manuscript in preparation*

N. J. Van Zee, B. Adelizzi, A. R. A. Palmans, E. W. Meijer, Chiral amplification enhanced through the binding of water within helical supramolecular polymers in apolar solvents. *Manuscript in preparation*

B. Adelizzi, A. Rösch, A. J. van Rijen, S. R. Martire, S. Esiner, M. Lutz, A. R. A. Palmans, E. W. Meijer, Chiral supramolecular dyes for reducing the production of water peroxide in water-splitting solar cells. *Submitted*

B. Adelizzi, N. J. Van Zee, L. N. J. de Windt, A. R. A. Palmans, E. W. Meijer, The future of supramolecular copolymers unveiled by reflecting on covalent copolymerization. *Submitted*

N. J. Van Zee, B. Adelizzi, M. F. J. Mabesoone, X. Meng, A. Aloi, R. H. Zha, M. Lutz, I. A. W. Filot, A. R. A. Palmans, E. W. Meijer, Potential enthalpic energy of water in oils exploited to control supramolecular structure. *Nature*, **2018**, 558, 100-103

B. Adelizzi, A. Aloi, A. J. Markvoort, H. M. M. Ten Eikelder, I. K. Voets, A. R. A. Palmans, and E. W. Meijer, Supramolecular Block Copolymers under Thermodynamic Control. *J. Am. Chem. Soc.* **2018**, 140 (23), 7168-7175
Spotlighted in: J. Am. Chem. Soc. **2018**, 140, 7045–7045

B. Adelizzi,† A. Aloi,† N. J. Van Zee, A. R. A. Palmans, E. W. Meijer, and I. K. Voets, Painting Supramolecular Polymers in Organic Solvents by Super-resolution Microscopy. *ACS Nano* **2018,** *12* (5), 4431-4439
† these authors equally contributed to the paper.

W. Mtangi, F. Tassinari, K. Vankayala, A. V. Jentzsch, B. Adelizzi, A. R. A. Palmans, C. Fontanesi, E. W. Meijer, and R. Naaman, Control of Electrons' Spin Eliminates Hydrogen Peroxide Formation During Water Splitting. *J. Am. Chem. Soc.* **2017**, *139* (7), 2794-2798

B. Adelizzi, I. A. W. Filot, A. R. A. Palmans, E. W. Meijer, Unravelling the Pathway Complexity in Conformationally Flexible *N*-Centered Triarylamine Trisamides. *Chem. Eur. J.* **2017**, 23, 6103

Acknowledgments

I still remember the weekend I moved to Eindhoven in January 2015, I was constantly oscillating between agitation (I totally did not know what to expect) and excitement (I did not know what to expect, but I knew it was going to be cool!). Today I can safely say that doing the PhD here has been the best experience of my life, I passed an incredibly beautiful and positive period. I learnt so much about science, and about myself, and I met an incredible group of people. Even if I feel like I just arrived, unfortunately my time at the TU/e has come to an end. So here it comes, the time to thank and say goodbye.

First of all, *Bert*, thank you for all. From taking interest in my PhD application, to all the time spent in discussing and brainstorming. Your guidance and your example as group leader will be impressed in my mind permanently. I still find incredible how you and Anja create a dreamily working research group where top-notch science goes perfectly along with kindness and humanity. Thanks for all the opportunity given to me in these four years, from the freedom of designing my own research projects, to the conferences and the collaboration with important research groups all around the world. All of this gave to me a constant great motivation to do the best I could.

Anja, you are a fundamental and indispensable pillar of the group, as I just said for Bert, the incredible working environment and efficiency of the group is possible also because of you. I really want to thank you for the great guidance you gave me in these years and your incredible attitude where dedication, resolution and sensitivity are so well mixed. Thank you for all the time spent discussing with me on scientific matters and not. It has always been incredibly useful. Some advice is indelibly impressed and I will keep considering it for building my future.

I would like to express my gratitude to all the member of the committee. Thank you for being part of my committee and for the review of this thesis. Prof. dr. *Roeland Nolte*, thank you for the time spent in reading my thesis and for the comments given. I enjoyed our fruitful discussion with dr. Nathan van Zee and Bert about the water–effect on supramolecular polymers. Prof. dr. *Jerome Lacour*, I am grateful for having had the chance to come to the Bürgenstock conference and help with the technical organization of the conference. It has been a pleasure meeting you as much as it has been a pleasant surprise meeting you again in Nagoya during our visiting stays. I enjoyed the stimulating conversations and I am especially grateful for the suggestions you gave me to pursue my academic career in Paris with Prof. dr. Ludovic Jullien, where I will be going next. Thank you for accepting the invitation of being part of my PhD committee and visiting Eindhoven. Dear prof. dr. *Rint Sijbesma*, dear Rint, thank you very much for all the fruitful discussions we had over these four years. I enjoyed collaborating with dr. Xiao Meng for testing tripyridylamine as ferroelectric materials and I am confident it will be concluded in a nice joint publication. Dear dr. *Stefan Meskers*, dear Stefan, I am thankful for the important constructive criticism you gave me on the thesis, which helped to improve the quality of the final version. Thank you for all the fruitful and open-minding discussions we had throughout these years and for all the help in the lab with advanced spectroscopy measurement. Dear prof. dr. *Alessandro Abbotto*, I want to thank you for the all guidance from my bachelor degree to the master degree. I appreciated your acceptance to be part of the PhD committee and I hope you will be able to join the defense in Eindhoven.

During these four years I had the opportunity to establish great and fruitful collaborations. I would like to thank *Ivo*, *Bart* and *Huub* for the collaboration on DFT simulation and mass-balance modelling. The excellent results we achieved together resulted fundamental for understanding the systems studied and obtaining such nice publications.

I want to thank all the people involved in the *Marie Curie Euro-sequence ITN* for all the great time spent together, the conferences and the parties. Especially I would like to thank prof. dr. *David Leigh* for hosting me during my secondment and for the great time had in Manchester with *Adrian* and *Javier* and all Leigh's group.

I want to thank prof. dr. *Ron Naaman* for the fruitful collaboration, which resulted in a beautiful publication on how chiral supramolecular polymers can positively affect water-splitting processes. Thank you for the inspiring conversations, meetings and for the hospitality in Israel. Thank you *Wilbert* and *Francesco* for the direct collaboration and the patience in explaining me the electrochemistry measurements and the CISS

effect. Francesco, special thanks for the help in polishing Chapter 3. *Chidambar*, thank you for sharing with me this amazing experience, and for all our subsequent discussions on the CISS effect.

Thank you *Xiao* and *Rint* for the collaboration on ferroelectric materials, I am excited for the submission of the paper. Dear *Ilja*, thank you for the fruitful collaboration with *Antonio* and *Nate* on painting supramolecular polymers in organic solvent. The collaboration resulted in great results and in a powerful and useful technique. Thank you *Nate* (and *Mathijs* for the incredible modeling) for discovering the role of water in oil (and for creating a great panic in the group with it!). I finally know why my results were irreproducible! Thank you also for the collaboration for the perspective with *Lafayette*. Dear *Lara*, I really enjoyed your period here and sharing the fume hood (and the CD troubles) with you. Thank you also for our weekend in Malaga, we should totally do it again!

I am then extremely grateful for the opportunity I had to collaborate with prof. dr. *Shigehiro Yamaguchi*. Thank you for accepting our proposal on collaborating on the B-N supramolecular copolymers and for hosting me in Nagoya. Special thanks to dr. *Naoki Tanaka* for the incredible dedication you put in our work and for helping me in obtaining amazing molecules in less than 2 weeks. Thanks to dr. *Aiko Fukazava* and dr. *Soichiro Ogi* for the highly interesting conversations and for the help in shipping back and forth the molecules. It has been a very pleasure meeting you. Thank you *Johannes* and *Ethan* for the nice time spent together (mainly eating ramen and chewy candies). Thank you then to the entire group for all the nice time, Japanese food tasting, and the incredible sympathy inside and outside the lab. It has been a wonderful experience. Related to B-N, thank you *Pongphak* to take over the project and continue to explore the "beauty" of B-N copolymers.

These four years would not have been the same without the students I had the pleasure to work with. *Evelien*, *Simone* and *Daan*, it has been a real pleasure working with you on incredibly challenging projects. Your dedication and enthusiasm is reflected in Chapter 4. A special thanks to *Daan* for creating the basis for all the consecutive work we did on the devices. Thank you for your stubborn, positive and prepositive attitude, it has been a great pleasure collaborate with you for the months you stayed after your internship. And after what Daan started, thank you *Andreas R.* to continue and conclude the experiments on the chiral-functionalized water-splitting solar cells. Dear *Serkan*, a great thank you for your immeasurable help with electrochemistry (theory and practice) and for your unbelievable patience and kindness.

I would like then to continue with my paranymphs, better called "*puttini*", a cute term for saying "*puttos*" (like the blond and the dark cherub angels, see the Raffaello painting if you are still puzzled). Your young aspect, curly hair and kindness cannot be better described by them. That is exactly why I thought it would have been the best idea having angels protecting me during my thesis defense (even if you were dressed more as penguins than as angels…fortunately!). However you are much more than puttos…*Anto*, I literally don't know where to start with thanking you. You have been a fundamental ~~pillar~~foundation of these 4 years in Eindhoven. I could start thanking you for your incredible energy and mood that is able to make even the saddest person in the world laugh, or for your patience in listening to me (and my anxiety), or for the incredible support (time-wise, physiologically-wise, taxi-wise, etc..) you gave me when I had the surgery. I don't know exactly what having a brother means, but I am sure it is not so different from having an Aloi as a friend... (and I have proof for it, my mum even calls you to make sure I am ok!...I think also my mum is considering you a bit my brother). *Mathijs*, you are the nicest, kindest, most open and most flexible Dutch person I ever met! Your arrival in Bert's group has been a great gain for me and, I believe, for the entire group. You are an incredible person all around, from your incredible chemistry skills and intelligence to your great personality. Your wide spectrum of interests from art to music, movies (better if without words), boardgames, beers, stamppot (thanks a lot for those great nights), places to visit, politics, economy, philosophy, and books make you one of the most interesting person to speak with (and to do pubquiz with). I always enjoyed speaking with you about the present and future, thank you for all. In addition, I totally have to thank you for having repetitively invited me and Nate to do things together…perfect timing, perfect choice of people (and perfect saddest movie ever).

The great thing of doing the PhD in such a collaborative environment is the opportunity of meeting many great people. Retreats, parties, colloquia, TGIFs have been always a pleasure and thanks to all the SMO family for it.

Special thanks to *Simone H*. and *Peter Paul* (PP, P², 2P) for sharing the office with me and for the nice environment. Simone thank you for all the help in dealing with the Dutch bureaucracy from day 1 to Form II (and beyond), thank you for your kindness and patience. Peter Paul, thank you for you endless philosophical approach to things. I still remember when TU/e was building the groene loeper and you compared that muddy mess to the first months of the PhD: "*you see…the beginning will be a muddy mess but then it will become a beautiful green park, really similar to a PhD in the end*".

Thank to my officemates of my last 6 months, *Mathijs*, *Brigitte*, *Silvia V.*, thank you for the great environment, the random chats and the coffee breaks. Thank you also for your patience on listening to my Italian curses every time Adobe illustrator crashed… Brigitte you are a great and strong woman, thank you for saying always what you think and for all the discussions we had. Silvia, thank you for all our morning coffees and our late evening chats, you kindness and sweetness helped me a lot during the writing period. You always had a nice word for me, thank you very much!

Thank you then to all the members (present and past) of Bert group. A gigantic thank will not be enough for *Carla* and *Martina*, the constant support for every issue, the laugh when needed and the help for bureaucracy, meetings, Dutch things, travels. You saved me years and years of stress, thank you! *Jolanda* and *Bas*, thank you for your constant help. Jolanda, thank you for keeping the labs perfectly clean and working (the job you do is just incredible), for all the fumehood chats, and for the building blocks you gave me. Bas, without you I will be still trying to purify my compounds, thanks for your help and kindness. Thanks to some former SMO member that marked my beginning here: *Hellen, Matt and Daan v.d.Z., Nick* (great memories of the trip in Rome and all the tips you gave me for my trip to New Orleans), *Andreas H., Andreas V., Misha* (see you in Paris!), *Bram* (especially for all the cardio core and body pump classes), *Sabrina, Maxime, Neus*,. A big thank to all the present group members (office by office to not forget anyone): *Sjors, Gijs, Andreas R., Simone, Martin, José, Katja, Marcel, René, Elisabeth, Julian, Lu, Lafayette, Chidambar, Ghislaine, Sandra, Silvia V., Brigitte, Mathijs, Giulia, Marcin, Ponghpak, Tomo, Cristiaan, Fabian*, and *Anjana*. Along with the nice science, I liked so much our lunch together and the nice environment created in the last period, the coffees and all the chats.

Following the line of people that had a fundamental role in my PhD. *Sabri*, without you I would have probably given up after my first month. But, you started to make me feel home as just an Italian would know how to do: by organizing incredibly tasty lunches and dinners! I still remember the incredibly warm feeling I had when we were having Sunday lunch together in Roermond (and I also totally remember that Babà…). Thank you for your unbelievable sweetness, wisdom, patience and kindness. Of course, *Luca*, Sabri did not do all alone, so thank you very much as well, for your availability, kindness, and hospitality and for all the chats about polymers and high-tech technology! *Marianna*, with two parents like that you could not be less amazing than what you are! Your happiness and energy are so contagious! Thank you also to the Italian family you created, thanks *Dario*, *Vito*, *Francesco S.*, *Maxime*, *Laura*, *Matilde*, *Rodi*, I loved our food and games oriented parties and especially cheating in codenames...

Caro *José*, Thank you for all your support from day 1 to day n. Thank you for being always there to discuss about chemistry and life (mainly in front of a coffee). A great thank for inviting us to spend the New Year in Rome. It has been a fantastic weekend. …The fact that they were always mistaking us for Americans just for being with Nate and Nic; the run to the supermarket for buying our new-year's eve dinner (Cacio e pepe rules); and the new-year's eve walking across entire Rome (I suppose we walked billions of kilometers in one night)!

DnD group(s): first of all (just for respect) thanks to the masters: *Alberto and Nate*, thank you for bringing us in fantastic worlds such as creepy-dark-dead-kids-oriented world (Alberto) or vampire-scifi-clippingtoes-Bob-bobby-oriented world (Nate). Thanks to all the members, *Gianmarco* (too evil to me chaotic neutral), *Fabio* (the best bard), *Anto and Lupino* (R.I.P., we still hate Vale for what did to you), *Tommy* (quite a dramatic change from "I'm lawful good I cannot do evil" to "let's recklessly go in rage" against every single thing in front of you), *Valerio D. P.* (we forgive but not forget what you did to poor Lupino), *Emily* (the best to resist in a drinking competition against the tavern's owner). Our DnD sessions were always full of fun, chips and 1s!

Thank you to the other Italian group, *Alberto*, *Anto* (oh but you are everywhere!), *Arianna*, *Francesco*, *Tommy*, *Valerio Z.*, *Sasa*, *Valerio D. P.*, *Serena*, *Ellen*, thank you for all the great time spent together for the nice dinners, GOT sessions, cards against humanity and especially for the incredibly positive atmosphere you can

create both as single person and as group. Alberto (maestro, jedi master, yoga master, zen master) grazie per tutto, dal cibo ripieno di burro, alle 3 ore di allenamento di fila, ai discorsi (forse troppo?) profondi. Arianna adoro la tua contagiosa energia positiva (e poi a quanto pare ci assomigliamo!).

A thank goes to all the (present and past) Climbing group. Especially to *Anto* (again? stop it!), *Alberto* (without your patience I would have quit the first day), *Valerio D. P.* (and our aim to do yellows before the PhD….) and *Christian* (I still don't understand how you can tolerate climbing with three crazy Italians, but thanks to do it, you are always fun!)

Thank you to *Noortje*, *Bregje* and *Elisabeth*, I loved training you and spending time together creating choreographies and stretching legs! (Apologies for all the time I mispronounced your names.)

Cimici, grazie per riuscire a mantere l'amicizia anche a 1000 Km di distanza. I vostri deliri chimici-cimici mi sono mancati molto qui, ma ogni volta che tornavo a casa ho potuto constatare che il livello di delirio é rassicuratantemente costante. Un grazie enorme a *Danette* (e *Luca Mascheprotti!!*), *Gian* e *Fede* per essermi venuti a trovare una o piu volte ed aver portato qui la giusta follia necessaria.

Grazie anche a tutti gli altri carissimi amici che in un modo o nell' alltro hanno fatto parte di questo cammino. *Marti B., Skiro, Chiara V., Mauro, Chiara e gli Amoretti*, grazie per aver sempre trovato del tempo per salutarmi quando venivo di corsa a casa e/o per essermi venuti a trovare in Olanda.

Thanks to all my Strasbourg friends, especially *Elena*, *Nadia*, *Thomas and Amparo,* for helping me to start my PhD here and for all the chats we had now and then.

Grazie a tutta la mia famiglia. *Nonna Maria, Nonna Vittoria, Zii, Zie e cugini.* Un grazie speciale a *Zio Pietro* e *Zia Livi* per ospitarci ad Alghero e farci rilassare quando piú ne avevamo bisogno. Grazie *Zia Cinzia* per i paracolli tattici da bicicletta, senza quelli non sarei mai potuta andare a lavoro!

Prima di finire, vorrei ringraziare ancora *Laura D. R.* e *Ambra*, se non fosse per tutto quello che mi avete insegnato e allenato a sopportare, affrontare un dottorato all'estero sarebbe stato molto piú difficile.

So che le pagine di questi ringraziamenti sono giá molte, e so anche che non ne basterebbero il doppio per ringraziare voi, *Mamma e papá*. Il vostro infinito e indistruttibile sostegno é stato il punto solido che mi ha permesso di riuscire in questo dottorato. Prima di ringraziarvi, mi voglio scusare per tutte le ansie e le sfuriate che avete sopportato quando ovviamente, non ne eravate la ragione. Grazie per capire e per supportarmi/sopportarmi. Grazie per avermi insegnato a mirare sempre in alto e, che con la giusta motivazione non c'é limite. Grazie per avermi insegnato a non adagiarmi e per avermi dato la spinta che mi serviva in ogni momento. Grazie Ma per essere corsa qui per le operazioni e grazie Pa per avere fatto 999999 km Lissone-Orio-Malpensa includendo anche partenze alle 4 o 5 del mattino…

And you, *my little Nate*…where to start? I should thank you for an uncountable amount of reasons, let's just begin with: "*Hey Bea, can I disturb you? After your colloquium I synthesized this molecule but I am not sure I understand these CD curves*"… Thanks for being the most supportive and understanding person I have ever met. Thank you for being exactly what you are, that is exactly what I need, in any situation. Thank you for the coffees, the best ideas we had were born exactly there. Half of the PhD (and of my papers) would have been completely different without those coffees (and you).

I am excited to continue our adventure in Paris, together.

Thank you all

Bea